IMPROVING SOLID OXIDE CELL PERFORMANCE AND DURABILITY BY OPTIMIZING IONIC AND ELECTRONIC TRANSPORT IN ELECTROLYTE

by

Lei Zhang

A dissertation submitted to the faculty of
The University of Utah
in partial fulfillment of the requirements for the degree of

Doctor of Philosophy

Department of Materials Science and Engineering

The University of Utah

December 2015

The University of Utah Graduate School

STATEMENT OF DISSERTATION APPROVAL

The dissertation of **Lei Zhang**

has been approved by the following supervisory committee members:

Anil V. Virkar	, Chair	**05/12/2015** Date Approved
Feng Liu	, Member	**05/12/2015** Date Approved
Dinesh K. Shetty	, Member	**05/12/2015** Date Approved
Hong-Yong Sohn	, Member	**05/12/2015** Date Approved
Ling Zang	, Member	**05/12/2015** Date Approved

and by **Feng Liu** , Chair/Dean of

the Department/College/School of **Materials Science and Engineering**

and by David B. Kieda, Dean of The Graduate School.

ABSTRACT

The current status of solid oxide fuel cell (SOFC) development is reviewed. A parametric model based on real cell materials and components was developed. Current cathode material and structure are sufficient, and the limiting factors are gas diffusion through the supporting layer and ohmic loss through the whole cell. Once the latter two losses can be minimized, SOFC can offer the best performance.

Most of the ohmic loss can be attributed to ionic resistance in the electrolyte, of which more than 50% is due to grain boundary resistance. A quantitative space charge theory is developed for YSZ by considering all the possible defect species and defect complex. Both oxygen vacancy depletion and yttrium segregation near the grain boundary contribute to the very high grain boundary resistivity. A nonequilibrium analysis suggests that quenching at higher temperature can improve both grain bulk and grain boundary conductivity.

Nowadays, reversible solid oxide cells (SOC) can be used in both fuel cell mode to generate energy and in electrolyser mode (SOEC) to store energy. However, a SOC degrades much faster when working in the SOEC mode. Oxygen chemical potential in the solid electrolyte near the oxygen electrode could be very high and leads to crack growth. Introducing finite electronic conductivity by doping can prohibit such crack growth.

A novel oxygen permeation technique has been developed to measure electronic

partial conductivities in solid electrolyte materials. Oxygen can be pumped into the sample by applying DC bias. As excess oxygen is stored in the cavity, the generated Nernst potential drives permeation current. At steady state, oxygen pumped into the cavity equals that which permeates out. When DC bias is turn off, Nernst potential follows a slow decay with time. Analysis of both steady state data and transient process data gives electronic resistance.

Proton exchange membrane fuel cell (PEMFC) is now used in electrical cars. The wide application of PEMFC is currently limited by its cost and degradation. Even with a trace amount of carbon monoxide, Pt catalyst will be poisoned. A novel technique is developed to study CO adsorption and desorption kinetics by monitoring the resistance variation.

CONTENTS

ACKNOWLEDGMENTS

With this work, I would like to give my sincere appreciation to Dr. Anil V. Virkar, who has guided me throughout my graduate study. I learned a lot of knowledge from you, and most importantly your conscientiousness deeply influenced me.

This work was supported partially by the US Department of Energy under Grant Number DE-FG02-06ER46086 and the US Department of Energy EFRC Grant Number SC0001061 as a flow-through from the University of South Carolina.

I would like to thank Dr. Feng Liu, Dr. Dinesh K. Shetty, Dr. Hong-Yong Sohn and Dr. Ling Zang for serving as my committee. Especially Dr. Feng Liu: without you, I would not have the opportunity to come to the University of Utah.

I would like to thank Dr. Liangzhu Zhu, who helped me a lot in experiments. We had extensive collaborations during the past two years. I would like to thank Dr. Greg Tao from MSRI, who offered me great help and advice.

At Last, I would like to express my grateful to my parents and my lovely wife. My father was a strong and wise man, and you live in my heart forever. My mother is a diligent and kind lady, and I love you. I share a lot of childhood memories with my wife, and I love the gift from you. You all made me who I am.

CHAPTER 1

INTRODUCTION TO SOLID OXIDE FUEL CELL

A fuel cell is a device that converts the chemical energy inside certain fuel into electrical energy through an electrochemical reaction with oxygen or another oxidant. The mechanism is first discovered and reported by W.R. Grove in 1839 [1]. However, in spite of the extremely high energy conversion efficiencies and environmental benefits associated with fuel cell technology, it has proved difficult to develop the early scientific experiments into commercial products. These problems often associate with the lack of appropriate materials or manufacturing routes that would enable the cost of electricity per kWh to compete with the existing technology. More than 120 years after Grove's invention, F.T. Bacon for the first time developed a commercializable fuel cell, which was later known as the alkaline fuel cell [2]. In 1969, the Bacon type fuel cell was used as the on-board power source for the NASA's Apollo space shuttle which enabled astronauts to land on the moon. Ever since then, huge development in fuel cell research has been achieved.

1.1 What Is a Fuel Cell?

A fuel cell usually consists of anode, cathode and electrolyte, as shown in Figure 1-1. The anode is exposed to fuel, like H_2, CO or natural gas; the cathode is exposed to

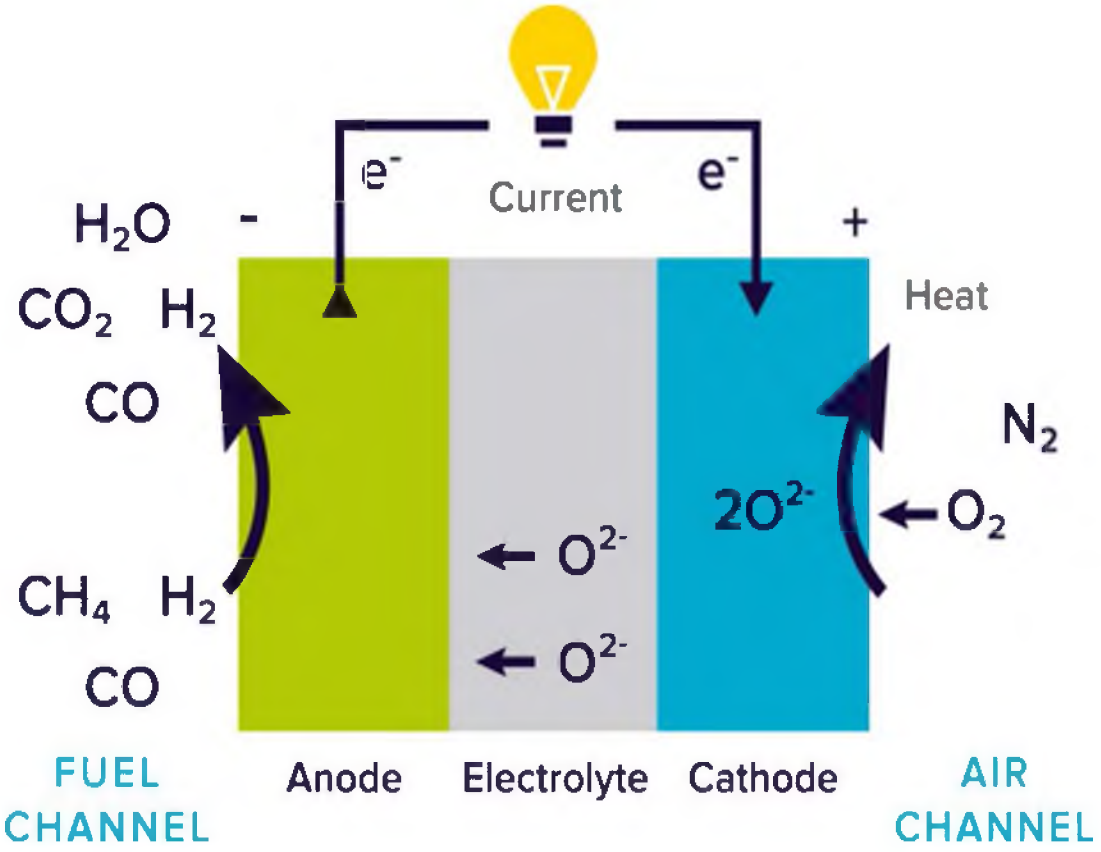

Figure 1-1: Schematics showing a sandwich structure of a typical fuel cell. At anode, fuel is oxidized; at cathode, oxidant is reduced. The electrolyte is usually ionic conductor and blocks electronic current.

oxidant, which is usually O_2. When the fuel cell is working, fuels are oxidized at the anode; oxidants are reduced at the cathode. The excess ions generated by the electrochemical reaction migrate through the electrolyte, and the excess electrons migrate through the external load and, as a result, electrical work is done. For the fuel cell illustrated in Figure 1-1, the overall electrochemical reaction is

$$H_2(g)+\frac{1}{2}O_2(g)\rightarrow H_2O(g) \tag{1.1}$$

The anode half-cell reaction is

$$H_2(g) + O^{2-} \rightarrow H_2O(g) + 2e^- \tag{1.2}$$

The cathode half-cell reaction is

$$\frac{1}{2}O_2(g) + 2e^- \rightarrow O^{2-} \tag{1.3}$$

The electrolyte is an oxygen ion conductor which allows oxygen ion to diffuse through and prevents the electron from diffusing through.

The electrical power output of a fuel cell is usually characterized by Figure 1-2. The x-axis is output current density, the left y-axis is output voltage and the right y-axis is output power density. At zero current, the voltage output is usually the emf of the overall reaction. For reaction (1.1), the emf is about 1.1 eV. As current density increases, output voltage decreases due to various losses, which will be discussed in Chapter 2.

As energy conversion device which utilized chemical energy inside fuels, fuel cell has significantly higher energy conversion efficiency than Carnot engine. This can be illustrated by Figure 1-3. As is well known, any type of Carnot engine follows the Carnot cycle (shown by the red curve). A Carnot cycle consists of four reversible processes, and the work output by a Carnot engine equals the area inside the Carnot cycle in the P-V diagram. Therefore the maximum (reversible) work for a Carnot cycle is

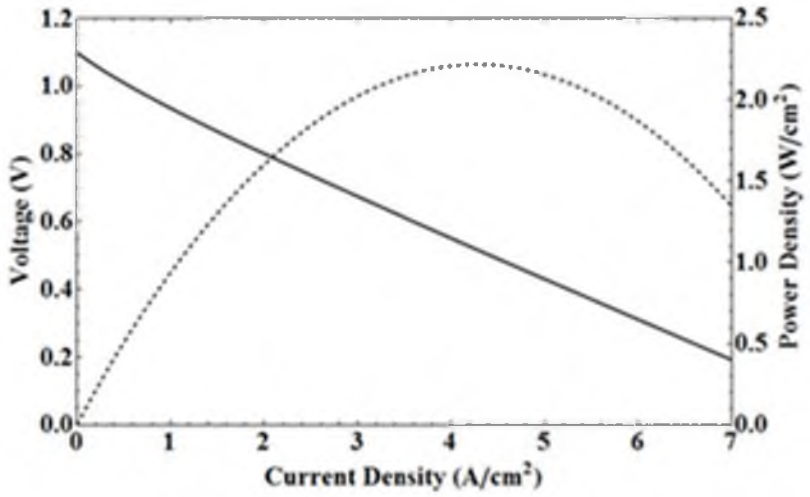

Figure 1-2: A most common way of characterizing fuel cell power output.

$$W_{Carnot}^{Max} = \frac{1}{2} R\left(T_{hot} - T_{cold}\right) \ln\left(\frac{p_{O_2}^{air}}{p_{O_2}^{fuel}}\right) \tag{1.4}$$

On the other hand, the maximum (reversible) work for a fuel cell is

$$W_{Fuel\,Cell}^{Max} = \frac{1}{2} R T_{hot} \ln\left(\frac{p_{O_2}^{air}}{p_{O_2}^{fuel}}\right) \tag{1.5}$$

Therefore, it is obvious that energy conversion efficiency is higher in a fuel cell.

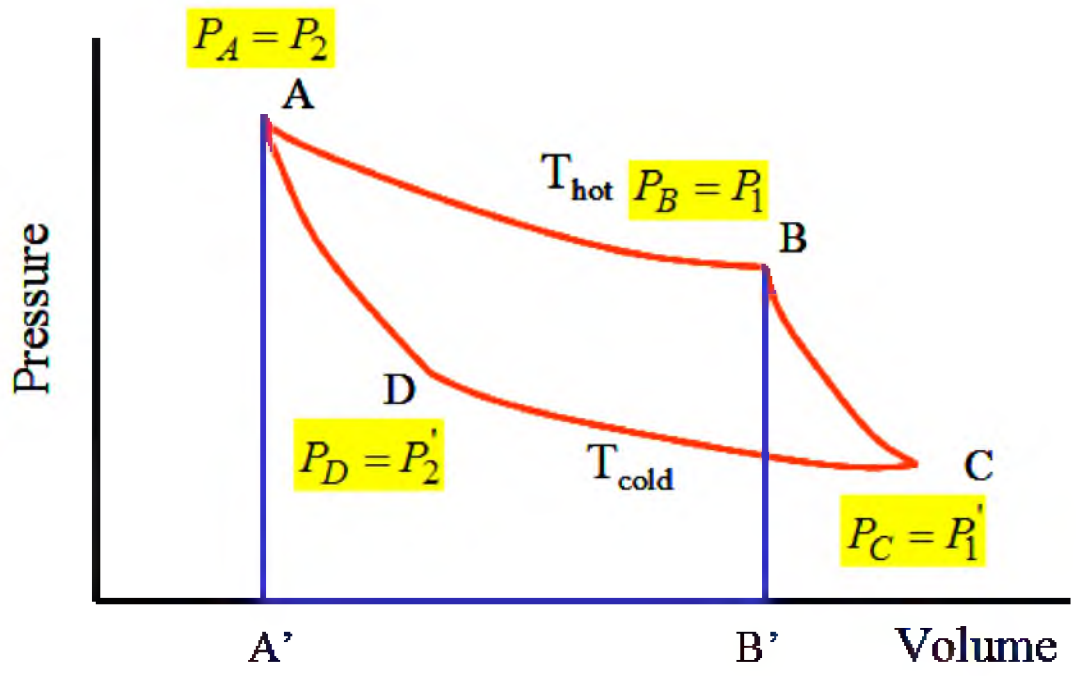

Figure 1-3: P-V diagram for a Carnot engine (red) and a fuel cell (blue).

1.2 Different Types of Fuel Cells

Although the way a fuel cell works can be easily demonstrated by Figure 1-1, the realization can be difficult and diversified. Based on the materials used, fuel cells can be divided into alkaline fuel cells (AFC), molten carbonate fuel cells (MCFC), phosphoric acid fuel cells (PAFC), proton exchange membrane fuel cells (PEMFC) and solid oxide fuel cells (SOFC) [3]. These five types of fuel cells are compared and summarized in Table 1-1, in terms of working temperature, stack size and efficiency.

Among the above five types of fuel cells, solid oxide fuel cells are most suitable for stationary power generation and proton exchange membrane fuel cells are most suitable for transportation power generation. My graduate research mainly focuses on these two types of fuel cells, especially SOFCs.

Table 1-1: Comparison between fuel cell technologies

Type	Temperature	Size	Efficiency
PEMFC	50-100°C	1-100kW	60%
AFC	150-200°C	10-100kW	60%
PAFC	150-200°C	100-400kW	40%
MCFC	600-700°C	0.3-3MW	45-50%
SOFC	600-1000°C	1kW-2MW	60%

Type	Advantage	Disadvantage
PEMFC	•Solid electrolyte •Low temperature •Quick start-up	•Expensive catalysts •Sensitive to fuel impurities •Low temperature waste heat
AFC	•Cathode reaction faster •Low cost components	•Sensitive to CO2 in gas •Electrolyte management
PAFC	•Increased tolerance to fuel impurities	•Expensive catalysts •Long start-up time •Low current and power
MCFC	•Fuel flexibility •Variety of catalysts •Suitable for CHP	•High temperature corrosion and breakdown of cell components •Long start up time •Low power density
SOFC	•High efficiency •Fuel flexibility •Variety of catalysts •Solid electrolyte •Suitable for CHP •Hybrid/GT cycle	•High temperature corrosion and breakdown of cell components •Long start up time

1.3 Solid Oxide Fuel Cells

SOFCs utilize solid state electrolyte which greatly improves device stability and durability. However, the ionic conductivity in solid state electrolyte is usually one or two orders of magnitude lower than that in liquid electrolyte. As a result, SOFCs need to work at elevated temperature often higher than 600°C.

The elevated working temperature introduces two problems for application. At high temperature, the kinetic process becomes faster, leading to a higher materials degradation rate, such as anode nickel particle coarsening, chromium poisoning of the cathode materials and oxidation of metal interconnect. Another problem is long start up time.

However, high working temperature is not always detrimental. At high temperature, noble metals, such as Pt, can be replaced by nickel or other perovskite materials such as electrode catalyst, which greatly reduces the cost. Also, flexible fuels, such as natural gas, can be used at high temperature. Another benefit is that the open circuit voltage increases at higher temperature leading to an even higher efficiency.

1.3.1 Layered Structure in SOFCs

Figure 1-4 shows an SEM image of a typical anode support SOFC. It consists of five layers from top to bottom, which are cathode current collect layer, cathode functional layer, dense electrolyte layer, anode functional layer and anode support layer.

Electrode reaction mainly occurs at the triple phase boundaries in cathode functional layer and anode functional layer. The exchange current density is proportional to the length of triple phase boundary. Therefore, in order to promote electrode reaction, finer grain size at both cathode and anode functional layers are required.

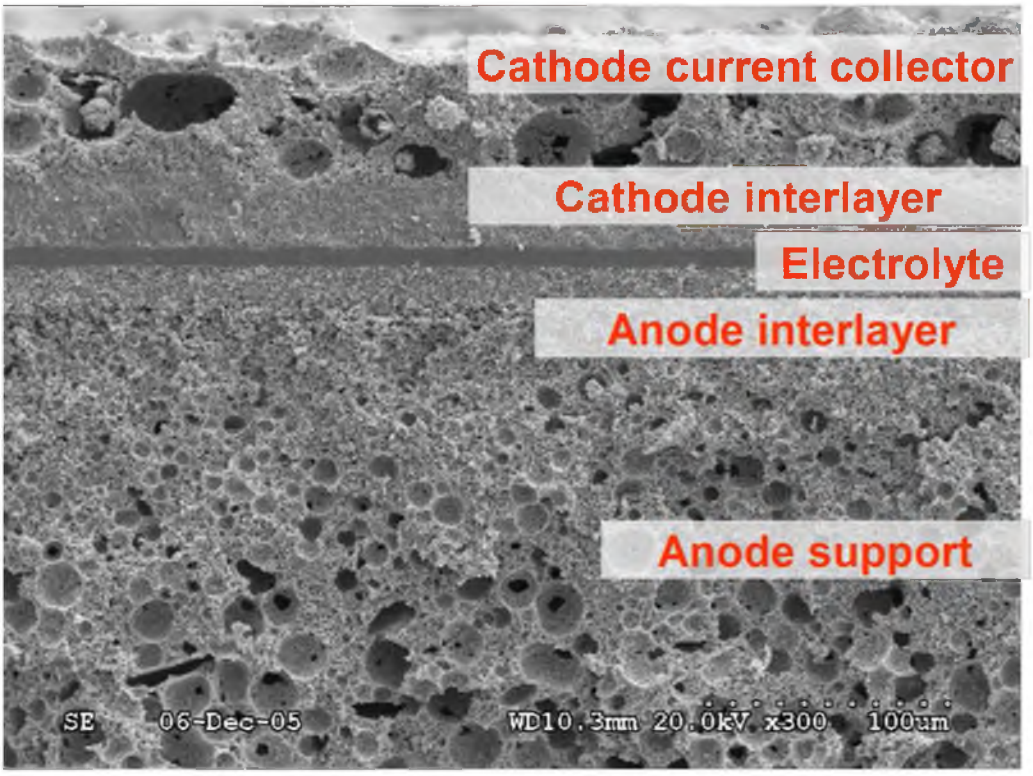

Figure 1-4: SEM image of a typical anode supported SOFC. It has five layers.

Anode support layer usually has a thickness of hundreds of microns. It provides mechanical support for the thin SOFC. In order to promote fuel gas diffusion, anode support layers are usually highly porous. This is also true for the cathode current collector layer.

The dense solid electrolyte layer has thickness about 10 microns. It blocks both gas diffusion and electronic current. Any fine crack in the solid electrolyte layer would lead to lower open circuit voltage. The internal resistance of SOFC mainly comes from solid electrolyte layer. As a result, thinner solid electrolyte is preferred and anode supported structure is widely accepted nowadays.

1.3.2 Materials Used in SOFCs

1.3.2.1 Electrolyte

The requirements for solid state electrolyte are high ionic conductivity, low electronic conductivity, stability in both oxidizing and reducing environments, good mechanical properties and long-term stability with respect to dopant segregation [4]. Currently, the most commonly used materials for electrolyte are yttria stabilized zirconia (YSZ) [5], gadolinium or samarium doped ceria (GDC or SDC) and strontium [6] and magnesium doped lanthanum gallate (LSGM) [7]. The oxygen ion conductivities of these three materials are summarized in Figure 1-5 [4]. Among the three, YSZ has the lowest conductivity, which is about one order of magnitude lower than that in GDC and LSGM. At temperatures above 500°C, LSGM has the highest conductivity, which is slightly higher than that in GDC. As mentioned in the previous section, the electrolyte thickness is usually 10 microns. In order to control the area specific resistance within $0.1\Omega cm^2$, the minimum operating temperatures for YSZ, GDC and LSGM are 700°C, 550°C and 550°C, respectively.

Currently the commercial SOFCs stack use YSZ as electrolyte due to its good mechanical properties at high temperature and low cost. However, YSZ suffers the problem of chemical instability with perovskite oxide electrodes. At high temperature, YSZ reacts with LSM to form La2Zr2O7 [8]; YSZ can easily react with LSCF to form highly resistive layers. The problem with LSGM is the chemical reaction between LSGM and NiO [9]. For GDC, it has good chemical stability with electrode materials. However, GDC itself has large stoichiometry change. At low oxygen partial pressure or at high temperature, Ce^{4+} is reduced to Ce^{3+} leading to significant electronic conductivity.

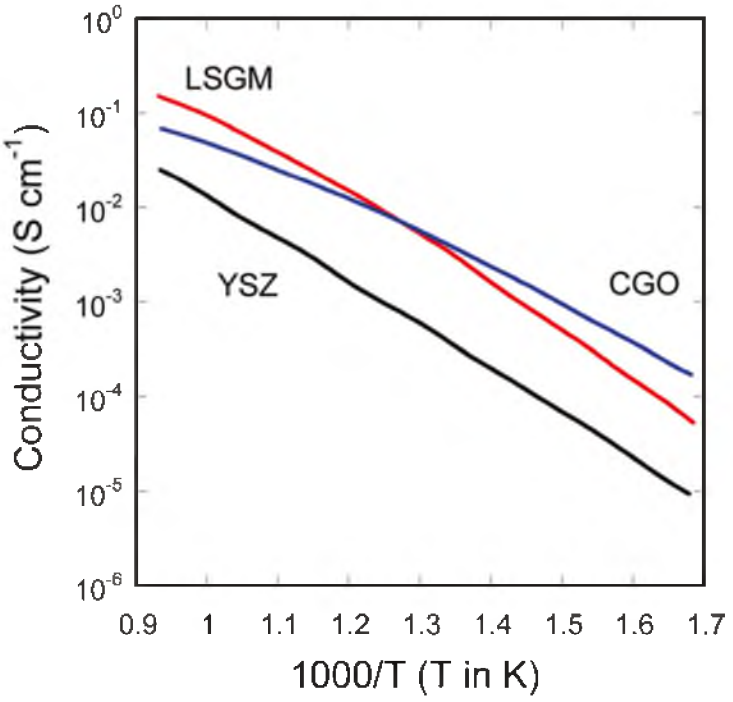

Figure 1-5: Oxygen ion conductivity in YSZ, GDC and LSGM.

1.3.2.2 Cathode

The requirements for cathode materials are high catalytic activity for oxygen reduction reaction, high electronic conductivity, matched thermal expansion coefficient and chemical stability with both electrolyte and interconnect, and chemical stability under oxidizing atmosphere [10]. Perovskite materials are commonly used as cathode materials in SOFCs. Perovskite materials have a general formula of ABO_3, like the structure shown in Figure 1-6. The A site and B site are cations, and their valence usually adds up to 6, which balances the negative change of the three oxygen ion. A site cations usually have larger size and lower valence, and they can be La, Sr, Ca, etc. B site cations on the other hand have smaller size and higher valence, and they can be Ti, Cr, Ni, Fe, Co, etc. Due to dopant, the total valence of A and B site cations could be less than 6, and this is balanced by oxygen vacancy formation.

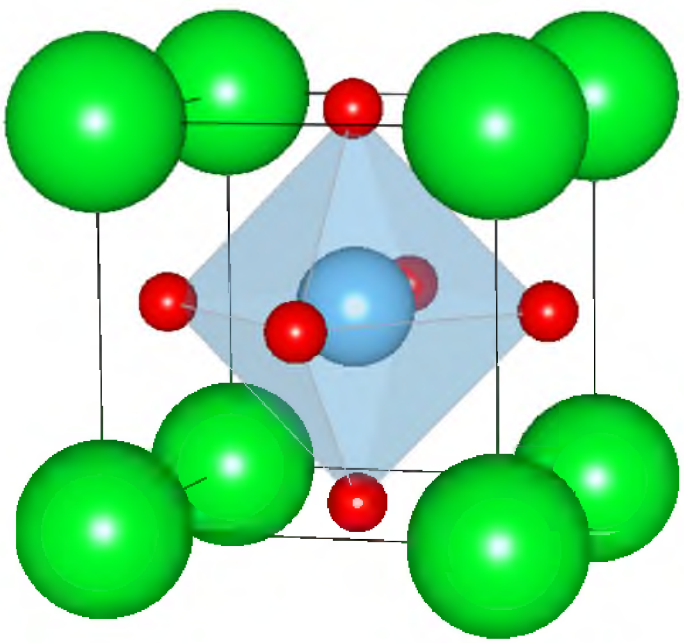

Figure 1-6: Lattice structure of perovskite materials. Green ball represents A site cation; blue ball represents B site cation; red ball represents anion.

The most widely used perovskite cathode materials are LSM and LSCF. In LSM, the A site cations are La3+ and Sr2+; the B site cations are Mn3+, and correspondingly there's oxygen vacancy formation. In LSCF, the A site cations are the same a LSM, but the B site cations are Co and Fe. The oxygen ion conductivities are more influenced by Sr concentration at the A site, and electronic conductivities is more influenced by the B site cation valence. Due to the higher ionic conductivity, LSFC usually exhibits better catalytic property.

1.3.2.3 Anode

The role of anode in SOFCs is to provide the sites for the fuel gas to react with the oxygen ions and also collect electrons or holes generated by the anode half reaction. Therefore, the requirements for anode materials are high catalytic activity for fuel

oxidation reaction, high electronic conductivity, matched thermal expansion coefficient and chemical stability with both electrolyte and interconnect, and chemical stability under reducing atmosphere [11]. The widely used anode material is a porous composite of nickel and ceramic, which is called cermet. Figure 1-7 shows a three-dimensional structure [12].

1.4 My Graduate Research in SOFCs

SOFC technology has been developed for a broad spectrum of power generation applications. SOFC systems can be designed as small as portable devices (less than 1kW), and also as big as SOFC/gas turbine hybrid system (several MW). In between, SOFC can

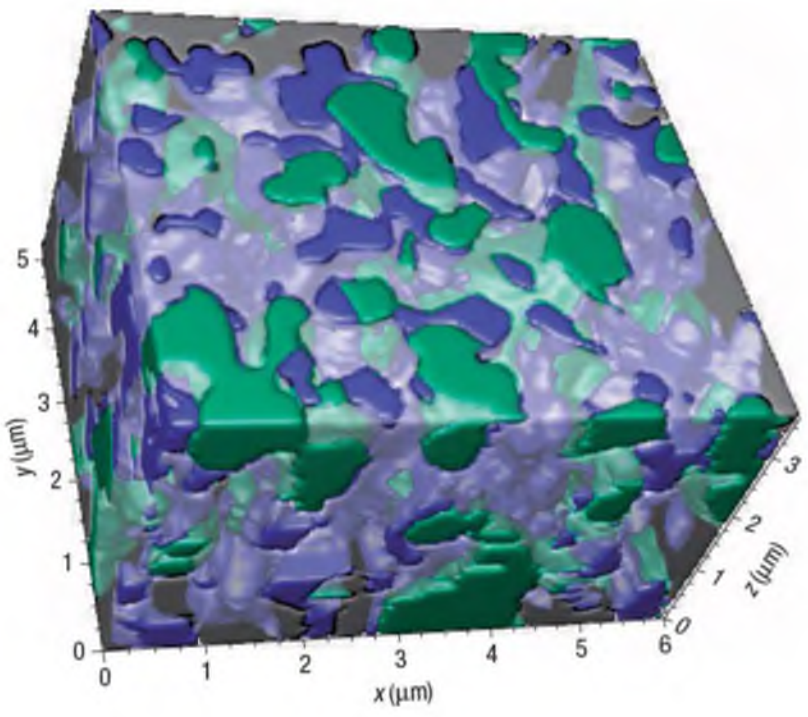

Figure 1-7: A view of the 3D reconstruction showing the Ni (green), YSZ (translucent/grey), and pore (blue) phases [12].

be design as combined heat and power (CHP) system (100-250kW) for distributed power generation. However, SOFC systems have not been widely commercialized. This is mainly due to the two disadvantages listed in Table 1-1, which are high temperature corrosion and breakdown of cell components as well as long start up time.

Developing intermediate temperature (600-800°C) or even low temperature (400-600°C) SOFCs has been part of the research motivations for years. As mentioned above, the high working temperature is required due to low ionic conductivity in solid state electrolyte. It is also pointed out that GDC and LSGM can meet the requirement at temperatures as low as 550°C. However, at low temperatures, electrode catalytic activity decreases. As a result, a lot of effort has been devoted to developing new electrolyte and electrode materials which can be used at low temperature.

For high temperature SOFCs, the research is focused on further improving energy conversion efficiency. The guidelines here are similar to that for developing low temperature SOFCs, which is to minimize area specific resistance as well as increase electrode catalytic activity. However, not much progress has been achieved in the past two decades. It turns out that, no matter how much better the new cathode materials are, the power density stays the same. Researchers have tried to build models to analyze which is the limited factor.

During my graduate research, I also analyzed all the power loss during SOFC operation and built a parametric model based on experimentally measurable parameters, which is discussed in Chapter 2. It is found that ohmic loss dominates as cathodes are getting more efficient nowadays.

Following this clue, I focused my graduate research on improving electrolyte ionic

conductivity. Since solid state electrolyte materials have an extremely high melting point, they can be used only in the form of polycrystalline or ceramic. Therefore, ion transportation through electrolyte includes diffusion through grain bulk and diffusion through grain boundaries. Due to space charge effect, grain boundary is usually of orders of magnitude more resistive than grain bulk. However, the no space charge theory has been established in the three common electrolyte materials. For the first time, I have developed a space charge theory in YSZ, which is discussed in Chapter 3.

My graduate research contains not only theoretical work but also experimental measurement. For resistance measurement in SOFCs, electrochemical impedance spectroscopy (EIS) is widely used. This technique enables people to measure resistance associated with different layers or different kinetic processes. However, the operation and interpretation is complex. There are a lot errors in the data presented in literature. Therefore, in Chapter 4, I discuss how to correctly do EIS measurement as well as interpreting EIS data. As far as the electrode kinetic process is concerned, I found it difficult to deconvolute the electrode impedance from the entire sample impedance.

A possible solution is to use an embedded probe, so that the electrode impedance can be measured separately. In Chapter 5, I used the finite element method to study what is the optimized geometry for an embedded probe.

Until quite recently, there has been a lot of interest in using SOFCs at the electrolysis mode to produce hydrogen or carbohydrates for energy storage. This technology can be used together with wind power or other power sources that are not stable. Take wind power for example, the power generation highly depends on the speed of wind, which is rather random. As a result wind electricity can hardly be integrated to the electric grid. A

possible solution is to use solid oxide electrolyser cells (SOECs) to do water electrolysis when wind is strong, and to use SOFCs to produce electricity from stored hydrogen or carbohydrates when wind is weak.

The problem of using SOFCs in the SOEC mode is device degradation. It is found that the degradation rate in SOEC mode is nearly five times higher than that in SOFC mode [13]. The degradation is associated with electrode delamination and crack growth in electrolyte due to very high oxygen chemical potential. In Chapter 5, the oxygen chemical potential distribution is also studied using finite element method.

In my graduate study, I found the embedded probe can not only precisely measure potentials at any position inside the cell, but it also can manipulate the material property through electrochemical reactions. In Chapter 6 and Chapter 7, I discussed two techniques to measure the extremely low electronic conductivity in YSZ using embedded Pt probe. These are very interesting application of the embedded probe designed in Chapter 5.

Although most of my graduate research focuses on SOFCs, I also spent some effort on the study of PEMFC catalyst. The catalyst used in PEMFCs is noble metal, such as platinum. These catalyst particles can be poisoned if CO or other detrimental gas presents in hydrogen. The adsorption and desorption kinetics of CO on Pt is seldom reported, because these studies always require delicate and expensive facilities, such as synchrotron light source or radioactive labeling isotope. Not many researchers have access to these facilities. In Chapter 8, I discussed a home designed electrical measurement system that can study the adsorption and desorption kinetics of CO at Pt surface.

1.5 References

1. W. R. Grove, *Philos. Mag. Ser. 3*, **14**, 127–130 (1839)

2. A. M. Adams, F. T. Bacon, and R. G. H. Watson, *Fuel Cells*, Academic Press (1963)

3. B. C. Steele and A. Heinzel, *Nature*, **414**, 345–52 (2001)

4. A. J. Jacobson, *Chem. Mater.*, **22**, 660–674 (2010)

5. N. Q. Minh and T. Takahashi, *Sci. Technol. Ceram. Fuel Cells*, Elsevier (1995)

6. B. Steele, *Solid State Ionics*, **129**, 95–110 (2000)

7. M. Feng and J. B. Goodenough, *Eur. J. Solid State Inorg. Chem.*, **31**, 663–672 (1994)

8. A. Mitterdorfer, *Solid State Ionics*, **111**, 185–218 (1998)

9. Z. Gao, E. C. Miller, and S. A. Barnett, *Adv. Funct. Mater.*, **24**, 5703–5709 (2014)

10. C. Sun, R. Hui, and J. Roller, *J. Solid State Electrochem.*, **14**, 1125–1144 (2009)

11. A. McEvoy, *High Temperature and Solid Oxide Fuel Cells*, Elsevier (2003)

12. J. R. Wilson et al., *Nat. Mater.*, **5**, 541–544 (2006)

13. A. V. Virkar, *Int. J. Hydrogen Energy*, **35**, 9527–9543 (2010)

CHAPTER 2

A PARAMETRIC MODEL FOR SOLID OXIDE FUEL CELLS BASED ON OUT OF CELL MEASUREMENTS

2.1 Introduction

Considerable work has been reported on solid oxide fuel cells (SOFC) over the past couple of decades [1-3]. Various materials for the three components, namely cathode, electrolyte and anode have been investigated over the past 30+ years. The state-of-the-art materials for SOFC are: 8 mol.% Y_2O_3-stabilized zirconia (YSZ) for the electrolyte, as a constituent in porous Ni + YSZ as the composite anode and as a constituent in porous Sr-doped $LaMnO_3$ (LSM) + YSZ as the composite cathode. Much of the early work was based on using porous LSM as the cathode without YSZ dispersed in it. Over the last couple of decades many other highly active cathodes have emerged, the vast majority of them being mixed ionic electronic conducting (MIEC) perovskites containing transition metals capable of exhibiting multiple valence states. Much of the early work was also based on using YSZ plates of 150 to 200 microns in thickness (or in some cases even thicker) for the electrolyte with screen-printed anode and cathode. Such cells are referred to as electrolyte-supported cells. In order to minimize the ohmic contribution to the total cell resistance such cells have to be operated at high temperatures, typically ~900 to 1000°C, to ensure reasonable performance (~0.25 Wcm^{-2}). The use of single phase LSM

also leads to generally poor cathode performance at temperatures below 900°C. High temperature operation poses significant challenges related to materials degradation especially when used in a planar geometry and with a metallic interconnect.

In the subsequent work in this field processes were developed for fabricating cells comprising thin YSZ electrolyte film supported on a porous electrode (typically the anode). This allowed for a significant lowering of the total ohmic contribution thereby enhancing performance. Using state-of-the-art materials maximum power densities approaching 2 Wcm^{-2} at a temperature as low as 800°C were demonstrated in anode-supported button cells [2,3]. This represented not only an order of magnitude improvement in performance but that too at a temperature 200 degrees lower. Many SOFC researchers have been involved in developing such high performance thin electrolyte, electrode-supported cells at lower operating temperatures over the past couple of decades. Further improvements in performance can be realized by using other perovskite cathodes, especially those containing Co and Fe as B-site constituents exhibiting mixed ionic electronic conducting (MIEC) properties. It is to be emphasized, however, that fine-grained two-phase LSM + YSZ (or LSM + rare earth oxide doped ceria) cathodes perform nearly as well as many single phase LSC and LSF-based cathodes assuming suitable microstructures have been developed. Also, some of the highest performance reported to date has been on cells made with composite cathodes. Finally, the lowering of the ohmic contribution requires the use of electrolyte materials with higher ionic conductivity than YSZ. These materials include Scandia-stabilized zirconia (ScSZ), Sr-doped and Mg-doped $LaGaO_3$ (LSGM) and rare earth oxide doped ceria. A limited amount of work has been reported on SOFCs made with these other

electrolyte materials in a thin film form.

While much progress has been made it also appears that there have not been significant further gains in performance, beyond those achieved about fifteen years ago. One of the difficulties has been in accurately measuring the various polarization losses which has made it challenging to target those areas requiring more effort. There are five sources of voltage loss: (a) Ohmic loss – voltage loss associated with the electrolyte, the electrodes and contact regions between the electrodes and the electrolyte; (b) Concentration polarization at the cathode – voltage loss associated with the transport of the oxidant through the porous cathode, (c) Concentration polarization at the anode – voltage loss associated with the transport of the fuel through the porous anode, (d) Activation polarization at the cathode – voltage loss associated with the electrochemical reduction of the active constituent in the oxidant (oxygen) and (e) Activation polarization at the anode – voltage loss associated with the electrochemical oxidation of the active constituent in the fuel (typically hydrogen). The activation polarization involves a number of series steps such as gas adsorption, dissociation, electron transfer and transfer of ionic species into (or out of) the electrolyte at the electrode catalyst (e.g. LSM)/electrolyte (e.g., YSZ) interface. In a typical cell it is usually difficult to separately measure anode and cathode polarization losses and also it is equally difficult to experimentally separate out concentration and activation polarization losses at either of the two electrodes. The most commonly used technique is electrochemical impedance spectroscopy (EIS). Almost always the EIS spectra overlap and it is often not possible to unequivocally determine the various contributions. And even if the EIS spectra can be described using a number of equivalent circuits it is generally difficult to assure

uniqueness (multiple equivalent circuits can be used to describe a given experimental data set thus making physical interpretation difficult). It appears that to realize further improvements in cell performance may require accurate identification of the various polarization losses, their sources and their dependence on material and microstructural parameters, atmosphere and temperature. The objective of this work is to use a parametric model for SOFC [4], quantitatively estimate the various polarization losses based on measurements made on cell materials and components and determine what parameters may need to be optimized to improve the performance, beyond what has been achieved to date.

2.2 A Parametric Model to SOFC

Several models which take into account gas transport through porous electrodes, electrochemical reactions at the electrodes (near electrode/electrolyte interfaces) including various reaction steps and the ohmic loss have been developed. The vast majority of them, however, are numerical in nature due to the analytical complexities involved. Also, the vast majority of the models are based on many assumed parameters regarding the microstructure of the electrodes, assumed chemical reaction steps and parameters related to the reaction steps (e.g., an assumed rate determining step). Thus, quantitative validation of virtually all of these models is generally difficult for lack of experimentally verifiable/measurable parameters used in many of the models. The main difficulty lies in the fact that multiple assumed parameters are required for modeling, while the experimental voltage vs. current density traces are featureless. As a consequence, the inverse problem of determining the various parameters from the

measured cell performance curves lacks uniqueness. Essentially the same difficulty arises in the use of Electrochemical Impedance Spectroscopy (EIS) on actual cells since the inverse problem of determining various cell parameters from EIS spectra lacks uniqueness.

It appears that an approach of using a parametric model which is based on parameters that can be experimentally measured on cell materials and components, at least in principle, could be the first step towards developing a thorough understanding of the various voltage losses that occur in a typical SOFC [4]. Calculation of cell performance curves based on parameters on cell materials and cell components is a forward problem, and thus in principle it has a unique solution for a given set of parameters [5]. Such an approach can estimate the dominant sources of voltage losses thus identifying areas which require further work in order to increase the performance. Detailed numerical modeling may then be the next step to allow for the inclusion of multidimensional features in addition to issues such as fuel utilization and nonisothermal operation.

A typical anode-supported SOFC consists of at least five distinct layers: (a) A porous anode-support characterized by high electronic conductivity to minimize the ohmic loss and high porosity for easy transport of gaseous fuel (to minimize anode concentration polarization); (b) A porous anode functional layer adjacent to the electrolyte characterized by fine microstructure for enhanced electrocatalysis (electrochemical oxidation of fuel; lowering of the anode activation polarization); (c) A dense, thin (to minimize the ohmic loss) film electrolyte; (d) A porous cathode functional layer adjacent to the electrolyte characterized by fine microstructure for enhanced electrocatalysis (electrochemical reduction of the oxidant; lowering of the cathode activation

polarization); and (e) A porous cathode current collector layer characterized by high electronic conductivity to minimize the ohmic loss and high porosity for easy transport of the oxidant (to minimize cathode concentration polarization). In a parametric model voltage vs. current density polarization curves of an SOFC may be adequately described by a generic equation of the form [3, 6]

$$V(i) = E_0 - iR_i - \eta_{act}^{a} - \eta_{act}^{c} - \eta_{conc}^{a} - \eta_{conc}^{c} \tag{2.1}$$

In equation (2.1), E_0 is the open circuit voltage, i is the current density, R_i is the ohmic area specific resistance ($\Omega \cdot cm^2$), η_{act}^{a} is the activation polarization at the anode, η_{act}^{c} is the activation polarization at the cathode, η_{conc}^{a} is the concentration polarization at the anode and η_{conc}^{c} is the concentration polarization at the cathode. The voltage vs. current density polarization curves may further be described by [3, 6]

$$V(i) = E_0 - iR_i - \eta_{act}^{a} - \eta_{act}^{a} + \frac{RT}{2F}\ln\left(\frac{p_{H_2(i)}^{'}(i)\,p_{H_2O}^{0}}{p_{H_2}^{0}\,p_{H_2O(i)}^{'}(i)}\right) + \frac{RT}{4F}\ln\left(\frac{p_{O_2(i)}^{'}(i)}{p_{O_2}^{0}}\right) \tag{2.2}$$

in which the η_{conc}^{a} is given in terms of partial pressures of hydrogen and water vapor on the anode side and η_{conc}^{c} is given in terms of oxygen partial pressures on the cathode side. In equation (2.2) R is the gas constant, F is the Faraday constant, T is the temperature, $p_{H_2}^{0}$ is the partial pressure of hydrogen in the fuel just outside the anode, $p_{H_2(i)}^{'}(i)$ is the partial pressure of hydrogen in the anode close to the anode functional layer/electrolyte

interface, $p^{0}_{H_2O}$ is the partial pressure of water vapor just outside the anode, $p'_{H_2O(i)}(i)$ is the partial pressure of water vapor in the anode close to the anode functional layer/electrolyte interface, $p^{0}_{O_2}$ is the partial pressure of oxygen just outside the cathode and $p'_{O_2(i)}(i)$ is the partial pressure of oxygen in the cathode close to the cathode functional layer/electrolyte interface. In some cases the activation polarization may be combined into a single equation described by the phenomenological Tafel equation, $\eta_{act} = a + b\ln i$, where a and b are the Tafel constants. The Tafel equation is valid only beyond some phenomenological exchange current density, i_0. The parameters, a and b, include contributions from both the anode and the cathode. Equation (2.2) albeit simple embodies essentially all relevant features inclusive of all voltage losses in a quantitative manner and provides a platform for relating cell performance to measurable parameters. Also note that all terms on the right side are expressed as functions of the current density, i, which is an experimentally controllable and a measureable parameter.

Equation (2.1) shows that the absolute minimum number of independent parameters required to describe cell performance of a five-layer cell is nine; a minimum of four parameters describing gas transport through the four porous layers whose porosities and microstructures can be independently varied (selected), four parameters which describe the total activation polarization at the two electrodes (wherein both activation polarizations contain two independent parameters – exchange current densities and transfer coefficients) and the ohmic contribution of the entire cell. However, virtually all experimentally measured voltage vs. current density plots are featureless and can be readily described as a polynomial in current density i containing no more than two or

three terms. This means regardless of the science of the problem only two or three fitting parameters are required to describe the voltage vs. current density plots. But the independent parameters are at least nine. This means it is not possible to obtain a unique set of nine parameters from cell performance curves when the phenomenological fit requires only two or three. This is the fundamental challenge related to uniqueness in this inverse problem. This is illustrated via an example of typical, experimentally measured voltage vs. current density traces on a cell shown in Figure 2-1(a) [6]. The data were obtained at 800°C, 700°C and 600°C [6]. The activation polarization at the two electrodes, the concentration polarizations at the two electrodes and the total cell ohmic resistance contribute to the observed cell performance. Their quantitative description entails a minimum of nine independent parameters. Figure 2-1(b) shows polynomial fits to the data at 800°C with the order ranging between 2 and 9. As seen in the figure, there is hardly any difference among the various fits and that a 2nd-order polynomial empirical fit describes the experimental data set quite well. In general a polynomial fit to a voltage, V(i), vs. current density, i, plot may be given by

$$V(i) = \sum_{k=0}^{n} a_k i^k = a_0 + a_1 i + a_2 i^2 + \ldots + a_k i^k + \ldots + a_n i^n \tag{2.3}$$

By comparing equation (2.1) with equation (2.3) and using Taylor series expansion of equation (2.1) around i = 0, note that

$$a_0 = E_0 \tag{2.4}$$

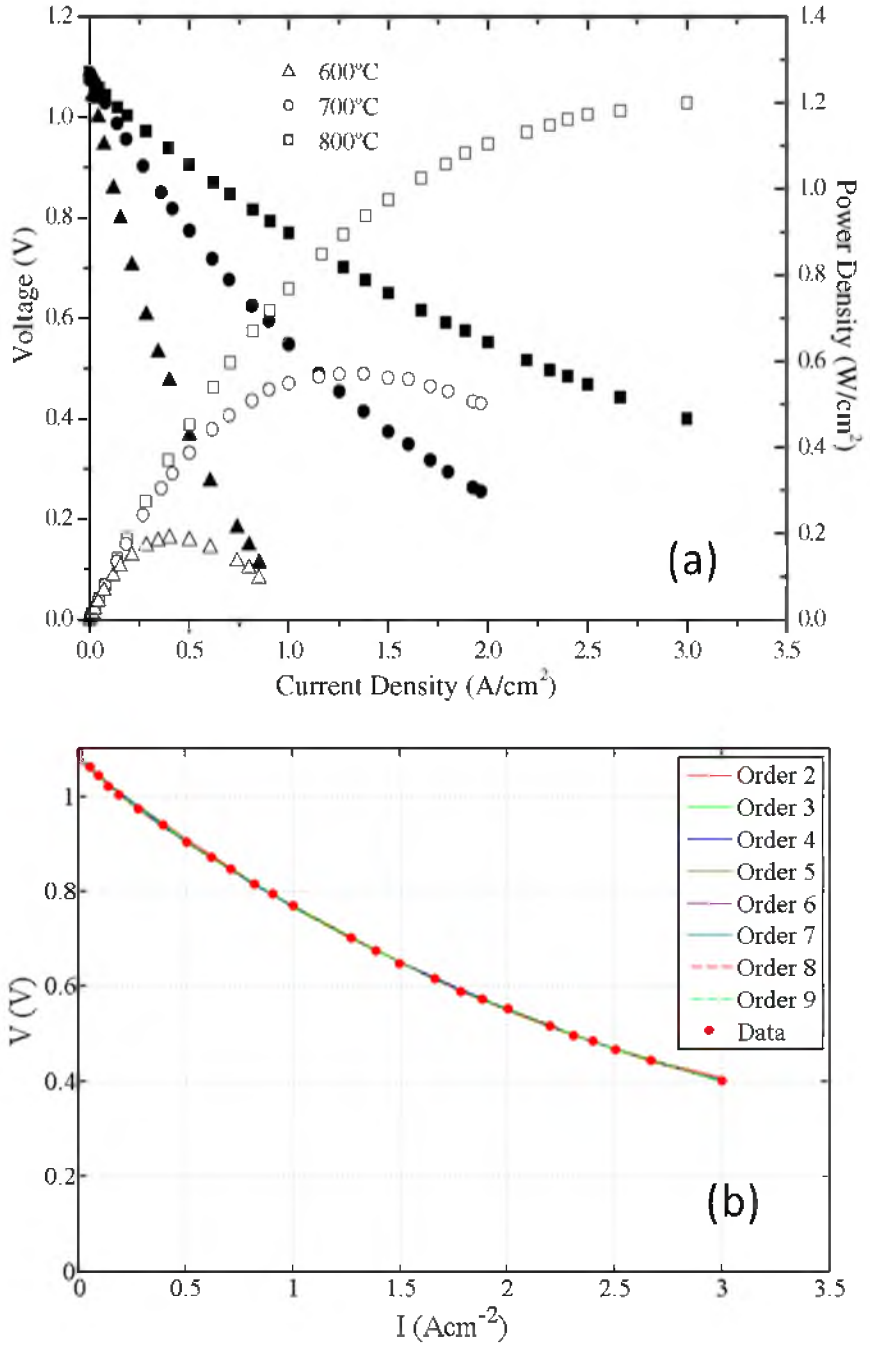

Figure 2-1: Power output in SOFC. (a) Experimental cell performance data from [6]. (b) Polynomial fits to the cell test data at 800°C from degree 2 to degree 9.

$$a_1 = -R_i - \left(\left. \frac{d\eta_{act}^{a}}{di} \right|_{i=0} + \left. \frac{d\eta_{act}^{c}}{di} \right|_{i=0} + \left. \frac{d\eta_{conc}^{a}}{di} \right|_{i=0} + \left. \frac{d\eta_{conc}^{c}}{di} \right|_{i=0} \right) \tag{2.5}$$

$$a_k = -\frac{1}{k!} \left(\left. \frac{d^k\eta_{act}^{a}}{di^k} \right|_{i=0} + \left. \frac{d^k\eta_{act}^{c}}{di^k} \right|_{i=0} + \left. \frac{d^k\eta_{conc}^{a}}{di^k} \right|_{i=0} + \left. \frac{d^k\eta_{conc}^{c}}{di^k} \right|_{i=0} \right) \tag{2.6}$$

The first coefficient, $a_0 = E_0$, is readily obtained from experimental cell test data as the open circuit voltage or can be calculated as the Nernst voltage (if the electronic conduction through the cell is negligible). The coefficient a_1 contains the ohmic resistance (R_i) and contributions from the activation and the concentration polarizations and thus contains up to nine unknown parameters. All other higher order coefficients (a_k for $k \geqslant 2$) include up to eight unknown parameters. If analytical forms of the various polarizations are known, which is rarely the case, analytical forms of the various coefficients can in principle be obtained. For example if the activation polarization at an electrode can be described using the Butler-Volmer equation, namely

$$i = i_0 \left\{ \exp\left[-\frac{\alpha z F \eta_{act}}{RT} \right] - \exp\left[\frac{(1-\alpha) z F \eta_{act}}{RT} \right] \right\} \tag{2.7}$$

the first two derivatives are given as follows:

$$\left. \frac{d\eta_{act}}{di} \right|_{i=0} = \frac{RT}{zFi_0} \tag{2.8}$$

$$\left.\frac{d^2\eta_{act}}{di^2}\right|_{i=0} = -\frac{(1-2\alpha)RT}{zFi_0^2} \tag{2.9}$$

Similar equations can be given for concentration polarization. Thus all coefficients in a polynomial fit have a fundamental origin. However, the exact forms of the various polarizations are generally not known. If one were to fit voltage vs. current density plots using a polynomial and if an excellent fit can be obtained to a polynomial of order 3, it means it is not possible to obtain nine unique parameters by fitting to experimental results. This also means the validity of any analytical/numerical model cannot be judged merely on the basis of the goodness of fit to cell test data regardless of how detailed and sophisticated a model may be. These difficulties are central to all inverse problems [5].

In the anode support and the cathode current collector the electrical current is essentially electronic and the corresponding gaseous fluxes are independent of position, assuming no internal reforming. However, over the thicknesses of the functional layers the current consists of two components – electronic and ionic with the total current being fixed; it varies from (nearly) purely ionic at the interface between the electrolyte and the functional layer to (nearly) purely electronic just outside the functional layers (into the current collectors). As a result gaseous fluxes depend on position within the functional layers. The typical thicknesses of the functional layers are ~10 to 25 microns. The analytical model given in equation (2.2) ignores this aspect.

In what follows three types of voltage losses or polarizations relevant to an SOFC are examined. They are: (1) Ohmic loss (occurs through the entire cell), (2) Activation polarization (occurs at both electrodes) and (3) Concentration polarization (occurs at both electrodes).

2.2.1 Sources of Voltage Loss

2.2.1.1 Ohmic Loss

It is often customary to attribute most of the cell ohmic contribution to the electrolyte since the electrolyte ionic resistivity is much greater than the electronic resistivities of the electrodes. In thin electrolyte film anode-supported cells, however, this assumption may not always be satisfactory. That is ohmic contributions from the other components to the net cell ohmic area specific resistance may not be negligible. The ohmic contribution in general may be given by [6]

$$R_i = \rho_e^{ionic} l_e + \rho_{c(1)}^{elect} l_{c(1)} + \rho_{c(2)}^{elect} l_{c(2)} + \rho_{a(1)}^{elect} l_{a(1)} + \rho_{a(2)}^{elect} l_{a(2)} + R_{contact} \qquad (2.10)$$

where ρ_e^{ionic} is the ionic resistivity of the electrolyte, l_e is the electrolyte thickness, $\rho_{c(1)}^{elect}$ is the electronic resistivity of the cathode current collector, $l_{c(1)}$ is the cathode current collector layer thickness, $\rho_{c(2)}^{elect}$ is the electronic resistivity of the cathode functional layer, $l_{c(2)}$ is the cathode functional layer thickness, $\rho_{a(1)}^{elect}$ is the electronic resistivity of the anode support, $l_{a(1)}$ is the anode support thickness, $\rho_{a(2)}^{elect}$ is the electronic resistivity of the anode functional layer, $l_{a(2)}$ is the anode functional layer thickness and $R_{contact}$ is the contact resistance associated with the interfaces between the various layers. The contact resistance is a function of the nature of contact between the layers; the poorer the contact (such as due to the presence of narrow interparticle necks or due to the presence of lateral voids or cracks along and parallel to interfaces) the higher this contribution. Analysis of cell microstructures reported in several studies shows that cracks or elongated regions at

electrolyte/electrode interfaces are quite common [7]. These cracks or elongated regions (or partial delamination) are thought to contribute to the contact resistance, which is not accounted for in the sum of the individual layer resistances. The results in many studies (typically EIS spectra) also show that the ohmic contribution is much larger than can be accounted for on the basis of component resistances. The possible formation of a thin layer of $La_2Zr_2O_7$ and $SrZrO_3$ at the cathode/electrolyte interface is an additional source of contact resistance [8]. It thus appears that contact resistances across interfaces can be significant contributors to the overall cell area specific resistance. In this context the nature of an interface between two adjacent layers may have a significant effect on the net ohmic contribution. In principle this contribution may be estimated by solving the appropriate boundary value problems (such as solution to the Laplace equation for mixed boundary conditions) if the geometry of the cracks or the voids is known and/or by measuring interface reaction layer formed between the cathode and the electrolyte. The resistivities of various regions can be independently (experimentally) measured. This has been done for the anode support, the cathode interlayer and the electrolyte thickness in one study [6]. However, with the exception of this study little information is available in the open literature. According to this one study the total ohmic loss at 800°C for an anode-supported cell with YSZ electrolyte, LSM + YSZ cathode and Ni + YSZ anode (of given compositions, porosities and microstructures) used in that study is given as [6]

$$R_i = 24 l_e + 3.92 l_{c(2)} + 0.24 l_{a(1)} + R'_{const} \tag{2.11}$$

$$R'_{const} = \rho^{elect}_{c(1)} l_{c(1)} + \rho^{elect}_{a(2)} l_{a(2)} + R_{contact} \tag{2.12}$$

The thicknesses of the layers have units of cm in equations (2.11) and (2.12). The experimentally measured area specific resistance (ASR) in [6] for a cell with 8 μm thick YSZ electrolyte was ~0.104 Ωcm^2. Equation (2.11) is valid only at 800°C and for the particular cells used in that study. It is, however, possible to obtain estimates of the ohmic contributions from the various layers using data reported in the literature on the temperature dependence of electrical conductivities of the various materials used. This is discussed in what follows.

For a cell containing Ni + YSZ in both the anode support and the anode functional layer, their total resistivities are expected to increase with temperature because the conducting phase is mainly metallic Ni. With both phases being contiguous, electrical conduction through the metallic phase dominates. For these two layers their resistivities may be described by the following empirical equation

$$\frac{1}{\sigma} = \rho = \rho_0 + \gamma T \tag{2.13}$$

where ρ_0 is the resistivity at the reference temperature of 0 K and γ is the temperature coefficient of resistivity in ΩcmK^{-1}. Experimental measurements on the effect of temperature on the total electrical resistivity of Ni + YSZ over a range of compositions have been reported by Anselmi-Tamburini et al. [9] and Marinsek et al. [10]. Data from these studies are plotted in Figure 2-2. As seen in the figure the plots of resistivity vs. temperature are linear over the range of temperatures the measurements were made in. In our studies the volume fraction of Ni was ~35vol.% for an anode support layer with

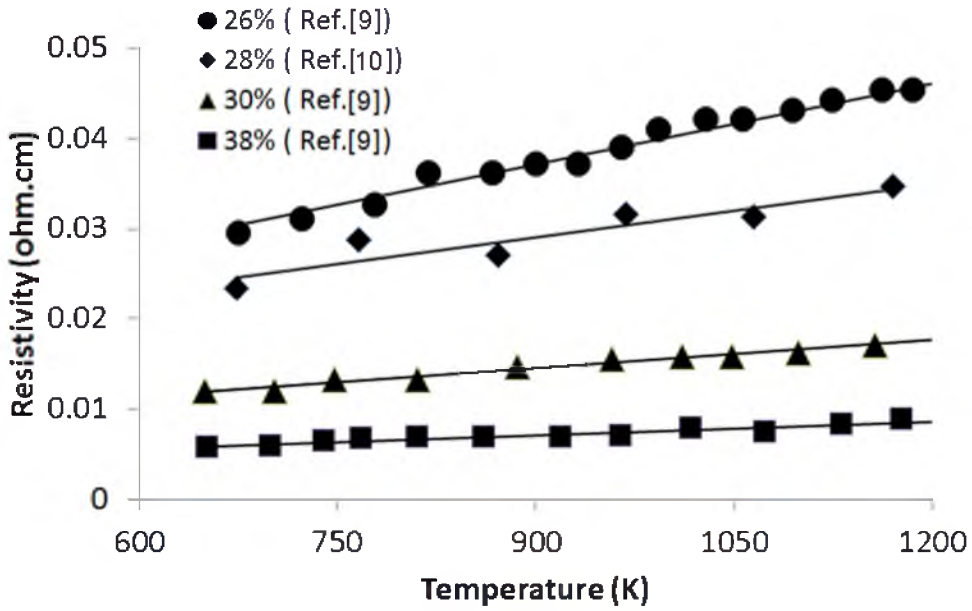

Figure 2-2: Measured electrical resistivity of Ni + YSZ anode containing various volume fractions of Ni as a function of temperature [9,10].

48vol.% porosity [6]. No data are available on samples with 35vol.% Ni. However, data are available for samples with 38vol.% Ni [9,10]. We will use the data corresponding to 38vol.% Ni from Figure 2-2 for the present calculations. Thus the line corresponding to 38vol.% Ni in Figure 2-2 is used to determine ρ_0 and γ for the anode support. For the anode functional layer we will use data for 23% porosity through which the H_2-H_2O binary effective diffusivity is available. The line corresponding to 26vol.% Ni in Figure 2-2 was selected for the estimation of the ohmic contribution of the anode functional layer.

For the rest of the cell components, the electrical resistivities exhibit an Arrhenius behavior [11-16]. Thus the electrical conductivities sharply increase with increasing temperature (electrical resistivities sharply decrease with increasing temperature). The

electrical conductivity may be given by an Arrhenius equation of the form

$$\sigma = \frac{\sigma_0}{T} \exp\left[-\frac{Q}{RT}\right] \tag{2.14}$$

where Q is the activation energy for conduction, σ_0 is the pre-exponential factor in units of $Scm^{-1}K$, R is the gas constant and T is the temperature in K. A plot of $\ln(\sigma T)$ vs. 1/T should be linear with slope equal to –Q/R and intercept equal to $\ln(\sigma_0)$. In the following calculations we will use two different materials for the electrolyte; YSZ and Gd_2O_3 doped CeO_2 (GDC) for which data on ionic conductivities as a function of temperature are well established. The cathode functional layer is selected as 50 vol.% LSM + 50 vol.% YSZ and the cathode current collector is selected as porous LSM. Table 2-1 lists the equations used to estimate the ohmic contributions of the various layers. At any given temperature the ohmic contributions are estimated for all five layers. In the present calculations even with GDC as the electrolyte, the anode and the anode functional layers selected are Ni + YSZ and the cathode current collector and the cathode functional layer contain LSM and LSM + YSZ, respectively. The reason the same materials for the anode and the cathode used for the YSZ electrolyte based cells are also selected for the GDC electrolyte based cells is because out-of-cell measurements are available only for these two sets of materials.

Table 2-1: Electrical conductivities of cell components

Materials	$\sigma\left(S\cdot cm^{-1}\right)$	References
Anode support (Ni + YSZ, 38 vol.% Ni)	$\left(1.03\times10^{-2}+3\times10^{-5}T\right)^{-1}$	[9]
Anode functional layer (Ni + YSZ, 26 vol.% Ni)	$\left(2.70\times10^{-2}+5\times10^{-6}T\right)^{-1}$	[9, 10]
Electrolyte (YSZ)	$\frac{3.60\times10^{5}}{T}\exp\left(\frac{-85.63\times10^{3}}{RT}\right)$	[11-13]
Electrolyte (GDC)	$\frac{4.62\times10^{4}}{T}\exp\left(\frac{-58.48\times10^{3}}{RT}\right)$	[14]
Cathode functional layer (50% LSM + YSZ)	$\frac{2.94\times10^{4}}{T}\exp\left(\frac{-17.40\times10^{3}}{RT}\right)$	[15]
Cathode current collector (LSM)	$\frac{1.02\times10^{4}}{T}\exp\left(\frac{-9.58\times10^{3}}{RT}\right)$	[16]

2.2.1.2 Contact Resistance

The origin of the 'contact resistance', $R_{contact}$, lies in the differing microstructures across the various interfaces which may lead to delamination, voids or cracks at interfaces across which no current flows, and the possible formation of a resistive layer at the cathode/electrolyte interface, most notably $La_2Zr_2O_7$ [8]. This effectively adds to the ohmic contribution. The $R_{contact}$ can in principle be measured by direct experiments wherein samples of different layer thicknesses can be made but with the same interface (or by measuring the resistance at various positions on either side of the interface and extrapolating the two segments to the interface). No such measurements appear to be available in the literature. Even though detailed information on the contact resistance between cell components, e.g., contact resistance between anode support and anode functional layer, or between electrolyte and cathode functional layer does not appear to

have been reported, a model which predicts the contact resistance between anode and interconnect as well as between cathode and interconnect has been proposed by Dey et al. [17]. Their model showed good agreement with experimental results given in [17] in which detailed morphology of the electrodes and contact with interconnects such as the contact radius for a single asperity, summit radius, height of an asperity and the inter-planar spacing were taken into account. Their study also showed that the contact resistance initially decreased rapidly with increasing externally applied pressure between the two layers and then saturated at larger pressures. Under an optimum pressure the measured contact resistances at 800°C between the anode and interconnect and between the cathode and interconnect were 0.048 Ωcm^2 and 0.033 Ωcm^2, respectively. These two values changed by a factor of less than two in the temperature range from 600 to 800°C.

In [6] the authors measured the ohmic resistance as a function of the thickness of the YSZ electrolyte, the Ni + YSZ anode support and the LSM + YSZ cathode functional layer. The resistivity of the corresponding layer was given by the slope. In all three plots the intercepts were nonzero [6]. Their magnitudes were, respectively, 0.087, 0.084 and 0.095 Ωcm^2 which all showed that there was some contact resistance in addition to the contributions from the various layers. However, because these authors did not measure the resistivities of the remaining two layers, namely, the anode functional layer and the cathode current collector, they were unable to estimate the contact resistance contribution to their cells. If we use the conductivity formulas in Table 2-1 for the anode functional layer and the cathode current collector obtained from the literature by using equations (2.11) and (2.12), the ohmic loss from the five layers can be calculated. The calculations show that the electrolyte and the anode support dominate the ohmic contribution.

Therefore, in what follows we calculate the ohmic resistances for cells of the same geometries as given in [6] and the results are compared in Table 2-2. As seen in Table 2-2 the calculated contact resistances from eight different cells range from 39% to 57% of the total ohmic resistance with the average being about 48% and a standard deviation of about 7%. It is also to be noted that the calculated resistances have the same magnitudes as those measured by Dey et al. [17]. This shows that, for the five-layer cell, the contact resistance attributed to the various interfaces is approximately 50% of the total ohmic resistance. Thus, in the following calculations we will assume that the contact resistance is about 50% of the total cell ohmic resistance which includes the possible existence of cracks along interfaces and the formation of resistive layers such as $La_2Zr_2O_7$.

2.2.1.3 Concentration Polarization

In what follows concentration polarizations at the cathode and at the anode are estimated using the measured effective binary diffusivities. It is assumed that the somewhat higher tortuosity factors (~6 to 10), typically obtained by fitting polarization curves, are the result of the neglect of Knudsen diffusion [18]. The use of the measured effective diffusivities is deemed more accurate than assuming a multiple of unknown parameters such as the tortuosity factor, the pore size and the possible role of surface diffusion along the pore surfaces done in some modeling studies. Also, the rationale is that the effective diffusivities can be experimentally measured but the tortuosity factors or the pore sizes (which need to be used in the approximate estimation of effective Knudsen diffusivities) are not easily measurable. In addition the pores are not of uniform shape and size. Thus, the use of the Dusty Gas Model [19] does not obviate the need for

Table 2-2: Measured and calculated ohmic resistance for different cells at 800°C

Anode support thickness 1 mm, anode interlayer thickness 20 μm, cathode functional layer thickness 20 μm, cathode current collector thickness 50 μm				
Electrolyte thickness (μm)	4	8	15	20
Measured ohmic resistance [4] (Ωcm^2)	0.10	0.104	0.114	0.14
Estimated ohmic resistance (5 layers) (Ωcm^2)	0.043	0.053	0.069	0.081
Estimated contact resistance (Ωcm^2)	0.057	0.051	0.045	0.059
Contact resistance proportion	57%	49%	39%	42%

Anode interlayer thickness 20 μm, electrolyte thickness 8 μm, cathode functional layer thickness 20 μm, cathode current collector thickness 50 μm				
Anode support thickness (mm)	0.5	1.0	1.5	2.45
Measured ohmic resistance [4] (Ωcm^2)	0.095	0.104	0.13	0.14
Estimated ohmic resistance (5 layers) (Ωcm^2)	0.041	0.053	0.064	0.087
Estimated contact resistance (Ωcm^2)	0.054	0.051	0.066	0.053
Contact resistance proportion	57	49	51	38

the details of electrode microstructures and their incorporation into realistic transport equations. For this reason an approach using effective diffusivities is deemed satisfactory as these can be experimentally measured. The concentration polarization at the cathode is given by [3, 6]

$$\eta_{conc}^{c} = -\frac{RT}{4F}\ln\left(\frac{p'_{O_2(i)}(i)}{p^{0}_{O_2}}\right) \tag{2.15}$$

where $p^{0}_{O_2}$ is the partial pressure of oxygen just outside the cathode, $p'_{O_2(i)}(i)$ is the partial pressure of oxygen in the cathode functional layer close to the cathode functional layer/electrolyte interface. The $p'_{O_2(i)}(i)$ for a two layer cathode can be calculated by [6]

$$p'_{O_2(i)}(i) \approx p^{0}_{O_2} - \left(\frac{iRT}{4Fp}\right)\left[\left(p - p^{0}_{O_2}\right)\left(\frac{l_{c(1)}}{D^{eff(1)}_{O_2-N_2}} + \frac{l_{c(2)}}{D^{eff(2)}_{O_2-N_2}}\right) + \frac{\left(p - p^{0}_{O_2}\right)}{p}\left(\frac{iRTl_{c(1)}l_{c(2)}}{4FD^{eff(1)}_{O_2-N_2}D^{eff(2)}_{O_2-N_2}}\right)\right] \tag{2.16}$$

where $l_{c(1)}$ and $l_{c(2)}$ are, respectively, the cathode current collector and the cathode functional layer thicknesses, $D^{eff(1)}_{O_2-N_2}$ and $D^{eff(1)}_{O_2-N_2}$ are, respectively, the effective binary diffusivities through the cathode current collector and the cathode functional layer and p is the total oxidant pressure (the sum of oxygen and nitrogen partial pressures).

The anode concentration polarization is similarly given by

$$\eta_{conc}^{a} = -\frac{RT}{2F}\ln\left(\frac{p'_{H_2(i)}(i)\,p^{0}_{H_2O}}{p^{0}_{H_2}\,p'_{H_2O(i)}(i)}\right) \tag{2.17}$$

where $p^{0}_{H_2}$ is the partial pressure of hydrogen in the fuel just outside the anode, $p^{'}_{H_2(i)}(i)$ is the partial pressure of hydrogen in the anode functional layer close to the anode functional layer/electrolyte interface, $p^{o}_{H_2O}$ is the partial pressure of water vapor just outside the anode and $p^{'}_{H_2O(i)}(i)$ is the partial pressure of water vapor in the anode functional layer close to the anode functional layer/electrolyte interface. The $p^{'}_{H_2(i)}(i)$ and $p^{'}_{H_2O(i)}(i)$ for a two-layer anode are given, respectively, by [6]

$$p^{'}_{H_2(i)}(i) = \frac{l_{a(2)}}{D^{eff(2)}_{H_2-H_2O}}\left[\frac{p^{o}_{H_2} D^{eff(2)}_{H_2-H_2O}}{l_{a(2)}} - \frac{iRTl_{a(1)}}{2FD^{eff(1)}_{H_2-H_2O}}\left(\frac{D^{eff(2)}_{H_2-H_2O}}{l_{a(2)}} + \frac{D^{eff(1)}_{H_2-H_2O}}{l_{a(1)}}\right)\right] \tag{2.18}$$

$$p^{'}_{H_2O(i)}(i) = \frac{l_{a(2)}}{D^{eff(2)}_{H_2-H_2O}}\left[\frac{p^{o}_{H_2O} D^{eff(2)}_{H_2-H_2O}}{l_{a(2)}} + \frac{iRTl_{a(1)}}{2FD^{eff(1)}_{H_2-H_2O}}\left(\frac{D^{eff(2)}_{H_2-H_2O}}{l_{a(2)}} + \frac{D^{eff(1)}_{H_2-H_2O}}{l_{a(1)}}\right)\right] \tag{2.19}$$

where $l_{a(1)}$ and $l_{a(2)}$ are, respectively, the anode support and the anode functional layer thicknesses, $D^{eff(1)}_{H_2-H_2O}$ and $D^{eff(2)}_{H_2-H_2O}$ are, respectively, the effective binary diffusivities through the anode support and the anode functional layer.

The effective diffusivities of mixed gases have been measured using techniques such as gas chromatography, steady-state diffusion cells, thermogravimetry using a microbalance, etc. However, measurements of effective diffusivities by these methods are typically conducted at one atmosphere pressure and in the temperature range from 30 to 300°C. In order to measure the effective binary diffusivity of O_2-N_2 through porous

media at the typical SOFC operating temperatures a special electrochemical concentration cell was fabricated by Zhao et al. [20]. Such a cell consists of a YSZ cylinder, a porous LSM disk attached to one side by a glass seal and a dense 8YSZ disc at the other end, also attached by a glass seal. A pair of porous platinum electrodes is applied on the YSZ disc and also across the YSZ cylinder wall. A DC voltage is applied across the YSZ disc with the platinum electrodes and the current flowing through the cell is measured. Oxygen can be pumped in or out of the chamber depending upon the polarity of the applied voltage. In steady state the net oxygen flux entering/leaving the chamber through the porous LSM disc is the same as the net oxygen flux leaving/entering the chamber through the YSZ disc. The oxygen partial pressure inside the chamber is measured using the pair of Pt electrodes applied across the YSZ cylinder wall which serves as a potentiometric sensor. From these measurements the effective binary diffusivity, $D^{eff}_{O_2-N_2}$, through the porous LSM disk was measured as a function of porosity and temperature [20].

The H_2-H_2O effective binary diffusivity in porous anodes was measured by He et al. [21] using a similar electrochemical cell as used in the O_2-N_2 effective diffusivity measurements. In both studies the Nernst potential on the oxygen sensor was continuously measured until the oxygen partial pressure inside the chamber did not appreciably change with time. For the H_2-H_2O effective diffusivity measurements also the temperature was varied between 650 and 800°C in a 50 degree interval.

In order to obtain effective diffusivities at other temperatures the following approach is used. For an A-B binary system the effective diffusivity, D^{eff}_{A-B}, is related to the A-B binary bulk diffusivity, D_{A-B}, through the phenomenological theory by [22]

$$D_{A-B}^{eff} = \frac{V_v}{\tau} D_{A-B} \tag{2.20}$$

where V_v is the volume fraction of porosity and τ is the tortuosity factor. The D_{A-B} at moderate temperatures and pressures can be estimated by the Chapman-Enskog relation [22]

$$D_{A-B} = \frac{0.00186 T^{\frac{3}{2}} \left(\frac{1}{M_A + M_B} \right)^{\frac{1}{2}}}{p \sigma_{A-B}^2 \Omega} \tag{2.21}$$

where p is the pressure, M_A and M_B are the molecular weights of the two gaseous species and Ω is the collision integral, a dimensionless quantity which accounts for the interaction between the two species via the Lennard-Jones potential. The σ_{A-B} is the collision diameter which is the arithmetic average of the diameters of the two gas species. Both O_2-N_2 and H_2-H_2O binary diffusivities can be found in [22].

Combining equations (2.20) with (2.21) gives

$$D_{A-B}^{eff} = k_p T^{\frac{3}{2}} \tag{2.22}$$

where $k_p = \frac{V_v}{\tau} \frac{0.00186 \left(\frac{1}{M_A + M_B} \right)^{\frac{1}{2}}}{p \sigma_{A-B}^2 \Omega}$ is a constant corresponding to the porosity and the tortuosity of a given porous medium and the total pressure. By substituting for the

measured O_2-N_2 and H_2-H_2O effective diffusivities at a given temperature into equation (2.22) the k_p was estimated. In our calculations the sets of values used for $D^{eff(1)}_{O_2-N_2}$ and $D^{eff(2)}_{O_2-N_2}$ at 800°C were, respectively, 0.14 cm^2s^{-1} (~45% porosity) and 0.04 cm^2s^{-1} (~26% porosity) obtained from the work of Zhao and Virkar [20]. The values of $D^{eff(1)}_{H_2-H_2O}$ and $D^{eff(2)}_{H_2-H_2O}$ at 800°C used were, respectively, 0.68 cm^2s^{-1} (~48% porosity) and 0.08 cm^2s^{-1} (~23% porosity) obtained from the work by He et al. [21]. Using these values the corresponding k_p was calculated to be 3.98 x 10^{-6} for $D^{eff(1)}_{O_2-N_2}$, 1.14 x 10^{-6} $D^{eff(2)}_{O_2-N_2}$, 1.93 x 10^{-5} for $D^{eff(1)}_{H_2-H_2O}$ and 2.28 x 10^{-6} for $D^{eff(2)}_{H_2-H_2O}$, all in $cm^2s^{-1}K^{-3/2}$. Using equation (2.22) D^{eff}_{A-B} for both the cathode and the anode were estimated at lower temperatures.

2.2.1.4 Activation Polarization

Activation polarizations at the two electrodes should strictly be described separately using parameters such as the exchange current densities and the transfer coefficients separately for the cathode and the anode. The difficulty has been in conducting accurate polarization measurements on actual cells and separating the cathode and the anode contributions. Measurements made using out-of-cell, the so-called three-electrode system under an applied DC bias, are often inaccurate and not representative of the true SOFC operating conditions [1, 23]. The principal problem is that the use of the out-of-cell three electrode system requires the application of an external voltage across the working and the counter electrodes. In the actual cell, however, there is no applied voltage – but a

Nernst voltage is generated under the application of a difference in chemical potentials across the two electrodes. The spatial distributions of chemical potentials through the electrolyte are very different in the two situations. As such the measured electrode kinetics (such as the oxygen reduction reaction) under an applied voltage can be quite different than under an internally generated Nernst voltage [23].

An alternative is to measure the charge transfer characteristics using the three-electrode system under no applied DC bias using electrodes of well-defined geometries, e.g., well-defined three-phase boundary (TPB) length, ℓ_{TPB}, on a planar (two-dimensional) surface. Such a measurement can give the exchange current density as a function of test conditions (temperature and atmosphere) for the given electrode geometry, e.g., ℓ_{TPB}. The exchange current densities at the cathode and the anode are dependent on both temperature and the partial pressure of the electroactive gaseous species in addition to ℓ_{TPB}. A parameter which may be defined as charge transfer resistivity, ρ_{ct}, for the oxygen reduction reaction (ORR) has been measured on LSM/YSZ and Pt/YSZ electrode systems using patterned electrodes deposited by micro photolithography [24, 25]. This parameter, ρ_{ct}, embodies the kinetics of the overall electrochemical reaction which depends upon a number of parameters such as the oxygen partial pressure, the temperature, the electronic and the ionic conductivities of the electrode and the electrolyte, adsorption, dissociation, electron transfer, etc. However, the ρ_{ct} is independent of geometry, that is independent of ℓ_{TPB}. The knowledge of ρ_{ct} facilitates the estimation of the exchange current density for an actual three-dimensional cathode – provided the details of geometrical (microstructural) features are known.

For a composite electrode with a functional layer thickness greater than the threshold

thickness the effective charge transfer resistance or the activation polarization resistance is given by [20]

$$R_{ct}^{eff} \approx \sqrt{\frac{d\rho_i \rho_{ct}}{(1-V_v)\ell_{TPB}}} = \frac{RT}{4Fi_o^{eff}} \tag{2.23}$$

where ρ_i is the ionic resistivity of the composite electrode (that of YSZ in the electrode, for example), d is the grain size of the composite electrode (that of YSZ in the electrode), V_v is the volume fraction porosity, ℓ_{TPB} is the three-phase boundary (TPB) length in the composite electrode (distributed on the surface of a three-dimensional porous structure), i_o^{eff} is the effective exchange current density of the composite electrode which takes into account the distributed electrochemical reaction through the thickness of the electrode and ρ_{ct} is the charge transfer resistivity, a fundamental, microstructure-independent parameter which describes the resistance to the charge transfer reaction. The ρ_{ct} is a measure of the kinetics of the overall intrinsic electrode reaction, namely $^1/_2O_2$ (gas) + 2e' (electrocatalyst, e.g., LSM) → O^{2-} (electrolyte, e.g., YSZ). There are a number of series steps in this reaction such as: (a) adsorption of O_2, (b) dissociation of the adsorbed O_2 into adsorbed 2O, (c) electron transfer to form O^{2-} and (d) its incorporation into the electrolyte which typically involves a vacancy mechanism. At the present no experimental or theoretical methods are known that can unequivocally determine each of the steps quantitatively and provide independent verification. However, the ρ_{ct} measured by patterned electrodes includes the effects of all of these steps. This is the parameter which can be measured and thus constitutes one of the input parameters in our model.

For cathode activation polarization, $\rho_{ct(c)}(T, p_{O_2})$ is of the form [24, 25]

$$\rho_{ct(c)}(T, p_{O_2}) \approx \rho''_{ct(c)}(T) + \frac{\rho''_{ct(c)}(T)}{b_c^*(T)\sqrt{p_{O_2}}} \tag{2.24}$$

where $b_c^*(T)$ is the Langmuir adsorption coefficient and $\rho''_{ct(c)}(T)$ is the charge transfer resistivity corresponding to an adsorbed oxygen surface coverage of unity. The $\rho_{ct(c)}(T, p_{O_2})$ is a measure of the overall charge transfer reaction and involves a number of series steps.

Substitution of the above parameters for a composite cathode gives [26]

$$i_{o(c)}^{eff} \approx \frac{RT}{4F}\sqrt{\frac{(1-V_{v(c)})}{\rho_i d_c}}\sqrt{\frac{\ell_{TPB(c)}}{\rho_{ct(c)}(T, p_{O_2})}} \tag{2.25}$$

which is the effective exchange current density for the composite, three-dimensional cathode given as a function of temperature and oxygen partial pressure in terms of measurable parameters (namely, $V_{v(c)}$, d_c, $\ell_{TPB(c)}$, ρ_i, and $\rho_{ct(c)}$) where subscript 'c' denotes cathode parameters. The preceding assumes dissociative adsorption of O_2.

To calculate the cathode activation polarization the experimentally measured charge transfer resistivities, $\rho_{ct(c)}(T, p_{O_2})$, using patterned electrodes are available for LSM/YSZ and Pt/YSZ systems [24, 25]. In those studies $\rho''_{ct(c)}(T)$ and $b_c^*(T)$ in equation (24) for LSM/YSZ and Pt/YSZ were measured over a temperature range from 650 to

800°C in 50 degree intervals. Since $\rho''_{ct(c)}(T)$ is thermally activated, it is of the form

$$\rho''_{ct(c)}(T) = \rho''_{ct(c)_o} \exp\left[\frac{Q_c}{RT}\right] \tag{2.26}$$

where $\rho''_{ct(c)_o}$ is a constant and Q_c is the activation energy. A plot of $\ln\left(\rho''_{ct(c)}(T)\right)$ vs. 1/T is expected to be linear with slope given by $\frac{Q_c}{R}$ and intercept given by $\ln\left(\rho''_{ct(c)_o}\right)$. Using the data given in [24, 25] and the plots of $\ln\left(\rho''_{ct(c)}(T)\right)$vs 1/T the activation energies of $\rho''_{ct(c)}(T)$ for LSM/YSZ and Pt/YSZ cathodes were estimated as ~143 and ~159 kJmol^{-1}, respectively. The pre-exponential constants $\rho''_{ct(c)_o}$ for LSM/YSZ and Pt/YSZ cathodes are 7.71×10^{-3} and 5.94×10^{-5} Ωcm, respectively. The plot of $\ln\left(b_c^*(T)\right)$ vs. 1/T does not follow a linear behavior. However, a plot of $b_c^*(T)$ as a function of 1/T is found to be linear, i.e.,

$$b_c^*(T) = \frac{a_c}{T} + b_c \tag{2.27}$$

The slopes are -1.12×10^3 atm$^{-1/2}$K for LSM/YSZ and 1.05×10^5 atm$^{-1/2}$K for Pt/YSZ, respectively. The intercepts, b_c, are 4.25 and -94.79 atm$^{-1/2}$, respectively, for LSM/YSZ and Pt/YSZ. Note that these are empirical fits. Thus, the observation that in one case b_c is negative has no specific meaning. What is important to note is that over the range of temperatures where equation (2.27) is used, the value of the Langmuir

adsorption coefficient, $b_c^*(T)$, is always positive as required.

In equation (2.25) for the exchange current density at the cathode it is understood that the partial pressure of the active species (oxygen) is that close to the functional layer/electrolyte interface, that is, $p'_{O_2(i)}(i)$. This partial pressure is a function of the porosities, the tortuosities, the thicknesses of the porous layers, the partial pressure of the oxidant in the incoming gas and the net current density, i. That is, $i_{o(c)}^{eff}$ is also affected by concentration polarization. Thus, it is first necessary to estimate $p'_{O_2(i)}(i)$ which is dictated by concentration polarization governed by the net current density, i, which is the independent variable in the model. For an arbitrarily chosen i, the $p'_{O_2(i)}(i)$ is estimated from equation (2.16). Using this value of $p'_{O_2(i)}(i)$, the $\rho_{ct(c)}(T, p'_{O_2(i)}(i))$ is estimated using equation (2.24) and from equation (2.25) the $i_{o(c)}^{eff}$ is estimated. Finally using the estimated value of $i_{o(c)}^{eff}$, which is a function of i, the cathode activation polarization is calculated as discussed later.

Thus, as discussed in the preceding, combining equations (2.23), (2.24) and (2.26), the charge transfer resistivity, $\rho_{ct(c)}(T, p_{O_2})$, can be estimated as a function of temperature and p_{O_2} which is used to estimate the effective exchange current density.

In the present work calculations of $i_{o(c)}^{eff}$ are presented for three different microstructures in the cathode functional layer: $d_c = 2$ μm, $d_c = 0.2$ μm, and $d_c = 0.02$ μm. The first is routinely achieved using typical ceramic powders. The second one can be achieved using processes that can form nanometer scale powders at low temperatures.

The third type of microstructure may be obtained by nanometer scale powders and low temperature processing. Corresponding to the three microstructures the three values of the three-phase boundary lengths, ℓ_{TPB}, used are: $\ell_{TPB} = 10{,}000$ cm^{-1}, $\ell_{TPB} = 100{,}000$ cm^{-1} and $\ell_{TPB} = 1{,}000{,}000$ cm^{-1}. These correspond to 50% surface coverage of the porous electrode interior surface by the electrocatalyst (LSM or Pt) particles of a size equal to $d_c/2$. The functional layer thickness was assumed to be $15d_c$ based on the prior modeling work [26]. The experimental work on microstructural features on the order of a few microns has shown that these estimates are very reasonable [27].

For anode activation polarization similar equations are given in what follows. In the case of the anode it is expected that the partial pressure dependence of the charge transfer resistivity is on p_{H_2}. Thus, for the anode one may write

$$i_{o(a)}^{eff} \approx \frac{RT}{4F}\sqrt{\frac{(1-V_{v(a)})}{\rho_i d_a}}\sqrt{\frac{\ell_{TPB(a)}}{\rho_{ct(a)}(T,p_{H_2})}} \tag{2.28}$$

where

$$\rho_{ct(a)}(T,p_{H_2}) \approx \rho''_{ct(a)}(T) + \frac{\rho''_{ct(a)}(T)}{b_a^*(T)\sqrt{p_{H_2}}} \tag{2.29}$$

The subscript 'a' denotes anode parameters. The preceding assumes that the electrochemical reaction involves one mole of O_2 and 2 moles of H_2. Also the preceding assumes dissociative adsorption of H_2.

Once again in order to study the anode activation polarization one of the challenges is to determine the relationship between the length of TPB and the charge-transfer

resistance in an actual electrode in order to determine the charge transfer resistivity, a microstructure-independent parameter. This is difficult to achieve using a conventional porous composite electrode and measurements on well-defined Ni/YSZ patterned electrodes are necessary. A few studies have reported on the charge transfer reaction mechanism for hydrogen electrochemical oxidation in SOFC using Ni/YSZ patterned anodes [28,29]. While these studies provided detailed discussions on the hydrogen oxidation mechanisms, direct relationship such as equation (2.29) between the charge transfer resistivity and hydrogen partial pressure which is needed to estimate anode activation polarization, was not given. However, based on the reported data on Ni/YSZ patterned anodes [28], it is possible to plot $\rho_{ct(a)}(T, p_{H_2})$ as a function of $1/\sqrt{p_{H_2}}$ at various temperatures using the methods described in [24, 25] and to fit the data to an equation similar to (2.26). Figure 2-3 shows similar plots of data given by Bieberle et al. [28]. As seen in Figure 2-3 such plots are linear where slope equals $\frac{\rho''_{ct(a)}(T)}{b_a^*(T)}$ and intercept equals $\rho''_{ct(a)}(T)$.

Since $\rho''_{ct(a)}(T)$ is also thermally activated it follows a similar equation as used for the cathode charge transfer resistivity, namely

$$\rho''_{ct(a)}(T) = \rho''_{ct(a)_o} \exp\left[\frac{Q_a}{RT}\right] \tag{2.30}$$

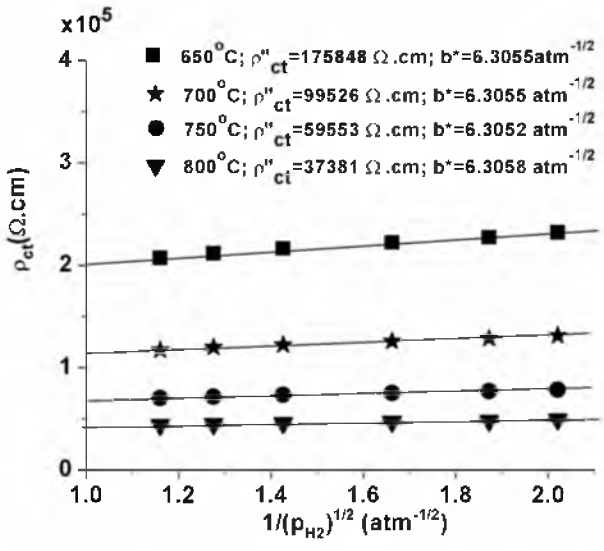

Figure 2-3: Plot of charge transfer resistivity, ρ_{ct}, for Ni/YSZ vs. $1/\sqrt{p_{H_2}}$ using data from Bieberle et al. [28].

where $\rho''_{ct(a)_o}$ is a constant and Q_a is the activation energy. A plot of $\ln \rho''_{ct(a)}(T)$ vs $1/T$ thus should be linear with slope given by $\frac{Q_a}{R}$ and intercept given by $\ln\left(\rho''_{ct(a)_o}\right)$. Using the data given in [28] and plotting $\ln \rho''_{ct(a)}(T)$ vs $1/T$, the activation energy of $\rho''_{ct(a)}(T)$ for Ni/YSZ anode is determined to be 85 kJmol^{-1}. The pre-exponential constant $\rho''_{ct(a)_o}$ is 2.72 Ωcm. The plot also shows that $b_a^*(T)$ is nearly a constant independent of temperature with a value of about 6.3 atm$^{-1/2}$.

For the estimation of the effective anode exchange current density, $i_{o(a)}^{eff^*}$, three different types of microstructures, namely $d_a = 2$ μm, $d_a = 0.2$ μm and $d_a = 0.02$ μm were used, the same as for the cathode functional layer. The corresponding three-phase boundary lengths are 10,000 cm^{-1}, 100,000 cm^{-1} and 1,000,000 cm^{-1}. The procedure for

the calculation of $i_{o(a)}^{eff}$ is similar to that of $i_{o(c)}^{eff}$. For given values of partial pressures of hydrogen, $p_{H_2}^o$, and water vapor, $p_{H_2O}^o$, in the anode gas and for an arbitrarily selected net current density, i, the $p'_{H_2(i)}(i)$ is estimated using equation (2.18). Then from equation (2.29) the corresponding charge transfer resistivity is calculated using equation (2.30), namely, $\rho_{ct(a)}(T, p'_{H_{2(i)}}(i)) \approx \rho''_{ct(a)}(T) + \frac{\rho''_{ct(a)}(T)}{b_a^*(T)\sqrt{p_{H_{2(i)}}(i)}}$, which is a function of the net current density, i. From this calculation using equation (2.28) the effective exchange current density, $i_{o(a)}^{eff} \approx \frac{RT}{4F}\sqrt{\frac{(1-V_{v(a)})}{\rho_i d_a}}\sqrt{\frac{\ell_{TPB(a)}}{\rho_{ct(a)}(T, p_{H_2(i)}(i))}}$, is estimated. Note that this is a function of the net current density.

The Tafel equation may be used to describe the dependence of activation polarization on current density for values of current density well above the effective exchange current density. For current densities lower than the effective exchange current density, i_o^{eff}, it is necessary to either simplify the Butler-Volmer equation and use a linear relationship or alternatively use the complete Butler-Volmer equation. In a typical SOFC at elevated temperatures effective exchange current densities can be quite high – several tens or even hundreds of $mAcm^{-2}$. For example for an $R_{ct(c)}^{eff}$ of 0.05 Ωcm^2, a value that has been reported on a number of highly active cathodes at 800°C, the corresponding cathode exchange effective current density, $i_{o(c)}^{eff}$, is ~460 $mAcm^{-2}$. Thus, the use of the Butler-Volmer equation may be necessary especially at lower current densities and the Tafel equation can only be used at much higher current densities. Either approach, however,

requires the knowledge of the transfer coefficient. In the absence of information on the transfer coefficient in what follows we assume a transfer coefficient of 0.5 which also facilitates writing an analytical equation for the activation polarization in terms of the current density (instead of using the Butler –Volmer equation with transfer coefficient different from 0.5 in which the current density is an implicit function of the overpotential).

Finally once the effective exchange current densities at both the anode and the cathode are known, the activation polarization at the two electrodes can be calculated separately. For the cathode the activation polarization may be given by

$$\eta_{act}^{c} = \frac{RT}{2F} \operatorname{arcsin h}\left(\frac{i}{2i_{o(c)}^{eff}}\right) \tag{2.31}$$

where we have assumed the transfer coefficient to be 0.5. Similarly, the activation polarization for the anode is given by

$$\eta_{act}^{a} = \frac{RT}{2F} \operatorname{arcsin h}\left(\frac{i}{2i_{o(a)}^{eff}}\right) \tag{2.32}$$

with once again the transfer coefficient assumed as 0.5. At present there does not appear to be a reliable method for measuring the transfer coefficient as this requires an experimental measurement of activation polarization on an actual cell and as a function of current density.

2.2.2 Procedure for Calculations

Values of $p^o_{H_2}$, $p^o_{H_2O}$ (fuel) and $p^o_{O_2}$ (oxidant) are selected corresponding to the typical operating conditions. For example for the incoming fuel the $p^o_{H_2}$ is ~0.97 atm and for the incoming oxidant the $p^o_{O_2}$ is ~0.21 atm. Calculations can be readily made for depleted fuel and oxidant and will represent local performance corresponding to given local fuel and oxidant utilizations. A set of effective diffusivities for the anode and the cathode are used based on out-of-cell measurements as described earlier. The cell ohmic ASR is estimated from the knowledge of the respective resistivities of the layers and the estimated contact resistances as described earlier.

The independent variable in the calculations is the net current density, i. All polarization losses are calculated for any given value of the current density. The corresponding cell voltage, $V(i)$, is given by the Nernst voltage minus all of the various polarizations (equation (2.1)). The short circuit current density is the one for which the $V(i)$ is zero.

For a given current density the ohmic loss is the product of the current density and the ohmic ASR.

For a given current density the partial pressures of hydrogen, $p'_{H_{2(i)}}(i)$, and water vapor, $p'_{H_2O(i)}(i)$, near the anode functional layer/electrolyte interface and the partial pressure of oxygen, $p'_{O_{2(i)}}(i)$, near the cathode functional layer/electrolyte interface were determined (using equations (2.16), (2.18) and (2.19)). This also allowed for the estimation of the respective concentration polarizations.

Using the estimated partial pressures close to the electrolyte/electrode functional layer interfaces, the corresponding charge transfer resistivities were estimated using out-of-cell data obtained by patterned electrodes [24, 25, 28]. For example for the cathode the relevant equation is (2.24). The effective charge transfer resistance (or exchange current density) was estimated (equations (2.23), (2.24), and (2.25)). The calculations were made for various microstructures for the functional layer, namely the grain size, d, volume fraction porosity, V_v, and the three-phase boundary length, ℓ_{TPB}. The values selected for the following calculations are those that are deemed experimentally realistic. For the cathode, calculations are made at a given temperature for a wide range of oxygen partial pressures, p_{O_2}. This effectively is a calculation corresponding to a given p'_{O_2}, the oxygen partial pressure close to the cathode functional layer/electrolyte interface. Depending upon the details of the electrode and the oxygen partial pressure in the oxidant, $p^o_{O_2}$, a given p'_{O_2} is achieved at some value of the operating current density, i. The exchange current density is a function of temperature, T, and oxygen partial pressure, p'_{O_2}, namely $i^{eff}_{o(c)}(T, p'_{O_2})$. Once this is obtained the activation polarization at the cathode, $\eta^c_{act}(i)$ is estimated using equation (2.31). This allows for the estimation of $\eta^c_{act}(i,T)$ as a function of temperature and current density since a given p'_{O_2} (which is a function of current density i, $p'_{O_2(i)}(i)$) is attained at a given current density which depends on details of the electrode (microstructure and thickness). Similar calculations are made for the anode activation polarization using equations (2.28), (2.29), (2.30) and (2.32). In this manner all polarization contributions were determined as a function of current density, i.

2.3 Results and Discussion

Figure 2-4(a) and Figure 2-4(b) are, respectively, the calculated values of the partial pressure of hydrogen, $p'_{H_2(i)}(i)$, in the anode functional layer close to the electrolyte and oxygen partial pressure, $p'_{O_2(i)}(i)$, in the cathode functional layer close to the electrolyte as a function of the net current density, i. As the current density increases the interface partial pressures decrease to maintain the corresponding gaseous fluxes. The lowest values of the interface partial pressures approach zero (but do not exactly become zero to ensure gas phase equilibria are maintained). The decrease in partial pressures at the interfaces affects the local charge transfer resistivities given by equation (2.24) at the cathode and equation (2.29) at the anode. As a result the effective exchange current density at the cathode, $i^{eff}_{o(c)}$, given by equation (2.25) and the effective exchange current density at the anode, $i^{eff}_{o(a)}$, given by equation (2.28) are also affected. Figure 2-5(a) shows the calculated $i^{eff}_{o(a)}$ as a function of current density and Figure 2-5(b) shows the calculated $i^{eff}_{o(c)}$ as a function of current density for electrode grain size of 2 μm. As seen in the figures as the current density increases the effective exchange current densities decrease. Finally Figure 2-6(a) and Figure 2-6(b), respectively, show the calculated activation polarization at the anode, η^a_{act}, as a function of current density and activation polarization at the cathode, η^c_{act}, as a function of current density. The very sharp increases in activation polarizations at high current densities are the result of local depletion of oxygen at the cathode functional layer/electrolyte interface and local depletion of hydrogen at the anode functional layer/electrolyte interface.

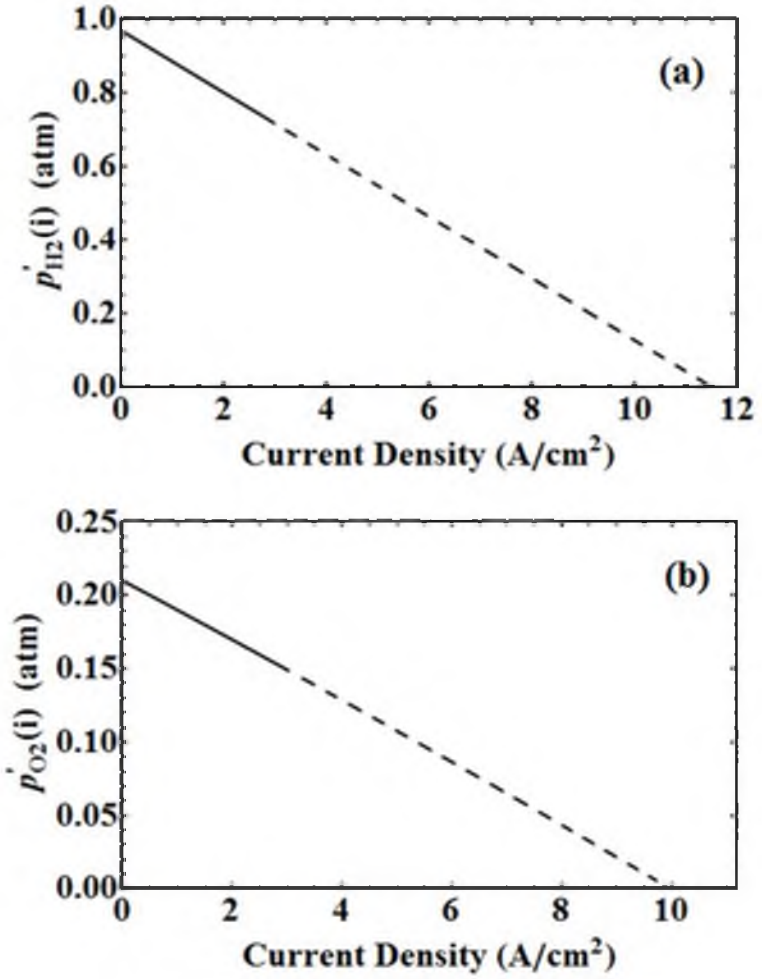

Figure 2-4: Partial pressure vs. current density. (a) A plot of hydrogen partial pressure, $p'_{H_2(i)}(i)$, at the anode functional layer/electrolyte interface in a cell with 2 μm electrode grain size as a function of current density, i. As the current density increases, the partial pressure at the interface decreases, its lowest value approaching zero (but not exactly zero to ensure gas phase equilibrium). (b) A plot of oxygen partial pressure, $p'_{O_2(i)}(i)$, at the cathode functional layer/electrolyte interface in a cell with 2 μm electrode grain size microstructure as a function of current density, i. As the current density increases, the partial pressure at the interface decreases, its lowest value approaching zero.

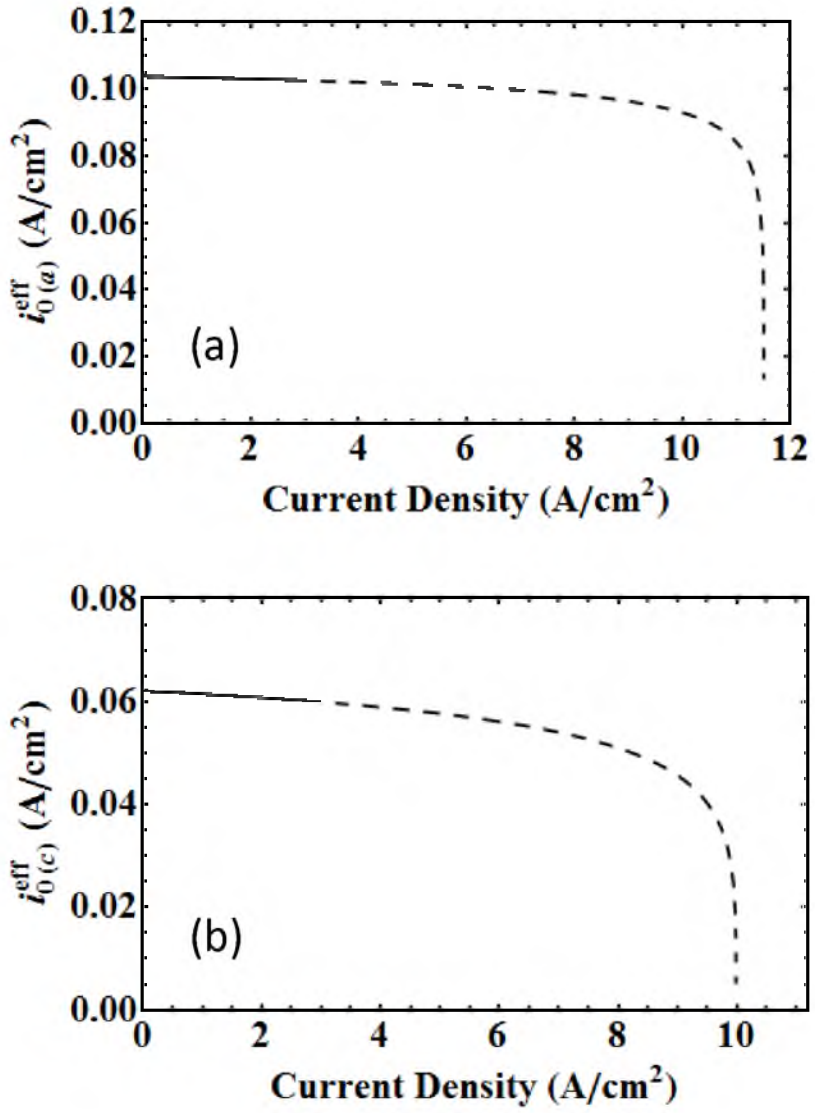

Figure 2-5: i^{eff} vs. current density. (a) Calculated effective exchange current density at the anode, $i^{eff}_{o(a)}$, as a function of current density for a cell with 2 μm electrode grain size. As current density increases, $p'_{H_2(i)}(i)$ decreases and thus the exchange current decreases. (b) Calculated effective exchange current density at the cathode, $i^{eff}_{o(c)}$, as a function of current density for a cell with 2 μm electrode grain size. As the current density increases, the $p'_{O_2(i)}(i)$ decreases and thus the exchange current density decreases.

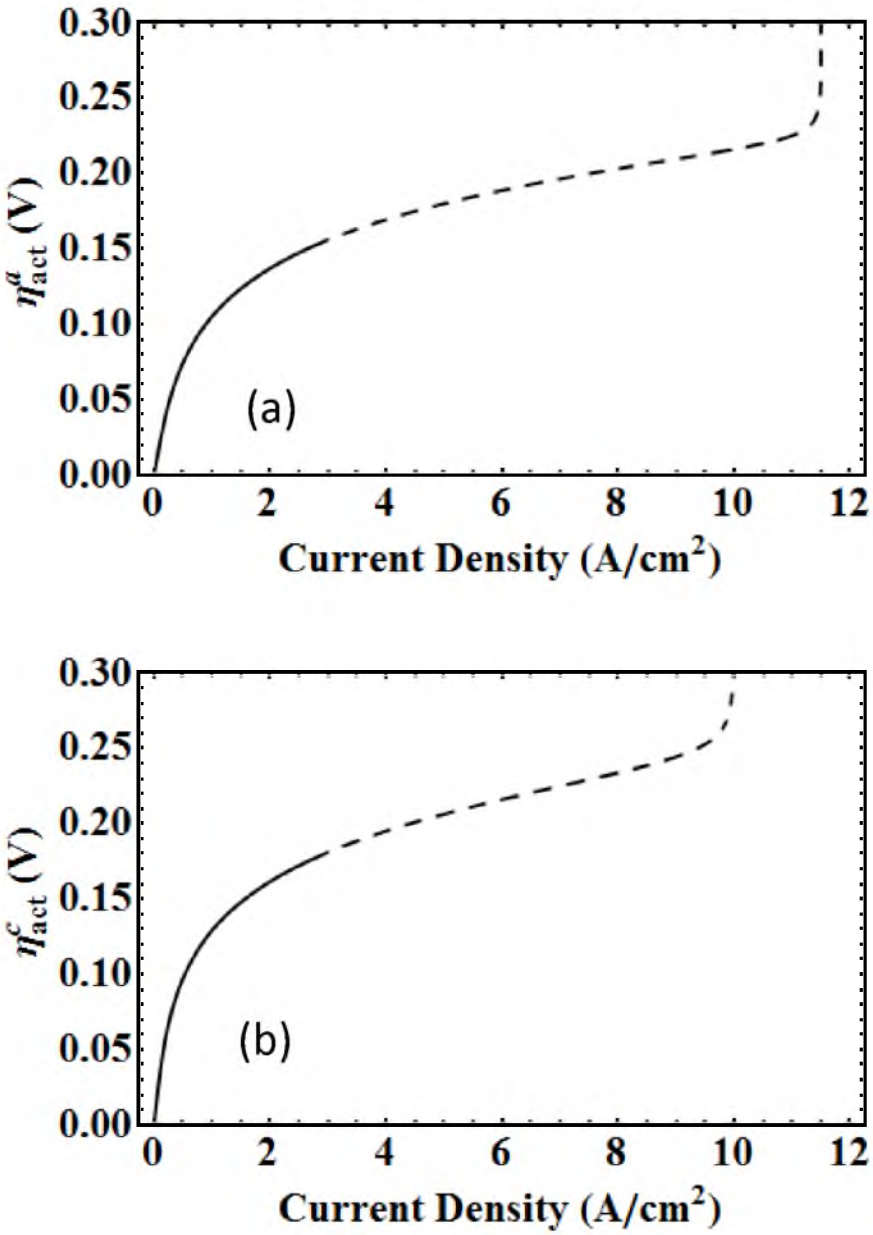

Figure 2-6: Activation polarization vs. current density. (a) Calculated activation polarization at the anode, η^a_{act}, as a function of current density for a cell with 2 μm electrode grain size. (b) Calculated activation polarization at the cathode, η^c_{act}, as a function of current density for a cell with 2 μm electrode grain size.

Figure 2-7(a) shows the calculated polarizations at 800°C for an anode-supported cell with an 8 μm thick YSZ electrolyte, Ni + YSZ anode support of thickness 1 mm, cathode LSM current collector of thickness 50 μm and YSZ grain size in the functional layers of 2 μm. The thicknesses of both the cathode and anode functional layers in each calculation were 15d. Thus, in this calculation the cathode and anode functional layer thicknesses were 30 μm each. The ohmic ASR was assumed to be 0.1 Ωcm^2 a value measured at 800°C in previous work [6]. At low current densities the dominant polarization losses are activation polarization losses at both the cathode and the anode. At higher current densities the ohmic loss dominates even with a thin YSZ film electrolyte. The concentration polarizations at both electrodes are rather small. The corresponding voltage vs. current density and power density vs. current density plots are given in Figure 2-7(b). It is seen that the initial part of the $V(i)$ vs. i curve shows a concave up curvature typical of activation polarization at low current densities. The maximum power density calculated is ~1.0 Wcm^{-2} a typical value reported in a number of studies, especially with relatively coarse electrode microstructures.

Figure 2-8(a) shows similar calculations of polarizations for a cell with electrode grain size of 0.2 μm. Thus, the corresponding functional layer thicknesses are 3 μm. All other parameters are the same as in Figure 2-7(a). Now it is seen that both activation and concentration polarization losses are much lower than the ohmic loss over the entire range of current densities. Figure 2-8(b) shows the corresponding voltage vs. current density and power density vs. current density plots. The $V(i)$ vs. i plot shows very little concave up curvature, since even at the lowest values of the current density the ohmic loss dominates. The maximum power density is about 1.8 Wcm^{-2}. Many studies have

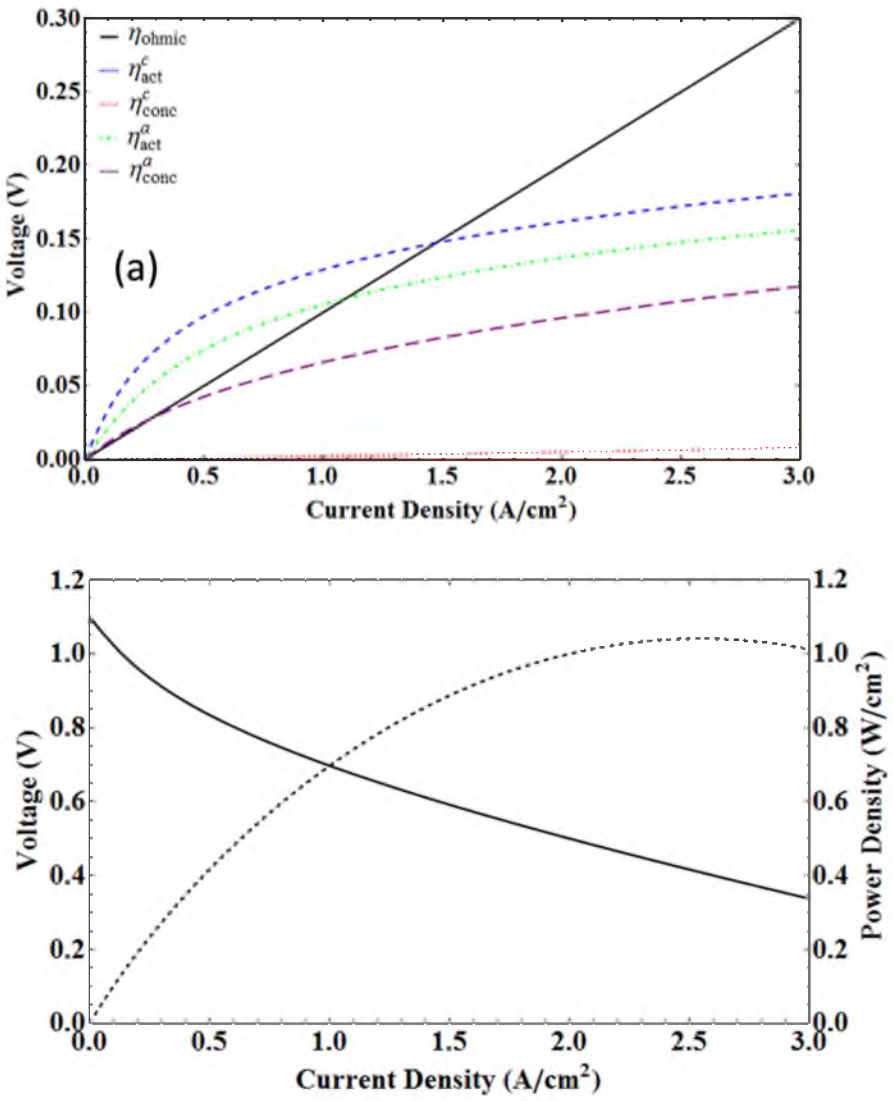

Figure 2-7: V-I curve. (a) Calculated polarizations at 800°C for a 5-layer cell with 8 μm thick YSZ electrolyte, anode support thickness 1 mm, cathode current collector thickness 50 μm, cathode and anode functional layer grain size of 2 μm and functional layer thicknesses of 15d = 30 μm. The ohmic resistance is 0.1 Ωcm^2. At lower current densities the activation polarizations dominate. At higher current densities the ohmic polarization dominates. (b) The corresponding voltage vs. current density and power density vs. current density plots.

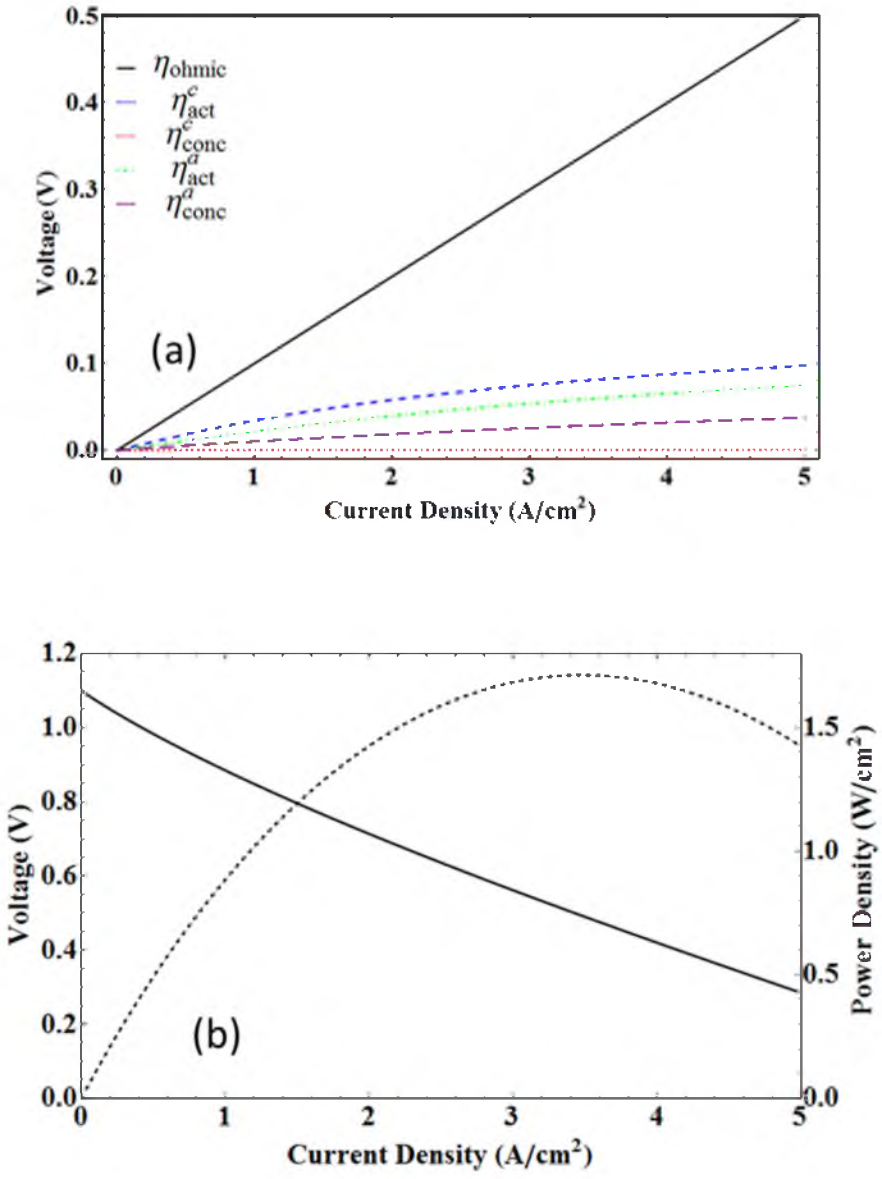

Figure 2-8: V-I curve. (a) Calculated polarizations at 800°C for a 5-layer cell with 8 μm thick YSZ electrolyte, anode support thickness 1 mm, cathode current collector thickness 50 μm, cathode and anode functional layer grain size of 0.2 μm and functional layer thicknesses of 15d = 3 μm. The ohmic resistance is 0.1 Ωcm^2. The ohmic polarization dominates over the entire current density range. (b) The corresponding voltage vs. current density and power density vs. current density plots.

reported similar power densities especially when the electrode microstructures are relatively fine. Figure 2-8(a) and Figure 2-8(b) thus suggest further improvement in electrode will not substantially increase performance.

Figure 2-9(a) and Figure 2-9(b) show similar calculations but now with electrode grain size of 0.02 μm. Such a fine electrode microstructure may be possible by low temperature processing. The activation polarization losses are even smaller and the ohmic loss continues to dominate. The voltage vs. current density plot is almost linear. The maximum power density is now higher (~2.2 Wcm^{-2}). But it is clear that further increase in performance can be realized only through lowering of the ohmic loss.

2.3.1 Calculation of Performance Curves

Figure 2-10 compares experimentally measured voltage vs. current density and power density vs. current density data [6] with *cell performance calculations* made in this study using the parametric model and out of cell data. An important point to note is that the calculations given in Figure 2-10 are based on out-of-cell measurements and the parametric model. Thus, this is a solution to the forward problem unlike commonly made measurements on cells such as using EIS, which cannot give unique values because of the inverse nature of the problem. At 800°C and 700°C, *the calculated performance* curves are in good agreement with experimentally measured. At 600°C, the agreement is good at low current densities (up to about 0.5 Acm^{-2}). Again an important point is that the cell performance curves are calculated using out of cell test data thus demonstrating that by appropriate selection of materials and microstructures, fundamental studies on charge transfer measurements and by conducting gas transport measurements, it is possible to

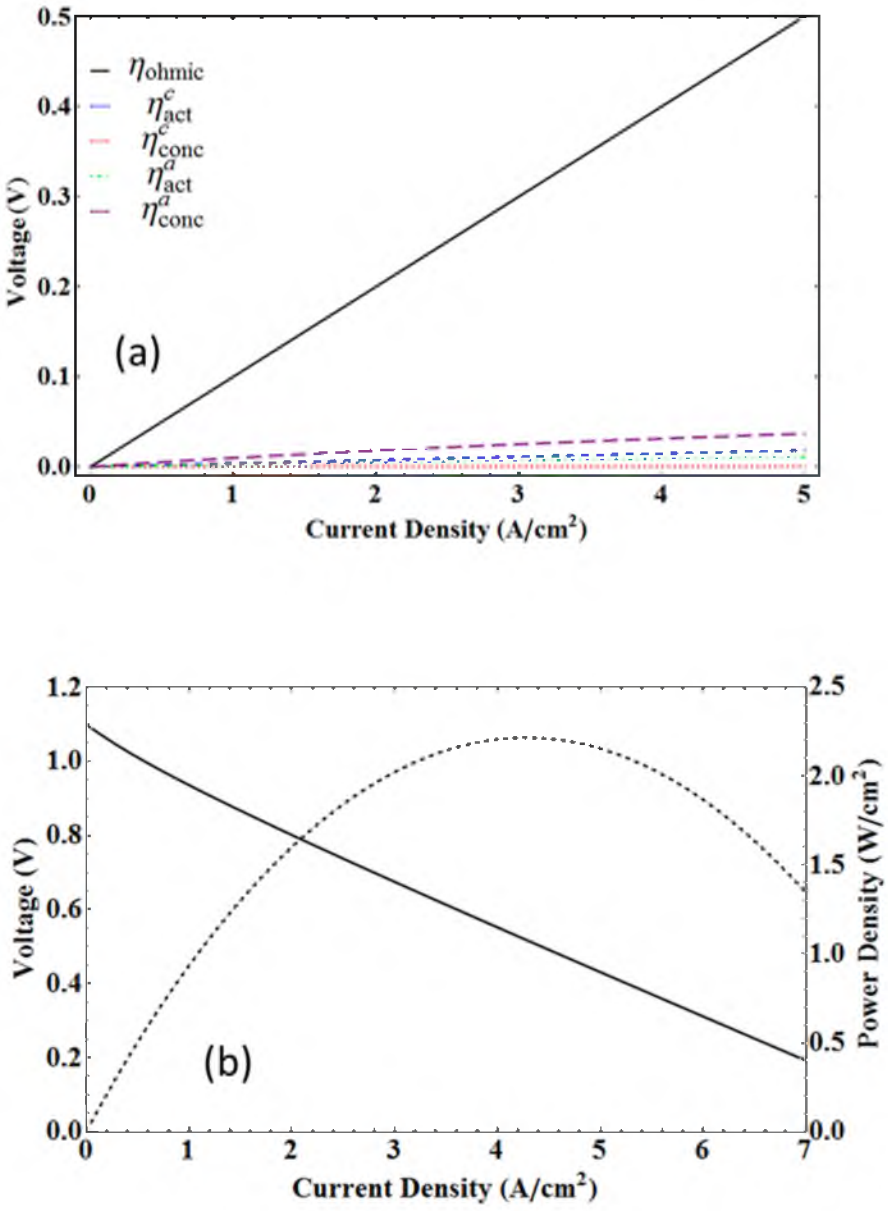

Figure 2-9: V-I curve. (a) Calculated polarizations at 800°C for a 5-layer cell with 8 μm thick YSZ electrolyte, anode support thickness 1 mm, cathode current collector thickness 50 μm, cathode and anode functional layer grain size of 0.02 μm and functional layer thicknesses of 15d = 0.3 μm. The ohmic resistance is 0.1 Ωcm^2. The ohmic polarization dominates over the entire current density range. (b) The corresponding voltage vs. current density and power density vs. current density plots.

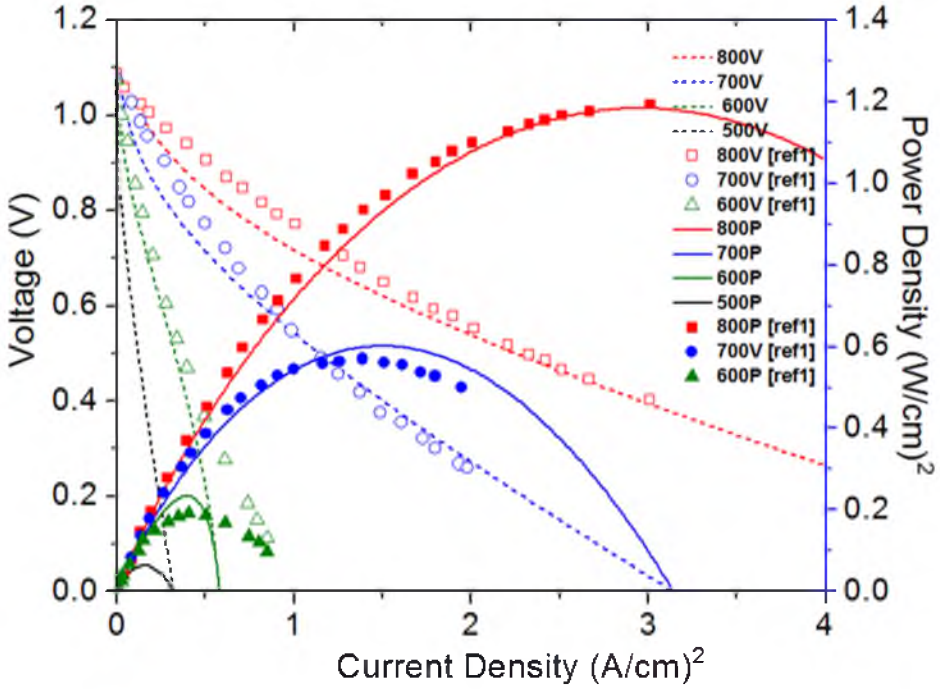

Figure 2-10: A comparison of experimental cell tests measurements from Zhao et al. [6] (symbols) with calculated performance curves using out of cell measurements and the parametric model.

design solid oxide fuel cells of given performance characteristics. The present results thus also suggest that such an approach may help develop solid oxide fuel cells exhibiting good performance characteristics at low operating temperatures. In what follows, now we examine how one might develop solid oxide fuel cells with high performance using known values of out of cell parameters and the parametric model described here.

2.3.2 Temperature Effects on Cell Performance

Figure 2-11 and Figure 2-12 show the calculated performance curves for cells with 8 μm YSZ electrolyte and electrode grain sizes of 2 μm and 0.2 μm, respectively, over a

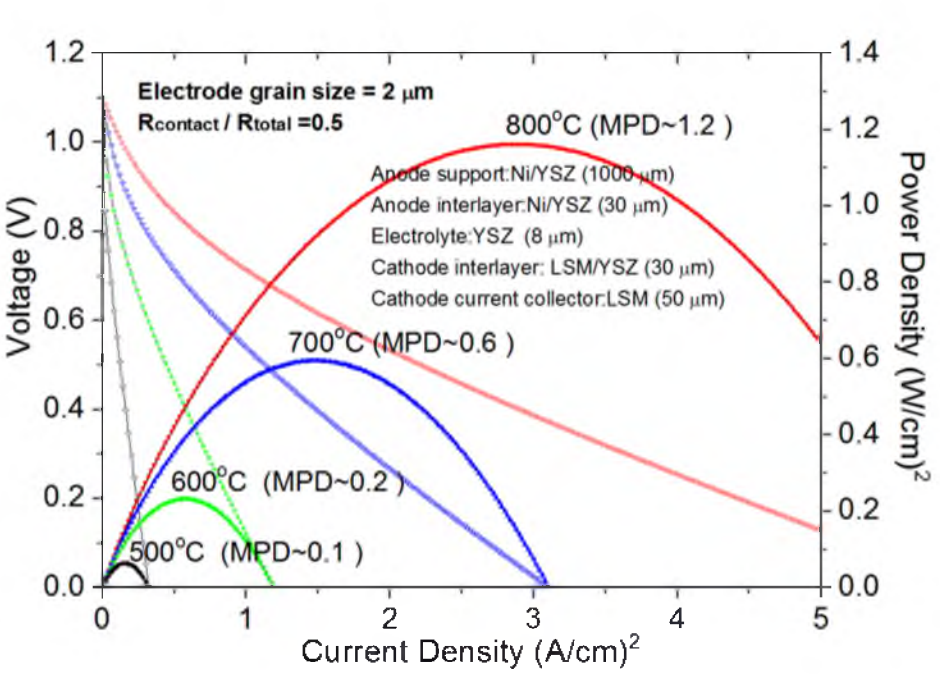

Figure 2-11: Calculated performance curves as a function of temperature for a cell with YSZ electrolyte of 8 μm in thickness and electrode grain size of 2 μm.

range of temperatures from 500°C and 800°C. The ohmic area specific resistance was calculated at each temperature using the equations given in Table 2-1. The contact resistance was assumed to be equal to the calculated ohmic area specific resistance (that is the contact resistance is 50% of the total ohmic resistance). Literature search shows that in many reported studies the ohmic contribution is much larger than can be accounted for based on individual component resistances suggesting that in many cells there is a significant contribution to the ohmic resistance from interlayer contacts. As seen from Figure 2-11 and Figure 2-12, at 800°C, the cell with 0.2 μm electrode grain size exhibits much higher performance than the cell with 2 μm electrode grain size. This is consistent with expectations since activation polarization contribution is significant in the cell with 2 μm electrode grain size. At 500°C, however, the most dominant

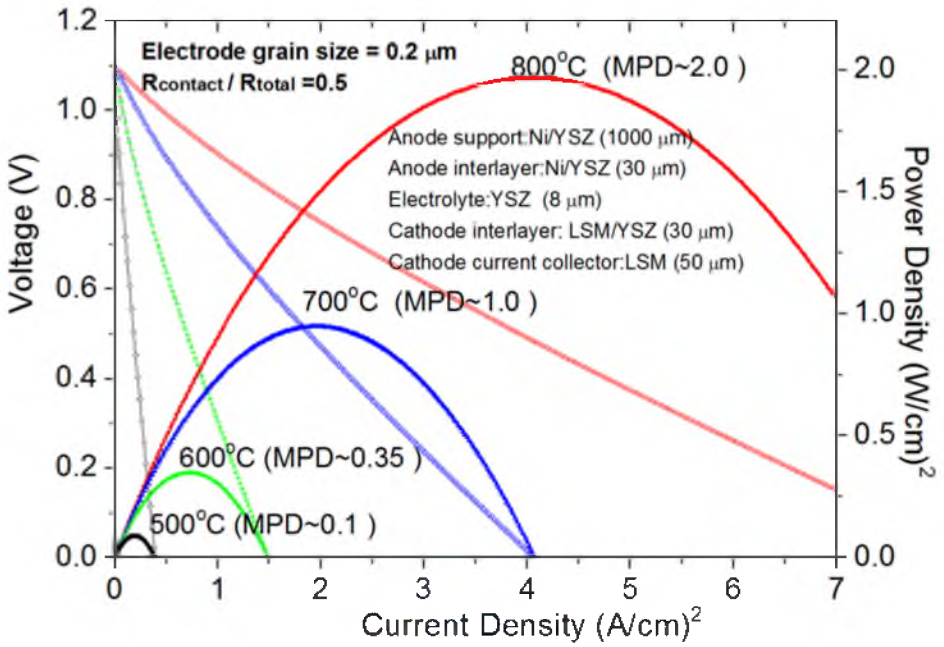

Figure 2-12: Calculated performance curves as a function of temperature for a cell with YSZ electrolyte of 8 μm in thickness and electrode grain size of 0.2 μm.

contribution is from the ohmic loss and the cell performance is not much affected by the electrode microstructure (over the range of electrode microstructures selected here for calculations). As a result more active electrodes do not lead to a proportionate increase in performance.

Figure 2-13 and Figure 2-14 are similar plots with GDC electrolyte of 8 μm thickness. The contact resistance was again assumed to be equal to the total calculated ohmic resistance of the five layers. Also, cathode and anode were, respectively, LSM + YSZ and Ni + YSZ since fundamental measurements are available only for these two sets of materials. Note that the performance is much higher with GDC electrolyte at all temperatures. Also, at 500°C the performance is higher with 0.2 μm electrode grain size compared to 2 μm electrode grain size. The ohmic contribution is much lower. As a result,

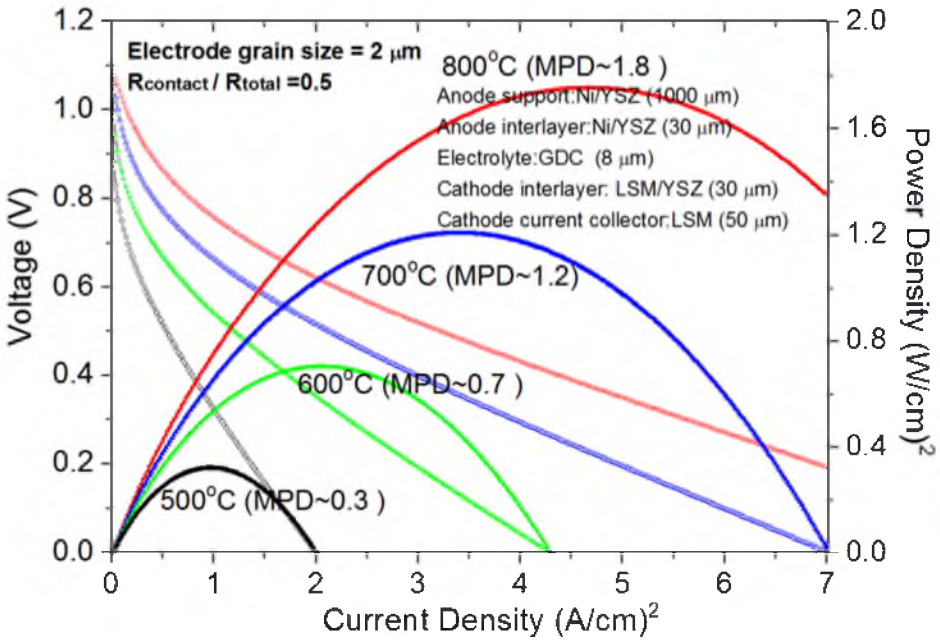

Figure 2-13: Calculated performance curves as a function of temperature for a cell with GDC electrolyte of 8 μm in thickness and electrode grain size of 2 μm.

improvement in electrode microstructure leads to an increase in performance. In these calculations it was assumed that a very thin layer exhibiting very high electronic resistance is deposited on the GDC electrolyte to block off the electronic leakage current.

The preceding shows that it should be possible to design cells exhibiting high performance at low to intermediate temperatures using fine LSM + YSZ cathode and Ni + YSZ anode of fine microstructures, and with higher ionic conductivity electrolyte materials such as GDC or LSGM. Possible reaction of these different electrolytes with the electrodes can be minimized or prevented by depositing suitable barrier layers. In order to incorporate other electrodes and use the parametric model, it would be necessary to measure charge transfer reaction kinetics using patterned electrodes. Such data are available with Pt + YSZ as the cathode [24]. Prior work has shown that Pt + YSZ is a

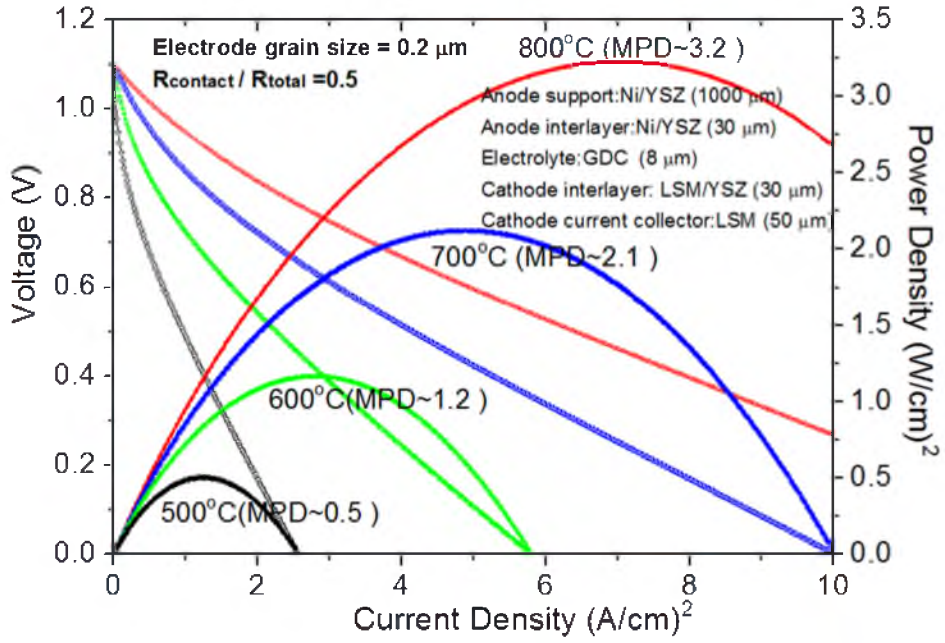

Figure 2-14: Calculated performance curves as a function of temperature for a cell with GDC electrolyte of 8 μm in thickness and electrode grain size of 0.2 μm.

more active cathode than LSM + YSZ. Thus we expect cells made with Pt + YSZ as the cathode should exhibit higher performance. Indeed, it is well known that the introduction of Pt into the cathodes by infiltration leads to higher performing cathodes and thus higher performing cells. Although Pt is an expensive catalyst, a small amount added as an infiltrant into standard cathodes such as LSM + YSZ may be cost effective at least in some applications.

2.4 Summary

A parametric model for anode-supported solid oxide fuel cells (SOFC) is presented to describe various polarizations, cell voltage and power density as function of current density. All polarizations or voltage losses are calculated based entirely on out of cell

measurements. This included the measurement of effective gas phase diffusivities through anode and cathode, charge transfer resistivities for oxygen reduction reaction at the cathode and hydrogen oxidation reaction at the anode using patterned electrodes and the out of cell measurements of electrical resistivities of cathode, anode and the electrolyte. Thus, what is presented here is not a model to fit experimental cell test data, but rather to generate performance curves based on out of cell materials property measurements, microstructural measurements, gas phase transport properties measurements and fundamental measurements on cathode and anode electrocatalysis. The calculated performance curves are in good agreement with a number of reported cell test data. Since the model is based entirely on parameters measured in out of cell tests, comparison of the model with actual cell test data provides an independent validation of the model. Also, the model thus provides guidelines for the design of high performance cells by judiciously selecting materials and microstructures for the various cell components.

One of the most important conclusions is that if sufficiently fine electrode microstructures can be achieved (electrode grain size of ~0.5 μm or smaller) with traditional electrodes (Ni + YSZ for the anode, LSM + YSZ for the cathode), even in thin YSZ electrolyte (~8 μm) anode-supported cells at 800°C, substantial voltage loss is associated with the ohmic contribution and not necessarily the polarization losses at the electrodes. At lower temperatures, the effect of the ohmic contribution becomes even larger. The observation that most YSZ electrolyte based anode-supported cells at 800°C exhibit a maximum power density of ~2 Wcm^{-2} despite using a variety of cathodes is consistent with the ohmic contribution being the dominant one. In the following chapters,

efforts are spent to reduce ohmic loss. Chapter 3 introduces how space charge leads to lower conductivity at electrolyte grain boundary and how to increase grain boundary conductivity. Chapter 4 introduces how contact resistance contribute to area specific resistance, and the way to reduce contact resistance.

2.5 References

1. A. V. Virkar and Y. Jiang, *ECS Transactions*, **7**, 1057–1067 (2005)

2. S. De Souza, S. J. Visco, and L. C. De Jonghe, *J. Electrochem. Soc.*, **144**, L35-L37 (1997)

3. J. W. Kim, A. V. Virkar, K.-Z. Fung, K. Mehta, and S. C. Singhal, *J. Electrochem. Soc.*, **146**, 69–78 (1999)

4. A. Virkar, M. C. Williams, and S. Singhal, *ECS Transactions*, **5**, 401–421 (2007)

5. R. Snieder and J. Trampert, *Int. Cent. Mech. Sci.*, **398**, 119–190 (1999)

6. F. Zhao and A. Virkar, *J. Power Sources*, **141**, 79–95 (2005)

7. M. Chen, Y.-L. Liu, A. Hagen, P. V. Hendriksen, and F. W. Poulsen, *Fuel Cells*, **9**, 833–840 (2009)

8. J. A. Labrincha, J. R. Frade, and F. M. B. Marques, *J. Mater. Sci.*, **28**, 3809–3815 (1993)

9. U. Anselmi-Tamburini, *Solid State Ionics*, **110**, 35–43 (1998)

10. M. Marinšek, S. Pejovnik, and J. Maček, *J. Eur. Ceram. Soc.*, **27**, 959–964 (2007)

11. J. R. Ferguson, J. M. Fiard, and R. Herbin, *J. Power Sources*, **58**, 109–122 (1996)

12. N. F. Bessette, W. J. Wepfer, and J. Winnick, *J. Electrochem. Soc.*, **142**, 3792–3800 (1995)

13. S. De Souza, S. J. Visco, and L. C. De Jonghe, *Proc. 2nd European Solid Oxide Fuel Cell Forum*, 677–685 (1996).

14. C. Xia, *Solid State Ionics*, **152**, 423–430 (2002)

15. T. Tsai and S. A. Barnett, *Solid State Ionics*, **98**, 191–196 (1997)

16. C.-C. T. Yang, W.-C. J. Wei, and A. Roosen, *Mater. Chem. Phys.*, **81**, 134–142 (2003)

17. T. Dey, D. Singdeo, M. Bose, R. N. Basu, and P. C. Ghosh, *J. Power Sources*, **233**, 290–298 (2013)

18. Y. Jiang and A. V. Virkar, *J. Electrochem. Soc.*, **150**, A942 (2003)

19. E. A. Mason and A. P. Malinauskas, *Gas Transport in Porous Media: The Dusty Gas Model*, Elsevier (1983)

20. F. Zhao, T. J. Armstrong, and A. V. Virkar, *J. Electrochem. Soc.*, **150**, A249 (2003)

21. W. He et al., *J. Power Sources*, **195**, 532–535 (2010)

22. E. L. Cussler, *Diffusion: Mass Transfer in Fluid Systems*, Cambridge Univ. Press (1984)

23. A. V. Virkar, *J. Power Sources*, **147**, 8–31 (2005)

24. R. Radhakrishnan, A. V. Virkar, and S. C. Singhal, *J. Electrochem. Soc.*, **152**, A927 (2005)

25. R. Radhakrishnan, A. V. Virkar, and S. C. Singhal, *J. Electrochem. Soc.*, **152**, A210 (2005)

26. C. W. Tanner, K. Z. Fung, and A. V. Virkar, *J. Electrochem. Soc.*, **144**, 21–30 (1997)

27. F. Zhao, Y. Jiang, G. Y. Lin, and A. V Virkar, *Solid Oxide Fuel Cell VII*, 501–510 (2001)

28. A. Bieberle, L. P. Meier, and L. J. Gauckler, *J. Electrochem. Soc.*, **148**, A646 (2001)

29. M. Vogler, A. Bieberle-Hütter, L. Gauckler, J. Warnatz, and W. G. Bessler, *J. Electrochem. Soc.*, **156**, B663 (2009)

CHAPTER 3

ON SPACE CHARGE AND SPATIAL DISTRIBUTION OF DEFECTS IN YTTRIA-STABILIZED ZIRCONIA

3.1 Introduction

Solid state ion conductors have been used as solid state electrolyte in many applications, like solid oxide fuel cells (SOFCs), solid state super capacitors, solid electrolyte batteries, etc. [1-3]. Compared to devices with liquid electrolyte, solid state devices have the merit of being more stable and more durable. However, their performance may be limited by their low ionic conductivity. Like in fuel cells, SOFCs made of yttria-stabilized zirconia (YSZ) are designed to work at 800°C or higher, while phosphoric acid fuel cells (PAFCs), with liquid electrolyte, can be operated at 150°C [4]. The rigid crystalline structure in solid state ion conductors prevents ions from moving easily, and therefore a significant amount of energy is wasted on mass transportation. The parametric model introduced in Chapter 2 has demonstrated that, rather than cathode polarization loss, ohmic loss is the bottleneck to further improving SOFCs performance.

Ionic resistance in SOFCs can be attributed to two processes: one is ion transporting through individual structures, like electrolyte or electrode; the other is ion transporting through interfaces between neighboring structures, which is often referred to as contact resistance. The first process is more related to materials' intrinsic properties, like ionic

resistivity. Due to their high melting point, single crystals are impractical for application, and polycrystalline ceramics are often used. Ion transporting through polycrystalline materials is more complicated provided both grain bulk and grain boundary resistivity play a role. In most cases, grain boundary turns out to have a much higher resistivity than grain bulk. Since grain bulk is always surrounded by grain boundary, ion transportation is thus hindered when polycrystalline materials are used.

The higher resistivity at grain boundary usually stems from an impurity phase or grain boundary space charge. Like in YSZ, siliceous phase at grain boundaries was found [5]. However, as the purity of ceramic powders is greatly improved nowadays, the grain boundary resistivity still remains high, which can only be explained by grain boundary space charge. The earliest space charge theories were developed more than half century ago and only simple rock-salt crystal structures were considered [6,7]. As for more complicated YSZ, although a few qualitative works exist [8,9], not much improvement on grain boundary resistivity has been achieved based on their results, due to the lack of quantitative description on defects distribution.

In the present work, we try to establish a general model that can quantitatively describe defects distribution as a function of temperature, doping concentration and crystal structure. Our model is based on the classic work by Kliewer and Koehler [7], in which defects distribution at thermal equilibrium is achieved by minimizing the Helmholtz free energy of the material. When applying our model to YSZ, three modifications are introduced: firstly, configurational entropy term is expressed specifically for fluorite structure; secondly, high doping modification is considered when defects concentration is not negligible compared to lattice site density; lastly, surface

charge constraint is applied based the experimental observation. Even as a general model, it is not designed to be applicable to any material without necessary adjustment, especially the configurational entropy term.

3.2 Theory and Simulation Details

3.2.1 Defect Concentration at Equilibrium

Pure cubic ZrO_2 has a stable fluorite structure at high temperatures. By doping with 8 mole percent of Y_2O_3, the cubic structure can be stabilized at lower temperatures. There are more defect species than in simple NaCl, contributing to total free energy of crystal containing defects. They are $V_O^{\bullet\bullet}$, $V_{Zr}^{''''}$, $Y_{Zr}^{'}$, $V_O^{\bullet\bullet}+V_{Zr}^{''''}$, $V_O^{\bullet\bullet}+Y_{Zr}^{'}$, $2V_O^{\bullet\bullet}+V_{Zr}^{''''}$ and $V_O^{\bullet\bullet}+2Y_{Zr}^{'}$.

According to Bjerrum theory of ion association, most bonded point defects are neutral pairs like $2V_O^{\bullet\bullet}+V_{Zr}^{''''}$ and $V_O^{\bullet\bullet}+2Y_{Zr}^{'}$. Therefore, $V_O^{\bullet\bullet}+V_{Zr}^{''''}$ and $V_O^{\bullet\bullet}+Y_{Zr}^{'}$ are neglected. The concentrations of $V_O^{\bullet\bullet}$, $V_{Zr}^{''''}$, $Y_{Zr}^{'}$, $2V_O^{\bullet\bullet}+V_{Zr}^{''''}$ and $V_O^{\bullet\bullet}+2Y_{Zr}^{'}$ are denoted by $n_a(x)$, $n_c(x)$, $n_{if}(x)$, $n_B(x)$ and $n_{ib}(x)$, respectively. The anion and cation site densities are denoted as N_a and N_c, respectively.

Kliewer and Koehler's model is followed in this paper, the crystal is considered to have two surfaces in x direction and to be infinite in y and z directions, so the problem is one-dimensional. The electrostatic potential $\Phi(x)$ which arises from vacancy distributions in the crystal follows Poisson's equation (3.1) with dielectric constant ε of this crystal.

$$\nabla^2\Phi(x) = d^2\Phi(x)/dx^2 = -4\pi\rho(x)/\varepsilon \qquad (3.1)$$

where $\rho(x)$ is the charge density with the following expression.

$$\rho(x) = e\{z_a n_a(x) + z_{if} n_{if}(x) + z_c n_c(x)\} \tag{3.2}$$

where z_a, z_c and z_{if} are the charge state. Electrons and holes are not considered here, because, in large band gap materials like YSZ, their concentration is very low.

The boundary conditions are

$$\Phi\big|_{x=0} = \Phi\big|_{x=2L} = 0 \tag{3.3}$$

$$d\Phi/dx\big|_{x=L} = 0 \tag{3.4}$$

The second boundary condition is based on the symmetry of the crystal model, and it is different from Lehovec's neutrality assumption [6].

Assuming the ionic crystal is in a state of thermal equilibrium, which is determined by minimization of Helmholtz free energy F of the crystal, the free energy per unit area of half of the disordered crystal is

$$F = \int_0^L dx\big[n_c(x)F_c + n_a(x)F_a + n_B(x)\{F_c + F_a - B\} + n_{ib}(x)\{F_c - B_c\} + \tfrac{1}{2}\rho(x)\Phi(x)\big] - TS_c \tag{3.5}$$

where F_c and F_a are the cation and anion vacancy formation energies, respectively. B and B_c are the binding energies associated with $2V_O^{\bullet\bullet} + V_{Zr}^{\prime\prime\prime\prime}$ and $V_O^{\bullet\bullet} + 2Y_{Zr}^{\prime}$. S_c is the

configurational entropy (Appendix 3A).

In thermal equilibrium, the variation of equation (3.5) should be zero (Appendix 3B). However, there are two additional constraints that should be considered.

The first constraint comes from the fact that the total Yttrium dopant is fixed, which is represented as follows:

$$\int_0^L dx\left(n_{if}(x)+2n_{ib}(x)\right)=N_c\overline{C}L \tag{3.6}$$

The second constraint comes from the fact that space charge is balanced by the surface charge at the interface between two neighboring grain boundaries (surface charge layer). Since the thickness of the surface charge layer is usually only one atomic layer [10], the amount of surface charge cannot exceed a certain value. In the present work, we estimate the maximum amount of surface charge, N_s, by assuming that the surface charge layer has (100) direction and a thickness of one atomic layer. If the total net charge in grain boundary space charge is negative, then the surface charge should be positive, and the maximum amount of surface charge is limited by the maximum oxygen vacancy density at the interface; if the total net charge is positive, then the surface charge should be negative, and the maximum amount of surface charge is limited by the maximum zirconium vacancy density at the interface. Unlike Y dopant, oxygen vacancy is thermally generated, and there will be more Y dopant in grain boundary leading to a negative space charge layer. Therefore, the surface charge layer should be positively charged, containing oxygen vacancies. In all calculations, surface charge layer is assumed to have (100) direction and a thickness of one atomic layer, unless otherwise specified.

The constraint is represented as follows:

$$\int_0^L dx\left(z_a n_a(x) + z_{if} n_{if}(x) + z_c n_c(x)\right) = -z_a n_s \tag{3.7}$$

Defects generation at surface charge layer is assumed to be determined only by its configurational entropy; there's no formation energy associated with this process. This assumption is reasonable, considering the surface charge layer is usually amorphous and full of point defects. Therefore, an additional configurational entropy term will be introduced to equation (3.5), which becomes

$$\begin{aligned} F = \int_0^L dx\big[&n_c(x)F_c + n_a(x)F_a + n_B(x)\{F_c + F_a - B\} + n_{ib}(x)\{F_c - B_c\} \\ &+ \tfrac{1}{2}\rho(x)\Phi(x)\big] - TS_c - TS_c^{surf} \end{aligned} \tag{3.8}$$

Using the above two constraints, setting the variation of equation (3.8) to zero gives

$$n_a = N_a \frac{B}{1 + B + \dfrac{Z_{nn} D}{(1+C)^2}} \tag{3.9}$$

$$n_c = N_c \frac{A}{1+C} \cdot \frac{(1+C)^2(1+B) - 3DZ_{nn}}{(1+C)^2(1+B) + DZ_{nn}} \tag{3.10}$$

$$n_{if} = N_c \frac{C}{1+C} \cdot \frac{(1+C)^2(1+B) - 3DZ_{nn}}{(1+C)^2(1+B) + DZ_{nn}} \tag{3.11}$$

$$n_{ib} = N_a \frac{z_{nn} D}{(1+B)(1+C)^2 + Z_{nn} D} \tag{3.12}$$

$$n_B = N_c \frac{z_n E}{(1+C)(1+B)^2} \cdot \frac{(1+C)^2(1+B) - 3DZ_{nn}}{(1+C)^2(1+B) + DZ_{nn}} \tag{3.13}$$

$$n_s = N_s \frac{M}{1+M} \tag{3.14}$$

where,

$$A \equiv \exp\left(-\frac{F_c + z_c e\Phi(x) + z_c \beta}{kT}\right) \tag{3.15}$$

$$B \equiv \exp\left(-\frac{F_a + z_a e\Phi(x) + z_a \beta}{kT}\right) \tag{3.16}$$

$$C \equiv \exp\left(-\frac{\alpha + z_{if} e\Phi(x) + z_{if} \beta}{kT}\right) \tag{3.17}$$

$$D \equiv \exp\left(-\frac{F_a - B_c + 2\alpha}{kT}\right) \tag{3.18}$$

$$E \equiv \exp\left(-\frac{F_c + F_a - B}{kT}\right) \tag{3.19}$$

$$M \equiv \exp\left(-\frac{z_a \beta}{kT}\right) \tag{3.20}$$

The combination of equation (3.1), (3.2), (3.3), (3.4) and (3.9) to (3.14) gives a one-dimensional boundary value problem (BVP), by solving which, the electrostatic potential and concentration of all defect species can be obtained.

3.2.2 Defects Distribution at Nonequilibrium

The above discussion assumes thermal equilibrium for both cation defects and anion vacancies. However, it is known that O^{2-} ion is the only mobile species in YSZ at temperatures lower than the sintering temperature, which is usually 1400°C. Therefore, the sluggish cations, like Zr^{4+} and Y^{3+} can hardly reach their equilibrium positions at low temperatures, but have to maintain their initial distribution at higher temperatures.

Kilo has measured diffusion coefficient of zirconium ion in YSZ using Zr^{96} tracer [11], which is summarized in Table 3-1. By assuming the thickness of space charge layer to be 0.1 micron and using equation (3.21), the time needed for cation to reach new equilibrium at different temperature are calculated and summarized in Table 3-1.

$$L_{gb} = 2\sqrt{Dt} \tag{3.21}$$

Table 3-1: Time needed for the slowest ion to diffuse through grain boundary.

T(°C)	T(K)	D(cm^2s^{-1})	t(s)	t(h)	t(day)
1600	1873	4.0E-14	6.25E2	0.17	0.01
1500	1773	8.0E-15	3.13E3	0.87	0.04
1400	1673	1.3E-15	1.92E4	5.34	0.22
1300	1573	1.9E-16	1.32E5	36.55	1.52
1200	1473	1.9E-17	1.32E6	365.5	15.23
1100	1373	2.0E-18	1.25E7	3472.22	144.68
1000	1273	1.0E-19	2.50E8	69444.44	2893.52

Thus, at temperatures lower than 1200°C, we can assume that cations and cation defects are frozen. This implies that the ceramic electrolytes used in SOFCs are almost always in their nonequilibrium states. Therefore, to give a quantitative explanation of grain boundary resistance, the nonequilibrium factor should always be considered.

Instead of one, two temperatures will be needed to describe nonequilibrium, T_q, which is quenching temperature, and T_a, which is annealing temperature. We assume ceramic materials are sintered or postannealed at T_a, and then quenched to T_q. Therefore, cations will be frozen at their equilibrium distribution at T_a, and anion will reach its new equilibrium distribution at T_q.

Defects distribution at T_a can be calculated using the model described in the previous section, and the results are noted as $n_a^a(x)$, $n_c^a(x)$, $n_{if}^a(x)$, $n_{ib}^a(x)$, $n_B^a(x)$. At T_q, cations distribution remain the same, which gives

$$n_c^q = n_c^a \tag{3.22}$$

$$n_{if}^q = n_{if}^a \tag{3.23}$$

$$n_{ib}^q = n_{ib}^a \tag{3.24}$$

$$n_B^q = n_B^a \tag{3.25}$$

Therefore, only anion defect distribution is unknown, and it is determined by the electrostatic potential $\Phi^q(x)$ at T_q.

$$\nabla^2\Phi^q(x) = d^2\Phi^q(x)/dx^2 = -4\pi\rho^q(x)/\varepsilon \tag{3.26}$$

where $\rho(x)$ is the charge density with the following expression.

$$\rho^q(x) = e\left\{z_a n_a^q(x) + z_{if} n_{if}^a(x) + z_c n_c^a(x)\right\} \tag{3.27}$$

By minimizing F with only mobile species, anion defect distribution is obtained

$$n_a^q = N_a \frac{B^q}{1 + B^q + \dfrac{Z_{nn} D^a}{\left(1 + C^a\right)^2}} \tag{3.28}$$

where

$$B^q \equiv \exp\left(-\frac{F_a + z_a e\Phi^q(x) + z_a\beta^q}{kT^q}\right) \tag{3.29}$$

$$C^a \equiv \exp\left(-\frac{\alpha^a + z_{if} e\Phi^a(x) + z_{if}\beta^a}{kT^a}\right) \tag{3.30}$$

$$D^a \equiv \exp\left(-\frac{F_a - B_c + 2\alpha^a}{kT^a}\right) \tag{3.31}$$

The combination of equations (3.3), (3.4) and (3.22) to (3.28) gives a similar one-dimensional BVP to that mentioned in the previous section. Solving the BVP gives the electrostatic potential and anion defect distribution.

3.2.3 Numerical Method

These BVPs cannot be solved analytically as Kliewer and Koehler did due to the fact that charge state of cation vacancy and anion vacancy are not unity as well as the inclusion of high doping modification and surface charge constraint. Here in this work, we choose to solve these BVPs numerically using Matlab.

The Matlab programs, bvp4c and bvp5c, developed by L.F. Shampine, are used[12]. The relative error tolerance is set to the default value of 10^{-3}, which is accurate enough to ensure the convergence. The Matlab code is listed in Section 3.7.

The formation energies for cation and anion vacancies are estimated using Trouton's rule, which is

$$\Delta\overline{S}_{vap} = \frac{\Delta H_{vap}}{T_{boil}} = 4.5R + R\ln T_{boil} \tag{3.32}$$

where $\Delta\overline{S}_{vap}$ is the entropy of vaporization; ΔH_{vap} is the enthalpy of vaporization; T_{boil} is the boiling temperature; and R is the gas constant.

In pure zirconia, to vaporized one mole of zirconia, eight moles of Zr-O bonds should be broken. So that the Zr-O bonding energy (E_{bond}) can be estimated as follows:

$$E_{bond} = \frac{\Delta H_{vap}}{8N_A} \tag{3.33}$$

where N_A is the Avogadro constant.

The boiling temperature of zirconia is 4573 K. Using equation (3.32) and (3.33), the Zr-O bonding energy is calculated to be 0.638 eV.

In pure cubic zirconia or YSZ, to form a zirconium vacancy, it is required to take one zirconium ion out of bulk and put it at the surface. That is to say, eight Zr-O bonds are broken in bulk, and four Zr-O bonds are formed at surface. Therefore, the formation energy of zirconium vacancy (F_c) is about four times the energy of a single Zr-O bond. To form an oxygen vacancy, it is required to take one oxygen ion out of bulk and put it at the surface. Four Zr-O bonds are broken in bulk, and two Zr-O bonds are formed at surface. Therefore, the formation energy of oxygen vacancy (F_a) is about two times the energy of a single Zr-O bond.

$$F_c = 4E_{bond} = 2.551eV \tag{3.34}$$

$$F_a = 2E_{bond} = 1.276eV \tag{3.35}$$

The binding energy within $2V_O^{\bullet\bullet} + V_{Zr}^{\prime\prime\prime\prime}$ (B) is not necessary due to fact that this defects association contributes neither to the electrostatic potential, nor to the defect concentration of interested species. Therefore, the value of B is not provided there. The binding energy within $V_O^{\bullet\bullet} + 2Y_{Zr}^{\prime}$ (B_c) has been calculated in Appendix 3C, and the value is 0.76 eV.

The maximum amount of surface charge, N_s, is determined by the crystal structure and thickness of the grain boundary surface charge layer. HRTEM observations confirm that the grain boundary surface charge layer usually has a thickness of one atomic layer [10]. The area site densities of different crystal layers are different. In this work, we simply assume that the surface charge layer has a (100) orientation. Therefore, the surface charge density can be easily calculated as $3.09*10^{15}$ C/cm^2.

3.3 Results and Discussion

3.3.1 Comparison with Other Models

Unlike NaCl, cubic ZrO_2 has a fluorite structure. The coordination number of cation is 8, and that of anion is 4. In NaCl, the coordination number for both cations and anions is 6. There are more charged species in ZrO_2, and they are not all singly charged. Therefore, the dominating point defects in ZrO_2 are much more complex than those in NaCl, as I

have discussed in section 3.2.1. As a result of these two differences, ZrO_2 has essentially different configurational entropy, the formula of which has been discussed in Appendix 3A. Since S_c determines the explicit form of defect distribution, it is important to express S_c in the correct way, even though it is very complex.

In Guo's paper, the Y dopant is assumed to be thermally generated by associating formation energy to it. By further ignoring zirconium vacancy, Guo simplified the YSZ problem to a NaCl problem, so that the solution could be easily obtained by using Kliewer and Koehler's results. However, the fact is Y dopant exists in the lattice immediately after doping, and no additional energy is required for its existence. Like in the case of $CaCl_2$ doped NaCl in Kliewer and Koehler's paper, we introduced a Lagrange condition to account for the contribution from Y doping. Also, we have considered all the dominating point defects, and therefore a comprehensive description of the YSZ crystal system is guaranteed.

3.3.2 High Doping Modification

Defect concentrations follows Boltzmann distribution (equations 3.77-3.82) at low doping concentration and at low equilibrium temperatures, where all defects densities are small compared to crystal site density. However, at high doping concentration like the case of 8YSZ, around 14.8% of cation lattice sites are occupied by Y. Therefore n_{if} or n_{ib} cannot be ignored in equations 3.71-3.76. By doping Y onto cation lattice, oxygen vacancies are generated with an amount of half of total Y dopant, and therefore na cannot be ignored in equations 3.71-3.76 either. Even at lower doping concentrations, defect concentrations may not be negligible at high equilibrate temperatures. In Kliewer and

Koehler's work, they assumed all defects concentrations were small compared to crystal lattice site density. Their assumption is reasonable, since they were studying pure and very low doped NaCl. In other works about space charge in YSZ, such low defects concentration assumption was assumed. In the present work, we find it important to introduce a so-called high doping modification (HDM) in order to have a correct quantitative description.

By keeping n_a, n_{if} and n_{ib} in equations 3.71-3.76, all defects concentrations are related with each other. The solution to equations 3.83-3.88 is shown as equations 3.89-3.94. Consider oxygen vacancy concentration for example, the Boltzmann factor now enters to a numerator, and it is modified by a denominator containing other defects' Boltzmann factors. This situation applies to all other defects.

HDM should be in consistent with low doping assumption at the extreme case where all defects concentrations are indeed small. Consider oxygen vacancy concentration for example, if the Boltzmann factors B, C and D are much smaller than unity, then 3.89-3.94 simplifies to 3.77-3.82. Similar simplification holds for all other defects.

The modification to the solution given by HDM can be explained from the difference between the black curves and green curves in Figure 3-1, Figure 3-2, Figure 3-3 and Figure 3-4, which correspond to 400°C, 800°C, 1600°C and 2600°C. The black curves plot the solutions without HDM and SC; the green curves plot the solutions with only HDM; the blue curves plot the solutions with only SC; the red curves plot solutions with both HDM and SC. To make a quantitative comparison, values of defect concentrations, charge density and electrostatic potential at both grain boundary and grain bulk are summarized in Table 3-2 and Table 3-3.

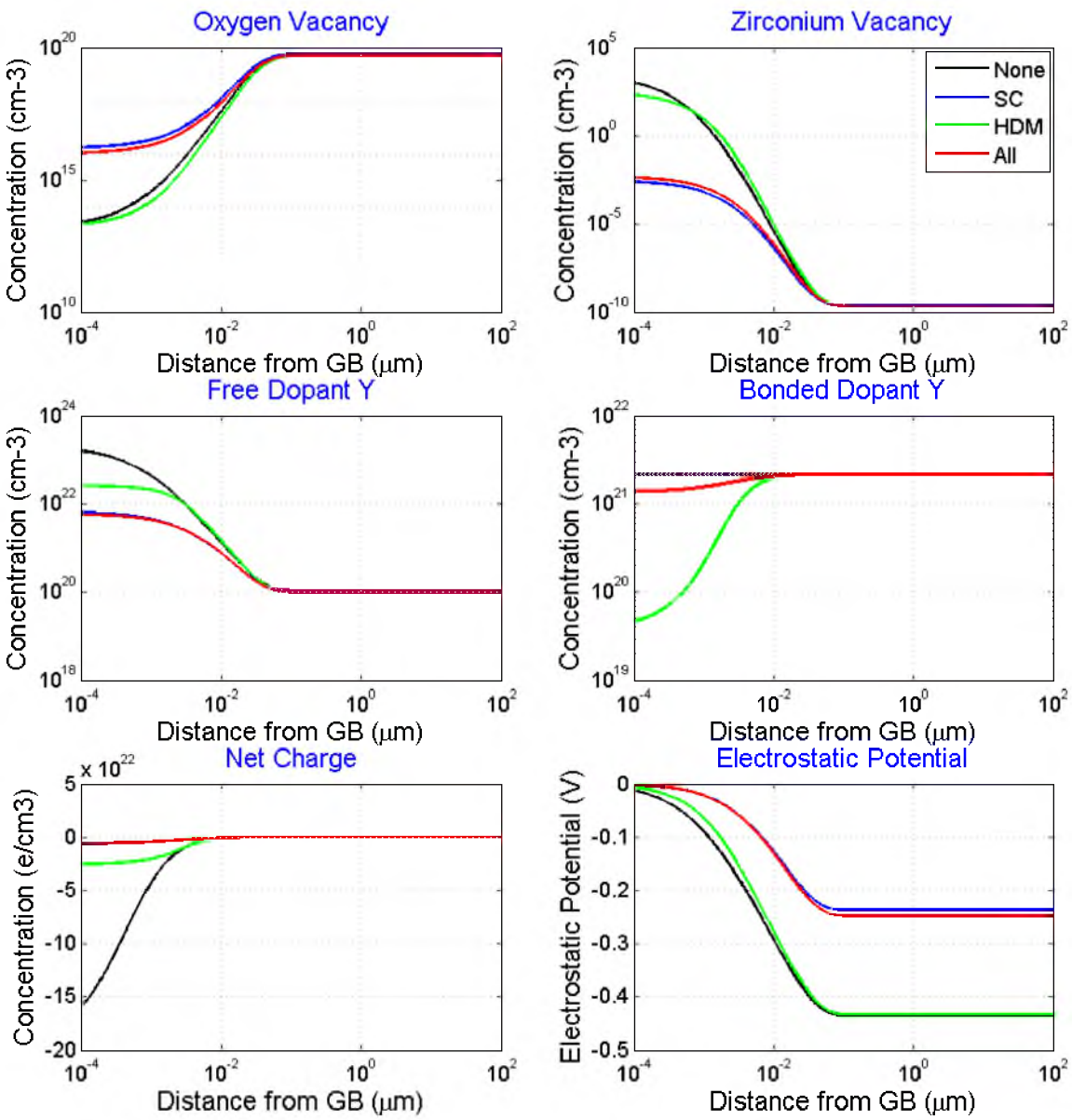

Figure 3-1: The effect of HDM and SC on solution at 400°C.

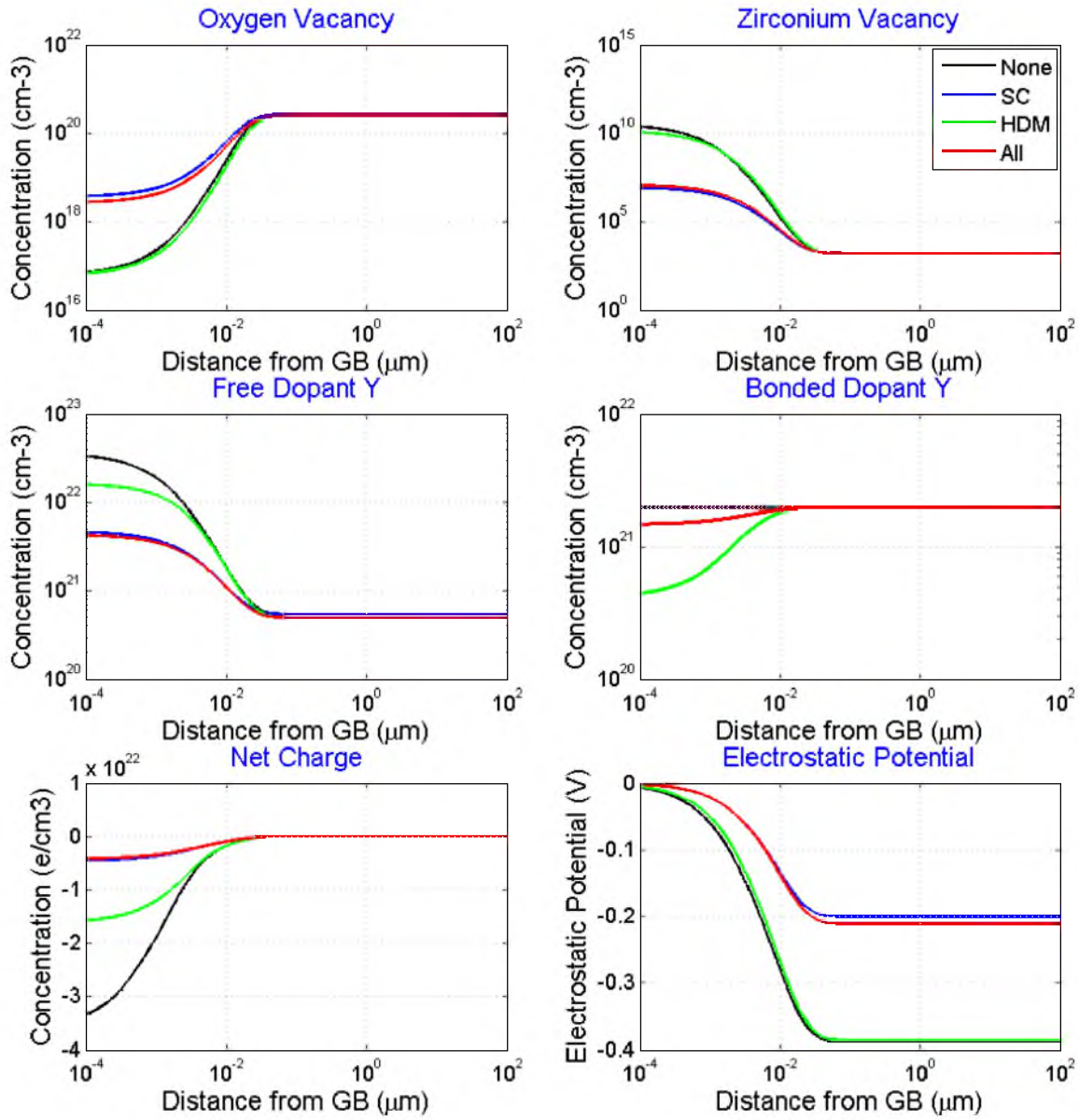

Figure 3-2: The effect of HDM and SC on solution at 800°C.

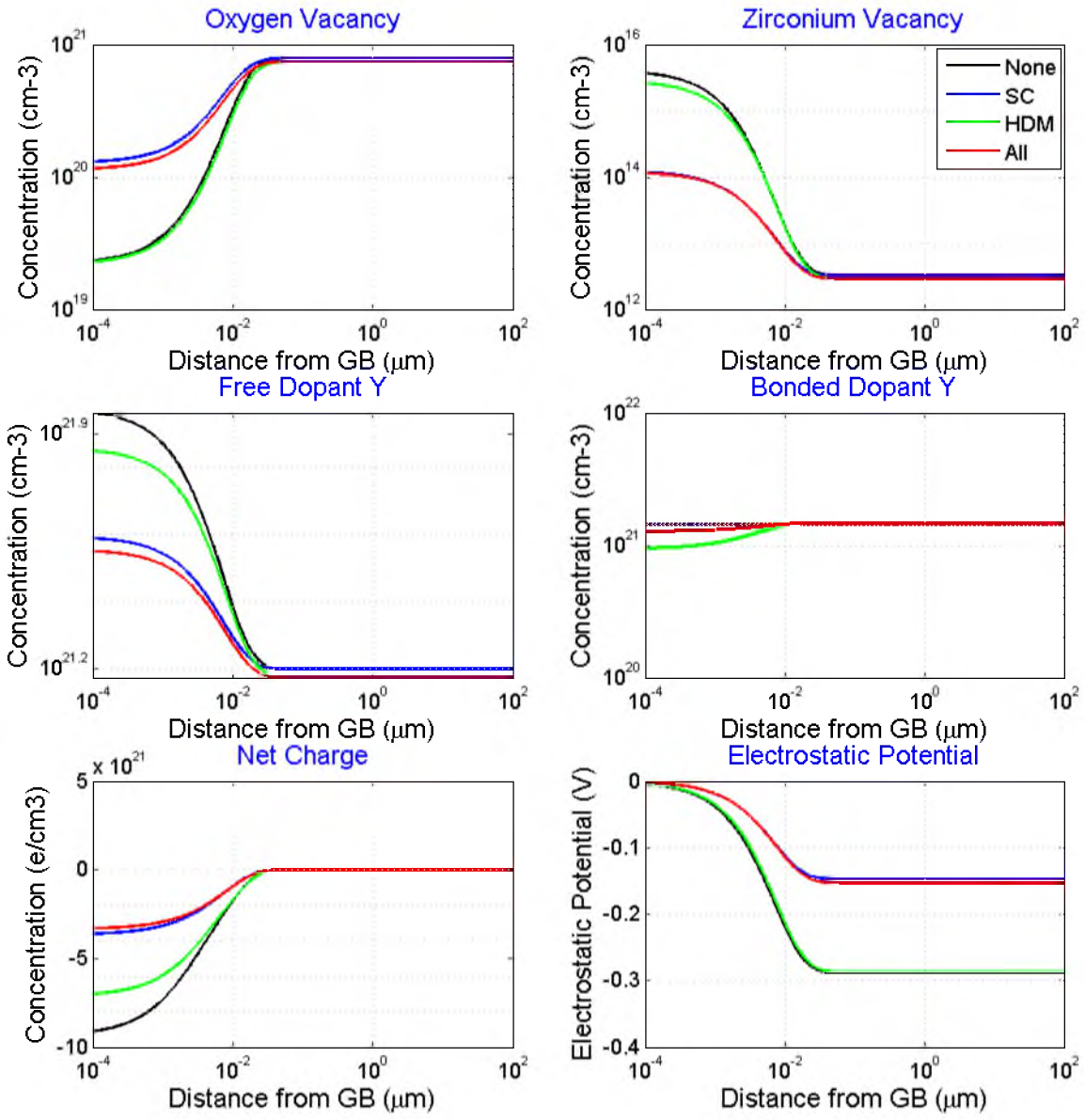

Figure 3-3: The effect of HDM and SC on solution at 1600°C.

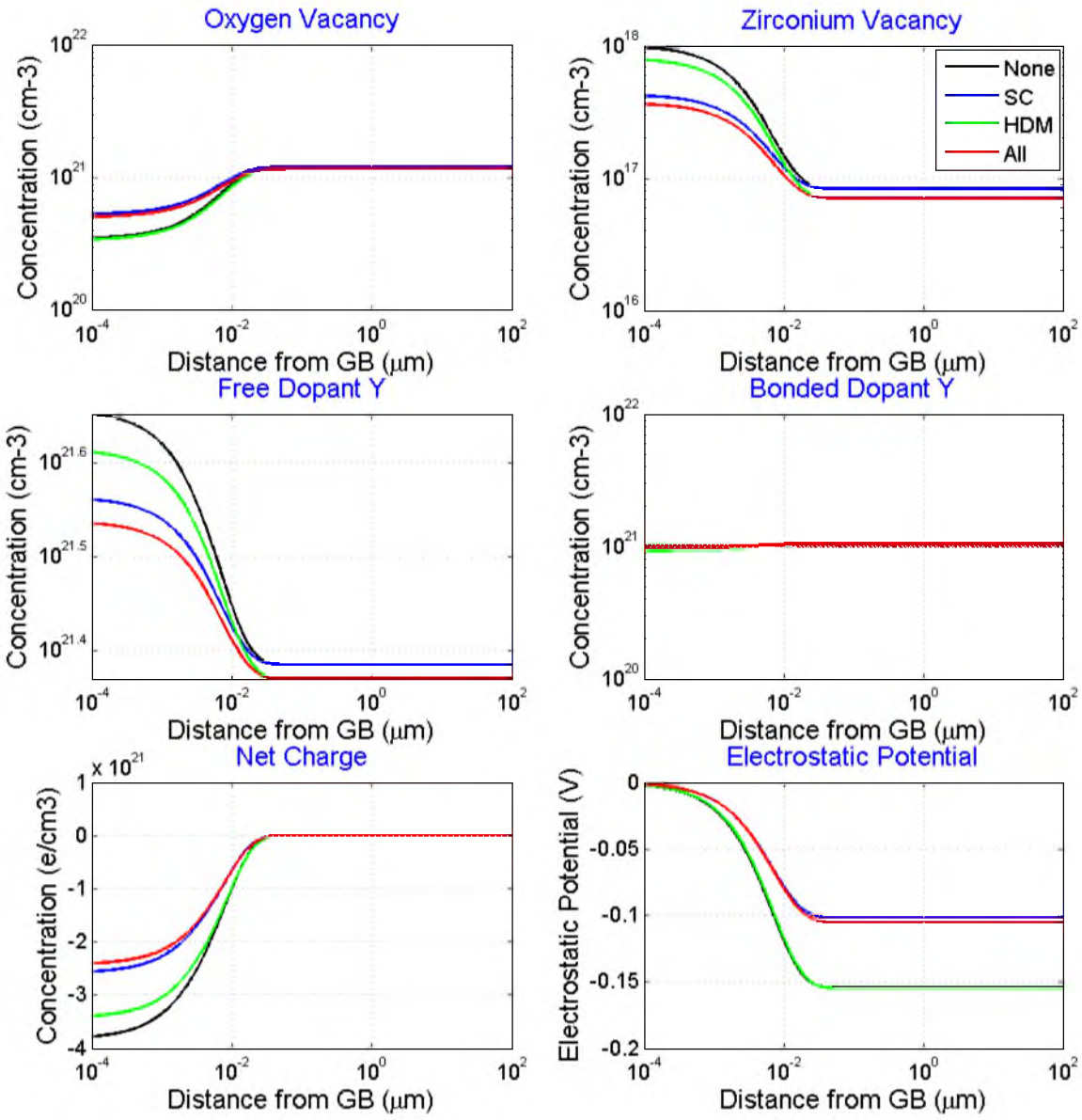

Figure 3-4: The effect of HDM and SC on solution at 2600°C.

Table 3-2: Defect concentrations and net charge density next to grain boundary core.

	T (°C)	n_a (cm^{-3})	n_c (cm^{-3})	n_{if} (cm^{-3})	n_{ib} (cm^{-3})	Charge (cm^{-3})
None	400	1.68 e13	2.37 e03	2.00 e23	2.17 e21	-2.00 e23
	800	6.11 e16	3.14 e10	3.61 e22	1.96 e21	-3.61 e22
	1600	2.22 e19	4.12 e15	9.40 e21	1.44 e21	-9.35 e21
	2600	3.48 e20	1.01 e18	4.52 e21	1.02 e21	-3.83 e21
HDM	400	1.67 e13	3.04 e02	2.62 e22	3.75 e19	-2.62 e22
	800	6.07 e16	1.35 e10	1.63 e22	4.18 e20	-1.63 e22
	1600	2.18 e19	2.88 e15	7.19 e21	9.43 e20	-7.14 e21
	2600	3.40 e20	8.08 e17	4.11 e21	9.34 e20	-3.44 e21
SC	400	1.53 e16	2.85 e-3	6.61 e21	2.17 e21	-6.61 e21
	800	3.57 e18	9.22 e06	4.72 e21	1.95 e21	-4.72 e21
	1600	1.28 e20	1.25 e14	3.92 e21	1.44 e21	-3.66 e21
	2600	5.33 e20	4.30 e17	3.66 e21	1.02 e21	-2.59 e21
All	400	9.60 e15	4.91 e-3	6.00 e21	1.36 e21	-6.00 e21
	800	2.61 e18	1.25 e07	4.32 e21	1.47 e21	-4.32 e21
	1600	1.13 e20	1.20 e14	3.58 e21	1.28 e21	-3.36 e21
	2600	5.06 e20	3.71 e17	3.45 e21	9.82 e20	-2.44 e21

Table 3-3: Defect concentrations and net charge density at grain bulk.

	T (°C)	n_a (cm^{-3})	n_c (cm^{-3})	n_{if} (cm^{-3})	n_{ib} (cm^{-3})	Potential (V)
None	400	5.51 e19	2.20 e-10	1.10 e20	2.17 e21	-0.435
	800	2.71 e20	1.60 e03	5.42 e20	1.96 e21	-0.388
	1600	7.88 e20	3.26 e12	1.58 e21	1.44 e21	-0.288
	2600	1.21 e21	8.30 e16	2.42 e21	1.02 e21	-0.155
HDM	400	4.97 e19	2.14 e-10	9.93 e19	2.18 e21	-0.433
	800	2.48 e20	1.51 e03	4.95 e20	1.98 e21	-0.386
	1600	7.43 e20	2.90 e12	1.49 e21	1.48 e21	-0.286
	2600	1.17 e21	7.04 e16	2.34 e21	1.06 e21	-0.155
SC	400	5.51 e19	2.20 e-10	1.10 e20	2.17 e21	-0.237
	800	2.71 e20	1.60 e03	5.42 e20	1.96 e21	-0.200
	1600	7.88 e20	3.26 e12	1.58 e21	1.44 e21	-0.147
	2600	1.21 e21	8.30 e16	2.42 e21	1.02 e21	-0.102
All	400	4.97 e19	2.14 e-10	9.93 e19	2.18 e21	-0.248
	800	2.48 e20	1.51 e03	4.95 e20	1.98 e21	-0.211
	1600	7.43 e20	2.90 e12	1.49 e21	1.48 e21	-0.153
	2600	1.17 e21	7.04 e16	2.34 e21	1.06 e21	-0.105

Defects concentrations are overestimated without HDM. At 800°C, oxygen vacancy concentration at grain bulk is overestimated by 9%; the integral of oxygen vacancy concentration through grain boundary without HDM is 39% higher than that with HDM. Considering equations 3.89-3.94, this can be easy understood. If one simply takes the denominator as unity, then the oxygen vacancy concentration will certainly be larger. This conclusion holds true for all other defects.

It is worth noticing that, at 400°C and 800°C, the free Y concentration next to grain boundary core is 2.0e23 cm^{-3} and 3.61e22 cm^{-3}, respectively. These two values are not reasonable, because they exceed the cation lattice site density, which is 3.01e22 cm^{-3}. By introducing HDM, free Y concentration is suppressed to a value smaller than cation site capacity.

Another significant difference is the distribution of bonded Y. From equation 3.80, it is obvious that bonded Y has a constant distribution throughout the whole grain, since its Boltzmann factor is independent of position. However, when HDM is considered, bonded Y concentration becomes position dependent. This leads to different defect reaction equilibrium constant at grain boundary than in grain bulk, which will be discussed more in section 3.3.5. Therefore, introducing HDM is not only necessary for getting more accurate solutions, but is also essential to make the model realistic.

3.3.3 Surface Charge Constraint

In Kliewer and Koehler's model, the electrostatic potential in grain bulk is not generated from the net charge in grain boundary space charge layer, but is generated from the dipole moment formed by the grain boundary space charge layer and the oppositely

charged grain boundary core. This charged grain boundary core is essential to maintain the electrical neutrality of the material. However, in Kliewer and Koehler's work, not much discussion is provided about grain boundary core, especially how charge is distributed in this layer.

In YSZ, oxygen vacancy and free Y dopant are the dominating charged species. The charge neutrality in grain bulk requires the ratio between oxygen vacancy concentration and free Y concentration to be one half. However, unlike Y dopant, oxygen vacancy is thermally generated. Therefore a negative electrostatic potential is needed in grain bulk to promote oxygen vacancy formation. In order to form such negative potential, grain boundary space charge layer should be negatively charged, while grain boundary core should be positively charged. The negatively charged grain boundary space charge layer leads to oxygen vacancy depletion and Y segregation, which is the reason why grain boundary has a low oxygen conductivity. The positively charged grain boundary core is assumed to consist of an amorphous layer which is rich in oxygen vacancy. From HRTEM measurement [10], it can be concluded that the grain boundary core has a thickness of one or two atomic layers. Further assuming the grain boundary core has a [100] direction, then the area density of oxygen atom is 1.545e15 cm^{-2}, which means the maximum amount of positive charge is 3.09e15 cm^{-2}. As a result of the limited charge capacity in grain boundary core, the net charge in grain boundary space charge layer also suffurs a limitation, which is realized by introducing SC.

Peoppel and Blakely first dicussed the surface charge constraint in NaCl [13]. Their work is also based on Kliewer and Koehler's classical model, but they have considered the limited charge capacity in grain boundary core. In their work, the surface charge

follows Boltzmann distribution, and the balance between surface charge and space charge leads to a Lagrange condition as described in section 3.2.1. They concluded that the limited surface charge capacity leads to a greatly reduced eletrostatic potential in grain bulk at elevated temperatures.

In the present work, a similar approach is used to address the effect of surface charge constraint. Comparing equations 3.77-3.82 and equations 3.100-3.104, it is interesting to notice that the Lagrange multiplier β acts like a potential energy term. Therefore the required electrostatic potential will be reduced. In Figure 3-1 through Figure 3-4, the blue curves plot the results calculated with only SC, and the difference between blue curves and black curves shows the effect of SC.

The difference is significant, and the regular pattern is that SC reduced the variation from grain bulk to grain boundary. Take 800°C for example: the electrostatic potential at grain bulk is redued from -0.388V to -0.2V. As a result, the net charge in grain boudnary space charge layer is also reduced. Since HDM is not considered in the blue curve, all defects follow exact Boltzmann distribution. The Boltzmann factors of oxygen vacancy, zirconium vacancy and free Y is position dependent, due to the fact that electrostatic potential exists in their Boltzmann factors. As electrostatic potential being reduced, oxygen vacancy depletion and zirconium vacancy and free Y segregation at grain boundary are also reduced, compared to the black curves. Regarding bonded Y, ts Boltzmann factor is position independent, and there's variation throughout the whole grain. As a result, SC doesn't change bonded Y distribution. However, when HDM is considered by comparing the green and red curves, SC again reduces the variation.

A paradox may appear that since a large electrostatic potential is need to promote

oxygen vacancy formation at grain bulk, why would the potential be reduced once SC is considered. The answer is the Lagrange multiplier β. From equations 3.100-3.104, β lowers the magnitude of electrostatic potential. At 800°C, β has a value of -0.188eV, which makes up the difference. At grain boundary, the electrostatic potential approaches zero, which is the boundary condition. A negative value of β will increase oxygen vacancy concentration, as well as decrease zirconium vacancy and free Y concentration. The change of defects concentrations at grain boundary is of the order of several magnitudes upon introducing SC. It is obvious that SC is essential to establish a correct space charge model.

3.3.4 The Consistency in the Model

In the previous two sections, the effects of HDM and SC are well discussed. By comparing the black curves with either green curves or blue curves, the calculated results consistently reflect the features in equations 3.89-3.94 and equations 3.100-3.104. As been discussed previously, a comprehensive space charge model should neither ignore HDM nor ignore SC, and the approaches described in section 3.2.1 actually meet such requirement. In Figure 3-1 through Figure 3-4, the red curves plot results when both HDM and SC are considered.

It is interesting to note that, regarding defects distribution at grain bulk, green curves and red curves eventually converge, and so do black curves and blue curves. This pattern may be more obvious in Figure 3-3 and Figure 3-4, and it can be understood by the fact that the effect of SC is to reduce the variation from grain boundary to grain bulk, while maintaining the grain bulk distribution. Another pattern is the similar change from blue to

red curves, and from black to green curves. This change is due to HDM, in which case the Boltzmann factor no longer acts solo, and the denominator lowers defects concentrations.

In the following sections, all discussions are based the results calculated with both HDM and SC.

3.3.5 Equilibrium Constant of Schottky Defects and Other Defects Association

The intrinsic defects in YSZ are the Schottky defect pairs, oxygen vacancy and zirconium vacancy. The defect reaction is as follows:

$$Null \rightarrow 2V_O^{\bullet\bullet} + V_{Zr}^{''''} \tag{3.36}$$

The formation energies of oxygen vacancy and zirconium vacancy are F_a and F_c, therefore the free energy change of the Schottky defect reaction is $2F_a + F_c = 5.104eV$. In order to verify the correctness of our model and calculation, the Schottky defects equilibrium constant is defined as follow, and, from its temperature dependence, the reaction energy is calculated.

$$K_S = \left[V_O^{\bullet\bullet}\right]^2 \cdot \left[V_{Zr}^{''''}\right] \tag{3.37}$$

The calculated oxygen vacancy and zirconium vacancy distributions at selected temperatures are plotted in Figure 3-5(a) and Figure 3-5(b). Schottky defect equilibrium

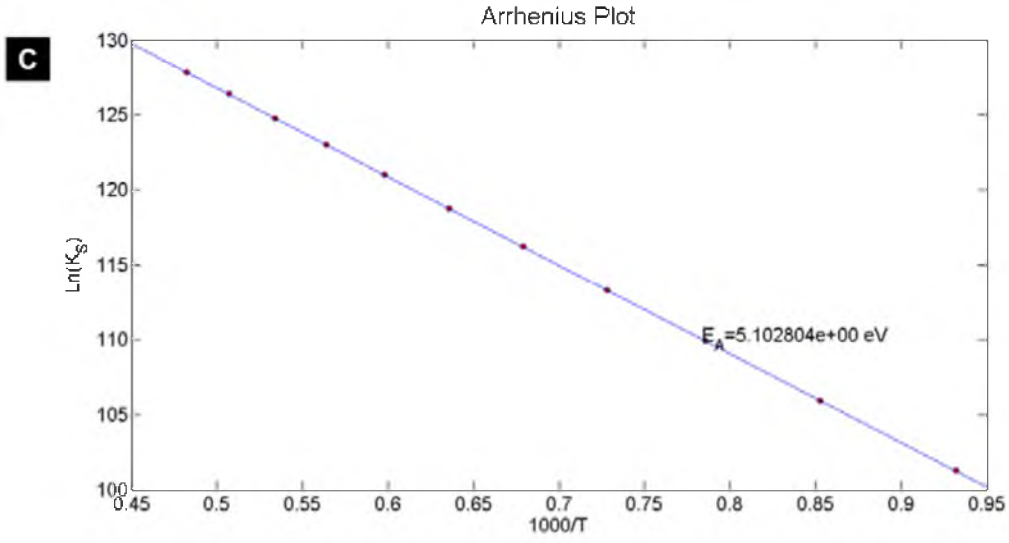

Figure 3-5: Distribution of Vo and Vzr; Arrhenius plot of Schottky defects equilibrium constant.

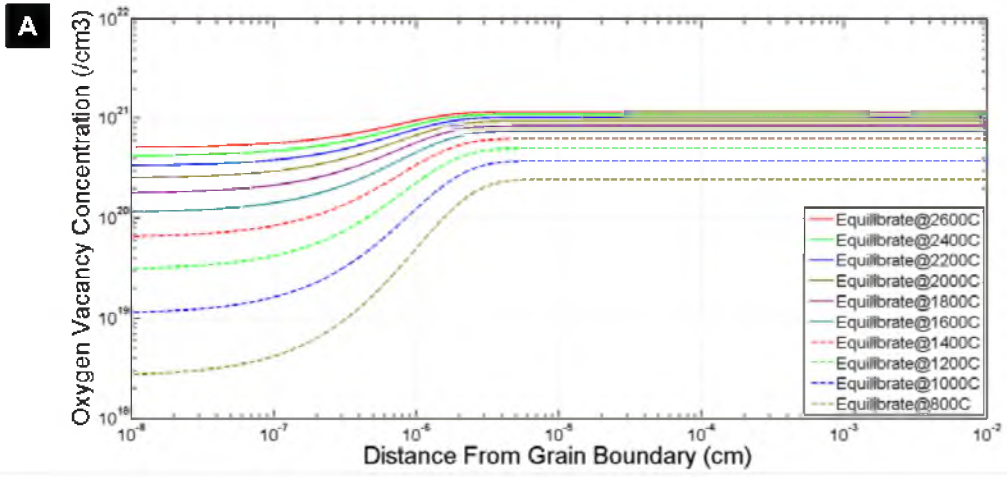
A
Oxygen Vacancy Concentration (/cm3)
Distance From Grain Boundary (cm)
Equilibrate@2600C
Equilibrate@2400C
Equilibrate@2200C
Equilibrate@2000C
Equilibrate@1800C
Equilibrate@1600C
Equilibrate@1400C
Equilibrate@1200C
Equilibrate@1000C
Equilibrate@800C

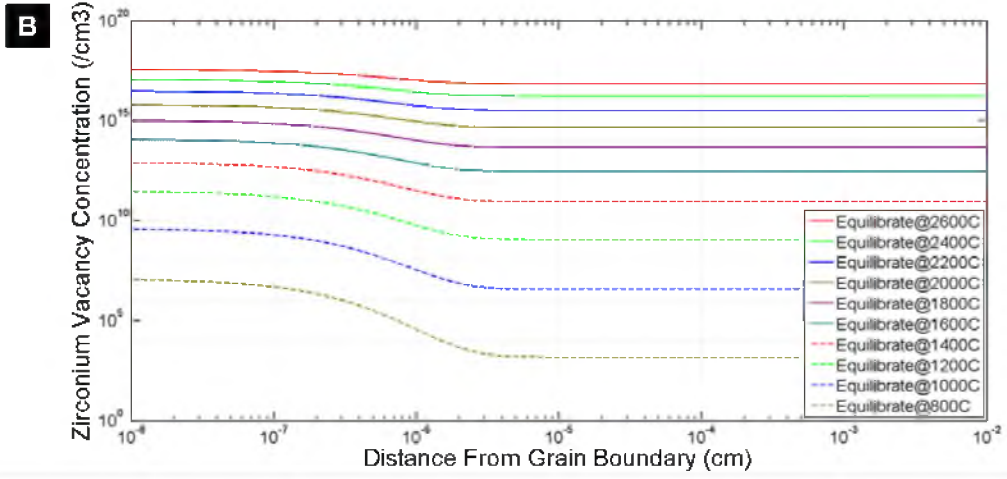
B
Zirconium Vacancy Concentration (/cm3)
Distance From Grain Boundary (cm)
Equilibrate@2600C
Equilibrate@2400C
Equilibrate@2200C
Equilibrate@2000C
Equilibrate@1800C
Equilibrate@1600C
Equilibrate@1400C
Equilibrate@1200C
Equilibrate@1000C
Equilibrate@800C

constant defined in equation (3.37) is plotted in Figure 3-5(c) in the Arrhenius fashion. K_S increases as the temperature increases, consistent with this defect reaction being endothermic. From the slope, the reaction energy is calculated to be 5.103eV, which is extremely close to $2F_a + F_c$. The tiny difference is due that with HDM oxygen vacancy and zirconium vacancy deviates from exact Boltzmann distribution.

Due to Coulomb interaction between charged defects, defect association can occur. The dominating defect complexes are $V_O^{\bullet\bullet} - V_{Zr}^{\prime\prime\prime\prime} - V_O^{\bullet\bullet}$ and $Y_{Zr}^{\prime} - V_O^{\bullet\bullet} - Y_{Zr}^{\prime}$. The first defect complex has no contribution to electrostatic potential, and its concentration is a constant throughout the whole grain. Therefore, it is not discussed here. The association reaction of $Y_{Zr}^{\prime} - V_O^{\bullet\bullet} - Y_{Zr}^{\prime}$ is as follows:

$$V_O^{\bullet\bullet} + 2Y_{Zr}^{\prime} \rightarrow Y_{Zr}^{\prime} - V_O^{\bullet\bullet} - Y_{Zr}^{\prime} \qquad (3.38)$$

The association energy is $B_c = 0.76eV$. Again, the law of mass action of this association reaction is defined in equation (3.39), and the Arrhenius plot is presented in Figure 3-6(c).

$$K_A = \frac{\left[Y_{Zr}^{\prime} - V_O^{\bullet\bullet} - Y_{Zr}^{\prime}\right]}{\left[V_O^{\bullet\bullet}\right]\left[Y_{Zr}^{\prime}\right]^2} \qquad (3.39)$$

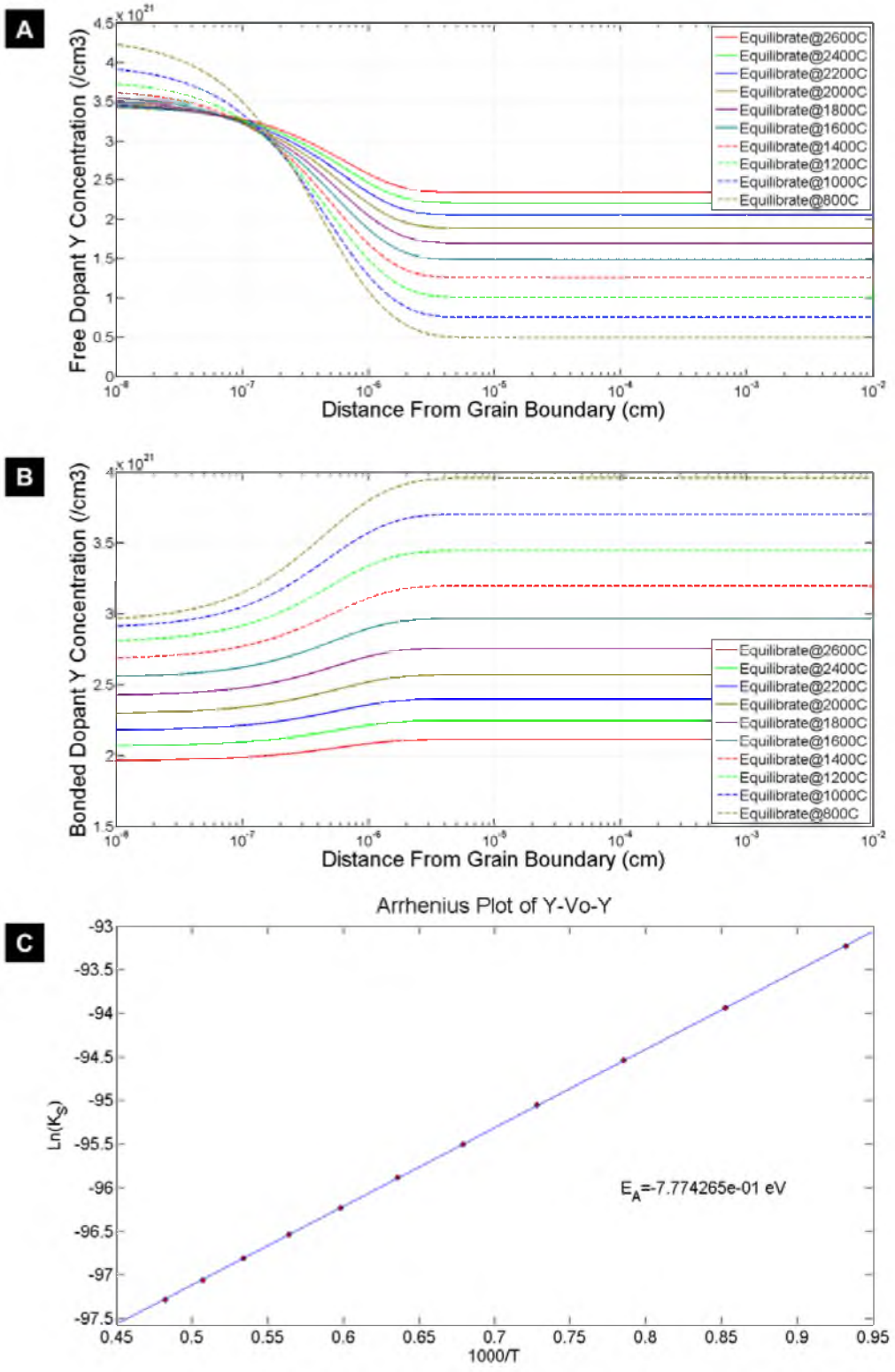

Figure 3-6: Distribution of free and bonded Y; Arrhenius plot of equilibrium constant for defects association.

The calculated free and bonded Y distributions at selected temperatures are plotted in Figure 3-6(a) and Figure 3-6(b). At low temperature (800°C), 88.88% of Y dopants are associated with oxygen vacancy; at high temperature (2600°C), the ratio drops to 47.47%. This result is consistant with the fact that the defect association reation is exothermic. The positive slope in Figure 3-6(c) also confirms the exothermic behavior. The association energy is calculated to be 0.777eV, very close to B_c. The little discrepancy is attributed to the deviation from exact Boltzmann distribution.

3.3.6 Y Segregation at Grain Boundary

Y segregation at grain boundary has been studied and reported in some literatures [14]. Theunissen and Burggraaf did a systematic AES and XPS measurements on Y segregation in YSZ. They found that, with heat treatment at 1000°C, Y segregated at grain boundary, and their results are summarized in Table 3-4 and Figure 3-7. They used a parameter called enrichment factor η, which is defined as equation (3.40), to evaluate Y segregation. They found η increased with decreasing doping concentration, and this result is consistent with our calculations. Defects distribution at different doping concentrations has been calculated and summarized in Table 3-4. In our calculations, η decreases from 3.18 at 4% doping to 1.21 at 26% doping.

$$\eta = C_{Surface} / C_{Bulk} \tag{3.40}$$

Table 3-4: Surface composition of ZrO_2-Y_2O_3 ceramics heat treated for 5 h as determined by AES (materials with compositions between 4 and 9 mol% $YO_{1.5}$ have a tetragonal structure; the others have a cubic (fluorite) structure) [14].

Bulk concentration (mol% $YO_{1.5}$)	Temperature treatment (°C)	Surface concentration (mol% $YO_{1.5}$)
4	600	5
4	1000	31
5	600	6
5	1000	30
6.1	600	6
6.1	700	14
6.1	1000	30
8.9	1000	29
13	600	11
13	700	12
13	1000	34
17	600	17
17	1000	35
17	1000	31
26.4	600	28
26.4	1000	34
32	600	33

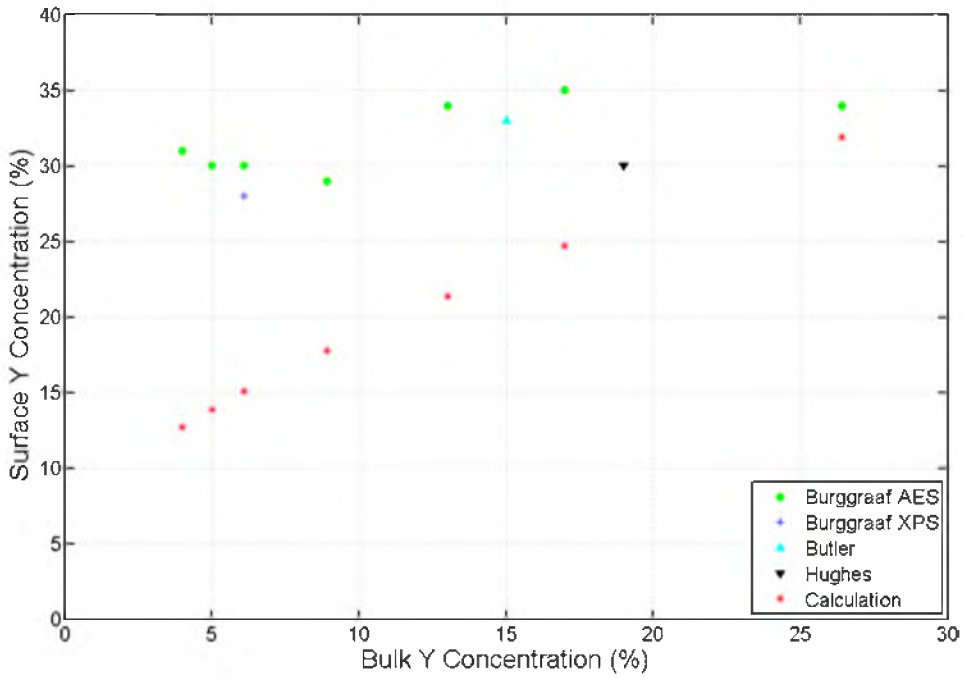

Figure 3-7: Y surface segregation.

Another conclusion in Burggraaf's work is that Y segregation shows a surface concentration in the range of 30%-34%, regardless of bulk concentration. Figure 3-7 plots their experiment results, together with our calculations. There's a discrepancy at low doping concentration. Our calculation predicts a lower Y surface concentration than that measured by Burggraaf. There are three possible reasons for this discrepancy. Firstly, their AES results did show an abrupt step change at doping concentration near 12%, which indicates, at low doping concentration, less Y segregates to grain boundary. Secondly, due to the overlapping between Y MNN peak (76eV) and Si LMM (76eV), AES measurement may overestimate Y surface concentration. In fact, their XPS results do show a lower Y surface concentration, considering Y peak and Si peak are well separated in XPS. Since no error analysis is provided in their work, it's not possible to

give a solid comparison. Thirdly, charge capacity in the surface charge layer controls defect concentration at grain boundary. We have assumed the surface charge layer to have (100) direction and a thickness of one atomic layer. However, the surface charge layer may have many different orientations and the thickness may vary between a few atomic layers. In Table 3-4 and Figure 3-7, we also present resulting calculations assuming surface charge layer has a (111) orientation. The Y surface concentration is higher compared to the case of (100) orientation.

3.3.7 The Origin of Lower Oxygen Conductivity at Grain Boundary

Oxygen vacancy depletion is widely accepted as the reason for lower oxygen conductivity at grain boundary. This is well demonstrated by equation (3.41) that conductivity is proportional to oxygen vacancy concentration. Previous space charge theory in YSZ qualitatively predicts oxygen vacancy depletion at grain boundary. In the present work, quantitative results confirm such depletion. In Figure 3-5(a), oxygen vacancy distribution throughout the whole grain is plotted. At 800°C, the concentration at grain boundary is 2.61e18 cm^{-3}, which is 100 times smaller than the concentration at grain bulk.

$$\sigma_{gb} = \left[V_O^{\bullet\bullet}\right] \times \mu_{V_O^{\bullet\bullet}} \tag{3.41}$$

Our calculations suggest another reason for lower oxygen conductivity, which is Y segregation. As is well known, 8YSZ, with a 14.8% bulk doping concentration, has the highest oxygen conductivity [15]. By further increasing Y doping, oxygen vacancy

concentration continues to increase. However oxygen conductivity decreases. This leads to the conclusion that oxygen ion mobility decreases significantly at high Y doping concentration. As has been discussed in the previous section, Y segregates to grain boundary. Figure 3-8 explicitly plots Y distribution throughout the whole grain. Even at optimized doping (14.8%), the Y concentration at grain boundary is significantly elevated. For example, at 800°C Y concentration at grain boundary reaches 24.15%. According to Wagner's work, the Y segregation greatly hinders oxygen ion migration.

3.3.8 Improving Oxygen Conductivity by Heat Treatment

The motivation of the present work is to develop a complete space charge theory which can provide quantitative understanding about the origin of grain boundary

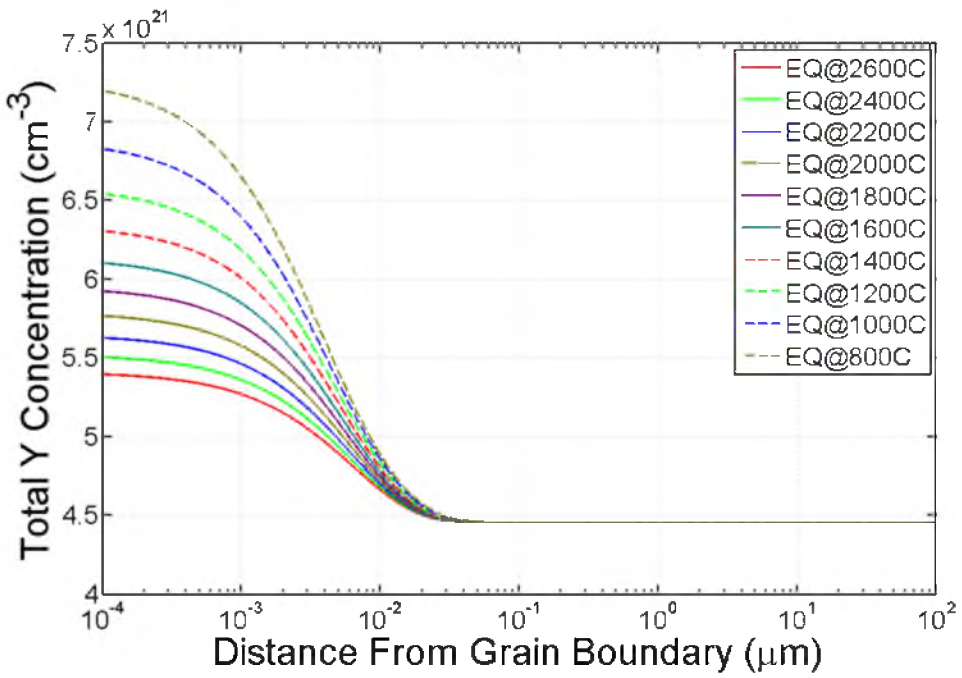

Figure 3-8: Y surface segregation.

resistance, as well as possible solutions to improve oxygen ion conduction through grain boundary layer. In the previous section, the origin of grain boundary resistance is discussed, and the conclusion suggests that increasing oxygen vacancy concentration or suppressing Y segregation will be helpful.

Manipulating doping element and doping concentration is a promising option. For example, introducing divalent cation dopant will double oxygen vacancy concentration compared to trivalent cation dopant. Also, increasing doping concentration leads to higher oxygen vacancy. However, oxygen ion mobility is another factor that needs to be optimized. Actually, a vast amount of effort has been devoted to finding the best dopant during the past several decades. In this work, we are not trying to find a better dopant than yttrium, but to provide possible ways to improve grain boundary conductivity in 8YSZ.

Thermal treat will be demonstrated as an effective method in the following discussion. Verkerk and Burggraaf found that grain boundary conductivity is strongly influenced by thermal history [16]. A YSZ sample was quenched from 1436 K to room temperature by removing it suddenly from a furnace and cooling by natural convection; another YSZ sample experienced a programmed slow cooling process [16]. They found that the grain boundary conductivity of the quenched sample was more than twice as much as that of the slow cooled sample. Little is known about this phenomenon, because this requires not only a quantitative space charge theory but also a nonequilibrium analysis.

Cations are only mobile at very high temperatures and are frozen otherwise, but oxygen ions have sufficient mobility even at low temperature (400°C). In Burggraaf's experiment, no matter at what temperature, cation defects in the quenched sample always

maintained the equilibrium distribution at 1436K due to slow kinetics; however, oxygen vacancy will reach new equilibrium distribution predicted by equation (3.27). Therefore, the duality of such nonequilibrium state is reflected in the nonequilibrium distribution of cation defects and a corresponding new equilibrium distribution of oxygen vacancy.

The way to determining defects distribution at nonequilibrium is introduced in section 3.2.2. In the nonequilibrium calculation, cation defects distribution at annealing temperature is set as known parameter, which is obtained from equilibrium calculation, and only oxygen vacancy distribution is unknown. By solving the BVP in section 3.2.2, defects distribution is obtained. Figure 3-9 plots the new equilibrium distribution of oxygen vacancy at 800°C with cation defects frozen at different annealing temperatures.

A detailed comparison between defects distribution at equilibrium and at non-

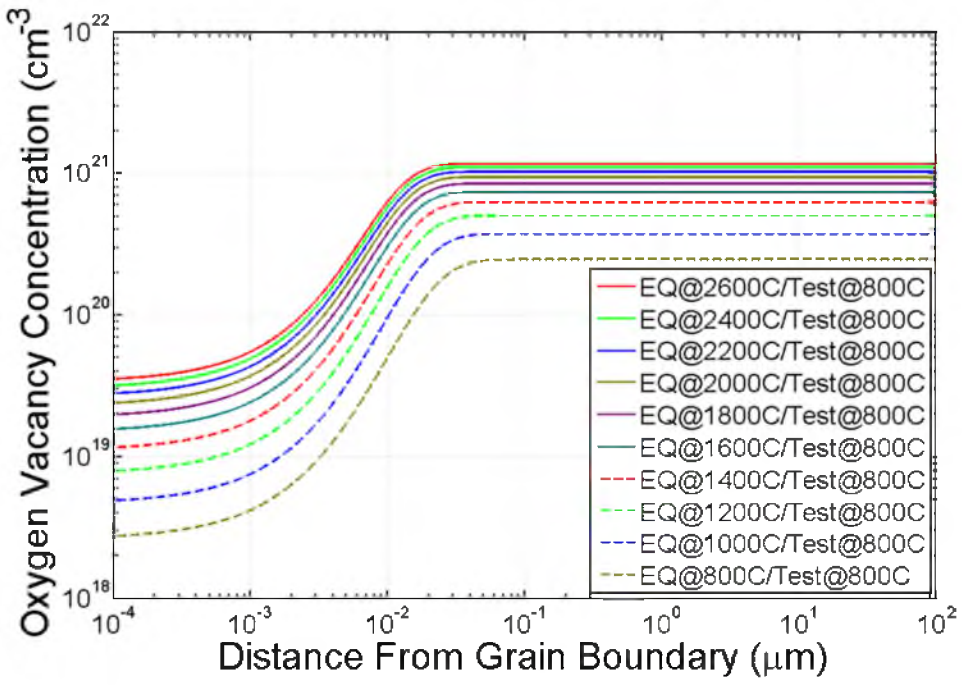

Figure 3-9: Oxygen vacancy distribution after thermal treatment.

equilibrium is summarized in Figure 3-10. The red curves correspond to a YSZ sample that is annealed at 1600°C and quenched to 800°C. The blue curves correspond to another YSZ sample that is annealed at 800°C for a long enough time, so that cation defects can reach equilibrium distribution. It turns out that the oxygen vacancy concentration at grain boundary in the first sample is almost 6 times as much as that in the second sample. This increase is significant considering that it can hardly be achieved if one tries the method of manipulating doping centration. The reason is that, in order to increase oxygen vacancy by 6 times, Y doping concentration should increase from 14.8% to 88.8%, which is unrealistic. Even if one manages to achieve this high doping, the oxygen ion conductivity may unfortunately decrease due to the lowered mobility, which is well discussed in the previous section. The advantage of thermal treatment not only lies within the increased oxygen vacancy, but more importantly the suppressed Y segregation at the mean time.

Figure 3-10 clearly shows that quenching at higher temperature leads to deceased Y concentration at grain boundary. Considering the two hypothetical samples mentioned above, Y concentration at grain boundary in the first sample is 20.38%, lower than that in the second sample (24.15%). According to Wagner's work [15], this slight difference can significantly increase oxygen ion mobility. Therefore, thermal treatment is very promising.

Aside from the qualitative comparison with Burggraaf's experiment, a quantitative comparison is currently impossible, because the temperature at which cations are frozen is unknown. Also, the dependence of measured grain boundary resistance on defect concentration is ambiguous as to which brick layer model may provide a perspective.

Thermal treatment can be easily implanted to the production of SOFCs. For anode

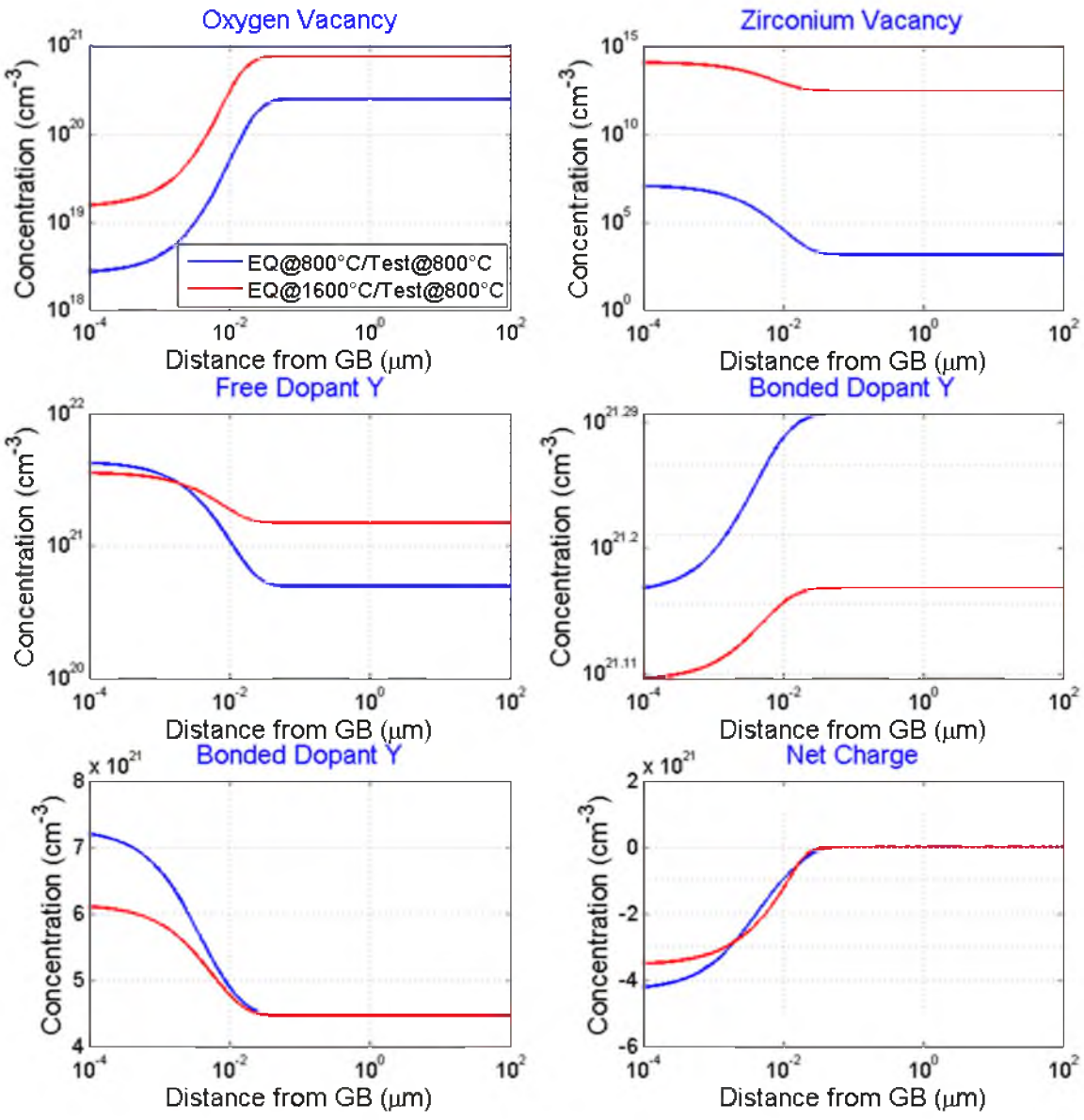

Figure 3-10: Comparison between defects distribution at equilibrium (Blue) and at nonequilibrium (Red).

supported SOFCs, since electrolyte layer is very thin, it would be possible to use laser to instantaneously heat up and quench the YSZ electrolyte. Provided the extreme high temperature laser generated, oxygen ion conductivity is expected to increase significantly. For electrolyte support SOFCs, before electrodes are applied, the thick YSZ electrolyte is suggested to anneal at the highest possible temperature and quench. A possible durability problem of thermal treatment is that, upon operating SOFCs at 1000°C or higher, cation may slowly redistribute and the improved performance may eventually vanish. Fortunately, the normal operating temperature of YSZ SOFCs is 800°C, and at this temperature it may take years or decades before significant degeneration.

3.3.9 Contribution of Free Vo and Bonded Vo on Oxygen Conduction

Oxygen ion conduction is realized by ion hopping to oxygen vacancy. Since part of oxygen vacancies are free and others are bonded to Y dopant, ion hopping to these two different vacancy sites should have a different energy barrier. A more detailed analysis on this will be pursued later.

3.4 Appendix A: Configurational Entropy of YSZ

3.4.1 Configurational Entropy of the Bulk Defects

Pure cubic ZrO_2 has a fluorite structure at high temperatures. By doping with 8 mole percent of Y_2O_3, the cubic structure can be stabilized to lower temperatures as shown in Figure 3-11. There are five predominant species which contribute to the total free energy. They are $V_O^{\bullet\bullet}$, $V_{Zr}^{''''}$, $Y_{Zr}^{'}$, $2V_O^{\bullet\bullet}+V_{Zr}^{''''}$ and $V_O^{\bullet\bullet}+2Y_{Zr}^{'}$. All other possible defects are neglected in what follows as their concentrations are expected to be much lower.

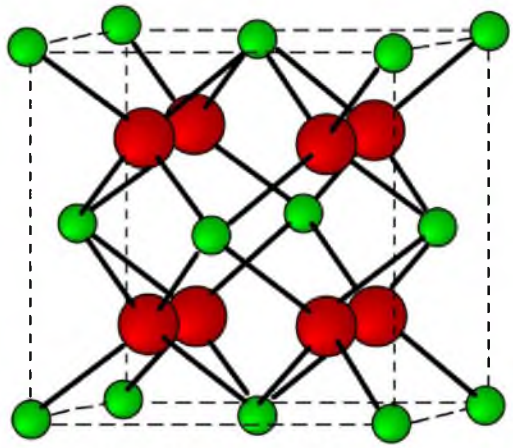

Figure 3-11: Schematics of fluorite structure. The red ball represents anion (O^{2-}), the green ball represents cation (Zr^{4+}).

In a volume V(x), which is small enough that each defect concentration is uniform but large enough that a continuum description is applicable, there are N_a anion sites per unit volume and N_c cation sites per unit volume. The local concentrations of the above defects are given respectively as $n_a(x)$, $n_c(x)$, $n_{if}(x)$, $n_B(x)$ and $n_{ib}(x)$. The configurational entropy is calculated as follows:

$$S_c(x) = k_B \ln \omega(x) \tag{3.42}$$

where

$$\omega(x) = \left\{ \binom{N_a}{n_{ib}(x)} \cdot \binom{4}{2}^{n_{ib}(x)} \right\} \cdot \left\{ \binom{N_c - 2n_{ib}(x)}{n_B(x)} \cdot \binom{8}{2}^{n_B(x)} \right\} \cdot \binom{N_c - 2n_{ib}(x) - n_B(x)}{n_{if}(x)} \cdot \binom{N_c - 2n_{ib}(x) - n_B(x) - n_{if}(x)}{n_c(x)} \cdot \binom{N_a - n_{ib}(x) - 2n_B(x)}{n_a(x)} \tag{3.43}$$

The first term, $\left\{\binom{N_a}{n_{ib}(x)}\cdot\binom{4}{2}^{n_{ib}(x)}\right\}$, calculates the number of ways to form $2Y_{Zr}^{'}+V_O^{\bullet\bullet}$. The second term, $\left\{\binom{N_c-2n_{ib}(x)}{n_B(x)}\cdot\binom{8}{2}^{n_B(x)}\right\}$, calculates the number of ways to form $2V_O^{\bullet\bullet}+V_{Zr}^{''''}$. The third term, $\binom{n_{if}(x)}{N_c-2n_{ib}(x)-n_B(x)}$, calculates the number of ways to form $Y_{Zr}^{'}$. The fourth term, $\binom{N_c-2n_{ib}(x)-n_B(x)-n_{if}(x)}{n_c(x)}$, calculates the number of ways to form $V_{Zr}^{''''}$. The last term, $\binom{N_a-n_{ib}(x)-2n_B(x)}{n_a(x)}$, calculates the number of ways to form $V_O^{\bullet\bullet}$.

Define $z_{nn}\equiv\binom{4}{2}$, which is the number of ways to form one $2Y_{Zr}^{'}+V_O^{\bullet\bullet}$, and $z_n\equiv\binom{8}{2}$, which is the number of ways to form one $2V_O^{\bullet\bullet}+V_{Zr}^{''''}$. Equation (3.43) can be expressed as

$$\omega(x)=\left(z_{nn}\right)^{n_{ib}(x)}\left(z_n\right)^{n_B(x)}\times\frac{N_a!\left(N_c-2n_{ib}(x)\right)!\left(N_a-n_{ib}(x)-2n_B(x)\right)!}{n_{ib}(x)!n_B(x)!n_{if}(x)!n_c(x)!n_a(x)!\left(N_a-n_{ib}(x)\right)!}\times\frac{1}{\left(N_c-2n_{ib}(x)-n_B(x)-n_{if}(x)-n_c(x)\right)!\left(N_a-n_{ib}(x)-2n_B(x)-n_a(x)\right)!} \tag{3.44}$$

Using Stirling's approximation, the configurational entropy can be expressed as

$$
\begin{aligned}
S_c(x)/k_B = \ln \omega(x) &= n_{ib}(x)\ln z_{nn} + n_B(x)\ln z_n \\
&+ N_a \ln N_a - N_a \\
&+ \left(N_c - 2n_{\bar{i}b}(x)\right)\ln\left(N_c - 2n_{\bar{i}b}(x)\right) - \left(N_c - 2n_{\bar{i}b}(x)\right) \\
&+ \left(N_a - n_{ib}(x) - 2n_B(x)\right)\ln\left(N_a - n_{ib}(x) - 2n_B(x)\right) - \left(N_a - n_{ib}(x) - 2n_B(x)\right) \\
&- \Big[n_{ib}(x)\ln n_{\bar{i}b}(x) - n_{ib}(x) + n_B(x)\ln n_B(x) - n_B(x) + n_{if}(x)\ln n_{if}(x) - n_{if}(x) \\
&\quad + n_c(x)\ln n_c(x) - n_c(x) + n_a(x)\ln n_a(x) - n_a(x) \\
&\quad + \left(N_a - n_{\bar{i}b}(x)\right)\ln\left(N_a - n_{\bar{i}b}(x)\right) - \left(N_a - n_{\bar{i}b}(x)\right) \\
&\quad + \left(N_c - 2n_{ib}(x) - n_B(x) - n_{if}(x) - n_c(x)\right)\ln\left(N_c - 2n_{\bar{i}b}(x) - n_B(x) - n_{if}(x) - n_c(x)\right) \\
&\quad - \left(N_c - 2n_{\bar{i}b}(x) - n_B(x) - n_{if}(x) - n_c(x)\right) \\
&\quad + \left(N_a - n_{ib}(x) - 2n_B(x) - n_a(x)\right)\ln\left(N_a - n_{\bar{i}b}(x) - 2n_B(x) - n_a(x)\right) \\
&\quad - \left(N_a - n_{\bar{i}b}(x) - 2n_B(x) - n_a(x)\right) \Big]
\end{aligned}
$$

$$
\begin{aligned}
&= n_{ib}(x)\ln z_{nn} + n_B(x)\ln z_n + N_a \ln N_a + \left(N_c - 2n_{\bar{i}b}(x)\right)\ln\left(N_c - 2n_{\bar{i}b}(x)\right) \\
&\quad + \left(N_a - n_{\bar{i}b}(x) - 2n_B(x)\right)\ln\left(N_a - n_{\bar{i}b}(x) - 2n_B(x)\right) \\
&\quad - \Big[n_{\bar{i}b}(x)\ln n_{\bar{i}b}(x) + n_B(x)\ln n_B(x) + n_{if}(x)\ln n_{if}(x) + n_c(x)\ln n_c(x) + n_a(x)\ln n_a(x) \\
&\qquad + \left(N_a - n_{ib}(x)\right)\ln\left(N_a - n_{ib}(x)\right) \\
&\qquad + \left(N_c - 2n_{ib}(x) - n_B(x) - n_{if}(x) - n_c(x)\right)\ln\left(N_c - 2n_{ib}(x) - n_B(x) - n_{if}(x) - n_c(x)\right) \\
&\qquad + \left(N_a - n_{\bar{i}b}(x) - 2n_B(x) - n_a(x)\right)\ln\left(N_a - n_{ib}(x) - 2n_B(x) - n_a(x)\right) \Big]
\end{aligned}
$$

(3.45)

Define

$$N_a^-(x) \equiv N_a - n_{ib}(x) - 2n_B(x) - n_a(x) \tag{3.46}$$

$$N_c^-(x) \equiv N_c - 2n_{ib}(x) - n_B(x) - n_{if}(x) - n_c(x) \tag{3.47}$$

The configurational entropy in the volume V can be expressed

$$
\begin{aligned}
S_c(x)/k_B = {} & n_{ib}(x)\ln z_{nn} + n_B(x)\ln z_n + N_a \ln N_a \\
& + \left(N_c - 2n_{ib}(x)\right)\ln\left(N_c - 2n_{ib}(x)\right) \\
& + \left(N_a - n_{ib}(x) - 2n_B(x)\right)\ln\left(N_a - n_{ib}(x) - 2n_B(x)\right) \\
& - \Big[n_{ib}(x)\ln n_{ib}(x) + n_B(x)\ln n_B(x) + n_{if}(x)\ln n_{if}(x) \\
& \quad + n_c(x)\ln n_c(x) + n_a(x)\ln n_a(x) \\
& \quad + \left(N_a - n_{ib}(x)\right)\ln\left(N_a - n_{ib}(x)\right) \\
& \quad + \left(N_c^-(x)\right)\ln\left(N_c^-(x)\right) + \left(N_a^-(x)\right)\ln\left(N_a^-(x)\right) \Big]
\end{aligned}
\tag{3.48}
$$

The total configurational entropy is obtained by integration

$$
S_c = \int_0^L dx S_c(x) \tag{3.49}
$$

The variation of the configurational entropy is as follows:

$$
\begin{aligned}
\delta S_c(x)/k_B = \delta \ln \omega(x) = {} & \delta n_{ib}(x)\Big[\ln z_{nn} - 2\left(\ln\left(N_c - 2n_{ib}(x)\right) + 1\right) \\
& - \left(\ln\left(N_a - n_{ib}(x) - 2n_B(x)\right) + 1\right) - \left(\ln n_{ib}(x) + 1\right) \\
& + \left(\ln\left(N_a - n_{ib}(x)\right) + 1\right) + 2\left(\ln\left(N_c^-(x)\right) + 1\right) + \left(\ln\left(N_a^-(x)\right) + 1\right) \Big] \\
& \delta n_B(x)\Big[\ln z_n - 2\left(\ln\left(N_a - n_{ib}(x) - 2n_B(x)\right) + 1\right) - \left(\ln n_B(x) + 1\right) \\
& \quad + \left(\ln\left(N_c^-(x)\right) + 1\right) + 2\left(\ln\left(N_a^-(x)\right) + 1\right) \Big] \\
& \delta n_{if}(x)\Big[-\left(\ln n_{if}(x) + 1\right) + \left(\ln\left(N_c^-(x)\right) + 1\right) \Big] \\
& \delta n_c(x)\Big[-\left(\ln n_c(x) + 1\right) + \left(\ln\left(N_c^-(x)\right) + 1\right) \Big] \\
& \delta n_a(x)\Big[-\left(\ln n_a(x) + 1\right) + \left(\ln\left(N_a^-(x)\right) + 1\right) \Big]
\end{aligned}
\tag{3.50}
$$

$$\begin{aligned}\delta(TS_c) = k_B T \int_0^L dx \Bigg\{ & \delta n_a(x)\left[\ln\left(\frac{N_a - n_{ib}(x) - 2n_B(x) - n_a(x)}{n_a(x)}\right)\right] \\ & + \delta n_c(x)\left[\ln\left(\frac{N_c - 2n_{ib}(x) - n_B(x) - n_{if}(x) - n_c(x)}{n_c(x)}\right)\right] \\ & + \delta n_{if}(x)\left[\ln\left(\frac{N_c - 2n_{ib}(x) - n_B(x) - n_{if}(x) - n_c(x)}{n_{if}(x)}\right)\right] \\ & + \delta n_B(x)\left[\ln\left(\frac{z_n\left(N_a - n_{ib}(x) - 2n_B(x) - n_a(x)\right)^2}{n_B(x)}\right.\right. \\ & \qquad \left.\left. \times \frac{\left(N_c - 2n_{ib}(x) - n_B(x) - n_{if}(x) - n_c(x)\right)}{\left(N_a - n_{ib}(x) - 2n_B(x)\right)^2}\right)\right] \\ & + \delta n_{ib}(x)\left[\ln\left(\frac{z_{nn}\left(N_a - n_{ib}(x)\right)\left(N_a - n_{ib}(x) - 2n_B(x) - n_a(x)\right)}{n_{ib}(x)\left(N_c - 2n_{ib}(x)\right)^2}\right.\right. \\ & \qquad \left.\left. \times \frac{\left(N_c - 2n_{ib}(x) - n_B(x) - n_{if}(x) - n_c(x)\right)^2}{\left(N_a - n_{ib}(x) - 2n_B(x)\right)}\right)\right] \Bigg\}, \end{aligned} \tag{3.51}$$

3.4.2 Configurational Entropy of the Surface Defects

The charge in grain boundary space charge layer is balanced by surface charge layer, which is assumed to have a limited charge capacity due to its limited thickness. It is assumed here that no energy is expended in forming surface defects. The only contribution to total free energy by surface charge is configurational entropy S_c^{surf}, defined as follows:

$$S_c^{surf} = k \ln \omega^{surf} \tag{3.52}$$

$$\omega^{surf} = \binom{N_s}{n_s} = \frac{N_s!}{n_s!(N_s - n_s)!} \tag{3.53}$$

where N_s is the number of oxygen sites per unit area on the surface, and n_s is the number of surface sites per unit area occupied by charged defects. If the charged defects are oxygen vacancies, then the maximum number of oxygen vacancies on the surface will be N_s.

$$\begin{aligned} \ln \omega^{surf} &= \ln\left(\frac{N_s!}{n_s!(N_s - n_s)!}\right) \\ &= N_s \ln N_s - N_s - \left[n_s \ln n_s - n_s + (N_s - n_s)\ln(N_s - n_s) - (N_s - n_s)\right] \\ &= N_s \ln N_s - n_s \ln n_s - (N_s - n_s)\ln(N_s - n_s) \end{aligned} \tag{3.54}$$

The variation of surface charge configurational entropy on n_s is as follows:

$$\delta\left(TS_c^{surf}\right) = k_B T \delta\left(\ln \omega^{surf}\right) = k_B T \delta n_s \ln\left(\frac{N_s - n_s}{n_s}\right) \tag{3.55}$$

3.5 Appendix B: Variation of Helmholtz Free Energy

The Helmholtz free energy of the crystal per unit area for half of the crystal can be expressed as

$$\begin{aligned} F = \int_0^L dx \big[& n_c(x)F_c + n_a(x)F_a + n_B(x)\{F_c + F_a - B\} + n_{ib}(x)\{F_c - B_c\} \\ & + \tfrac{1}{2}\rho(x)\Phi(x)\big] - TS_c - TS_c^{surf} \end{aligned} \tag{3.56}$$

In order to obtain the equilibrium state, the above free energy function should be minimized subject to some constraints that describe the overall physical process and the system. The two constraints are

$$I \equiv \int_0^L dx\left(n_{if}(x)+2n_{ib}(x)\right)=N_c\bar{C}L \tag{3.57}$$

$$I_s \equiv \int_0^L dx\left(z_a n_a(x)+z_{if}n_{if}(x)+z_c n_c(x)\right)=-z_a n_s \tag{3.58}$$

Equation (3.57) states that the total number of yttrium is fixed. Some of the yttrium dopants are free, given by $n_{if}(x)$ and the rest of them are bonded to oxygen vacancies, given by $n_{ib}(x)$. Equation (3.58) states that that there is an upper limit to the total number of charges that can reside on the surface. This upper limit is dictated by the number of atomic/ionic site densities (sites/unit area).

The variation of the Helmholtz free energy is as follows:

$$\begin{aligned}\delta F=\int_0^L dx\Big[&\delta n_c(x)F_c+\delta n_a(x)F_a+\delta n_B(x)\{F_c+F_a-B\}+\delta n_{ib}(x)\{F_c-B_c\}\\&+\tfrac{1}{2}\delta\left(\rho(x)\Phi(x)\right)\Big]-T\delta S_c-T\delta S_c^{surf}\end{aligned} \tag{3.59}$$

Following Appendix A in Kliewer and Koehler's paper, it can be shown that [7]

$$\tfrac{1}{2}\int_0^L dx\delta\left(\rho(x)\Phi(x)\right)=\int_0^L dx\Phi(x)\delta\rho(x) \tag{3.60}$$

The variation of the two configurational entropies, δS_c and δS_c^{surf}, are shown in equation (3.51) and equation (3.55).

Using the Lagrange multiplier method, a master function is defined as

$$\Im = F + \alpha\left(I - N_c\bar{C}L\right) + \tau\left(I_s + z_a n_s\right) \tag{3.61}$$

where α and τ are the undetermined Lagrange multipliers. They are to be determined by minimizing the master function, $\Im$, which also minimizes the free energy, F. The variation of equation (3.57) and (3.58) are as follows:

$$\delta I \equiv \int_0^L dx\left(\delta n_{if}(x) + 2\delta n_{ib}(x)\right) \tag{3.62}$$

$$\delta I_s \equiv \int_0^L dx\left(z_a \delta n_a(x) + z_{if}\delta n_{if}(x) + z_c \delta n_c(x)\right) \tag{3.63}$$

At equilibrium, $\delta\Im$ should be zero

$$\begin{aligned}\delta\Im = \int_0^L dx\Big[&\delta n_c(x)\left\{F_c + z_c e\Phi(x) + z_c\tau\right\} + \delta n_a(x)\left\{F_a + z_a e\Phi(x) + z_a\tau\right\} \\ &+\delta n_B(x)\left\{F_c + F_a - B\right\} + \delta n_{if}\left\{z_{if}e\Phi(x) + \alpha + z_{if}\tau\right\} \\ &+\delta n_{ib}\left\{F_c - B_c + 2\alpha\right\} + \delta n_s\left\{z_a\tau\right\}\Big] - T\delta S_c - T\delta S_c^{surf} = 0\end{aligned} \tag{3.64}$$

Since $n_a(x)$, $n_c(x)$, $n_{if}(x)$, $n_B(x)$, $n_{ib}(x)$ and n_s can be independently varied. This means $\delta n_a(x) \neq 0$, $\delta n_c(x) \neq 0$, $\delta n_{if}(x) \neq 0$, $\delta n_B(x) \neq 0$, $\delta n_{ib}(x) \neq 0$ and $\delta n_s \neq 0$.

Thus, in order to have the master function $\Im$ minimized, each of the coefficients of $\delta n_a(x)$, $\delta n_c(x)$, $\delta n_{if}(x)$, $\delta n_B(x)$, $\delta n_{ib}(x)$ and δn_s in $\delta\Im = 0$ should be zero. This leads to

$$\left[\left(F_c + z_c e\Phi(x) + z_c\tau\right) - k_B T \ln\left(\frac{N_c - 2n_{ib}(x) - n_B(x) - n_{if}(x) - n_c(x)}{n_c(x)}\right)\right] = 0 \quad (3.65)$$

$$\left[\left(F_a + z_a e\Phi(x) + z_a\tau\right) - k_B T \ln\left(\frac{N_a - n_{ib}(x) - 2n_B(x) - n_a(x)}{n_a(x)}\right)\right] = 0 \quad (3.66)$$

$$\left[\left(z_{if} e\Phi(x) + \alpha + z_{if}\tau\right) - k_B T \ln\left(\frac{N_c - 2n_{ib}(x) - n_B(x) - n_{if}(x) - n_c(x)}{n_{if}(x)}\right)\right] = 0 \quad (3.67)$$

$$\begin{aligned}&\Big[\left(F_a - B_c + 2\alpha\right)\\ &\quad -k_B T \ln\left(\frac{z_{im}\left(N_a - n_{ib}(x)\right)\left(N_a - n_{ib}(x) - 2n_B(x) - n_a(x)\right)}{\left(N_a - n_{ib}(x) - 2n_B(x)\right)}\right.\\ &\qquad \left.\times\frac{\left(N_c - 2n_{ib}(x) - n_B(x) - n_{if}(x) - n_c(x)\right)^2}{n_{ib}(x)\left(N_c - 2n_{ib}(x)\right)^2}\right)\Big] = 0\end{aligned} \quad (3.68)$$

$$\begin{aligned}&\Big[\left(F_c + F_a - B\right)\\ &\quad -k_B T \ln\left(\frac{z_n\left(N_a - n_{ib}(x) - 2n_B(x) - n_a(x)\right)^2}{\left(N_a - n_{ib}(x) - 2n_B(x)\right)^2}\right.\\ &\qquad \left.\times\frac{\left(N_c - 2n_{ib}(x) - n_B(x) - n_{if}(x) - n_c(x)\right)}{n_B(x)}\right)\Big] = 0\end{aligned} \quad (3.69)$$

$$\left[z_a \tau - k_B T \ln\left(\frac{N_s - n_s}{n_s} \right) \right] = 0 \tag{3.70}$$

Equations (3.65) to (3.70) give the equilibrium vacancy distribution as follows:

$$\frac{n_c(x)}{N_c - 2n_{ib}(x) - n_B(x) - n_{if}(x) - n_c(x)} = \exp\left(-\frac{F_c + z_c e\Phi(x) + z_c \tau}{k_B T} \right) \equiv A(x) \tag{3.71}$$

$$\frac{n_a(x)}{N_a - n_{ib}(x) - 2n_B(x) - n_a(x)} = \exp\left(-\frac{F_a + z_a e\Phi(x) + z_a \tau}{k_B T} \right) \equiv B(x) \tag{3.72}$$

$$\frac{n_{if}(x)}{N_c - 2n_{ib}(x) - n_B(x) - n_{if}(x) - n_c(x)} = \exp\left(-\frac{\alpha + z_{if} e\Phi(x) + z_{if} \tau}{k_B T} \right) \equiv C(x) \tag{3.73}$$

$$\frac{n_{ib}(x)\left(N_a - n_{ib}(x) - 2n_B(x)\right)\left(N_c - 2n_{ib}(x)\right)^2}{z_{mi}\left(N_a - n_{ib}(x)\right)\left(N_c - 2n_{ib}(x) - n_B(x) - n_{if}(x) - n_c(x)\right)^2\left(N_a - n_{ib}(x) - 2n_B(x) - n_a(x)\right)} = \exp\left(-\frac{F_a - B_c + 2\alpha}{k_B T} \right) \equiv D \tag{3.74}$$

$$\frac{n_B(x)\left(N_a - n_{ib}(x) - 2n_B(x)\right)^2}{z_n\left(N_c - 2n_{ib}(x) - n_B(x) - n_{if}(x) - n_c(x)\right)\left(N_a - n_{ib}(x) - 2n_B(x) - n_a(x)\right)^2} \tag{3.75}$$

$$= \exp\left(-\frac{F_c + F_a - B}{k_B T}\right) \equiv E$$

$$\frac{n_s}{N_s - n_s} = \exp\left(-\frac{z_a \tau}{k_B T}\right) \equiv M \tag{3.76}$$

3.5.1 The Effect of Surface Charge Confinement Only

At low yttrium doping concentration, $n_a(x)$, $n_c(x)$, $n_{if}(x)$, $n_B(x)$ and $n_{ib}(x)$ are small compared to N_a and N_c. The equilibrium concentrations then can be expressed in simplified form as

$$n_c(x) = N_c \exp\left(-\frac{F_c + z_c e\Phi(x) + z_c \tau}{k_B T}\right) \tag{3.77}$$

$$n_a(x) = N_a \exp\left(-\frac{F_a + z_a e\Phi(x) + z_a \tau}{k_B T}\right) \tag{3.78}$$

$$n_{if}(x) = N_c \exp\left(-\frac{\alpha + z_{if} e\Phi(x) + z_{if} \tau}{k_B T}\right) \tag{3.79}$$

$$n_{ib}(x) = z_{nn} N_a \exp\left(-\frac{F_a - B_c + 2\alpha}{k_B T}\right) \tag{3.80}$$

$$n_B(x) = z_n N_c \exp\left(-\frac{F_c + F_a - B}{k_B T}\right) \tag{3.81}$$

$$n_s = N_s \exp\left(-\frac{z_a \tau}{k_B T}\right) \tag{3.82}$$

3.5.2 The Effect of Both Surface Charge Confinement and High Doping Modification

At high doping, $n_a(x)$, $n_{if}(x)$ and $n_{ib}(x)$ are not negligible. In such a case, the following equations need to be used to calculate defect concentrations

$$\frac{n_c(x)}{N_c - n_{if}(x) - 2n_{ib}(x)} = \exp\left(-\frac{F_c + z_c e\Phi(x) + z_c \tau}{k_B T}\right) \equiv A(x) \tag{3.83}$$

$$\frac{n_a(x)}{N_a - n_a(x) - n_{ib}(x)} = \exp\left(-\frac{F_a + z_a e\Phi(x) + z_a \tau}{k_B T}\right) \equiv B(x) \tag{3.84}$$

$$\frac{n_{if}(x)}{N_c - n_{if}(x) - 2n_{ib}(x)} = \exp\left(-\frac{\alpha + z_{if} e\Phi(x) + z_{if} \tau}{k_B T}\right) \equiv C(x) \tag{3.85}$$

$$\frac{n_{ib}(x)\left(N_c - 2n_{ib}(x)\right)^2}{z_{nn}\left(N_c - n_{if}(x) - 2n_{ib}(x)\right)^2\left(N_a - n_a(x) - n_{ib}(x)\right)} = \exp\left(-\frac{F_a - B_c + 2\alpha}{k_B T}\right) \equiv D \quad (3.86)$$

$$\frac{n_B(x)\left(N_a - n_{ib}(x)\right)^2}{z_{nn}\left(N_c - n_{if}(x) - 2n_{ib}(x)\right)\left(N_a - n_a(x) - n_{ib}(x)\right)^2} = \exp\left(-\frac{F_c + F_a - B}{k_B T}\right) \equiv E \quad (3.87)$$

$$\frac{n_s}{N_s - n_s} = \exp\left(-\frac{z_a \tau}{k_B T}\right) \equiv M \quad (3.88)$$

By solving equations (3.83) to (3.88), $n_a(x)$, $n_c(x), n_{if}(x), n_B(x), n_{ib}(x)$ and n_s can be expressed as

$$n_a(x) = N_a \frac{B(x)}{\left(1 + B(x) + \frac{Z_{nn} D}{\left(1 + C(x)\right)^2}\right)} \quad (3.89)$$

$$n_c(x) = N_c \frac{A(x)}{\left(1 + C(x)\right)} \cdot \left(\frac{\left(1 + C(x)\right)^2\left(1 + B(x)\right) - 3DZ_{nn}}{\left(1 + C(x)\right)^2\left(1 + B(x)\right) + DZ_{nn}}\right) \quad (3.90)$$

$$n_{if}(x) = N_c \frac{C(x)}{\left(1 + C(x)\right)} \cdot \left(\frac{\left(1 + C(x)\right)^2\left(1 + B(x)\right) - 3DZ_{nn}}{\left(1 + C(x)\right)^2\left(1 + B(x)\right) + DZ_{nn}}\right) \quad (3.91)$$

$$n_{ib}(x) = N_a \frac{z_{nn} D}{\left(\left(1 + B(x)\right)\left(1 + C(x)\right)^2 + Z_{nn} D\right)} \quad (3.92)$$

$$n_B(x) = N_c \frac{z_n E}{\left(1+C(x)\right)\left(1+B(x)\right)^2} \cdot \left(\frac{\left(1+C(x)\right)^2\left(1+B(x)\right) - 3DZ_{nn}}{\left(1+C(x)\right)^2\left(1+B(x)\right) + DZ_{nn}} \right) \tag{3.93}$$

$$n_s = N_s \frac{M}{\left(1+M\right)} \tag{3.94}$$

3.5.3 The Effect of High Doping Modification Only

If surface charge layer has an infinite charge capacity, then the surface charge confinement vanishes. By ignoring the surface charge configurational entropy in equation (3.56), the variation of free energy gives

$$\left[\left(F_c + z_c e\Phi(x)\right) - k_B T \ln\left(\frac{N_c - 2n_{ib}(x) - n_B(x) - n_{if}(x) - n_c(x)}{n_c(x)} \right) \right] = 0 \tag{3.95}$$

$$\left[\left(F_a + z_a e\Phi(x)\right) - k_B T \ln\left(\frac{N_a - n_{ib}(x) - 2n_B(x) - n_a(x)}{n_a(x)} \right) \right] = 0 \tag{3.96}$$

$$\left[\left(z_{if} e\Phi(x) + \alpha\right) - k_B T \ln\left(\frac{N_c - 2n_{ib}(x) - n_B(x) - n_{if}(x) - n_c(x)}{n_{if}(x)} \right) \right] = 0 \tag{3.97}$$

$$\left[\left(F_a - B_c + 2\alpha\right) - k_B T \ln\left(\frac{z_{nn}\left(N_c - 2n_{ib}(x) - n_B(x) - n_{if}(x) - n_c(x)\right)^2}{\left(N_a - n_{ib}(x) - 2n_B(x)\right)} \times \frac{\left(N_a - n_{ib}(x)\right)\left(N_a - n_{ib}(x) - 2n_B(x) - n_a(x)\right)}{n_{ib}(x)\left(N_c - 2n_{ib}(x)\right)^2}\right)\right] = 0 \tag{3.98}$$

$$\left[\left(F_c + F_a - B\right) - k_B T \ln\left(\frac{z_n\left(N_c - 2n_{ib}(x) - n_B(x) - n_{if}(x) - n_c(x)\right)}{n_B(x)} \times \frac{\left(N_a - n_{ib}(x) - 2n_B(x) - n_a(x)\right)^2}{\left(N_a - n_{ib}(x) - 2n_B(x)\right)^2}\right)\right] = 0 \tag{3.99}$$

With low doping assumption, defect distributions are as follows:

$$n_c(x) = N_c \exp\left(-\frac{F_c + z_c e\Phi(x)}{k_B T}\right) \tag{3.100}$$

$$n_a(x) = N_a \exp\left(-\frac{F_a + z_a e\Phi(x)}{k_B T}\right) \tag{3.101}$$

$$n_{if}(x) = N_c \exp\left(-\frac{\alpha + z_{if} e\Phi(x)}{k_B T}\right) \tag{3.102}$$

$$n_{ib}(x) = n_{ib} = z_{mn} N_a \exp\left(-\frac{F_a - B_c + 2\alpha}{k_B T}\right) \tag{3.103}$$

$$n_B(x) = n_B = z_n N_c \exp\left(-\frac{F_c + F_a - B}{k_B T}\right) \tag{3.104}$$

3.6 Appendix C: Binding Energy Calculation for Defect Complex

Point defects interact with each other through Coulomb force. As we know, Coulomb force is a long range interaction, and it correlates two charged species even if they are far apart. This makes the energy calculation very complicated. Here in the present work, an assumption is made that defects only have interaction with each other when they are nearest neighbors and have no interaction otherwise. This assumption is also adopted by Kliewer and Koehler.

When two Y dopants come to the nearest neighbor sites of an oxygen vacancy, the three form a defect complex, noted as $Y'_{Zr} - V_O^{\bullet\bullet} - Y'_{Zr}$. Without losing generality, oxygen vacancy is supposed to be at $(\frac{1}{4},\frac{1}{4},\frac{1}{4})a$, and the two Y dopants are at $(0,0,0)a$ and $(\frac{1}{2},\frac{1}{2},0)a$. The binding energy is calculated considering Coulomb interaction.

$$E_{binding} = 2E_{Y-V_O} + E_{Y-Y} \tag{3.105}$$

$$E_{Y-V_O} = \frac{1}{4\pi\varepsilon_0\varepsilon_r}\frac{z_Y z_{V_O} e^2}{r_{Y-V_O}} \tag{3.106}$$

$$E_{Y-Y} = \frac{1}{4\pi\varepsilon_0\varepsilon_r}\frac{(z_Y e)^2}{r_{Y-Y}} \tag{3.107}$$

$$E_{binding} = -0.76eV \tag{3.108}$$

The binding energy for this defect complex is calculated to be -0.76eV.

3.7 Appendix D: Numerical Computation Codes

The one-dimensional BVP problem can't be solved analytically, and instead a numerical method is adopted here. The following set of codes are based the BVP solver '`bvp5c`', which was developed by Dr. L.F. Shampine [12]. Since the equilibrium (EQ) problem is quite different from the nonequilibrium (NEQ) problem, two set of codes are developed.

Firstly, the code developed to solve equilibrium problem is listed in the following. This set of codes contains: Main function; BVP solver; BVP solver repeater; Continuation – boundary extender; Calculation results interpreter; Defect distribution calculator; and Results checker.

3.7.1 EQ Main Function

```
batch = 1; %counter for rotations
kk = 1; %counter for Temperature: 1 for highest; n for lowest

T_low =  400;
T_high = 2600;
T_int = 100;
TT = T_high:-T_int:T_low;
n = (T_high-T_low)/T_int+1;

if exist('calib','var') == 1;
```

```
else
    calib = zeros(1001,2,n,10);
    calib(:,1,:,:) = 0;
    calib(:,2,:,:) = 1;
    calibnib(n,10) = 0;
    xint = [0,logspace(-8,-2,1000)];
    xint(end) = xint(end)*(1+1e-8); % This slight augment is to avoid
exceeding boundary.
end

calib_tmp = ones(1001,4);
calib_tmp(:,4) = xint;

alpha = -2;
beta = -3;

for i = 1:n;

    T = TT(i)+273

    calib_tmp(:,1) = calib(:,1,i,batch);
    calib_tmp(:,2) = calibnib(i,batch)*ones(1001,1);
    calib_tmp(:,3) = calib(:,2,i,batch);
    %The first batch first temperature needs initial guess
    %The first batch non-first temperature use former temperature as
    %initial value
    %The non-first batch use former batch as initial value.
    if batch==1 && kk == 1;
        warning('none');
        sol = yszacharge(T,alpha,beta,calib_tmp);
    elseif batch == 1 && kk ~= 1;
        warning('none');
        sol = yszacharge(T,alpha,beta,calib_tmp,sol);
    elseif batch ~= 1;
        warning('none');
        eval(sprintf('sol = cs_sol_raw_b%d_%d;',batch-1,TT(i)));
        sol = yszacharge(T,alpha,beta,calib_tmp,sol);
%        eval(sprintf('sol =
yszacharge(T,alpha,beta,calib_tmp,cs_sol_raw_b%d_%d);',batch-1,TT(i)));
    end

    %Continue calculate until converge
    while ~strcmp(lastwarn,'none')
        warning('none');
        sol = yszacharge_continue(sol,T,C,calib_tmp);
    end

    %Continuation method by extending the grain size
    for j = 1:4;
        j

        sol = yszacharge_extend(sol,L,kappa);

        warning('none');
        sol = yszacharge_continue(sol,T,C,calib_tmp);
```

```
            while ~strcmp(lastwarn,'none')
             warning('none');
             sol = yszacharge_continue(sol,T,C,calib_tmp);
        end
    end

    %wrap up the results and feeds for next calculation.

    %alpha = sol.parameters(1)*(T/(T-100))^0.5;

    %beta = sol.parameters(2)*(T/(T-100))^0.5;

    sol_int = yszacharge_intp(sol,lambda,kappa,kT,L);
    ntr = dtr(sol_int,kT,calib_tmp);
    eval(sprintf('print(gcf,''-r100'',''-
dpng'',''cs_ntr_b%d_%d'')',batch,TT(i)));
    [ntr_check,calib(:,:,i,batch+1),calibnib(i,batch+1)] =
yszacharge_check_eql(kT,ntr,sol_int);
    eval(sprintf('print(gcf,''-r100'',''-
dpng'',''cs_ntr_check_b%d_%d'')',batch,TT(i)));

    kk = kk+1;
    eval(sprintf('cs_sol_b%d_%d=sol_int;',batch,TT(i)));
    eval(sprintf('cs_sol_raw_b%d_%d=sol;',batch,TT(i)));
    eval(sprintf('cs_ntr_b%d_%d=ntr;',batch,TT(i)));
    eval(sprintf('cs_ntr_check_b%d_%d=ntr_check;',batch,TT(i)));
    close all;

end
```

3.7.2 EQ BVP Solver

```
function sol = yszacharge(T,alpha,beta,calib,sol_init)
%Surface Layer now has a constrain!!!!!

%Renormalization is used to make the BVPs less stiff.
%Lagrange condition is converted to an additional differential equation.
%High doping is considered.
%The structure of calib:
%    calib is a 1001X4 matrix
%    first column is calibration for na
%    second column is calibration for nib
%    third column is calibration for nc & nif
%    fourth column is spacing - sint

epsl = 29*8.854e-10;    %%permitivity of simulated crystal in F*cm-1
e = 1.60217657E-19;     %%electron charge in coulombs
k = 8.6173324E-5;       %%Boltzmann constant in eV*K-1

%T = 700+273;               %%Temperature in K
C = 14.8E-2;              %%doping concentration
L = 1e-6;
```

```
nnc = 3.01E22;          %%cation site density in cm-3
nna = nnc*2;            %%anion site
%nnsurf = 3.09E15;        %%# of charge at surface layer
%nsurf = nnsurf*calib(4);
nsurf = 1.545E15;        %%# of charge at surface layer
zn = 28;                %%# of nearest unlike neighbours, 6 for NaCl
znn = 6;                %%# of nearest like neighbours, 12 for NaCl

za = 2;                 %%anion vacancy charge
zc = -4;                %%cation vacancy charge
zi = -1;                %%dopant charge

Fc = 2.551;             %%Free energy change by forming cation vacancy
Fa = 1.276;             %%Free energy change by forming anion vacancy
Bc = 0.76;              %%Free energy change by forming paired dopant

kappa = (4*pi*e*nnc/(epsl*k*T))^0.5;
%lambda = (epsl*k*T*nnc/(4*pi*e))^0.5;
lambda = nnc/kappa;
kT = k*T;

%sL = 10^(ceil(log10(kappa*L)));
%solinit = bvpinit([0, logspace(-2,log10(sL),1000)],@init,[-2 -3]);

xint = [0,logspace(-8,log10(L),1000)];
sint = xint*kappa;
sL = sint(end);

switch nargin
    case 4
        solinit = bvpinit(sint,@init,[alpha beta]);
    case 5
        solinit = bvpinit(sint,@init,[alpha beta]);
        solinit.x = sint;
        solinit.y = deval(sint,sol_init);
        solinit.parameters = sol_init.parameters;
end
options = bvpset('RelTol',1e-4);

sol = bvp5c(@ode, @bc, solinit, options);

assignin('base','lambda',lambda)
assignin('base','kappa',kappa)
assignin('base','kT',kT)
assignin('base','T',T)
assignin('base','C',C)
assignin('base','L',L)

    function dy = ode(x,y,gamma)

            dy = [  y(2)
                    -(zc*exp(-Fc/kT)*exp(-zc*y(1))*exp(-
zc*gamma(2))+zi*exp(-gamma(1))*exp(-zi*y(1))*exp(-
zi*gamma(2)))/(1+exp(-gamma(1))*exp(-zi*y(1))*exp(-
zi*gamma(2)))*clb(x,3)-2*za*exp(-Fa/kT)*exp(-za*y(1))*exp(-
```

```
za*gamma(2))/(1+exp(-Fa/kT)*exp(-za*y(1))*exp(-za*gamma(2))+clb(x,1))
                    exp(-gamma(1))*exp(-zi*y(1))*exp(-
zi*gamma(2))/(1+exp(-gamma(1))*exp(-zi*y(1))*exp(-
zi*gamma(2)))*clb(x,3)+4*znn*exp(-(Fa-Bc)/kT)*exp(-
2*gamma(1))/((1+exp(-Fa/kT)*exp(-za*y(1))*exp(-za*gamma(2)))*(1+exp(-
gamma(1))*exp(-zi*y(1))*exp(-zi*gamma(2)))^2+calib(1,2))
                    (zc*exp(-Fc/kT)*exp(-zc*y(1))*exp(-
zc*gamma(2))+zi*exp(-gamma(1))*exp(-zi*y(1))*exp(-
zi*gamma(2)))/(1+exp(-gamma(1))*exp(-zi*y(1))*exp(-
zi*gamma(2)))*clb(x,3)+2*za*exp(-Fa/kT)*exp(-za*y(1))*exp(-
za*gamma(2))/(1+exp(-Fa/kT)*exp(-za*y(1))*exp(-za*gamma(2))+clb(x,1))];

    end

    function res = bc(ya,yb,gamma)
        res = [ ya(1)
                ya(3)
                ya(4)
                yb(2)
                yb(3)-C*sL
                yb(4)+za*kappa*nsurf/nnc*exp(-gamma(2)*za)/(1+exp(-
gamma(2)*za))];
    end

    function v = init(x)
        v = [   -0.1
                -0.1
                C*x
                -x*kappa*za*nsurf/(sL*nnc)];
    end

    function q = clb(s,i)
        x = s/kappa;
        q = interp1(calib(:,4),calib(:,i),x);
    end


end
```

3.7.3 EQ BVP Solver Repeater

```
function sol = yszacharge_continue(solinit,T,C,calib)
%Surface Layer now has a constrain!!!!!

%Renormalization is used to make the BVPs less stiff.
%Lagrange condition is converted to an additional differential equation.
%High doping is considered.

%The structure of calib:
%    calib is a 1001X4 matrix
%    first column is calibration for na
%    second column is calibration for nib
```

```
%    fourth column is spacing - sint

epsl = 29*8.854e-10;     %%permitivity of simulated crystal in F*cm-1
e = 1.60217657E-19;      %%electron charge in coulombs
k = 8.6173324E-5;        %%Boltzmann constant in eV*K-1

nnc = 3.01E22;           %%cation site density in cm-3
nna = nnc*2;             %%anion site
%nnsurf = 3.09E15;         %%# of charge at surface layer
%nsurf = nnsurf*calib(4);
nsurf = 1.545E15;         %%# of charge at surface layer
zn = 28;                 %%# of nearest unlike neighbours, 6 for NaCl
znn = 6;                 %%# of nearest like neighbours, 12 for NaCl

za = 2;                  %%anion vacancy charge
zc = -4;                 %%cation vacancy charge
zi = -1;                 %%dopant charge

Fc = 2.551;              %%Free energy change by forming cation vacancy
Fa = 1.276;              %%Free energy change by forming anion vacancy
Bc = 0.76;               %%Free energy change by forming paired dopant

kappa = (4*pi*e*nnc/(epsl*k*T))^0.5;
%lambda = (epsl*k*T*nnc/(4*pi*e))^0.5;
lambda = nnc/kappa;
kT = k*T;

sL = solinit.x(end);
options = bvpset('RelTol',1e-4);

sol = bvp5c(@ode, @bc, solinit, options);

    function dy = ode(x,y,gamma)

            dy = [  y(2)
                    -(zc*exp(-Fc/kT)*exp(-zc*y(1))*exp(-
zc*gamma(2))+zi*exp(-gamma(1))*exp(-zi*y(1))*exp(-
zi*gamma(2)))/(1+exp(-gamma(1))*exp(-zi*y(1))*exp(-
zi*gamma(2)))*clb(x,3)-2*za*exp(-Fa/kT)*exp(-za*y(1))*exp(-
za*gamma(2))/(1+exp(-Fa/kT)*exp(-za*y(1))*exp(-za*gamma(2))+clb(x,1))
                    exp(-gamma(1))*exp(-zi*y(1))*exp(-
zi*gamma(2))/(1+exp(-gamma(1))*exp(-zi*y(1))*exp(-
zi*gamma(2)))*clb(x,3)+4*znn*exp(-(Fa-Bc)/kT)*exp(-
2*gamma(1))/((1+exp(-Fa/kT)*exp(-za*y(1))*exp(-za*gamma(2)))*(1+exp(-
gamma(1))*exp(-zi*y(1))*exp(-zi*gamma(2)))^2+calib(1,2))
                    (zc*exp(-Fc/kT)*exp(-zc*y(1))*exp(-
zc*gamma(2))+zi*exp(-gamma(1))*exp(-zi*y(1))*exp(-
zi*gamma(2)))/(1+exp(-gamma(1))*exp(-zi*y(1))*exp(-
zi*gamma(2)))*clb(x,3)+2*za*exp(-Fa/kT)*exp(-za*y(1))*exp(-
za*gamma(2))/(1+exp(-Fa/kT)*exp(-za*y(1))*exp(-za*gamma(2))+clb(x,1))];

    end

    function res = bc(ya,yb,gamma)
        res = [ ya(1)
```

```
                ya(3)
                ya(4)
                yb(2)
                yb(3)-C*sL
                yb(4)+za*kappa*nsurf/nnc*exp(-gamma(2)*za)/(1+exp(-
gamma(2)*za))];
    end

    function q = clb(s,i)
        x = s/kappa;
        q = interp1(calib(:,4),calib(:,i),x);
    end


end
```

3.7.4 EQ Continuation – Boundary Extender

```
function sol = yszacharge_extend(sol_in,L,kappa)
%THIS FUNCTION EXTEND THE SOLUTION TO A LARGER VALUE OF L & sL

L = L*10;
sL = kappa*L;

%sol = bvpxtend(sol,sL,'constant');
sol = bvpxtend(sol_in,sL,'linear');
assignin('base','L',L)

end
```

3.7.5 EQ Calculation Results Interpreter

```
function sol_int = yszacharge_intp(sol,lambda,kappa,kT,L)

    xint = [0,logspace(-8,log10(L),1000)];
    sint = xint*kappa;
    sol_tmp = deval(sint,sol);

    sol_int = sol;
    sol_int.x = xint;
    sol_int.y = sol_tmp;
    sol_int.y(1,:) = sol_tmp(1,:)*kT;
    sol_int.y(2,:) = sol_tmp(2,:)*kT*kappa;
    sol_int.y(3,:) = sol_tmp(3,:)*lambda;
    sol_int.y(4,:) = sol_tmp(4,:)*lambda;
    sol_int.parameters = sol.parameters*kT;

end
```

3.7.6 EQ Defect Distribution Calculator

```
function ntr = dtr(sol,kT,calib)

nnc = 3.01E22;          %%cation site density in cm-3
nna = nnc*2;            %%anion site
zn = 28;                %%# of nearest unlike neighbours, 6 for NaCl
znn = 6;                %%# of nearest like neighbours, 12 for NaCl

za = 2;                 %%anion vacancy charge
zc = -4;                %%cation vacancy charge
zi = -1;                %%dopant charge

Fc = 2.551;             %%Free energy change by forming cation vacancy
Fa = 1.276;             %%Free energy change by forming anion vacancy
Bc = 0.76;               %%Free energy change by forming paired dopant

na = nna*exp(-Fa/kT)*exp(-za*sol.y(1,:)./kT)*exp(-
za*sol.parameters(2)/kT)./(1+exp(-Fa/kT)*exp(-za*sol.y(1,:)./kT)*exp(-
za*sol.parameters(2)/kT)+calib(:,1)');
nc = nnc*exp(-Fc/kT)*exp(-zc*sol.y(1,:)./kT)*exp(-
zc*sol.parameters(2)/kT)./(1+exp(-sol.parameters(1)/kT)*exp(-
zi*sol.y(1,:)./kT)*exp(-zi*sol.parameters(2)/kT)).*calib(:,3)';
nif = nnc*exp(-sol.parameters(1)/kT)*exp(-zi*sol.y(1,:)./kT)*exp(-
zi*sol.parameters(2)/kT)./(1+exp(-sol.parameters(1)/kT)*exp(-
zi*sol.y(1,:)./kT)*exp(-zi*sol.parameters(2)/kT)).*calib(:,3)';
nib = nna*znn*exp(-(Fa-Bc)/kT)*exp(-2*sol.parameters(1)/kT)./((1+exp(-
Fa/kT)*exp(-za*sol.y(1,:)./kT)*exp(-za*sol.parameters(2)/kT)).*(1+exp(-
sol.parameters(1)/kT)*exp(-zi*sol.y(1,:)./kT)*exp(-
zi*sol.parameters(2)/kT)).^2+calib(1,2));

charge = za*na+zc*nc+zi*nif;
ks_ozo = nc.*na.^2;
ks_yoy = nib./(nif.^2.*na);

ntr =
struct('xint',sol.x,'na',na,'nc',nc,'nif',nif,'nib',nib,'charge',charge
,'ks_ozo',ks_ozo,'ks_yoy',ks_yoy);

figure;
set (gcf, 'PaperPositionMode','auto')
set (gcf, 'Position',[0,0,1000,900], 'color', 'w')

subplot(4,2,1)
loglog(sol.x,na,'-r','LineWidth',2)
title('Oxygen Vacancy','Color','blue','fontsize',12)
set(gca,'fontsize',10)
xlabel('Distance from GB (cm)','fontsize',10)
ylabel('Concentration (cm-3)','fontsize',10)

subplot(4,2,2)
loglog(sol.x,nc,'-r','LineWidth',2)
title('Zirconium Vacancy','Color','blue','fontsize',12)
set(gca,'fontsize',10)
```

```
xlabel('Distance from GB (cm)','fontsize',10)
ylabel('Concentration (cm-3)','fontsize',10)

subplot(4,2,3)
loglog(sol.x,nif,'-r','LineWidth',2)
title('Free Dopant Y','Color','blue','fontsize',12)
set(gca,'fontsize',10)
xlabel('Distance from GB (cm)','fontsize',10)
ylabel('Concentration (cm-3)','fontsize',10)

subplot(4,2,4)
loglog(sol.x,nib,'-r','LineWidth',2)
title('Bonded Dopant Y','Color','blue','fontsize',12)
set(gca,'fontsize',10)
xlabel('Distance from GB (cm)','fontsize',10)
ylabel('Concentration (cm-3)','fontsize',10)

subplot(4,2,5)
semilogx(sol.x,ks_ozo,'-r','LineWidth',2)
title('Schottky Defect Equilibrium
Constant','Color','blue','fontsize',12)
set(gca,'fontsize',10)
xlabel('Distance from GB (cm)','fontsize',10)
ylabel('K_S','fontsize',10)

subplot(4,2,6)
semilogx(sol.x,ks_yoy,'-r','LineWidth',2)
title('Equilibrium Constant of Y-Vo-Y','Color','blue','fontsize',12)
set(gca,'fontsize',10)
xlabel('Distance from GB (cm)','fontsize',10)
ylabel('K_S','fontsize',10)

subplot(4,2,7)
semilogx(sol.x,charge,'-r','LineWidth',2)
title('Net Charge','Color','blue','fontsize',12)
set(gca,'fontsize',10)
xlabel('Distance from GB (cm)','fontsize',10)
ylabel('Concentration (e/cm3)','fontsize',10)

subplot(4,2,8)
semilogx(sol.x,sol.y(1,:),'-r','LineWidth',2)
title('Electrostatic Potential','Color','blue','fontsize',12)
set(gca,'fontsize',10)
xlabel('Distance from GB (cm)','fontsize',10)
ylabel('Electrostatic Potential (V)','fontsize',10)

end
```

3.7.7 EQ Results Checker

```
function [ntr_check, calib, calibnib] = yszacharge_check_eql(kT,ntr,sol)
%This function checks whether the assumptions used in the calculation
```

```
%met or not in the result.
%The first one is surface confirment. This is checked by calculating
%ns/Ns, if
%The seconde one is high doping concentration.

%k = 8.6173324E-5;       %%Boltzmann constant in eV*K-1
%kT = k*(T+273);

nnc = 3.01E22;          %%cation site density in cm-3
nna = nnc*2;            %%anion site
%zn = 28;                %%# of nearest unlike neighbours, 6 for NaCl
znn = 6;                %%# of nearest like neighbours, 12 for NaCl

za = 2;                 %%anion vacancy charge
zc = -4;                %%cation vacancy charge
zi = -1;                %%dopant charge

Fc = 2.551;             %%Free energy change by forming cation vacancy
Fa = 1.276;             %%Free energy change by forming anion vacancy
Bc = 0.76;              %%Free energy change by forming paired dopant

%construct ntr_check
na = nna*exp(-Fa/kT)*exp(-za*sol.y(1,:)./kT)*exp(-
za*sol.parameters(2)/kT)./(1+exp(-Fa/kT)*exp(-za*sol.y(1,:)./kT)*exp(-
za*sol.parameters(2)/kT)+znn*exp(-(Fa-Bc)/kT)*exp(-
2*sol.parameters(1)/kT)./(1+exp(-sol.parameters(1)/kT)*exp(-
zi*sol.y(1,:)./kT)*exp(-zi*sol.parameters(2)/kT)).^2);
nc = nnc*exp(-Fc/kT)*exp(-zc*sol.y(1,:)./kT)*exp(-
zc*sol.parameters(2)/kT)./(1+exp(-sol.parameters(1)/kT)*exp(-
zi*sol.y(1,:)./kT)*exp(-zi*sol.parameters(2)/kT)).*(((1+exp(-
sol.parameters(1)/kT)*exp(-zi*sol.y(1,:)./kT)*exp(-
zi*sol.parameters(2)/kT)).^2.*(1+exp(-Fa/kT)*exp(-
za*sol.y(1,:)./kT)*exp(-za*sol.parameters(2)/kT))-3*exp(-(Fa-
Bc)/kT)*exp(-2*sol.parameters(1)/kT)*znn)./((1+exp(-
sol.parameters(1)/kT)*exp(-zi*sol.y(1,:)./kT)*exp(-
zi*sol.parameters(2)/kT)).^2.*(1+exp(-Fa/kT)*exp(-
za*sol.y(1,:)./kT)*exp(-za*sol.parameters(2)/kT))+exp(-(Fa-
Bc)/kT)*exp(-2*sol.parameters(1)/kT)*znn));
nif = nnc*exp(-sol.parameters(1)/kT)*exp(-zi*sol.y(1,:)./kT)*exp(-
zi*sol.parameters(2)/kT)./(1+exp(-sol.parameters(1)/kT)*exp(-
zi*sol.y(1,:)./kT)*exp(-zi*sol.parameters(2)/kT)).*(((1+exp(-
sol.parameters(1)/kT)*exp(-zi*sol.y(1,:)./kT)*exp(-
zi*sol.parameters(2)/kT)).^2.*(1+exp(-Fa/kT)*exp(-
za*sol.y(1,:)./kT)*exp(-za*sol.parameters(2)/kT))-3*exp(-(Fa-
Bc)/kT)*exp(-2*sol.parameters(1)/kT)*znn)./((1+exp(-
sol.parameters(1)/kT)*exp(-zi*sol.y(1,:)./kT)*exp(-
zi*sol.parameters(2)/kT)).^2.*(1+exp(-Fa/kT)*exp(-
za*sol.y(1,:)./kT)*exp(-za*sol.parameters(2)/kT))+exp(-(Fa-
Bc)/kT)*exp(-2*sol.parameters(1)/kT)*znn));
nib = nna*znn*exp(-(Fa-Bc)/kT)*exp(-2*sol.parameters(1)/kT)./((1+exp(-
Fa/kT)*exp(-za*sol.y(1,:)./kT)*exp(-za*sol.parameters(2)/kT)).*(1+exp(-
sol.parameters(1)/kT)*exp(-zi*sol.y(1,:)./kT)*exp(-
zi*sol.parameters(2)/kT)).^2+znn*exp(-(Fa-Bc)/kT)*exp(-
2*sol.parameters(1)/kT));
ns = exp(-sol.parameters(2)*za/kT)/(1+exp(-sol.parameters(2)*za/kT));
charge = za*na+zc*nc+zi*nif;
```

```
ks_ozo = nc.*na.^2;
ks_yoy = nib./(nif.^2.*na);

ntr_check =
struct('xint',sol.x,'na',na,'nc',nc,'nif',nif,'nib',nib,'charge',charge
,'ks_ozo',ks_ozo,'ks_yoy',ks_yoy,'ns',ns);

%calibration factors
%calibration factors are currently calculated by mean values
%space specific calibration factors will be implanted in later versions.
BBB  =  exp(-Fa/kT)*exp(-za*sol.y(1,:)./kT)*exp(-za*sol.parameters(2)/kT);
CCC = exp(-sol.parameters(1)/kT)*exp(-zi*sol.y(1,:)./kT)*exp(-
zi*sol.parameters(2)/kT);
DDD = exp(-(Fa-Bc)/kT)*exp(-2*sol.parameters(1)/kT);
GGG = exp(-sol.parameters(2)*za/kT);

calib = ones(1001,2);
calib(:,1) = znn*DDD./(1+CCC').^2;
calib(:,2) = ((1+CCC').^2.*(1+BBB')-
3*DDD*znn)./((1+CCC').^2.*(1+BBB')+DDD*znn);
calibnib = znn*DDD;


%plot the checked results
figure;
set (gcf, 'PaperPositionMode','auto')
set (gcf, 'Position',[0,0,1000,900], 'color', 'w')

subplot(4,2,1)
hold on
plot(sol.x,na,'go','markersize',2)
plot(ntr.xint,ntr.na,'-r','linewidth',1)
hold off
tmp = abs((cumtrapz(sol.x,na)-
cumtrapz(sol.x,ntr.na))/cumtrapz(sol.x,na))*100;
stmp = [num2str(tmp,3),'%'];
title(['Oxygen Vacancy ',stmp],'Color','blue','fontsize',12)
set(gca,'xscale','log')
set(gca,'yscale','log')
box on
set(gca,'fontsize',10)
xlabel('Distance from GB (cm)','fontsize',10)
ylabel('Concentration (cm-3)','fontsize',10)

subplot(4,2,2)
hold on
plot(sol.x,nc,'go','markersize',3)
plot(ntr.xint,ntr.nc,'-r','linewidth',1)
hold off
tmp = abs((cumtrapz(sol.x,nc)-
cumtrapz(sol.x,ntr.nc))/cumtrapz(sol.x,nc))*100;
stmp = [num2str(tmp,3),'%'];
title(['Zirconium Vacancy ',stmp],'Color','blue','fontsize',12)
set(gca,'xscale','log')
set(gca,'yscale','log')
```

```
box on
set(gca,'fontsize',10)
xlabel('Distance from GB (cm)','fontsize',10)
ylabel('Concentration (cm-3)','fontsize',10)

subplot(4,2,3)
hold on
plot(sol.x,nif,'go','markersize',3)
plot(ntr.xint,ntr.nif,'-r','linewidth',1)
hold off
tmp = abs((cumtrapz(sol.x,nif)-
cumtrapz(sol.x,ntr.nif))/cumtrapz(sol.x,nif))*100;
stmp = [num2str(tmp,3),'%'];
title(['Free Y ',stmp],'Color','blue','fontsize',12)
set(gca,'xscale','log')
%set(gca,'yscale','log')
box on
set(gca,'fontsize',10)
xlabel('Distance from GB (cm)','fontsize',10)
ylabel('Concentration (cm-3)','fontsize',10)

subplot(4,2,4)
hold on
plot(sol.x,nib,'go','markersize',3)
plot(ntr.xint,ntr.nib,'-r','linewidth',1)
hold off
tmp = abs((cumtrapz(sol.x,nib)-
cumtrapz(sol.x,ntr.nib))/cumtrapz(sol.x,nib))*100;
stmp = [num2str(tmp,3),'%'];
title(['Bonded Y ',stmp],'Color','blue','fontsize',12)
set(gca,'xscale','log')
%set(gca,'yscale','log')
box on
set(gca,'fontsize',10)
xlabel('Distance from GB (cm)','fontsize',10)
ylabel('Concentration (cm-3)','fontsize',10)

subplot(4,2,5)
hold on
plot(sol.x,ks_ozo,'go','markersize',3)
plot(ntr.xint,ntr.ks_ozo,'-r','linewidth',1)
hold off
tmp = abs((cumtrapz(sol.x,ks_ozo)-
cumtrapz(sol.x,ntr.ks_ozo))/cumtrapz(sol.x,ks_ozo))*100;
stmp = [num2str(tmp,3),'%'];
title(['K_S Vo-Vzr-Vo ',stmp],'Color','blue','fontsize',12)
set(gca,'xscale','log')
%set(gca,'yscale','log')
box on
set(gca,'fontsize',10)
xlabel('Distance from GB (cm)','fontsize',10)
ylabel('K_S','fontsize',10)

subplot(4,2,6)
hold on
plot(sol.x,ks_yoy,'go','markersize',3)
```

```
plot(ntr.xint,ntr.ks_yoy,'-r','linewidth',1)
hold off
tmp = abs((cumtrapz(sol.x,ks_yoy)-
cumtrapz(sol.x,ntr.ks_yoy))/cumtrapz(sol.x,ks_yoy))*100;
stmp = [num2str(tmp,3),'%'];
title(['K_S Y-Vo-Y ',stmp],'Color','blue','fontsize',12)
set(gca,'xscale','log')
%set(gca,'yscale','log')
box on
set(gca,'fontsize',10)
xlabel('Distance from GB (cm)','fontsize',10)
ylabel('K_S','fontsize',10)

subplot(4,2,7)
hold on
plot(sol.x,charge,'go','markersize',3)
plot(ntr.xint,ntr.charge,'-r','linewidth',1)
hold off
tmp = abs((cumtrapz(sol.x(1:300),charge(1:300))-
cumtrapz(sol.x(1:300),ntr.charge(1:300)))/cumtrapz(sol.x(1:300),charge(
1:300)))*100;
stmp = [num2str(tmp,3),'%'];
title(['Net Charge ',stmp],'Color','blue','fontsize',12)
set(gca,'xscale','log')
%set(gca,'yscale','log')
box on
set(gca,'fontsize',10)
xlabel('Distance from GB (cm)','fontsize',10)
ylabel('Concentration (e/cm3)','fontsize',10)

subplot(4,2,8)
pie([1-ns,ns])
labels = {'Unoccupied','Occupied'};
legend(labels,'Location','Eastoutside','Orientation','vertical')
title('Surface Charge Occupation','Color','blue','fontsize',12)
set(gca,'fontsize',10)

end
```

The code developed to solve the nonequilibrium problem is listed in the following sections. This set of codes contains: Main function; Initial value feeder; BVP solver; BVP solver repeater; Continuation – boundary extender; Calculation results interpreter; Defect distribution calculator.

3.7.8 NEQ Main Function

```
T_low = 300;
T_high = 2700;
T_int = 100;
TT = T_high:-T_int:T_low;
n = (T_high-T_low)/T_int+1;

calib_cfix = ones(1001,2,n);
calib_tmp = ones(1001,3);

for i = 1:n;
    eval(sprintf('sol = cs_sol_b4_%d;',TT(i)));
    calib_cfix(:,:,i) = yszacharge_cfix_ABCD(TT(i),sol);
end

    xint = [0,logspace(-8,-2,1000)];
    xint(end) = xint(end)*(1+1e-8); % This slight augment is to avoid
exceeding boundary.
    calib_tmp(:,3) = xint;

for i = 1:n;

    kkk = 1;
    T_eql = TT(i)+273
    eval(sprintf('sol_eql = cs_sol_raw_b4_%d;',TT(i)));
    eval(sprintf('ntr_eql = cs_ntr_b4_%d;',TT(i)));
    calib_tmp(:,1:2) = calib_cfix(:,:,i);

    for j = TT(i):-T_int:T_low;

        T = j+273
        %nsurf = nsurf_tot*1e-6/0.01; %don't forget here if you change
L

        if kkk == 1;
            warning('none');
            sol = yszacharge_cfix(T_eql,T,calib_tmp,sol_eql);
        else
            warning('none');
            sol = yszacharge_cfix(T_eql,T,calib_tmp,sol);
        end

        while ~strcmp(lastwarn,'none')
            warning('none');
            sol = yszacharge_cfix_continue(T,calib_tmp,sol);
        end

        for kk = 1:4;
            kk

            sol = yszacharge_cfix_extend(sol,L,kappa);

            warning('none');
```

```
            sol = yszacharge_cfix_continue(T,calib_tmp,sol);

            while ~strcmp(lastwarn,'none')
                warning('none');
                sol = yszacharge_cfix_continue(T,calib_tmp,sol);
            end
        end

        sol_int = yszacharge_cfix_intp(sol,lambda,kappa,kT,L);
        ntr_cfix = dtr_cfix(sol_int,ntr_eql,kT);
        kkk = kkk+1;

        eval(sprintf('cs_sol_%d_%d=sol_int;',TT(i),j));
        eval(sprintf('cs_sol_raw_%d_%d=sol;',TT(i),j));
        eval(sprintf('cs_ntr_%d_%d=ntr_cfix;',TT(i),j));
        eval(sprintf('print(gcf,''-r100'',''-
dpng'',''cs_ntr_%d_%d'')',TT(i),j));
        close all;
    end
end
```

3.7.9 NEQ Initial Value Feeder

```
function calib = yszacharge_cfix_ABCD(T,sol)

%This function summarize AAA,CCC,DDD in a table, for later use.

k = 8.6173324E-5;       %%Boltzmann constant in eV*K-1
kT = k*(T+273);

%nnc = 3.01E22;          %%cation site density in cm-3
%nna = nnc*2;            %%anion site
%zn = 28;                %%# of nearest unlike neighbours, 6 for NaCl
znn = 6;                %%# of nearest like neighbours, 12 for NaCl

za = 2;                 %%anion vacancy charge
zc = -4;                %%cation vacancy charge
zi = -1;                %%dopant charge

Fc = 2.551;             %%Free energy change by forming cation vacancy
Fa = 1.276;             %%Free energy change by forming anion vacancy
Bc = 0.76;              %%Free energy change by forming paired dopant

AAA = exp(-Fc/kT)*exp(-zc*sol.y(1,:)./kT)*exp(-zc*sol.parameters(2)/kT);
BBB = exp(-Fa/kT)*exp(-za*sol.y(1,:)./kT)*exp(-za*sol.parameters(2)/kT);
CCC = exp(-sol.parameters(1)/kT)*exp(-zi*sol.y(1,:)./kT)*exp(-
zi*sol.parameters(2)/kT);
DDD = exp(-(Fa-Bc)/kT)*exp(-2*sol.parameters(1)/kT);

calib = ones(1001,2);
calib(:,1) = znn*DDD./(1+CCC').^2;
calib(:,2) = (zc*AAA'+zi*CCC')./(1+CCC').*((1+CCC').^2.*(1+BBB')-
```

```
3*DDD*znn)./((1+CCC').^2.*(1+BBB')+DDD*znn);

end
```

3.7.10 NEQ BVP Solver

```
function sol = yszacharge_cfix(T_eql,T,calib,sol_init)
%Surface Layer now has a constrain!!!!!
%nif, nib, nc are fixed in their equilibrium concentration

epsl = 29*8.854e-10;     %%permitivity of simulated crystal in F*cm-1
e = 1.60217657E-19;      %%electron charge in coulombs
k = 8.6173324E-5;        %%Boltzmann constant in eV*K-1

%C = 14.8E-2;                %%doping concentration
L = 1e-6;

nnc = 3.01E22;           %%cation site density in cm-3
%nna = nnc*2;             %%anion site
nsurf = 1.545E15;        %%# of anion site at surface layer
%zn = 28;                 %%# of nearest unlike neighbours, 6 for NaCl
%znn = 6;                 %%# of nearest like neighbours, 12 for NaCl

za = 2;                  %%anion vacancy charge
%zc = -4;                 %%cation vacancy charge
%zi = -1;                 %%dopant charge

%Fc = 2.551;              %%Free energy change by forming cation vacancy
Fa = 1.276;              %%Free energy change by forming anion vacancy
%Bc = 0.76;              %%Free energy change by forming paired dopant

kappa = (4*pi*e*nnc/(epsl*k*T))^0.5;
kappa_eql = (4*pi*e*nnc/(epsl*k*T_eql))^0.5;
lambda = nnc/kappa;
lambda_eql = nnc/kappa_eql;
kT = k*T;
kT_eql = k*T_eql;

xint = [0,logspace(-8,log10(L),1000)];
sint = xint*kappa;

%set initial guess based on sol_init
solinit = bvpinit(sint,@init,sol_init.parameters(2));
tmp = deval(sint,sol_init);
solinit.y(1:2,:) = tmp(1:2,:);
solinit.y(3,:) = tmp(4,:);
%end of initial guess setting

options = bvpset('RelTol',1e-4);

sol = bvp5c(@ode, @bc, solinit, options);
```

```
assignin('base','lambda',lambda)
assignin('base','lambda_eql',lambda_eql)
assignin('base','kappa',kappa)
assignin('base','kappa_eql',kappa_eql)
assignin('base','kT',kT)
assignin('base','T',T)
assignin('base','kT_eql',kT_eql)
assignin('base','T_eql',T_eql)
assignin('base','L',L)

    function dy = ode(x,y,beta)

        dy = [  y(2)
                -clb(x,2)-2*za*exp(-Fa/kT)*exp(-za*y(1))*exp(-
za*beta)/(1+exp(-Fa/kT)*exp(-za*y(1))*exp(-za*beta)+clb(x,1))
                clb(x,2)+2*za*exp(-Fa/kT)*exp(-za*y(1))*exp(-
za*beta)/(1+exp(-Fa/kT)*exp(-za*y(1))*exp(-za*beta)+clb(x,1))];

%         dy = [  y(2)
%                 -clb(x,2)-2*za*BBB/(1+BBB+clb(x,1))
%                 clb(x,2)+2*za*BBB/(1+BBB+clb(x,1))];

% AAA = exp(-Fc/kT)*exp(-zc*y(1))*exp(-zc*beta);
% BBB = exp(-Fa/kT)*exp(-za*y(1))*exp(-za*beta);
% CCC = exp(-alpha)*exp(-zi*y(1))*exp(-zi*beta);
% DDD = exp(-(Fa-Bc)/kT)*exp(-2*alpha);

    end %ode

    function res = bc(ya,yb,beta)
        res = [ ya(1)
                ya(3)
                yb(2)
                yb(3)+za*kappa*nsurf/nnc*exp(-beta*za)/(1+exp(-
beta*za))];
    end %bc

    function v = init(x)
        v = [   0
                0
                0];
    end %init

    function q = clb(s,i)
        x = s/kappa;
        q = interp1(calib(:,3),calib(:,i),x);
    end %clb

end
```

3.7.11 NEQ BVP Solver Repeater

```
function sol = yszacharge_cfix_continue(T,calib,solinit)

epsl = 29*8.854e-10;     %%permitivity of simulated crystal in F*cm-1
e = 1.60217657E-19;      %%electron charge in coulombs
k = 8.6173324E-5;        %%Boltzmann constant in eV*K-1

nnc = 3.01E22;           %%cation site density in cm-3
%nna = nnc*2;             %%anion site
nsurf = 1.545E15;        %%# of anion site at surface layer
%zn = 28;                 %%# of nearest unlike neighbours, 6 for NaCl
%znn = 6;                 %%# of nearest like neighbours, 12 for NaCl

za = 2;                  %%anion vacancy charge
%zc = -4;                 %%cation vacancy charge
%zi = -1;                 %%dopant charge

%Fc = 2.551;              %%Free energy change by forming cation vacancy
Fa = 1.276;              %%Free energy change by forming anion vacancy
%Bc = 0.76;               %%Free energy change by forming paired dopant

kappa = (4*pi*e*nnc/(epsl*k*T))^0.5;
%kappa_eql = (4*pi*e*nnc/(epsl*k*T_eql))^0.5;
%lambda = nnc/kappa;
%lambda_eql = nnc/kappa_eql;
kT = k*T;
%kT_eql = k*T_eql;

%sL = solinit.x(end);
options = bvpset('RelTol',1e-4);

sol = bvp5c(@ode, @bc, solinit, options);

    function dy = ode(x,y,beta)

        dy = [  y(2)
                -clb(x,2)-2*za*exp(-Fa/kT)*exp(-za*y(1))*exp(-
za*beta)/(1+exp(-Fa/kT)*exp(-za*y(1))*exp(-za*beta)+clb(x,1))
                clb(x,2)+2*za*exp(-Fa/kT)*exp(-za*y(1))*exp(-
za*beta)/(1+exp(-Fa/kT)*exp(-za*y(1))*exp(-za*beta)+clb(x,1))];

    end %ode

    function res = bc(ya,yb,beta)
        res = [ ya(1)
                ya(3)
                yb(2)
                yb(3)+za*kappa*nsurf/nnc*exp(-beta*za)/(1+exp(-
beta*za))];
    end %bc

    function q = clb(s,i)
        x = s/kappa;
```

```
        q = interp1(calib(:,3),calib(:,i),x);
    end %clb

end
```

3.7.12 NEQ Continuation – Boundary Extender

```
function sol = yszacharge_cfix_extend(sol_in,L,kappa)

L = L*10;
sL = kappa*L;
sol = bvpxtend(sol_in,sL,'linear');
assignin('base','L',L)

end
```

3.7.13 NEQ Calculation Results Interpreter

```
function sol_int = yszacharge_cfix_intp(sol,lambda,kappa,kT,L)

    xint = [0,logspace(-8,log10(L),1000)];
    sint = xint*kappa;
    sol_tmp = deval(sint,sol);

    sol_int = sol;
    sol_int.x = xint;
    sol_int.y = sol_tmp;
    sol_int.y(1,:) = sol_tmp(1,:)*kT;
    sol_int.y(2,:) = sol_tmp(2,:)*kT*kappa;
    sol_int.y(3,:) = sol_tmp(3,:)*lambda;
    sol_int.parameters = sol.parameters*kT;

end
```

3.7.14 NEQ Defect Distribution Calculator

```
function ntr_cfix = dtr_cfix(sol,ntr,kT,calib)

nnc = 3.01E22;          %%cation site density in cm-3
nna = nnc*2;            %%anion site
zn = 28;                %%# of nearest unlike neighbours, 6 for NaCl
znn = 6;                %%# of nearest like neighbours, 12 for NaCl

za = 2;                 %%anion vacancy charge
zc = -4;                %%cation vacancy charge
zi = -1;                %%dopant charge
Fc = 2.551;             %%Free energy change by forming cation vacancy
```

```
Fa = 1.276;              %%Free energy change by forming anion vacancy
Bc = 0.76;               %%Free energy change by forming paired dopant

na = nna*exp(-Fa/kT)*exp(-za*sol.y(1,:)./kT)*exp(-
za*sol.parameters/kT)./(1+exp(-Fa/kT)*exp(-za*sol.y(1,:)./kT)*exp(-
za*sol.parameters/kT)+calib(:,1)');
ns = exp(-sol.parameters*za/kT)/(1+exp(-sol.parameters*za/kT));
charge = za*na+zc*ntr.nc+zi*ntr.nif;
ks_ozo = ntr.nc.*na.^2;
ks_yoy = ntr.nib./(ntr.nif.^2.*na);

ntr_cfix =
struct('xint',sol.x,'na',na,'ns',ns,'charge',charge,'ks_ozo',ks_ozo,'ks
_yoy',ks_yoy);


figure;
set (gcf, 'PaperPositionMode','auto')
set (gcf, 'Position',[0,0,1500,900], 'color', 'w')


subplot(3,3,1)
loglog(sol.x,na,'-r','LineWidth',2)
title('Oxygen Vacancy','Color','blue','fontsize',12)
set(gca,'fontsize',10)
xlabel('Distance from GB (cm)','fontsize',10)
ylabel('Concentration (cm-3)','fontsize',10)

subplot(3,3,2)
loglog(sol.x,ntr.nc,'-r','LineWidth',2)
title('Zirconium Vacancy','Color','blue','fontsize',12)
set(gca,'fontsize',10)
xlabel('Distance from GB (cm)','fontsize',10)
ylabel('Concentration (cm-3)','fontsize',10)

subplot(3,3,3)
loglog(sol.x,ntr.nif,'-r','LineWidth',2)
title('Free Dopant Y','Color','blue','fontsize',12)
set(gca,'fontsize',10)
xlabel('Distance from GB (cm)','fontsize',10)
ylabel('Concentration (cm-3)','fontsize',10)

subplot(3,3,4)
loglog(sol.x,ntr.nib,'-r','LineWidth',2)
title('Bonded Dopant Y','Color','blue','fontsize',12)
set(gca,'fontsize',10)
xlabel('Distance from GB (cm)','fontsize',10)
ylabel('Concentration (cm-3)','fontsize',10)
 subplot(3,3,5)
semilogx(sol.x,charge,'-r','LineWidth',2)
title('Net Charge','Color','blue','fontsize',12)
set(gca,'fontsize',10)
xlabel('Distance from GB (cm)','fontsize',10)
ylabel('Concentration (e/cm3)','fontsize',10)
```

```
subplot(3,3,6)
semilogx(sol.x,sol.y(1,:),'-r','LineWidth',2)
title('Electrostatic Potential','Color','blue','fontsize',12)
set(gca,'fontsize',10)
xlabel('Distance from GB (cm)','fontsize',10)
ylabel('Electrostatic Potential (V)','fontsize',10)

subplot(3,3,7)
semilogx(sol.x,ks_ozo,'-r','LineWidth',2)
title('Schottky Defect Equilibrium
Constant','Color','blue','fontsize',12)
set(gca,'fontsize',10)
xlabel('Distance from GB (cm)','fontsize',10)
ylabel('K_S','fontsize',10)

subplot(3,3,8)
semilogx(sol.x,ks_yoy,'-r','LineWidth',2)
title('Equilibrium Constant of Y-Vo-Y','Color','blue','fontsize',12)
set(gca,'fontsize',10)
xlabel('Distance from GB (cm)','fontsize',10)
ylabel('K_S','fontsize',10)

subplot(3,3,9)
pie([1-ns,ns])
labels = {'Unoccupied','Occupied'};
legend(labels,'Location','Eastoutside','Orientation','vertical')
title('Surface Charge Occupation','Color','blue','fontsize',12)
set(gca,'fontsize',10)
end
```

3.8 Summary

In order to improve grain boundary resistivity, space charge distribution at grain boundaries needs to be studied. In YSZ, there are five dominating defect species, which include free oxygen vacancy, free zirconium vacancy, free Y dopant, neutral association between oxygen vacancy and zirconia vacancy, and neutral association between oxygen vacancy and Y dopant. Concentration of these defect species are obtained by minimizing Helmholtz free energy of the crystal. Formation energy of defect species, space charge electrical potential and configurational entropy contribute to the total Helmholtz free energy. The configurational entropy is developed explicitly for the fluorite structure as well as considering all the defect species. High doping modification is introduced for the

first time due to the high Y doping concentration. At high doping condition, defect distribution follows modified Boltzmann distribution. Surface charge constrain is considered since space charge need to be balanced by surface charge, which has limited amount. In order to study the space charge distribution in real materials, nonequilibrium calculation is necessary, because at working temperature (800°C) cations vacancies follow equilibrium distribution at sintering temperature.

Grain boundary resistance is widely considered to be due to oxygen vacancy depletion. This study finds that not only oxygen vacancy depletion but also Y segregation leads to the extremely high grain boundary resistivity. The results of nonequilibrium calculation indicate an effective way to reduce grain boundary resistivity. Sintering or postannealing at higher temperature and quenching to lower temperature can significantly increase oxygen vacancy depletion as well as reducing Y segregation at grain boundaries. As a result, oxygen ion conductivity through grain boundary will be greatly improved. In the meantime, grain boundary thickness decreases when annealing at higher temperature. Therefore, the total grain boundary resistance decreases. Grain bulk resistivity can also be reduced. Annealing at higher temperature leads to reduced defect association between oxygen vacancy and Y dopant. When quenching to low temperature, free oxygen vacancy and free Y dopant cannot form associations, because free Y dopant cannot move to the required sites. As a result, the oxygen vacancy concentration in grain bulk is significantly higher and the conductivity increases.

3.9 References

1. S. Singhal, *Solid State Ionics*, **135**, 305–313 (2000)

2. Y. Yoon, W. Cho, J. Lim, and D. Choi, *J. Power Sources*, **101**, 126–129 (2001)

3. T. Ohzuku, S. Takeda, and M. Iwanaga, *J. Power Sources*, **81-82**, 90–94 (1999)

4. M. Watanabe, K. Tsurumi, T. Mizukami, T. Nakamura, and P. Stonehart, *J. Electrochem. Soc.*, **141**, 2659–2668 (1994)

5. J.-H. Lee et al., *J. Electrochem. Soc.*, **147**, 2822 (2000)

6. K. Lehovec, *J. Chem. Phys.*, **21**, 1123–1128 (1953)

7. K. Kliewer and J. Koehler, *Phys. Rev.*, **140**, A1226 (1965)

8. X. Guo, *Solid State Ionics*, **96**, 247–254 (1997)

9. X. Guo and J. Maier, *J. Electrochem. Soc.*, **148**, E121 (2001)

10. K. L. Merkle, G.-R. Bai, Z. Li, C.-Y. Song, and L. J. Thompson, *Phys.Status Solidi*, **166**, 73–89 (1998)

11. M. Kilo, G. Borchardt, and B. Lesage, *J. Eur. Ceram. Soc.*, **20**, 2069–2077 (2000)

12. L. F. Shampine, M. W. Reichelt, and J. Kierzenka, (2000) http://www.mathworks.com/bvp_tutorial.

13. J. M. Blakely and S. Danyluk, *Surf. Sci.*, **40**, 37–60 (1973)

14. G. S. A. M. Theunissen, A. J. A. Winnubst, and A. J. Burggraaf, *J. Mater. Sci.*, **27**, 5057–5066 (1992)

15. A. Nakamura and J. Wagner, *J. Electrochem. Soc.*, **133**, 1542–1548 (1986)

16. M. Verkerk, B. Middelhuis, and A. Burggraaf, *Solid State Ionics*, **6**, 159–170 (1982)

CHAPTER 4

A STUDY OF GADOLINIA-DOPED CERIA ELECTROLYTE BY ELECTROCHEMICAL IMPEDANCE SPECTROSCOPY

The previous three chapters focused on theoretical analysis and simulation on SOFCs' power losses. It is also important and necessary to measure resistance of each layer. In experiments, electrochemical impedance spectroscopy (EIS) is widely used to measure resistance of different layers in SOFCs. In this chapter, the operation and interpretation of EIS is introduced. Samples of Gd_2O_3-doped CeO_2 (GDC) were fabricated by conventional sintering of powder compacts. Impedance spectra were measured from 400°C to 675°C in air by EIS using the two-terminal method. Above ~500°C, the high frequency arc was not semicircular but could be fitted with a constant phase element (CPE). Above ~625°C, the high frequency arc could not be resolved and there was a significant contribution from the inductive load. The impedance spectra were described using a simple equivalent circuit which included the leads/instrument impedance. The impedance of the lead wires/instrument was measured over a range of frequencies and as a function of temperature. The high frequency part of the sample impedance once the leads/instrument impedance was subtracted could be fully resolved even at the highest measurement temperature and could be described by a semicircle representative of transport across grain boundaries. From these measurements, grain and grain boundary

resistivities were determined. The corresponding activation energies were 0.69 eV and 1.11 eV, respectively. The grain boundary capacitance was nearly independent of temperature. The present results show that in GDC grain boundary effects can be adequately described by a resistor and a capacitor in parallel. The significance is that fitting can be achieved using a single parameter unlike a CPE which requires two parameters. The observed spectra were interpreted using a simple equivalent circuit analysis. Relevant equivalent circuit parameters were obtained from intercepts, maxima and minima in impedance diagrams.

4.1 Introduction

Electrochemical Impedance Spectroscopy (EIS) is a technique which measures the response of a sample under an AC stimulus in which the frequency is varied over a wide range. EIS has wide applicability, and has been used for the study of ionic conductors, dielectric materials, semiconductors, solar cells, fuel cells, batteries and corrosion. With improvements in equipment over the years, four types of techniques are typically used to measure and interpret the impedance. They are: AC bridge, Lissajous analysis, phase-sensitive detection and Fourier analysis. The general approach involves the application of a single frequency input and the measurement of the corresponding current (I) flowing through and the potential drop (V) across the sample. From the measurement of I and V as well as the phase difference over a wide range of frequencies, the real and the imaginary parts of the impedance as a function of frequency can be determined. In 1969, Bauerle in a landmark paper in solid state ionics investigated transport through yttria-stabilized zirconia (YSZ) samples with various applied electrodes and in several

atmospheres using electrochemical admittance spectroscopy [1]. Bauerle showed that the measured admittance data could be fitted to semicircles or depressed semicircles in the admittance plane. These semicircles at high frequencies correspond to transport properties through the grain interiors and across the grain boundaries, and at low frequencies correspond to electrode effects [1]. Bauerle used an equivalent circuit comprising a pure resistor and a pure capacitor in parallel to describe the sample behavior at high frequencies which accurately reproduced the measured spectra. Electrode effects were in part represented using Warburg impedance. Since this original paper, the use of EIS has become commonplace in the study of solid state ionics [2].

The resolution of grain and grain-boundary effects usually requires a high frequency input, often exceeding 100 kHz. It is well known that at high frequencies, there can be a significant contribution from an inductive load, the origin of which lies in the lead wires used to connect to the sample as well as parts of the instrumentation. The effect of the inductive load reflects as an imaginary part of the impedance below the x-axis when the real part is plotted on the positive x-axis and negative of the imaginary part is plotted on the positive y-axis. Thus, in a typical plotting scheme, the capacitive effects appear above the x-axis and the inductive effects appear below the x-axis. When both capacitive and inductive contributions are present to a significant extent, their effects are reflected in the spectra regardless of whether the actual spectra lie above or below the x-axis. Many studies have shown that it is essential to subtract the effects of the leads/instrument before data can be adequately interpreted [2-4]. In a study of ($La_{1-x}Sr_xCo_{1-y}Fe_yO_{3-\delta}$) LSCF cathodes using EIS, Esquirol et al. measured the leads/instrument inductance as ~125 nH, and the corresponding leads/instrument impedance was subtracted from the raw EIS data

[3]. Samson et al. [4] also measured the impedance of an empty cell and subtracted it from the raw data in their study of Sr-doped $LaCoO_3$ (LSC) cathodes [4]. In many recent studies, however, the approach used has been to ignore that part of the impedance which lies below the x-axis and fit the remaining portion above the x-axis (which is generally not semicircular) using a CPE [5-8]. However, such a procedure does not account for the impedance of the leads/instrument and as such may not represent an accurate measurement of the sample impedance. For example, in a study of electrolyte resistivity, Suzuki et al. did not remove the leads/instrument impedance [5]. They noted that there was a large difference in the measured electrolyte resistance from that expected from separate measurements on bulk samples [5]. They attributed the observed large difference in the electrolyte resistance between the expected value and the measured value to the multilayer structure of their sample [5]. However, the leads/instrument impedance is expected to contain both resistive and inductive contributions, which right-shift the arc leading to an intercept at a larger value (than the sample resistance) on the real axis unless the leads/instrument impedance has been subtracted out. Wang et al. [6] investigated $La_{0.8}Sr_{0.2}MnO_{3-\delta}/Zr_{0.92}Y_{0.08}O_2$ porous electrodes by EIS. In their work the high frequency intercept was equated to the electrolyte and the lead resistance. However, inductive effects of the leads were neglected. Similarly, Zajac et al. investigated the resistivity of doped ceria by EIS [7,8]. In their study, the data below the x-axis were cutoff and the remaining data were analyzed by a CPE as the arcs clearly were not semicircular [7, 8].

The use of a CPE generally leads to a better fit to the data than using a capacitor. This of course is not surprising as fitting with a CPE requires two parameters unlike a

capacitor, which only needs one parameter. However, the use of a CPE often makes it difficult to offer a unique physical interpretation of the data as the fitting itself may lack uniqueness. In this work, we investigated the conductivity of GDC samples with the objective being the determination of grain and grain boundary ion transport properties. The leads/instrument impedance was separately measured and was subtracted from the data before fitting. The measurements were conducted using the two-terminal method. While many studies in the past have emphasized the need to subtract the leads/instrument contribution [2-4], the continual use of procedures in which the inductive part is cutoff and the rest of the data are fitted using a CPE suggests that revisiting this issue may be of value. The present study also analyzes the data in light of simple equivalent circuits but with the inclusion of the leads/instrument impedance. The present work also attempts to extract relevant parameters of the equivalent circuit from intercepts, maxima and minima in the impedance diagrams.

4.2 Experimental Procedure

Pellets of Gd_2O_3-doped ceria (GDC) powder of composition 80 mol.% CeO_2 – 20 mol.% $GdO_{1.5}$ were die-pressed and sintered in air at 1400°C for 2 h. The typical thickness of the pellets was ~1.4 mm. Pt paste was applied on both sides of the pellets and they were fired at 800°C in air for 1 h. Samples of two different electrode geometries (sizes) were used in this study; one set of samples with electrodes 15.8 mm in diameter and the other with electrodes 4.8 mm in diameter.

Impedance spectra were obtained on the samples in air over a range of temperatures between 400°C and 675°C in 25 degree intervals using the two-terminal method. The

impedance measurements were conducted using Solartron 1260 Frequency Response Analyzer over a frequency (f) range between 0.1 Hz and 1 MHz. Impedance spectra over the same range of temperatures and frequencies were also obtained without the sample (the empty cell) by shorting the two lead wires. This corresponds to the inductive-resistive contribution of the lead wires and the testing setup.

4.3 Results and Discussion

4.3.1 Lead Impedance Subtraction

The density of the sintered samples was measured to be 7.0426 g/ml, which is about 97.37% of theoretical. Figure 4-1 shows a scanning electron micrograph (SEM) of a polished and thermally etched sample of a GDC sample. The microstructure is equiaxed and the average grain size is ~1.1 μm. Figure 4-2 shows an example of how the impedance was measured and interpreted. The corresponding equivalent circuits are shown as insets. Also, an inset in Figure 4-2 shows schematics of the two samples used with different electrode areas. For simplicity, the electrodes were also modeled using a parallel R-C circuit. However, it is clear that the electrodes cannot be represented by this simplified circuit element. Other circuit elements, such as Warburg, and CPE will likely be required to interpret the low frequency data in light of physically realistic mechanisms; e.g., gas diffusion through porous electrodes, adsorption, dissociation, charge transfer. Thus, most of the fitting in this manuscript was restricted to the high frequency part of the impedance spectra even though the analysis includes the electrodes modeled with a parallel R-C circuit. The low frequency part was fitted using a CPE in selected cases for completeness and to obtain a better fit with the data corresponding to the electrode effects.

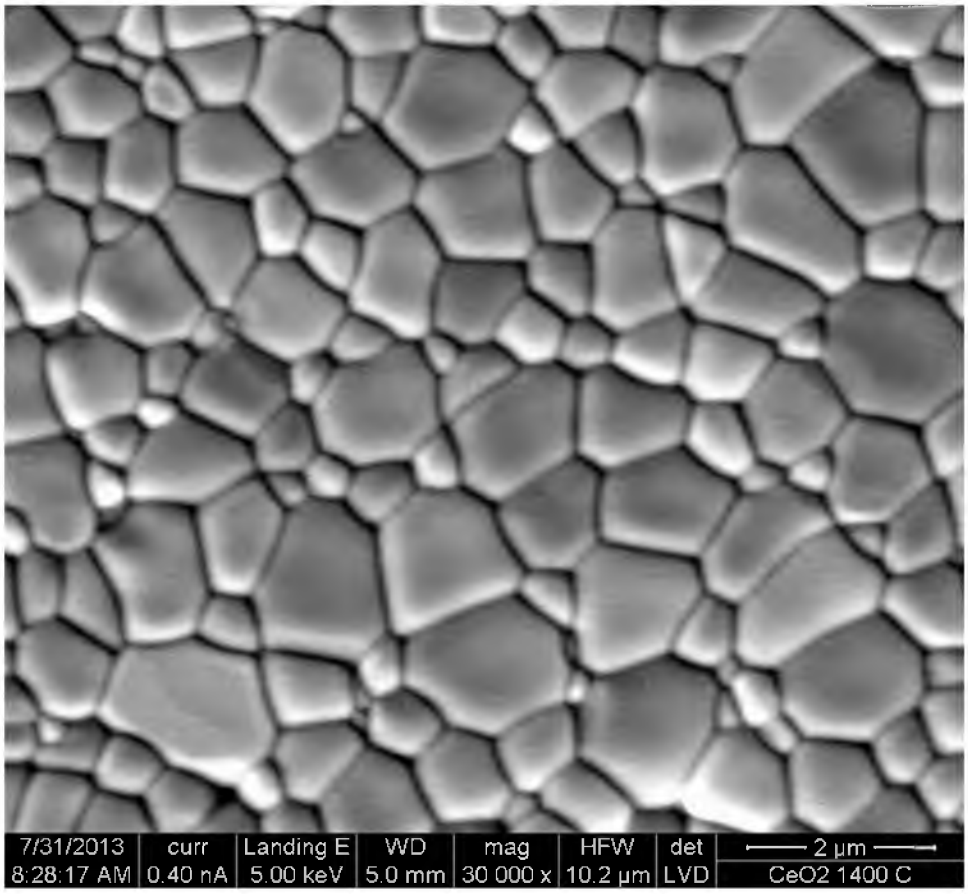

Figure 4-1: An SEM image of the GDC sample showing an equiaxed microstructure. The average grain size is ~1.1 µm.

The measured impedance of the entire setup including the sample at 600°C is shown in Figure 4-2(a). Figure 4-2(b) shows an enlarged part of the high frequency region of Figure 4-2(a). The impedance of the setup without the sample with the leads shorted is given in Figure 4-2(c). The leads/instrument impedance (Figure 4-2(c)) was then subtracted from the measured total impedance (Figure 4-2(a)). The difference, which should be the sample impedance without the effects of the leads/instrument impedance, is plotted in Figure 4-2(d). Finally, the high frequency portion of the impedance from Figure 4-2(d) is plotted in Figure 4-2(e). The data points in Figure 4-2(e) are then fitted

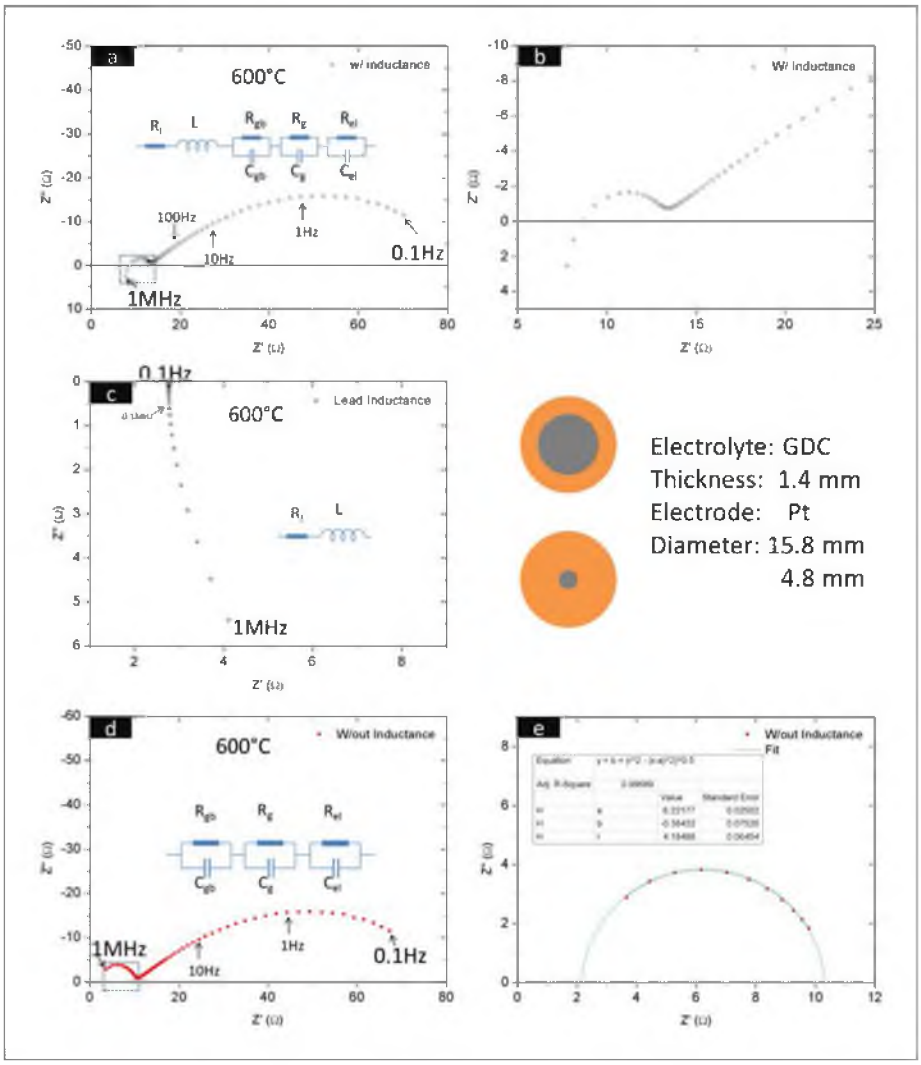

Figure 4-2: Experimental approach used for impedance measurements and data interpretation. Inset shows samples with two different electrode areas. (a): Measured impedance of the whole setup, including the sample and the leads/instrument at 600°C; (b): Enlarged view of the high frequency region in (a); (c): Measured leads/instrument impedance by shorting the leads without the sample; (d): Sample impedance obtained by subtracting the leads/instrument impedance (c) from the measured sample-setup impedance (a); (e): Enlarged view of the boxed part in (d). These data are fitted to a semicircle. From the semicircle, the grain resistance, the grain boundary resistance and the grain boundary capacitance are readily obtained.

using a semicircle. As seen in Figure 4-2(e), the data can be fitted very well with a semicircle, which represents transport across grain boundaries. Fitting with a semicircle suggests that the grain boundary effects could be adequately represented by a resistor and a capacitor in parallel. Also important to note is that the data point corresponding to the highest frequency of 10^6 Hz (angular frequency, $\omega = 2\pi f = 2\pi \times 10^6$) appears above the x-axis suggesting that the leads inductive-resistive effects appear to have been removed.

Impedance data obtained on a sample with electrodes 15.8 mm in diameter over a temperature range from 400°C to 675°C before subtracting the leads/instrument impedance are plotted in Figure 4-3(a) and Figure 4-3(b). The low frequency regime, as is well known, represents the electrode effects. In this work primarily the high frequency effects were investigated. At low temperatures (below 525°C) the effects of the leads/instrument impedance are not obvious (although still present) as the entire measured spectra over the range of frequencies between 0.1 Hz and 1 MHz lie above the x-axis. The near semicircular feature of the high frequency data can be seen in Figure 4-3(a). For measurements at 550°C and above (Figure 4-3(b)), the high frequency arc appears as a depressed or a flattened semicircle. At the measurement temperatures of 650°C and 675°C, the high frequency arc completely disappears. Also, the leads/instrument inductive effects are clearly seen at higher temperatures, as evidenced by part (or even most) of the measured impedance data lying below the x-axis. The leads/instrument impedance comprising inductive and resistive contributions was found to be weakly dependent on temperature, unlike the sample impedance (resistive part) which exhibits Arrhenius behavior and thus rapidly decreases with increasing temperature.

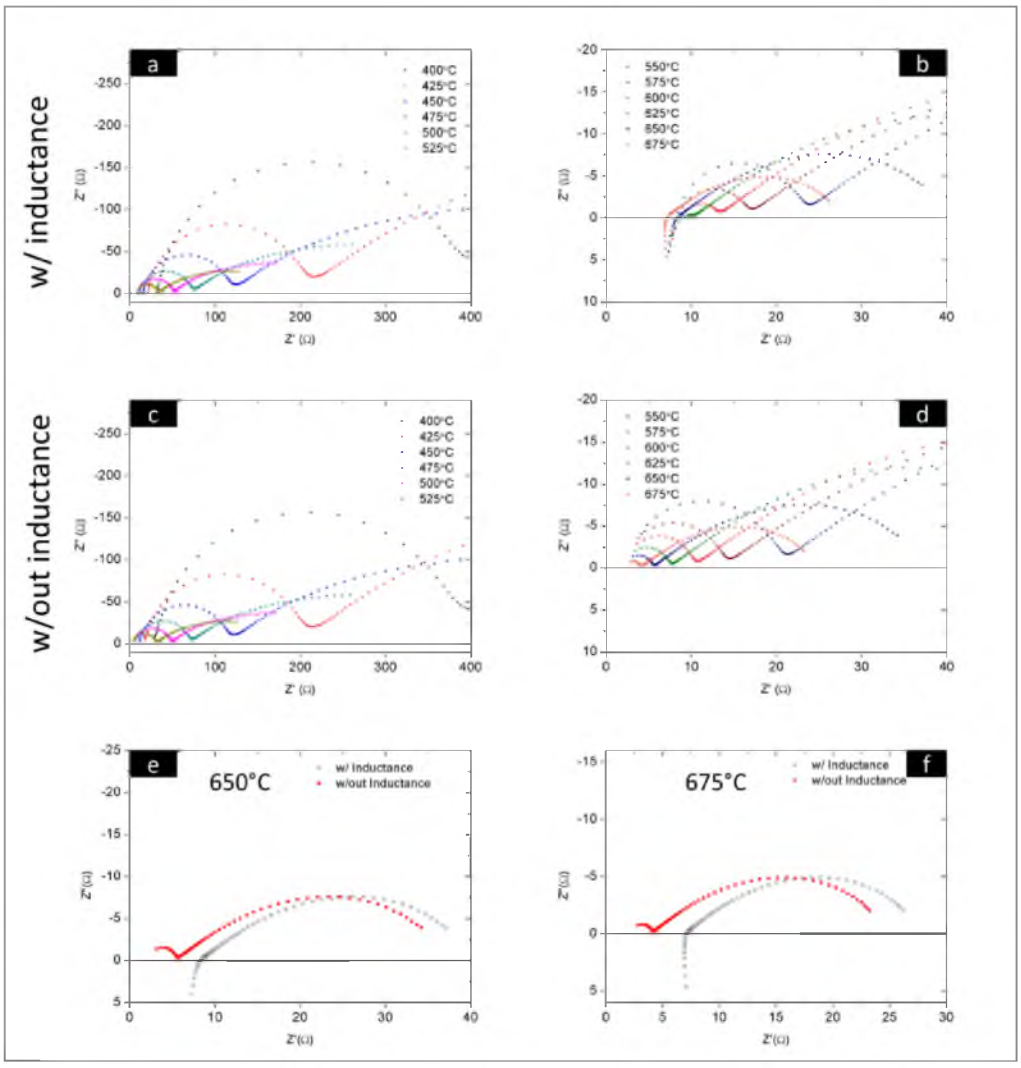

Figure 4-3: EIS data. (a) and (b) are the as-measured impedance spectra for the sample including the leads/instrument impedance from 400°C to 675°C; (c) and (d) are the corresponding impedance spectra after subtracting the leads/instrument impedance over the same temperature range; (e) and (f) compare the plots with and without the leads/instrument effects at 650°C and 675°C, respectively. Note that once the leads/instrument effects are subtracted out, the high frequency arcs are resolved and that they are semicircular in shape.

Figure 4-3(c) and Figure 4-3(d) show the same data, respectively, from Figure 4-3(a) and Figure 4-3(b), but from which the leads/instrument impedance has been subtracted. Thus, the data in Figure 4-3(c) and Figure 4-3(d) represent the sample impedance without any leads/instrument effects. All high frequency arcs now appear perfectly semicircular. Also, no data points lie below the x-axis showing that the effects of the leads/instrument have been subtracted out. Also note that even at the highest measurement temperature of 675°C, the high frequency semicircular arc is fully resolved and is clearly visible. Figure 4-3(e) and Figure 4-3(f), respectively, show the measured data at 650°C and 675°C, in which the plots include data with and without leads/instrument effects. As clearly seen, the semicircle representing the grain resistance, the grain boundary resistance, and the grain boundary capacitance can be clearly resolved once the leads/instrument impedance is subtracted, unlike the raw data in which no high frequency arcs can be seen.

For the high frequency data, such as at 1 MHz noted in Figure 4-3(e) and Figure 4-3(f), the change in impedance after subtracting the leads/instrument impedance consists of both the real part and the imaginary part corresponding to the leads/instrument resistance and the leads/instrument inductance. With decreasing frequency, the effect of the leads/instrument inductance decreases, but naturally the resistive (ohmic) contribution remains the same. At very low frequencies, such as at a few Hz and below, the inductive part essentially disappears and only the real part from the leads/instrument resistance remains. Electrolyte transport properties are reflected typically in the high frequency EIS data, so the leads/instrument impedance needs to be accounted for. Information concerning the electrode kinetics is typically reflected in the low to intermediate frequency EIS data, and thus one generally needs to correct only for the ohmic part.

Therefore, no matter whether the electrolyte or the electrodes are investigated in an EIS study, subtraction of the leads/instrument impedance is necessary when the two-terminal method is used.

4.3.2 Analysis of Impedance Spectra Including Electrode, Grain Boundary and Grain Effects

The most general case but assuming simple resistor-capacitor elements is examined in what follows. At very high frequencies, the effects of grain resistance, R_g, and grain capacitance, C_g, may become observable. This will likely be the case at low temperatures when $R_g^2 C_g$ is large in relation (or comparable) to the leads/instrument inductance, L. The real and the imaginary parts of the impedance are given, respectively, by

$$\mathrm{Re}\, z(\omega) = R_l + \frac{R_g}{\left(1 + R_g^2 \omega^2 C_g^2\right)} + \frac{R_{gb}}{\left(1 + R_{gb}^2 \omega^2 C_{gb}^2\right)} + \frac{R_E}{\left(1 + R_E^2 \omega^2 C_E^2\right)} \tag{4.1}$$

where R_l is the leads/instrument resistance and

$$\mathrm{Im}\, z(\omega) = \omega \left[L - \frac{R_g^2 C_g}{\left(1 + R_g^2 \omega^2 C_g^2\right)} - \frac{R_{gb}^2 C_{gb}}{\left(1 + R_{gb}^2 \omega^2 C_{gb}^2\right)} - \frac{R_E^2 C_E}{\left(1 + R_E^2 \omega^2 C_E^2\right)} \right] \tag{4.2}$$

Equation (4.2) shows that $\mathrm{Im}\, z(\omega) \to 0$ as $\omega \to 0$. The corresponding real part is

given by

$$\mathrm{Re}\, z(\omega = 0) = R_l + R_g + R_{gb} + R_E \tag{4.3}$$

In what follows, we will assume that over some range of temperatures

$$L < R_g^2 C_g + R_{gb}^2 C_{gb} + R_E^2 C_E \tag{4.4}$$

Thus, there is a range of frequencies over which an arc exists above the x-axis in the plot of $-\mathrm{Im}\, z(\omega)$ vs. $\mathrm{Re}\, z(\omega)$, and at a sufficiently high angular frequency, we have

$$\left[L - \frac{R_g^2 C_g}{\left(1 + R_g^2 \omega^2 C_g^2\right)} - \frac{R_{gb}^2 C_{gb}}{\left(1 + R_{gb}^2 \omega^2 C_{gb}^2\right)} - \frac{R_E^2 C_E}{\left(1 + R_E^2 \omega^2 C_E^2\right)} \right] = 0 \tag{4.5}$$

If, however, $L > R_g^2 C_g + R_{gb}^2 C_{gb} + R_E^2 C_E$, no arc is observed above the x-axis. Such a situation can occur in a given system above a certain temperature. Typically, R_g, R_{gb} and R_E all exhibit an Arrhenius behavior and thus decrease with increasing temperature, while L is generally temperature independent. Equation (4.5) is a cubic equation in ω^2 and should have one real positive root, which we will denote by ω^{*2}. For angular frequencies above ω^* the $\mathrm{Im}\, z(\omega) > 0$, and will appear below the x-axis. Over the angular frequency range $\omega^* > \omega > 0$, the $\mathrm{Im}\, z(\omega) < 0$ and will appear as an arc above the x-axis. The general shape of the plot with $-\mathrm{Im}\, z(\omega)$ on the y-axis and $\mathrm{Re}\, z(\omega)$ on the x-axis is shown in Figure 4-4(a).

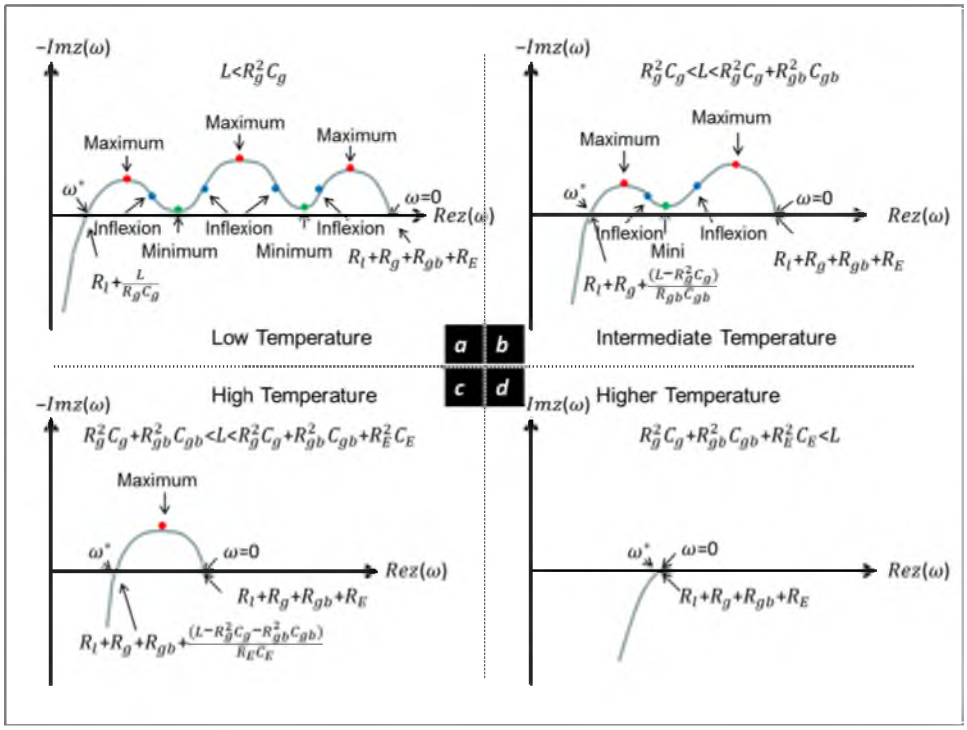

Figure 4-4: Schematics showing the expected impedance plot at different temperatures when grain, grain boundary and electrode effects can be described by parallel R-C circuits and when the time constants for the three processes are sufficiently far apart. (a): The impedance plot exhibits 3 maxima at low temperature. (b): The impedance plot exhibits 2 maxima at intermediate temperature. (c): The impedance plot exhibits 1 maximum at high temperature. (d): There is no arc above the x-axis at extremely high temperature.

The general shape of the impedance spectra over the range $\omega^* > \omega > 0$ is characterized by: (a) three maxima, (b) two minima, and (c) four inflexion points. These correspond to: (a) $\frac{d(-\mathrm{Im}\, z(\omega))}{d(\mathrm{Re}\, z(\omega))} = 0$, $\frac{d^2(-\mathrm{Im}\, z(\omega))}{d(\mathrm{Re}\, z(\omega))^2} < 0$; (b) $\frac{d(-\mathrm{Im}\, z(\omega))}{d(\mathrm{Re}\, z(\omega))} = 0$, $\frac{d^2(-\mathrm{Im}\, z(\omega))}{d(\mathrm{Re}\, z(\omega))^2} > 0$; and (c) $\frac{d^2(-\mathrm{Im}\, z(\omega))}{d(\mathrm{Re}\, z(\omega))^2} = 0$. As long as $\frac{d(\mathrm{Re}\, z(\omega))}{d\omega}$ is finite and nonzero, the above conditions may also be given as: (a) $\frac{d(-\mathrm{Im}\, z(\omega))}{d\omega} = 0$, $\frac{d^2(-\mathrm{Im}\, z(\omega))}{d\omega^2} < 0$; (b) $\frac{d(-\mathrm{Im}\, z(\omega))}{d\omega} = 0$, $\frac{d^2(-\mathrm{Im}\, z(\omega))}{d\omega^2} > 0$; and (c) $\frac{d^2(-\mathrm{Im}\, z(\omega))}{d\omega^2} = 0$. Depending upon the relative values of the various parameters and the range of frequencies, it is possible to have: (i) Three maxima, two minima, and four inflexion points; (ii) Two maxima, one minimum, and two inflexion points; (iii) One maximum, and one or two inflexion points; (iv) One maximum. (v) No maxima, no minima, and no inflexion points. This last situation corresponds to the case where the entire spectra appear below the x-axis. In what follows, we will first examine some limiting cases.

4.3.2.1 Low Temperature Range

Suppose the temperature is sufficiently low such that

$$L < R_g^2 C_g \tag{4.6}$$

(and thus also naturally $L < R_g^2 C_g + R_{gb}^2 C_{gb} + R_E^2 C_E$). We also assume that $R_E C_E >> R_{gb} C_{gb} >> R_g C_g$, which are the time constants, respectively, for the electrode, the grain boundary and the grain transport processes. This may lead to distinct arcs corresponding to electrode, grain boundary, and grain effects. The corresponding observed behavior will be that shown in Figure 4-4(a). If however the time constants are not sufficiently different for the three processes, overlapping spectra are expected and three distinct arcs may not be observed. When $\omega = 0$, the corresponding real part of the impedance is given by $\mathrm{Re}\, z(\omega = 0) = R_l + R_g + R_{gb} + R_E$, which is the same as equation (4.3). Assuming $R_E C_E >> R_{gb} C_{gb} >> R_g C_g$, at sufficiently high values of the angular frequency

$$\mathrm{Im}\, z(\omega) \approx \omega \left[L - \frac{R_g^2 C_g}{\left(1 + R_g^2 \omega^2 C_g^2\right)} \right] \tag{4.7}$$

in which we have substituted $R_E C_E \omega >> R_{gb} C_{gb} \omega >> 1$. Thus, the corresponding ω (which we will denote ω^*) at which $\mathrm{Im}\, z(\omega) = 0$ is given by

$$\left[L - \frac{R_g^2 C_g}{\left(1 + R_g^2 \omega^{*2} C_g^2\right)} \right] = 0 \tag{4.8}$$

The ω^* is thus the angular frequency at which capacitive and inductive parts of the impedance are equal in magnitude (but opposite in sign).

Thus

$$\omega^* = \frac{1}{R_g C_g}\sqrt{\frac{R_g^2 C_g - L}{L}} \tag{4.9}$$

The corresponding real part of the impedance is given by

$$\mathrm{Re}\, z(\omega^*) = R_l + \frac{L}{R_g C_g} \tag{4.10}$$

At angular frequencies $\omega > \omega^*$ given by equation (4.9), the impedance spectra appear below the x-axis. We expect the general expression for $-\mathrm{Im}\, z(\omega)$ to be described by equation (4.2) and the plot of $-\mathrm{Im}\, z(\omega)$ vs. $\mathrm{Re}\, z(\omega)$ given by Figure 4-4(a). Such a plot thus should exhibit three maxima, two minima and four inflexion points, assuming the frequency range is wide enough.

4.3.2.2 Intermediate Temperature Range

At some temperature (higher than for section 5.3.2.1), the relative value of the leads/instrument inductance may be such that $R_g^2 C_g < L < R_g^2 C_g + R_{gb}^2 C_{gb}$. The point $\omega = 0$ gives the real part, the same as equation (4.3), and $-\mathrm{Im}\, z(0) = 0$. As the angular frequency is increased, there will be a frequency at which

$$\mathrm{Im}\, z(\omega^*) = \omega^* \left[L - R_g^2 C_g - \frac{R_{gb}^2 C_{gb}}{\left(1 + R_{gb}^2 \omega^{*2} C_{gb}^2\right)} \right] = 0 \tag{4.11}$$

in which we have substituted $R_E C_E \omega >> 1 >> R_g C_g \omega$. The corresponding ω^* is given by

$$\omega^* = \frac{1}{R_{gb} C_{gb}} \sqrt{\frac{R_{gb}^2 C_{gb} + R_g^2 C_g - L}{L - R_g^2 C_g}} \tag{4.12}$$

and the corresponding real part of the impedance is given by

$$\mathrm{Re}\, z(\omega^*) = R_l + R_g + \frac{\left(L - R_g^2 C_g\right)}{R_{gb} C_{gb}} \tag{4.13}$$

At angular frequencies higher than ω^* given by equation (4.12), the impedance spectra appear below the x-axis. The plot of $-\mathrm{Im}\, z(\omega)$ vs. $\mathrm{Re}\, z(\omega)$ may likely exhibit two maxima, one minimum, and two inflexion points. Figure 4-4(b) shows a schematic.

We will now examine the minimum in $-\mathrm{Im}\, z(\omega)$ shown in Figure 4-4(b). The $\mathrm{Im}\, z(\omega)$ over the range of frequencies may be approximately given by

$$\mathrm{Im}\, z(\omega) = \omega \left[L - R_g^2 C_g - R_{gb}^2 C_{gb} - \frac{R_E^2 C_E}{1 + R_E^2 \omega^2 C_E^2} \right] \tag{4.14}$$

in which we have substituted $R_g^2 \omega^2 C_g^2 << R_{gb}^2 \omega^2 C_{gb}^2 << 1$. The minimum in $-\mathrm{Im}\, z(\omega)$ is given by

$$\frac{d\,\mathrm{Im}\,z(\omega)}{d\omega} = L - R_g^2 C_g - R_{gb}^2 C_{gb} + \frac{1}{C_E \omega^2} = 0 \tag{4.15}$$

which gives

$$\omega_{\min}^2 = \frac{1}{C_E\left(R_g^2 C_g + R_{gb}^2 C_{gb} - L\right)} \tag{4.16}$$

It is easily verified that equation (4.16) corresponds to a minimum in $-\mathrm{Im}\,z(\omega)$. Substitution for $\omega_{\min}^2$ into the equation for the real part of the impedance gives the real part of the impedance corresponding to the minimum by

$$\begin{aligned}\mathrm{Re}\,z(\omega_{\min}) = R_i + R_g &+ \frac{R_{gb} C_E \left(R_g^2 C_g + R_{gb}^2 C_{gb} - L\right)}{C_E\left(R_g^2 C_g + R_{gb}^2 C_{gb} - L\right) + R_{gb}^2 C_{gb}^2} \\ &+ \frac{R_E C_E \left(R_g^2 C_g + R_{gb}^2 C_{gb} - L\right)}{C_E\left(R_g^2 C_g + R_{gb}^2 C_{gb} - L\right) + R_E^2 C_E^2}\end{aligned} \tag{4.17}$$

Thus the arc length between $\omega = 0$ and $\omega = \omega_{\min}$ is given by

$$\begin{aligned}\mathrm{Re}\,z(\omega = 0) - \mathrm{Re}\,z(\omega = \omega_{\min}) = &\frac{R_{gb}^3 C_{gb}^2}{C_E\left(R_g^2 C_g + R_{gb}^2 C_{gb} - L\right) + R_{gb}^2 C_{gb}^2} \\ &+ \frac{R_E^3 C_E^2}{C_E\left(R_g^2 C_g + R_{gb}^2 C_{gb} - L\right) + R_E^2 C_E^2}\end{aligned} \tag{4.18}$$

Note that only if $R_E^2 C_E^2 >> \left(R_g^2 C_g + R_{gb}^2 C_{gb} - L\right) C_E >> R_{gb}^2 C_{gb}^2$, equation (18) reduces to R_E as the arc length.

4.3.2.3 Higher Temperature Range

At some higher temperatures (higher than for section 5.3.2.2), the relative value of the leads/instrument inductance may be such that $R_g^2 C_g + R_{gb}^2 C_{gb} < L < R_g^2 C_g + R_{gb}^2 C_{gb} + R_E^2 C_E$ The point $\omega = 0$ still gives the real part the same as equation (4.3) and the $-\operatorname{Im} z(0) = 0$. As the angular frequency is increased, there will be a frequency at which

$$\operatorname{Im} z(\omega^*) = \omega^* \left[L - R_g^2 C_g - R_{gb}^2 C_{gb} - \frac{R_E^2 C_E}{1 + R_E^2 \omega^{*2} C_E^2} \right] = 0 \tag{4.19}$$

in which we have substituted $R_g C_g \omega << R_{gb} C_{gb} \omega << 1$. The corresponding ω^* is given by

$$\omega^* = \frac{1}{R_E C_E} \sqrt{\frac{R_E^2 C_E + R_{gb}^2 C_{gb} + R_g^2 C_g - L}{L - R_g^2 C_g - R_{gb}^2 C_{gb}}} \tag{4.20}$$

The corresponding real part is given by

$$\operatorname{Re} z(\omega^*) = R_l + R_g + R_{gb} + \frac{L - R_g^2 C_g - R_{gb}^2 C_{gb}}{R_E C_E} \tag{4.21}$$

A plot of $-\mathrm{Im}\, z(\omega)$ vs. $\mathrm{Re}\, z(\omega)$ will likely exhibit one maximum, no minima, and no inflexion points. Figure 4-4(c) shows a schematic.

4.3.2.4 An Even Higher Temperature Range

Suppose the leads/instrument inductance, L, is such that

$$L > R_g^2 C_g + R_{gb}^2 C_{gb} + R_E^2 C_E \tag{4.22}$$

a situation that may occur at rather high temperatures. In such a case, the entire impedance curve lies below the x-axis – no arc is seen above the x-axis. When $\omega = 0$, the $-\mathrm{Im}\, z(\omega) = 0$ and the corresponding real part of the impedance is given by

$$\mathrm{Re}\, z(\omega = 0) = R_l + R_g + R_{gb} + R_E \tag{4.23}$$

which is the same as equation (4.3). Also, therefore, in this case $\omega^* = 0$. Thus, assuming data can be realistically obtained at very low frequencies ($\omega \to 0$), the corresponding intercept on the x-axis corresponds to the total resistance including all components regardless of the relative values of the various parameters. Figure 4-4(d) shows a schematic. Thus, in the event that with increasing temperature the arc above the x-axis completely disappears, the corresponding intercept as $\omega \to 0$ is still the total resistance.

4.3.3 Interpretation of the Experimental Results

In light of the preceding analysis, we will now examine the impedance spectra in Figure 4-3(a) and Figure 4-3(b) obtained on a GDC sample measured over a temperature range from 400°C to 675°C in air and over a frequency (f) range from 0.1 Hz to 1 MHz using the two-terminal method. Up to 525°C, almost the entire spectra are above the x-axis. This means up to 525°C, the ω^* is greater than the maximum angular frequency at which measurements were made, that is, for temperatures up to 525°C, $\omega^* > 2\pi \times 10^6$. Above 525°C, part of the measured spectra lie below the x-axis, and thus above 525°C, $\omega^* < 2\pi \times 10^6$. The spectra also show that up to 600°C, a distinct high frequency arc can be seen. Thus, over the range of frequencies investigated, between about 425°C and 600°C, the observed spectra contain one maximum, one minimum, and two inflexion points. Thus, over the range of experimental parameters (both the sample and the testing parameters), the low temperature case (section 5.3.2.1, Figure 4-4(a)) is not observed. Over the temperature range from 400°C to 600°C, the observed spectra correspond to section 5.3.2.2 (Figure 4-4(b)), in which $R_g^2 C_g < L < R_g^2 C_g + R_{gb}^2 C_{gb}$. Spectra at 650°C and 675°C do not exhibit a high frequency arc.

Over the temperature range from 400°C to 600°C, the high frequency arc is clearly visible. As stated earlier, the highest angular frequency at which measurements were made was $\omega_{\max} = 2\pi \times 10^6$ s^{-1} in all experiments. Over the temperature range from 400°C to 450°C the entire spectra are above the x-axis. This means the corresponding $\omega^* > \omega_{\max}$. The ω^* thus may be obtained by extrapolation. Also, extrapolation to the x-axis gives the corresponding real part which is identified with

$\mathrm{Re}\, z(\omega^*) = R_l + R_g + \frac{\left(L - R_g^2 C_g\right)}{R_{gb} C_{gb}}$, namely equation (4.13). Over the temperature range 450°C to 600°C, the high frequency arc can be seen and at the same time some of the data lie below the x-axis. In these cases, $\omega^* < \omega_{\max}$. The real part of the impedance corresponding to ω^* is again given by equation (4.13).

At 650°C and 675°C, no high frequency arc is observed. This temperature thus corresponds to the range $R_g^2 C_g + R_{gb}^2 C_{gb} < L < R_g^2 C_g + R_{gb}^2 C_{gb} + R_E^2 C_E$. This corresponds to section 5.3.2.3, Figure 4-4(c). The real part of the impedance corresponding to ω^* is thus given by $\mathrm{Re}\, z(\omega^*) = R_l + R_g + R_{gb} + \frac{\left(L - R_g^2 C_g - R_{gb}^2 C_{gb}\right)}{R_E C_E}$ which is equation (4.21). In view of the fact that the electrode effects cannot be adequately described by a parallel $R_E - C_E$ circuit element, the applicability of equation (4.21) to the present data may only be treated as being approximate.

4.3.4 Simulation and Data Fitting

Experimental results shown in Figure 4-3(a) and Figure 4-3(b) were analyzed using the simple equivalent circuit in which electrode, grain boundary and grain processes are described using parallel $R-C$ circuits. The fitting of the electrode effects by a parallel $R_E - C_E$ circuit is not accurate since clearly the electrode arc is not semicircular. The primary focus of the fitting, however, is the high frequency regime – namely grain boundary and grain. Also, it was assumed that the grain capacitance C_g is very small over the range of frequencies and thus can be set to zero (actually, this means $L >> R_g^2 C_g$). This assumption, however, is not expected to be valid at lower

temperatures. Thus, the simulation does not include the low temperature section 5.3.2.1, which was not observed in the present work.

Table 4-1 gives the experimental values and the fitted values of the various parameters over a range of temperatures between 400°C and 700°C in 50 degree intervals. Experimental data in Figure 4-3 correspond to one minimum below 600°C (the schematic corresponding to Figure 4-4(b)). This minimum corresponds to section 5.3.2.2, the intermediate temperature case. The corresponding $\omega_{\min}^2$ is given by equation (4.16). Table 4-1 shows the values of L, R_l, R_g, R_{gb}, C_{gb}, R_E and C_E (with C_g assumed to be zero). Note that the L is essentially independent of temperature (it very slightly decreases with increasing temperature) and R_l slightly increases with increasing temperature. Table 4-1 also lists $\omega_{\min}$ over the temperature range from 400°C to 600°C. At 650°C and above, which corresponds to section 5.3.2.3, no high frequency arc is observed, and $\omega_{\min}^2 < 0$, which means no minimum exists (that is at and above 650°C, $L > R_{gb}^2 C_{gb}$). The values of the various parameters in Table 4-1 indeed show that at and above 650°C, $L > R_{gb}^2 C_{gb}$. The estimated values of R_E and C_E from the simulation are very close to the set values of R_E and C_E.

Figure 4-5(a) through Figure 4-5(f) are the simulated EIS spectra over the temperature range 400°C to 650°C in 50 degree intervals and over the frequency range from 0.1 Hz to 10^6 Hz. Also shown in each of the figures (from Figure 4-5(a) through Figure 4-5(e)) is an inset corresponding to the minimum in $-\mathrm{Im}\, z(\omega)$ corresponding to $\omega_{\min}$.

Table 4-1: Simulation of impedance spectra and fitting to EIS spectra given in Figure 4-3.

T (°C)	L (nH)	R_L (Ω)	R_g (Ω)	C_g (nF)	R_{gb} (Ω)	C_{gb} (nF)	τ_{gb} (μs)
400	882	3.68	28.4	0	364	34.7	12.6
450	874	3.78	10.8	0	107	33.3	3.56
500	871	3.88	4.69	0	41	30.9	1.26
550	866	4.01	2.37	0	18.4	34.5	0.634
600	861	4.10	2.06	0	8.32	38.2	0.318
650	858	4.20	2.16	0	3.4	66.2	0.225

T (°C)	Set R_e (Ω)	Set C_e (mF)	τ_e (s)	Simulated Real(Z) (Ω)	Measured Real(Z) (Ω)	ω (kHz)
400	2.6k	0.81	2.13	396	413	0.52
450	577	1.86	1.07	122	129	1.19
500	229	4	0.915	49.6	51.4	2.21
550	141	5.52	0.776	24.7	24.8	4.1
600	82.5	7.09	0.585	14.5	13.4	8.89
650	36	9.4	0.338			

T (°C)	**Simulated R_e (Ω)**	**Simulated C_e (mF)**	**ΔR_e (%)**	**ΔC_e (%)**
400	2.6k	0.81	-1.5	-0.19
450	584	1.86	1.22	0.29
500	232	4.01	1.56	0.09
550	139	5.52	-1.2	-0.15
600	83.6	7.1	1.34	0.04

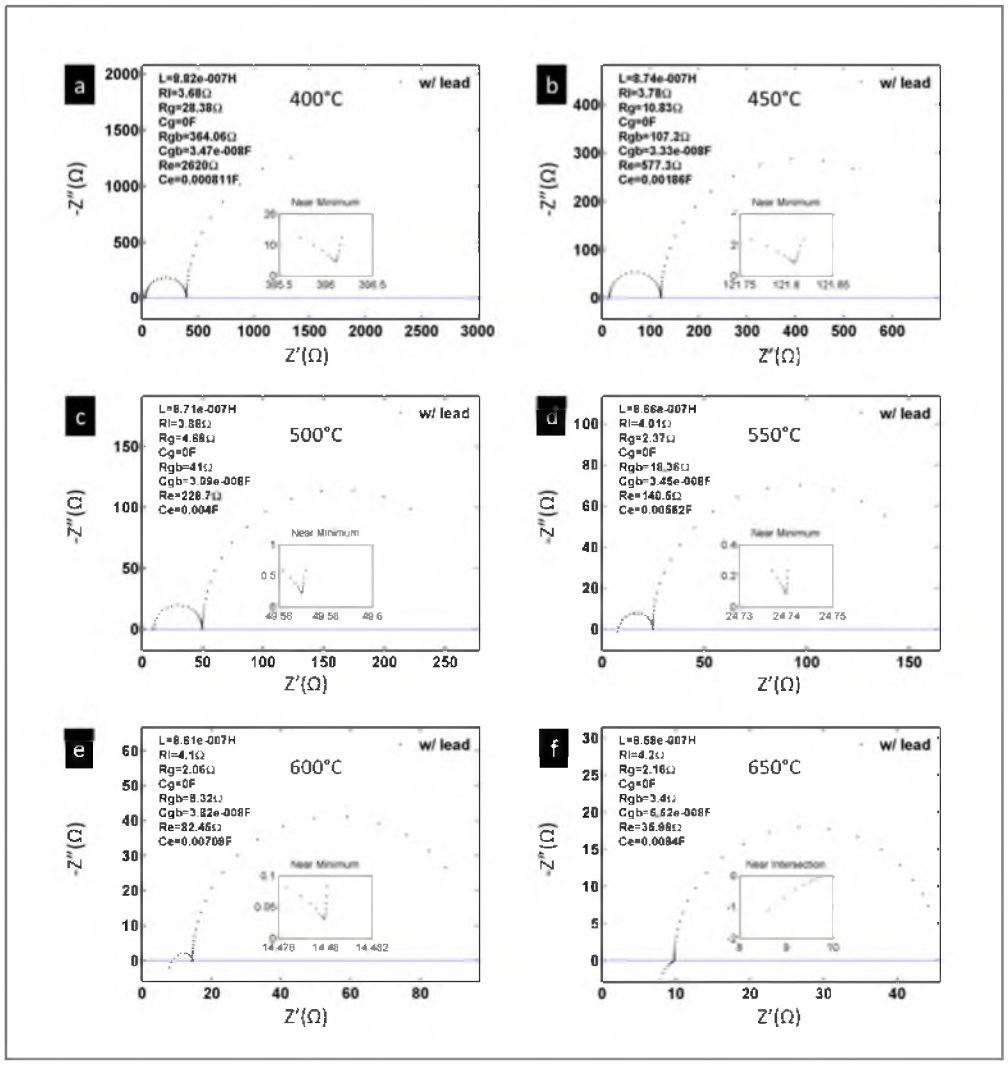

Figure 4-5: Simulated impedance spectra: (a): 400°C, (b): 450°C, (c): 500°C, (d): 550°C, (e): 600°C, and (f): 650°C.

From each of the minima, the corresponding $\mathrm{Re}\,z(\omega_{\min})$ was estimated, also shown in the insets. The experimental values of $\mathrm{Re}\,z(\omega_{\min})$ were determined from the measured spectra given in Figure 4-3(a) and Figure 4-3(b). These values are also listed in Table 4-1. The agreement between the two is very good. In Figure 4-5(f), which shows spectra at 650°C, no high frequency arc is observed. The inset shows an enlarged view of

the data near the intersection with the x-axis.

Table 4-1 also lists the values of R_g and R_{gb} as a function of temperature. The R_g varies between ~28.8 Ω at 400°C and ~2.04 Ω at 575°C. Over the same range of temperatures, the R_{gb} varies between ~364 Ω and 11.94 Ω. These results show that even at 575°C, the R_{gb} is greater than R_g. Above about 600°C, the R_g appears to be independent of temperature. But this observation is related to inaccuracies in the measurements (errors involved in the removal of the leads impedance). It is the expectation that both R_g and R_{gb} will continue to decrease with increasing temperature. In order to improve the accuracy of measurements, one would need to use samples of larger total resistance (smaller electrode area and/or thicker samples) compared to the ones used in the present work. The R_{gb} continues to decrease with increasing temperature. There likely are greater uncertainties in both values above 600°C. The observation, however, that even at a temperature as high as 650°C the R_{gb} is comparable to (or greater than) R_g implies that the absence of a high frequency arc in the measured spectra (when not corrected for the leads/instrument impedance) cannot be interpreted to mean that the grain boundary resistance is negligible compared to the grain resistance.

Table 4-1 shows that the C_{gb} is essentially independent of temperature over the range 400°C to 600°C, and seems to increase slightly above 600°C. This apparent increase in C_{gb} at higher temperatures is again related to the inaccuracies in the measurements and samples of appropriate geometries will be required to obtain accurate values of all three parameters, namely R_g, R_{gb} and C_{gb}. The C_{gb} is expected to be essentially independent of temperature over a very wide range since impurity and dopant profiles near the grain

boundaries and the associated space charge effects are practically frozen in from the sintering temperature [9-12].

As stated earlier, the electrode effects cannot be accurately described by a parallel R-C circuit element given the nature of many complex processes that occur at the electrodes, such as gas phase diffusion through porous electrodes, adsorption and dissociation of O_2 molecules, electron transfer corresponding to the oxygen reduction reaction (ORR) as well as the oxygen ion oxidation reaction (the reverse of ORR), and the incorporation/extraction of O^{2-} at the electrode/electrolyte interface (typically at three phase boundaries, TPBs). However, if electrode effects can be adequately described in any given system by a parallel R-C circuit, the present work shows that it may be possible to obtain both R_E and C_E from the minimum in $-\mathrm{Im}\, z(\omega)$ when it is impractical to make measurements at ultralow angular frequencies. Table 4-1 compares the estimated values of R_E and C_E from the minima in $-\mathrm{Im}\, z(\omega)$ with those used in the simulations. It is observed that the error in R_E is typically less than 2% and that in C_E is much lower. In the present work, measurements were made at frequencies ≥ 0.1 Hz, which precluded the estimation of the R_E from the arc length. Thus, the values of electrode parameters, namely R_E and C_E, were obtained from the minimum, especially at lower temperatures. An examination of Figure 4-3(a) and Figure 4-3(b) shows that if the low frequency arcs are extrapolated to zero angular frequency (to the x-axis), the values obtained for R_E are on the same order of magnitude as selected for the simulation and the ones estimated from the minima in $-\mathrm{Im}\, z(\omega)$. Although these estimates are not expected to be accurate, some conclusions may nevertheless be drawn from the values obtained for R_E and C_E.

Over the temperature range from 400°C and 600°C, the R_E varies between 2620 Ω and 82.45 Ω, or by a factor of ~31, clearly showing that the overall electrode reaction exhibits a strong temperature dependence. It is well known that the reaction of charge transfer, described by such models as the Butler-Volmer equation, is usually thermally activated, and a strong temperature dependence is to be expected, as observed here. The other temperature-dependent processes which affect R_E include gas phase adsorption and dissociation. Indeed, in the original landmark paper by Bauerle [1], the resistance describing the electrode reaction exhibited a thermally activated behavior. Over the same range of temperatures, the electrode capacitance, the C_E varies from 8.11 x 10^{-4} f at 400°C to 7.09 x 10^{-3} f at 600°C. That is the C_E varies by ~9 times. Such a large variation in C_E is consistent with the nature of processes that occur at the electrodes. One of the important processes that occur at the electrolyte/electrode interface is that of O_2 adsorption and its dissociation. This determines the surface coverage of adsorbed O_2 (or O) and thus would dictate the overall charge transfer reaction. The temperature dependence of the adsorption and dissociation processes would thus be expected to affect the C_E resulting in a temperature dependence of C_E. Thus, unlike the grain boundary capacitance, C_{gb}, which is expected to be essentially temperature-independent, the electrode capacitance, C_E, would likely exhibit temperature dependence. As stated earlier, the description of electrode effects by a parallel resistor-capacitor circuit element is an oversimplification. In principle, however, it should be possible to develop similar analysis as given here but with a realistic circuit element for the electrodes (e.g., CPE). If this can be done, it may be possible to estimate the electrode parameters from the analysis

of the minima in $-\mathrm{Im}\,Z(\omega)$ vs. ω; that is from $\omega_{\min}$.

The analysis given here assumes that the time constants for the three processes, namely, grain, grain boundary and electrode, are sufficiently far apart so that impedance spectra should exhibit distinct arcs. In the simulation, the grain capacitance, C_g was set to zero, that is, its time constant was set to zero. From the values of R_E and C_E, the estimated time constant for the electrode process, $\tau_E = R_E C_E$, varies between ~2.12 s at 400°C and ~0.59 s at 600°C. Similarly, from the values of R_{gb} and C_{gb}, the estimated time constant for the grain boundary process, $\tau_{gb} = R_{gb} C_{gb}$, varies between ~1.26 x 10^{-5} s at 400°C and ~3.18 x 10^{-7} s at 600°C. Clearly, the time constants for the electrode and the grain boundary processes are sufficiently far apart which should lead to distinct arcs. This also means that the disappearance of the high frequency arc at high temperatures is not related to any overlapping spectra, but is rather related to a large contribution from the leads/instrument inductive effects.

The typical electrode thickness was about 25 microns. Also, the electrodes exhibited a sufficiently high level of porosity (typically ~30% based on prior work). The approximate estimate of the time constant (not strictly a time constant as the corresponding differential equation does not lead to a single time constant) for gas diffusion through the porous electrodes is estimated to be less than 0.01 s. The origin of the estimated long time constants for the electrode processes probably lies in sluggish electrode reaction of charge transfer (including adsorption, dissociation and charge transfer).

4.3.5 A Comparison Between Subtraction and Cutoff

The measured impedance spectra at 600°C given in Figure 4-2(b) are reproduced in Figure 4-6(a) along with the equivalent circuit used for fitting (the high frequency regime). The inductive effects at high frequencies are clearly seen in the figure. In Figure 4-6(b), the data below the x-axis are cutoff and an arc is fit to the data using a CPE. Note that the arc is not semicircular, as expected due to the presence of inductive effects. In accord with the equivalent circuit analysis given, the high frequency intercept is given approximately by $R_l + R_g + \frac{L}{R_{gb}C_{gb}}$. The magnitude of the intercept from Figure 4-6(b) is ~8.45 Ω. The magnitude of the intercept estimated using values from Table 4-1 is ~8.87 Ω showing good agreement. The low frequency intercept from Figure 4-6(b) is ~13.95 Ω. The value of the low frequency intercept estimated from Table 4-1 is ~14.48 Ω, again showing good agreement. The arc length from the extrapolation of the data is ~5.5 Ω, while that based on values from Table 4-1 is ~5.61 Ω, which shows very good agreement.

Figure 4-6(c) shows the high frequency data from which the measured leads/instrument impedance was subtracted. As seen in the figure, the entire spectra now lie above the x-axis. In Figure 4-6(d) the high frequency part of the arc from Figure 4-6(c) is reproduced, and to which a semicircular arc is fitted. Note that the arc can be fitted to a semicircle quite well. The high frequency intercept in Figure 4-6(d) is identified with R_g. From Figure 4-6(d), the estimated value of R_g is ~2.15 Ω. From Table 4-1, the value of R_g is ~2.06 Ω, showing very good agreement. The low frequency intercept in Figure 4-6(d) is identified with $R_g + R_{gb}$, whose magnitude is ~10.3 Ω. From Table 4-1, the

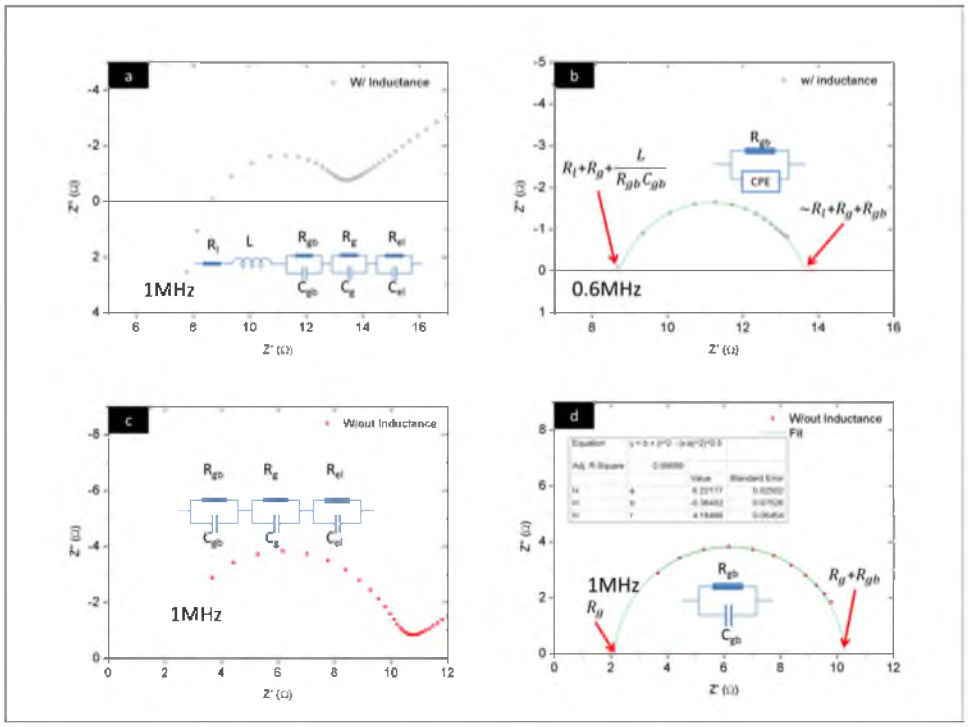

Figure 4-6: Comparison between leads/instrument impedance subtraction and inductive cutoff, as well as between capacitance-fitting and CPE-fitting. (a): The high frequency regime of the measured impedance with large Pt electrodes at 600°C. (b): The high frequency arc from (a) after cutting off the data below the x-axis. The arc is not semicircular and was fitted with a CPE. (c): The high frequency arc from (a) after subtracting the leads/instrument impedance. (d): The high frequency arc from (c). The arc could be accurately fitted as a semicircle.

estimated value of $R_g + R_{gb}$ is ~10.38 Ω, again showing very good agreement. The preceding shows that after subtraction of the leads/instrument impedance, the high frequency data, which represent grain and grain boundary effects, can be well represented by a parallel $R_{gb} - C_{gb}$ circuit element.

4.3.6 CPE Fits to Low Frequency Data

Figure 4-3(e) (650°C) and Figure 4-3(f) (675°C) are reproduced, respectively, as Figure 4-7(a) and Figure 4-7(b). The points in black correspond to the as-measured data. The points in red correspond to the data after subtracting the leads/instrument impedance. The high frequency semicircular arcs are well resolved once the leads/instrument impedance is removed. Figure 4-7(c) and Figure 4-7(d) show the corresponding simulated spectra in which the low frequency electrode effects are described by a CPE. The corresponding parameters are given in Table 4-2. As seen, the simulated spectra are in good agreement with the observed ones. However, as stated earlier, two parameters are needed for a CPE fit unlike a capacitor which requires only one. While the fits with a CPE can be well matched with the experimental data, physical interpretation is often elusive. It would appear that equivalent circuit elements that represent relevant physical/chemical phenomena are necessary. Results of fitting with a CPE are given only to demonstrate that electrode effects can be adequately fitted with a parallel CPE-resistor circuit.

Table 4-2: Parameters used for fitting data at 650°C and 675°C from Figure 4-3 using a CPE for the low frequency arc. The CPE fits to the data are shown in Figure 4-7(a) and Figure 4-7(b).

T (°C)	L (H)	R_L (Ω)	R_g (Ω)	R_{gb} (Ω)	R_e (Ω)	C_{gb} (F)	CPE-T	CPE-P
650	8.58E-7	4.2	2.16	3.4	35.99	6.62E-8	9.4E-3	0.48
675	8.57E-7	4.25	2.28	1.88	22.24	1.2E-7	0.01	0.51

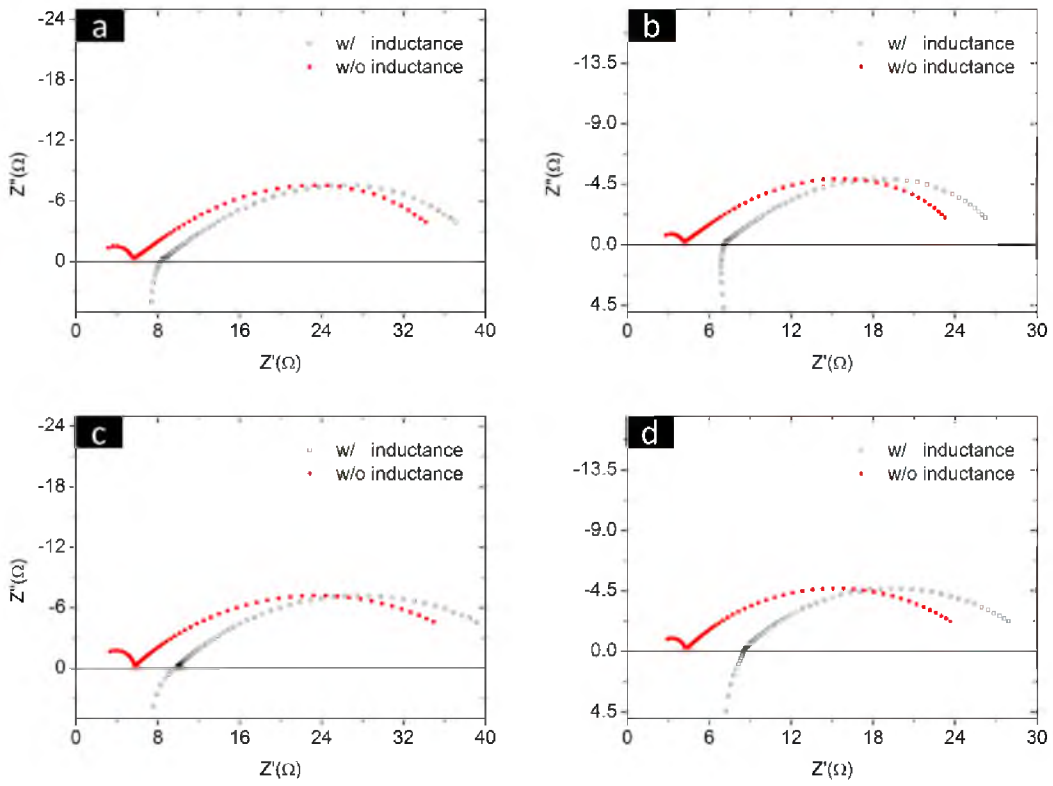

Figure 4-7: EIS spectra at 650°C and 675°C. (a) 650°C measured spectra and after subtracting the leads/instrument impedance. (b) 675°C measured spectra and after subtracting the leads/instrument impedance. (c) 650°C simulated spectra (with a CPE) with and without the leads/instrument impedance. (d) 650°C simulated spectra (with a CPE) with and without the leads/instrument impedance.

4.3.7 Estimation of Grain and Grain Boundary Parameters

In order to determine R_g, R_{gb}, and C_{gb}, the leads/instrument impedance was subtracted from the measured impedance spectra. Each of the high frequency arcs, once the leads/instrument impedance was subtracted out (Figure 4-3), could be adequately described by a semicircle. In all cases, the semicircular arcs were extrapolated to the x-axis. The high frequency intercept of the semicircle corresponds to the grain resistance, R_g, and the low frequency intercept corresponds to the grain + grain boundary

resistance, $R_g + R_{gb}$ [1]. The corresponding Arrhenius plots, namely, $\ln\left(\frac{R_g}{T}\right)$ vs. $\frac{1000}{T}$ and $\ln\left(\frac{R_{gb}}{T}\right)$ vs. $\frac{1000}{T}$, are shown in Figure 4-8. In Figure 4-8(a) and Figure 4-8(b) first the raw data are shown on Arrhenius plots, from which the leads/instrument impedance was not subtracted out. The data exhibit a linear behavior on the Arrhenius plots only up to a temperature of ~500°C. Above 500°C, the high frequency arc is not clearly resolved in the impedance spectra. This reflects as an apparent deviation from the linear behavior on the Arrhenius plots and the corresponding error is ~20 Ω. It is to be noted that the non-removal of the leads/instrument impedance means that despite Arrhenius-like behavior below 500°C, the measured activation energies likely contain errors related to the non-removal of the leads/instrument impedance.

Figure 4-8(c) and Figure 4-8(d) show the same data after subtracting the leads/instrument impedance. The linear behavior on Arrhenius plots is now preserved up to a temperature of 600°C and the corresponding error level is reduced to ~2 Ω. The data shown in Figure 4-8(a) through Figure 4-8(d) were obtained on a sample with large platinum electrodes (15.8 mm diameter) and with platinum leads. Finally, Figure 4-8(e) and Figure 4-8(f) show data obtained using small platinum electrodes (4.8 mm diameter) and with silver leads, after subtracting out the leads/instrument impedance. The linear behavior is now observed up to ~675°C and the error level is further reduced to ~6 Ω. It is to be noted that on a relative basis an error of 6 Ω with smaller electrodes is actually lower than an error of 2 Ω with larger electrodes.

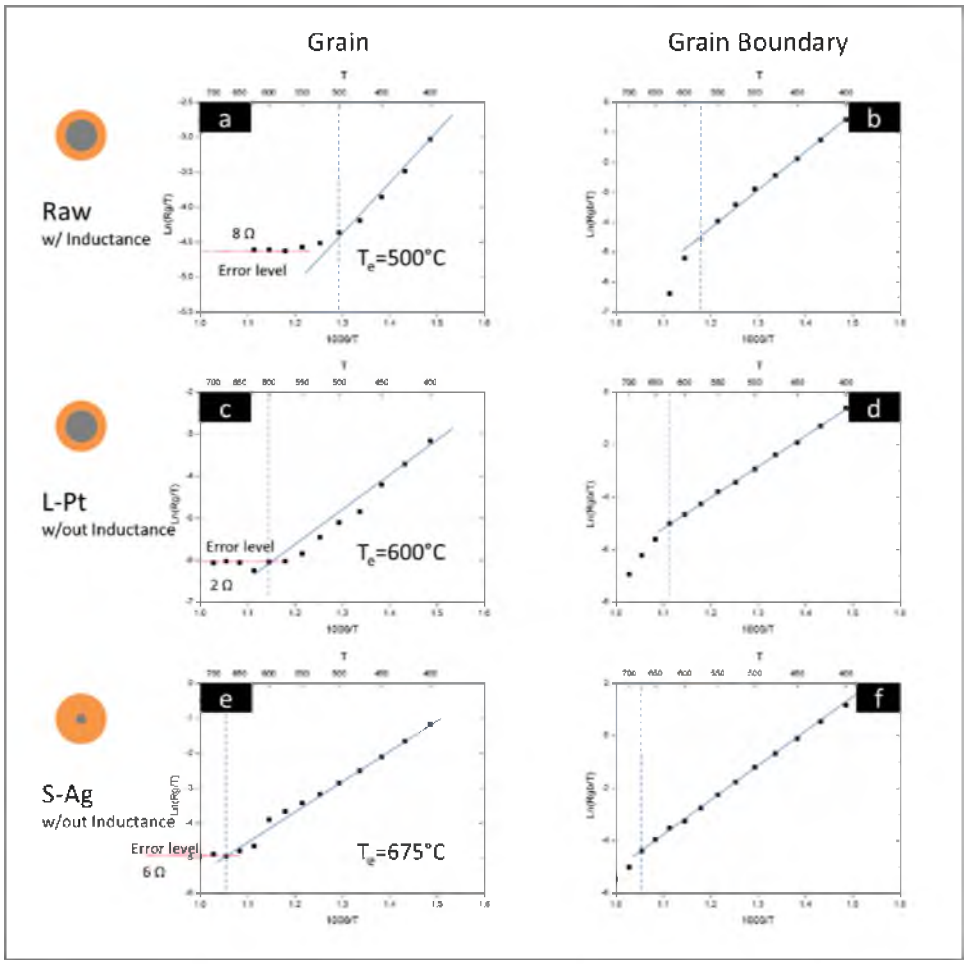

Figure 4-8: Arrhenius plots corresponding to $\ln\left(\frac{R_g}{T}\right)$ vs. $\frac{1000}{T}$ (a, c, e) and $\ln(\frac{R_{gb}}{T})$ vs. $\frac{1000}{T}$ (b, d, f) where R_g is the grain resistance and R_{gb} is the grain boundary resistance. (a) and (b) correspond to the intercepts obtained with large Pt electrodes and Pt leads without subtracting the leads/instrument impedance. (c) and (d) correspond to the intercepts obtained using data from (a) and (b) but after subtracting the leads/instrument impedance. (e) and (f) correspond to the intercepts obtained with small Pt electrodes and Ag leads after subtracting the leads/instrument impedance.

The present results thus show that by a suitable choice of a sample geometry and subtracting the leads/instrument impedance, the high frequency arc could be recovered and could be fitted well to a semicircle consistent with the description of the grain boundary effects using a resistor and a capacitor, as originally shown by Bauerle in his landmark paper [1]. It should be further possible to choose a sample of an appropriate geometry to increase its resistance relative to the leads/instrument impedance and extend the linear regime of the Arrhenius plots to even higher temperatures.

The data from Figure 4-8(a), Figure 4-8(c) and Figure 4-8(e) can be fitted to [1]

$$R_g = R_g^o T \exp\left(\frac{Q_g}{k_B T}\right) \tag{4.24}$$

for describing the temperature dependence of the grain resistance with R_g^o as the pre-exponent (units of ΩK^{-1}) and Q_g as the activation energy. Similarly, data from Figure 4-8(b), Figure 4-8(d) and Figure 4-8(f) can be fitted to

$$R_{gb} = R_{gb}^o T \exp\left(\frac{Q_{gb}}{k_B T}\right) \tag{4.25}$$

for describing the temperature dependence of the grain boundary resistance with R_{gb}^o as the pre-exponent (units of ΩK^{-1}) and Q_{gb} as the activation energy. The data obtained with small electrodes and silver wires correspond to the largest linear range on the Arrhenius plots. For the sample with large electrodes (Figure 4-8(c) and Figure 4-8(d)),

the corresponding values were estimated to be: R_g^o = 1.2275 x 10^{-7} ΩK^{-1} and Q_g = 0.73 eV for the grain resistance and R_{gb}^o = 1.3684 x 10^{-8} ΩK^{-1} and Q_{gb} = 1.01 eV for the grain boundary resistance. For the sample with small electrodes (Figure 4-8(e) and Figure 4-8(f)), the corresponding values were estimated to be: R_g^o = 2.0148 x 10^{-6} ΩK^{-1} and Q_g = 0.69 eV for the grain resistance and R_{gb}^o = 1.5741 x 10^{-8} ΩK^{-1} and Q_{gb} = 1.11 eV for the grain boundary resistance. The measured activation energies are compared with literature values in Table 4-3 [13]. The values of the activation energies determined in the present work from samples with small electrodes, namely Q_g = 0.69 eV and Q_{gb} = 1.11 eV, are deemed more accurate than those measured using larger electrodes.

Table 4-3: Activation energies

	Q_g (eV)	Q_{gb} (eV)
Raw	0.67	1.05
L-Pt	0.73	1.01
L-Ag	0.7	1.03
S-Ag	0.69	1.11
Literature [13]	0.78	0.8-1

From equations (4.24) and (4.25), one may estimate grain and grain boundary resistances of the samples at other temperatures. At 800°C, the estimated values of the grain resistance (small electrodes) is 3.764 Ω and that of the grain boundary resistance is 2.762 Ω. Thus, approximately ~58% of the resistance at 800°C is attributed to the grain resistance and ~42% of the resistance is attributed to the grain boundary resistance. At lower temperatures, the contribution of the grain boundary resistance will be even greater. Thus, the present work shows that in order to lower the electrolyte resistance, it is necessary to reduce the grain boundary contribution. The main contributors to grain boundary resistance are the grain size (the smaller the grain size, the higher is the grain boundary contribution to the total resistance) and space charge effects. Note that the sample grain size in the present work was rather small, ~1.1 μm.

From the high frequency semicircle, the grain boundary capacitance can be obtained from the maximum in $-\mathrm{Im}\, z(\omega)$. This is given by [1]

$$C_{gb} = \frac{1}{\omega_m R_{gb}} \tag{4.26}$$

where ω_m is the angular frequency at which $-\mathrm{Im}\, z(\omega)$ is a maximum.

The C_{gb} determined using the data obtained with Pt and Ag leads with large Pt electrodes and Ag leads with small Pt electrodes are plotted in Figure 4-9 vs. the measurement temperature. The data obtained with large electrodes show an increase with increasing temperature above about 600°C. This, however, is attributed to errors associated with the incomplete removal of the leads/instrument impedance which results

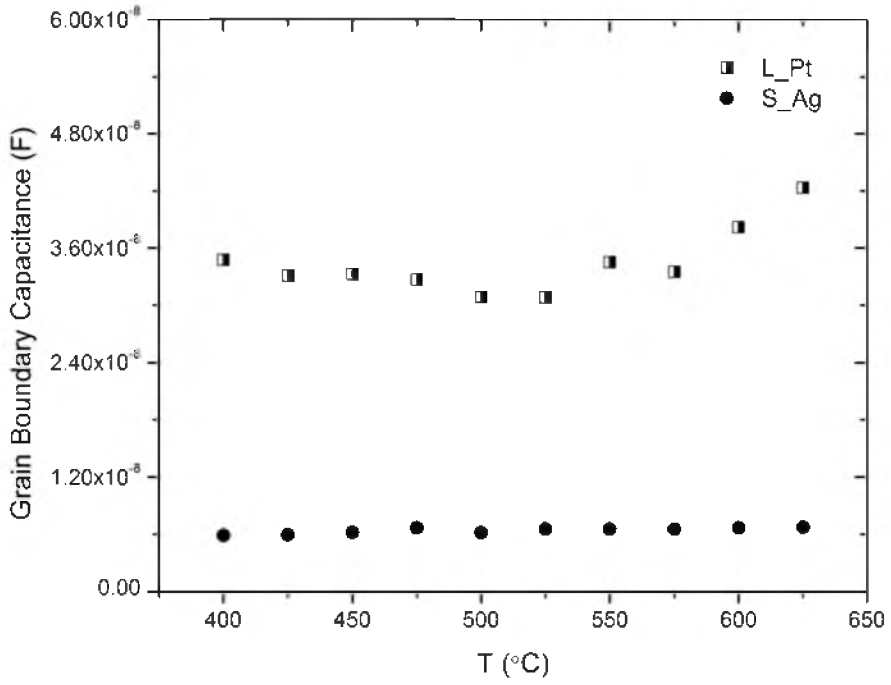

Figure 4-9: Grain boundary capacitance, C_{gb}, obtained by fitting to the high frequency semicircle. L_Pt corresponds to the sample with large electrodes and measured using Pt leads; S_Ag corresponds to the sample with small Pt electrodes and measured using Ag leads.

in significant errors in resolving the spectra at higher temperatures for the aforementioned reasons. The data obtained with small electrodes, however, show that the measured grain boundary capacitance is essentially independent of temperature over the range of temperatures over which data were obtained. This is consistent with expectations in that the grain boundary capacitance is likely determined by the grain boundary structure and chemistry [9-12], which is virtually frozen in at low temperatures over which the measurements were made. Figure 4-8 and Figure 4-9, respectively, give absolute values

of R_g & R_{gb} and C_{gb} instead of area specific values. The difference in the capacitance values for electrodes of smaller and larger diameters are in part due to the sizes of the electrodes. There is also an edge effect, because of which neither the capacitance nor the resistance values scale exactly with the form factors (ratio of the electrode area to the sample thickness) of the electrodes.

4.4 Summary

EIS measurements were made on GDC disc-shaped samples with Pt electrodes of two different sizes; 4.8 mm in diameter and 15.8 mm diameter. Measurements were made over a range of temperatures between 400°C and 675°C in 25 degree intervals. Above ~500°C, the high frequency spectra of the samples appeared to be flattened semicircles. At 650°C and 675°C, no high frequency arcs were observed. Also, a significant portion of the measured impedance at high frequencies was below the x-axis consistent with a significant contribution from the leads/instrument inductance. The leads/instrument impedance was separately measured by shorting the lead wires without the sample. Once the lead impedance was subtracted from the measured total (sample + leads/instrument) impedance, the high frequency arcs could be recovered at the highest measurement temperature of 675°C. Also, the arcs could be fitted accurately with a semicircle in each case, consistent with the corresponding equivalent circuit being a resistor and a capacitor in parallel corresponding to transport across the grain boundaries. From the measurements, after subtracting the leads/instrument impedance, the grain resistance, R_g, the grain boundary resistance, R_{gb}, and the grain boundary capacitance, C_{gb}, could be resolved. The grain resistance and the grain boundary resistance exhibited thermally

activated behavior with the corresponding activation energies of $Q_g \cong 0.69$ eV and $Q_{gb} \cong 1.11$ eV, respectively. The grain boundary capacitance was essentially independent of temperature. The present work underscores the importance of subtracting the leads/instrument impedance [2-4]. Once the leads/instrument impedance is subtracted out, the high frequency arc could be accurately fitted with a capacitor (one parameter) and a resistor, and it was not necessary to use a CPE (which requires two fitting parameters).

The as-measured spectra were also fitted to a simple equivalent circuit in which grain, grain boundary, and electrode effects were represented by parallel R-C circuit elements. The representation of the electrode effects by a parallel R-C circuit is an over simplification. Nevertheless, many salient features of the observed spectra could be deduced by analyzing maxima of the $-\mathrm{Im}\, z(\omega)$ vs. $\mathrm{Re}\, z(\omega)$ plots as well as minima of the $-\mathrm{Im}\, z(\omega)$ vs. $\mathrm{Re}\, z(\omega)$ plots. It was shown that from the minima in $-\mathrm{Im}\, z(\omega)$ vs. $\mathrm{Re}\, z(\omega)$ plots, one can obtain parameters representing the equivalent circuit. Thus, in cases in which the experimental range is not sufficient to estimate the parameters from the maxima and the intercepts, such as for example R_E and C_E, approximate estimates may be obtained from the minima. The present work also shows that an apparent disappearance of the grain boundary arc in measured EIS spectra at high frequencies is likely the result of not having removed the leads/instrument impedance and cannot always be interpreted to mean that the grain boundary resistance is negligible in relation to the grain resistance. Also, the cathode impedance data often overlap with anode impedance data, and it is impossible to deconvolute any of the two electrode impedance from the whole sample impedance. Although people have use symmetric cell design or

side reference electrode to measure the impedance of any one of the two electrode, the results are not reliable. In the next chapter, a concept of embedded probe is introduced in order to conduct impedance measurement or potential measurement more accurately.

4.5 References

1. J. E. Bauerle, *J. Phys. Chem. Solids*, **30**, 2657–2670 (1969)

2. E. Barsoukov and J. R. Macdonald, *Impedance Spectroscopy*, John Wiley & Sons Inc. (2005)

3. A. Esquirol, N. P. Brandon, J. A. Kilner, and M. Mogensen, *J. Electrochem. Soc.*, **151**, A1847 (2004)

4. A. Samson, M. Sogaard, R. Knibbe, and N. Bonanos, *J. Electrochem. Soc.*, **158**, B650 (2011)

5. T. Suzuki et al., *J. Power Sources*, **199**, 170–173 (2012)

6. J. Wang, Y. Zhang, T. Liang, C. Deng, and J. Xu, *J. Power Sources*, **208**, 415–420 (2012)

7. W. Zając and J. Molenda, *Solid State Ionics*, **192**, 163–167 (2011)

8. W. Zajac, *Solid State Ionics*, **179**, 154–158 (2008)

9. K. Lehovec, *J. Chem. Phys.*, **21**, 1123–1128 (1953)

10. K. Kliewer and J. Koehler, *Phys. Rev.*, **140**, A1226 (1965)

11. X. Guo and J. Maier, *J. Electrochem. Soc.*, **148**, E121 (2001)

12. X. Guo, W. Sigle, and J. Maier, *J. Am. Ceram. Soc.*, **86**, 77–87 (2003)

13. B. Steele, *Solid State Ionics*, **129**, 95–110 (2000)

CHAPTER 5

OXYGEN CHEMICAL POTENTIAL SIMULATION AND EMBEDDED PROBE DESIGN

Oxygen chemical potential exceeding boundary values due to interface resistance and the extreme low electronic conductivity is found to be the reason for solid oxide electrolyser cell degradation. By doping YSZ with GDC, the electronic conductivity can be modified, and therefore the durability can be improved. As for the measurement of oxygen chemical potential inside the electrolyte, an embedded probe with insulating shell is found to be the preferred design.

5.1 Introduction

Solid oxide electrolyser cells (SOEC) are widely used for water splitting or syngas production [1]. Compared to conventional low temperature electrolysis cells, SOEC consumes less electrical energy due to the more favorable thermodynamic driving force and faster kinetic process at high temperature. However, the durability of SOEC is found to be not as good as that of SOFC, although they share the same material and cell structure. Usually the cell voltage degradation rate in SOFC is less 1% per thousand hours; but the degradation rate in SOEC is commonly found to be around 5% per thousand hours or even worse. Microstructure analysis after testing has found crack

growth in the electrolyte [2], [3] as well as electrode delamination [4].

The oxygen chemical potential distribution through mixed ionic and electronic conducting materials has been numerically studied by several literatures [5]–[7]. In these works, no matter how different the potential distribution, the potential is always limited within the boundary values outside the electrodes. Dr. Virkar for the first time pointed out that the resistances associated with electrode interface could not be ignored because they might lead to very high oxygen chemical potential inside the electrolyte [8].

In the present work, the oxygen chemical potential distribution inside solid electrolyte is studied again by considering the interface resistances. The simulations here are based on two assumptions. First, transport of a charged species is driven by its electrochemical potential gradient. Second, local equilibrium exists. Doping YSZ electrolyte with GDC has been found to improve SOEC durability [9]. This is simulated by increasing the electronic conductivity of the electrolyte.

The objective here is not only to simulate the oxygen chemical potential distribution, but also to measure it. Measurement of oxygen chemical potential with embedded electrodes (probes) has also been reported [10], [11]. Finite element analysis is used to optimize the embedded probe design.

5.2 Theory and Simulation Details

5.2.1 Governing Equations

According to Dr. Virkar's theory [8], global nonequilibrium and local equilibrium can co-exist in a solid electrolyte cell working in steady state, where current density is constant. Therefore, the following reaction reaches equilibrium in a finite small volume

inside the SOC.

$$\frac{1}{2}O_2 + 2e^- \rightarrow O^{2-} \tag{5.1}$$

$$\frac{\mu_{O_2}}{2} + 2\tilde{\mu}_{e^-} = \tilde{\mu}_{O^{2-}} \tag{5.2}$$

where μ_{O_2} is the chemical potential of neutral oxygen molecule; $\tilde{\mu}_{e^-}$ is the electrochemical potential of electron; $\tilde{\mu}_{O^{2-}}$ is the electrochemical potential of oxygen ion. Defining,

$$\varphi \equiv -\frac{\tilde{\mu}_{e^-}}{e} = -\frac{\mu_{e^-}}{e} + \Phi \tag{5.3}$$

equation (5.2) can be expressed as,

$$\frac{\mu_{O_2}}{4e} - \varphi = \frac{\tilde{\mu}_{O^{2-}}}{2e} \tag{5.4}$$

Since the conducting species are oxygen ion and electron (or holes), at steady state, ionic current and electronic current are constant. So that,

$$\nabla\left(\sigma_i(x)\nabla\left(\tilde{\mu}_{O^{2-}}(x)\right)\right) = 0 \tag{5.5}$$

$$\nabla\left(\sigma_e(x)\nabla\left(\varphi(x)\right)\right)=0 \tag{5.6}$$

Ionic conductivity, $\sigma_i(x)$, in electrolyte is constant since oxygen vacancy concentration is determined by cation doping. Electronic conductivity, $\sigma_e(x)$, in electrolyte is, however, not constant and highly depends on oxygen chemical potential.

$$\sigma_e(x)=f\left[\mu_{O_2}(x)\right]=f\left[4e\varphi(x)+2\tilde{\mu}_{O^{2-}}(x)\right] \tag{5.7}$$

Equation (5.5) can be solved simply by integration, the results is a linear function in the one-dimensional case. Once the explicit expression of equation (5.7) is known, $\varphi(x)$ can be obtained from the self-consistent solution of equations (5.5) to (5.7).

5.2.2 Model Description: Potential Distribution

The relationship between electronic conductivity and oxygen chemical potential has been experimentally studied [12]–[14]. The total electronic conductivity in YSZ consists of both electron and hole conductivity, which can be illustrated by Figure 5-1.

The explicit expression of equation (5.7) is highly nonlinear. As a result, the differential equation (5.6) cannot be solved with the finite element method. The one-dimensional version of equation (5.6) can be solved using the BVP solver developed by Dr. Shampine [15].

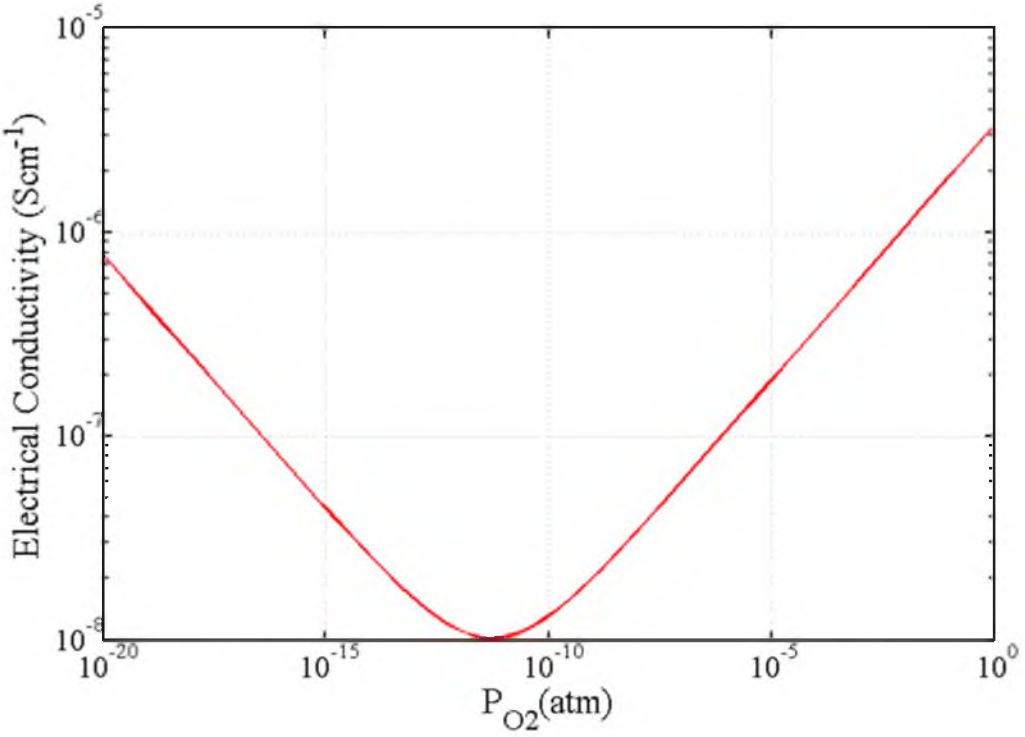

Figure 5-1: The red curve shows the relation between electronic conductivity and oxygen partial pressure. Both the horizontal and vertical axis are in log scale. At higher oxygen partial pressure (the right linear region), hole conduction dominates; at lower oxygen partial pressure (the left linear region), electron conduction dominates.

Figure 5-2 shows the layered structure in an SOC. At steady state, $\varphi(x)$ can be assumed constant in anode and cathode, because electronic conductivity is very high in these two layers. The anode interface and cathode interface play a role in the electrode reaction, and they have a thickness of only several nanometers. There's significant potential drop across these two interfaces due to charge transfer resistance and nonohmic contact. However, since these two interfaces are so thin and charge transfer resistance is nonohmic, there's no interest in knowing the detailed potential distribution inside them.

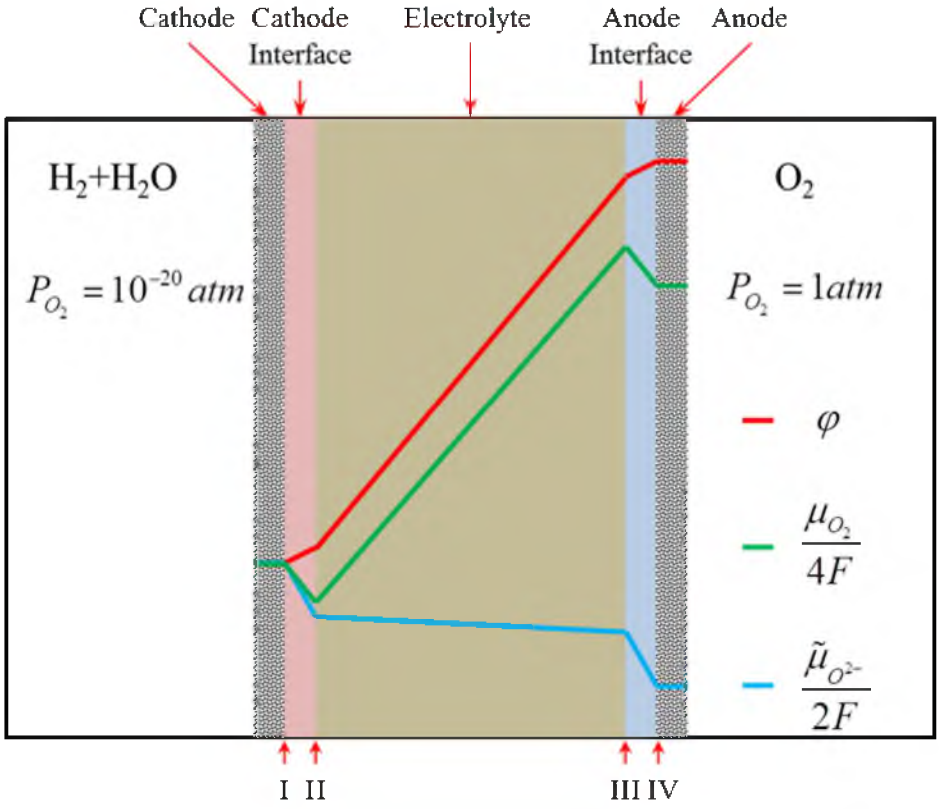

Figure 5-2: One-dimensional model illustrating the layered structure in an SOEC. The anode and cathode have porous structure; the electrolyte is a dense layer. The interface between anode and electrolyte and the interface between cathode and electrolyte are extremely thin. The green, blue and red lines schematically show the potential distribution.

In the solid electrolyte, the electrochemical potential distribution of oxygen ion and electron are determined by equations (5.5) and (5.6) subjected to the boundary values at position II and III in Figure 5-2. Since the electrolyte layer of SOC usually has a thickness of around 10 microns, it is reasonable to assume the two parallel dimensions to be infinite. Therefore, the model becomes one-dimensional.

5.2.3 Model Description: Embedded Probe Design

A one-dimensional model cannot describe the real SOC with an embedded probe. Figure 5-3 shows the two-dimensional model used for this simulation. Two typical cell geometries are considered in the simulation: one is an anode-supported cell (Figure 5-3 (a)); the other is an electrolyte-supported cell (Figure 5-3 (b)). These cells were simulated under a fuel cell mode and an oxygen separation mode (under an applied voltage). Again, both anode and cathode have constant potential; anode interface and cathode interface play a role in the electrode reaction, and there's potential drop due to charge transfer resistance; the electrochemical potential distribution inside the electrolyte is determined by equations (5.5) and (5.6). The uncovered surfaces of electrolyte are subjected to Neumann condition, which requires flux in the normal direction to be zero.

There's an assumption made in this simulation, that is electronic conductivity is constant. This assumption is necessary because Shampine's method cannot solve two-dimensional BVPs and only the finite element method can handle the complex two-dimensional cell geometry.

5.2.4 Boundary Values

Dr. Virkar for the first time claimed that the chemical potential of oxygen molecule inside SOEC electrolyte may not be limited within the values in anode and cathode.

For a real SOEC, the boundary conditions are determined by its working condition, which includes the supplied gas at anode and cathode, as well as the applied DC bias across the cell. In Figure 5-2, the cell is assumed to work with $P_{O_2}^{c} = 1atm$ and $P_{O_2}^{a} = 10^{-20} atm$; applied potential is 1.5V. Therefore,

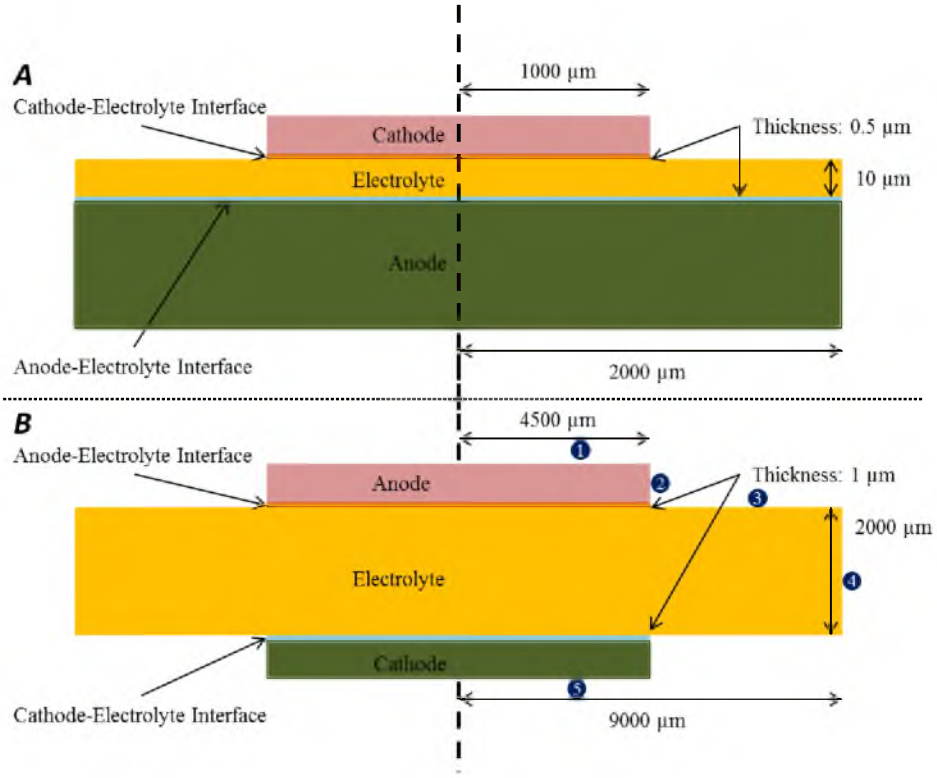

Figure 5-3: Dimensions of the simulated model. A shows the structure of an anode supported solid oxide fuel cell; in the simulation, it is operated in a fuel cell mode (open circuit condition described here). B shows the structure of an electrolyte supported solid oxide oxygen separation cell. In both cells, the electrodes are equipotential, so their potentials are represented by the potentials at the outer surfaces of the interface layers.

$$\frac{\mu_{O_2}^a}{4F} = 0V, \quad \frac{\mu_{O_2}^c}{4F} = 1.0645V \tag{5.8}$$

$$\varphi^a = 0V, \quad \varphi^c = -1.5V \tag{5.9}$$

In order to calculate the oxygen molecule chemical potential distribution in electrolyte, the electrochemical potential of oxygen ion need to be obtained by solving equation (5.5). The corresponding boundary condition is determined from equation (5.2) as

$$\frac{\tilde{\mu}_{O^{2-}}^a}{2F} = 0V, \quad \frac{\tilde{\mu}_{O^{2-}}^c}{2F} = -0.4355V \tag{5.10}$$

However, the three sets of boundary values are associated to position I and IV. The values associated to position II and III are needed, and they can be determined by Ohm's law, provided the resistance of each layer in SOEC is known.

Both the ionic and electronic area specific resistances of the cathode interface between GDC and LSC were measured by Dr. Lim [10]. The resistances of the anode interface between GDC and Ni-GDC was assumed to be zero [10]. There are no interface resistance data for SOEC made of YSZ. In the following simulation, the interface resistances are assigned the same value as measured by Dr. Lim.

The ionic and electronic resistivities of the electrolyte (YSZ and GDC) have been reported [12]. The ionic resistance is usually constant at the working condition, because there's much less intrinsic oxygen vacancy than that generated by doping. However, electronic resistivity highly depends on the local oxygen chemical potential [12].

Therefore, the boundary conditions for oxygen ion electrochemical potential can be easily calculated; but that for reduced electron electrochemical potential is actually an implicit function of φ. This further increases the complexity of the self-consistent BVP.

All the simulation parameters are summarized in Table 5-1. The electrolyte thickness is chosen to be 10 microns, which is very common in SOECs. At 800°C, the electrolyte ionic ASR is 0.044 $\Omega \cdot cm^2$ for YSZ and 0.0163 $\Omega \cdot cm^2$ for GDC. The electronic conductivity in electrolyte was measured by Park for YSZ [12] and by Lubke for GDC [14], which can be expressed as

$$\sigma_e^{YSZ} = 1.31 \times 10^7 \exp\left(-3.88 / \mathrm{kT}\right) P_{O_2}^{-1/4} \tag{5.11}$$

$$\sigma_h^{YSZ} = 2.35 \times 10^2 \exp\left(-1.67 / \mathrm{kT}\right) P_{O_2}^{1/4} \tag{5.12}$$

$$\sigma_e^{GDC} = 1.95 \times 10^7 \exp\left(-2.73 / \mathrm{kT}\right) P_{O_2}^{-1/4} \tag{5.13}$$

$$\sigma_h^{GDC} = 1.47 \times 10^1 \exp\left(-1.16 / \mathrm{kT}\right) P_{O_2}^{1/4} \tag{5.14}$$

$$\sigma_{electronic} = \sigma_e + \sigma_h \tag{5.15}$$

The electronic ASR in the electrolyte can be expressed as

$$r_e^{ele} = \int_0^L dx / \sigma_{electronic}(x) \tag{5.16}$$

Table 5-1: Simulation parameters

	Electronic ASR			Ionic ASR		
	Cathode Interface	Electrolyte	Anode Interface	Cathode Interface	Electrolyte	Anode Interface
units	$\Omega \cdot cm^2$		$\Omega \cdot cm^2$	$\Omega \cdot cm^2$	$\Omega \cdot cm^2$	$\Omega \cdot cm^2$
YSZ-1	1.5	Park	0	0.3	0.044	0
YSZ-2	0	Park	0	0	0.044	0
YSZ-3	1.5	Park	0	0.3	0.044	0
YSZ-4	1.5	Park*	0	0.3	0.044	0
YSZ-5	1.5	Park**	0	0.3	0.044	0
YSZ-6	1.5	Park***	0	0.3	0.044	0
GDC-1	1.5	Lubke	0	0.3	0.0163	0
GDC-2	1.5	Lubke	0	0.3	0.0163	0
GDC-3	1.5	Lubke	0	0.3	0.0163	0
GDC-4	1.5	Lubke	0	0.3	0.0163	0
GDC-5	1.5	Lubke	0	0.3	0.0163	0
GDC-6	1.5	Lubke	0	0.3	0.0163	0

	φ		p_{O_2}		T
	Cathode	Anode	Cathode	Anode	
units	V	V	atm	atm	°C
YSZ-1	-1.5	0	1	10^{-20}	800
YSZ-2	-1.5	0	1	10^{-20}	800
YSZ-3	-1.2	0	1	10^{-20}	800
YSZ-4	-1.5	0	1	10^{-20}	800
YSZ-5	-1.5	0	1	10^{-20}	800
YSZ-6	-1.5	0	1	10^{-20}	800
GDC-1	-1.5	0	1	10^{-20}	800
GDC-2	-1.5	0	1	10^{-15}	800
GDC-3	-1.5	0	1	10^{-10}	800
GDC-4	-1.2	0	1	10^{-10}	800
GDC-5	-1.0	0	1	10^{-10}	800
GDC-6	-0.8	0	1	10^{-10}	800

The boundary values at position II and III can be obtained using Ohm's law, which is

$$\varphi^{II} = \varphi^{a} + \left(\varphi^{c} - \varphi^{a}\right) \cdot \frac{r_e^{a}}{r_e^{a} + r_e^{ele} + r_e^{c}} \tag{5.17}$$

$$\varphi^{III} = \varphi^{a} + \left(\varphi^{c} - \varphi^{a}\right) \cdot \frac{r_e^{a} + r_e^{ele}}{r_e^{a} + r_e^{ele} + r_e^{c}} \tag{5.18}$$

$$\tilde{\mu}_{O^{2-}}^{II} = \tilde{\mu}_{O^{2-}}^{a} + \left(\tilde{\mu}_{O^{2-}}^{c} - \tilde{\mu}_{O^{2-}}^{a}\right) \cdot \frac{r_i^{a}}{r_i^{a} + r_i^{ele} + r_i^{c}} \tag{5.19}$$

$$\tilde{\mu}_{O^{2-}}^{III} = \tilde{\mu}_{O^{2-}}^{a} + \left(\tilde{\mu}_{O^{2-}}^{c} - \tilde{\mu}_{O^{2-}}^{a}\right) \cdot \frac{r_i^{a} + r_i^{ele}}{r_i^{a} + r_i^{ele} + r_i^{c}} \tag{5.20}$$

where r_e^{a}, r_e^{ele} and r_e^{c} are the electronic ASR in anode interface, electrolyte and cathode interface, respectively; r_i^{a}, r_i^{ele} and r_i^{c} are the ionic ASR in anode interface, electrolyte and cathode interface, respectively.

5.2.5 Complete Description of the One-Dimensional BVP

The solution of oxygen ion electrochemical potential is a linear function. In the electrolyte adjacent to anode interface, it has the value of $\tilde{\mu}_{O^{2-}}^{II}$; in the electrolyte adjacent to cathode interface, it has the value of $\tilde{\mu}_{O^{2-}}^{III}$. Therefore, it can be expressed as

$$\tilde{\mu}_{O^{2-}}(x) = \tilde{\mu}^{II}_{O^{2-}} + \left(\tilde{\mu}^{III}_{O^{2-}} - \tilde{\mu}^{II}_{O^{2-}}\right)\cdot\frac{x}{L} \tag{5.21}$$

Take the YSZ cell for example, $\tilde{\mu}^{II}_{O^{2-}}/2F = -0.4355\times\dfrac{0}{0+0.044+0.3} = 0V$,

$\tilde{\mu}^{III}_{O^{2-}}/2F = -0.4355\times\dfrac{0+0.044}{0+0.044+0.3} = -0.056V$. Therefore, $\tilde{\mu}_{O^{2-}}(x) = -0.056V\times\dfrac{x}{L}$.

The electronic conductivity in electrolyte is a function of oxygen partial pressure, $p_{O_2}(x)$, which follows,

$$p_{O_2}(x) = p^a_{O_2}\exp\left(\frac{\mu_{O_2}(x)}{RT}\right) \tag{5.22}$$

since oxygen chemical potential at anode is defined to be zero. Substituting equations (5.2) and (5.22) into equation (5.15), the electronic conductivity in YSZ electrolyte can be expressed as

$$\begin{aligned}\sigma^{YSZ}_{electronic}(x) = {} & 1.31\times10^{7}\exp\left(\frac{-3.88}{\mathrm{kT}}\right)P_{O_2}^{a\ -1/4}\exp\left(-\frac{F\varphi(x)+\mu_{O^{2-}}(x)/2}{RT}\right)\\ & +2.35\times10^{2}\exp\left(\frac{-1.67}{\mathrm{kT}}\right)P_{O_2}^{a\ 1/4}\exp\left(\frac{F\varphi(x)+\mu_{O^{2-}}(x)/2}{RT}\right)\end{aligned} \tag{5.23}$$

In the one-dimensional case, equation (5.6) can be expressed as,

$$\frac{d}{dx}\left[\sigma_e(x)\frac{d}{dx}\varphi(x)\right]=0 \tag{5.24}$$

In order to solve the second-order differential equation with Dr. Shampine's BVP solver, equation (5.24) needs to be expressed with two first-order differential equations by defining

$$\begin{aligned} y_1(x) &\equiv \varphi(x) \\ y_2(x) &\equiv \sigma_e(x)\frac{d}{dx}\varphi(x) \end{aligned} \tag{5.25}$$

Therefore the two first-order differential equations are

$$\frac{d}{dx}y_1(x)=\frac{y_2(x)}{\sigma_e(x)} \tag{5.26}$$

$$\frac{d}{dx}y_2(x)=0 \tag{5.27}$$

The boundary conditions are

$$y_1(0)=\varphi^{II}\left(r_e^{ele}\right),\ y_1(L)=\varphi^{III}\left(r_e^{ele}\right) \tag{5.28}$$

However, φ^{II} and φ^{III} are coupled with the integrating of electronic resistivity. Therefore, an additional differential equation is needed by defining

$$y_3(x) \equiv \int_0^x dt/\sigma_e(t) \text{ or } \frac{d}{dx} y_3(x) \equiv \frac{1}{\sigma_e(x)} \tag{5.29}$$

By definition, $y_3(x)$ is actually the accumulated electronic ASR from anode interface to a certain point (x) in the electrolyte. Obviously, $y_3(L)$ is the total electronic ASR through electrolyte. Therefore, the boundary conditions of the three first-order differential equations are

$$y_1(0) = \varphi^{II}(y_3(L)),\ y_1(L) = \varphi^{III}(y_3(L)),\ y_3(0) = 0 \tag{5.30}$$

The combination of equations (5.26), (5.27), (5.29) and (5.30) gives the complete description of the one-dimensional boundary value problem.

5.2.6 Finite Element Simulation Details on Embedded Probe Design

Simulations were performed using both two-dimensional and three-dimensional finite element analysis (FEA). In two-dimensional FEA, PLANE77, a 2-D 8-Node Thermal Solid, is used for meshing as shown in Figure 5-4(a); in three-dimensional FEA, SOLID90, a 3-D 20-Node Thermal Solid, is used for meshing as shown in Figure 5-4(b) and Figure 5-4(c). FEA is performed by ANSYS. In all simulations the embedded probe is placed in the middle of electrolyte layer.

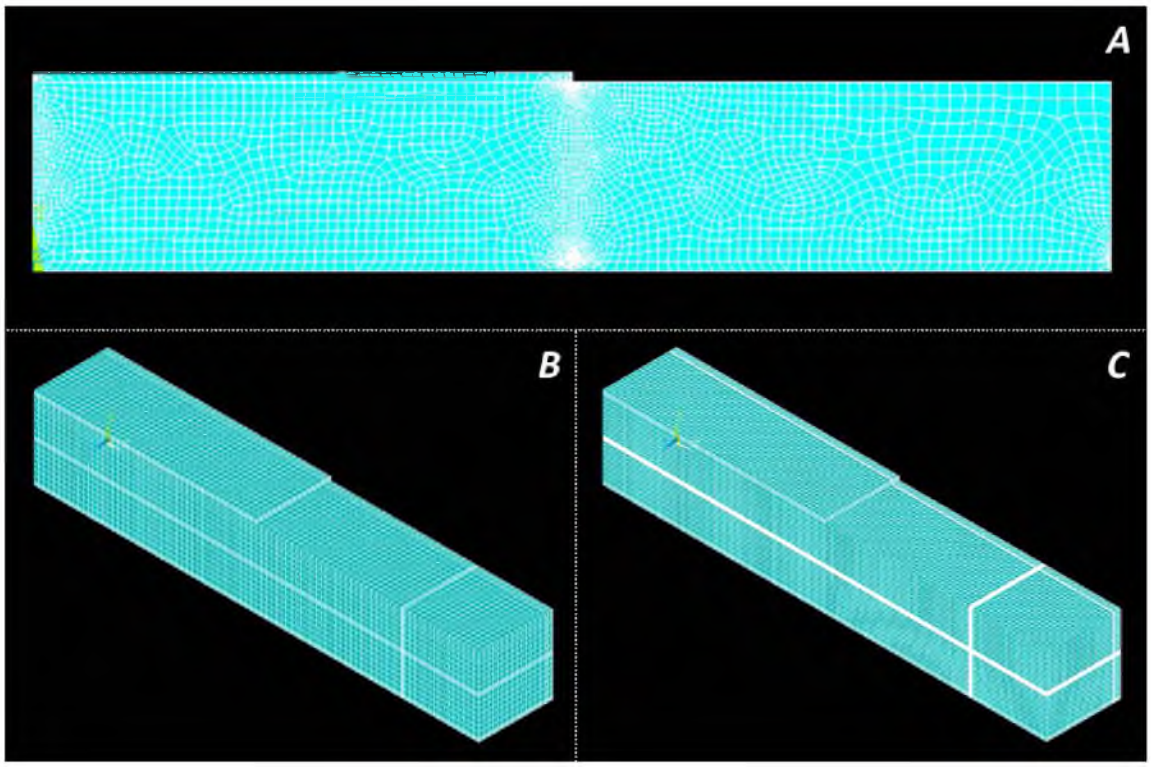

Figure 5-4: Finite element meshing. A shows the meshing used in the two-dimensional finite element simulation; B and C show the meshing used in the three-dimensional simulation. All meshing is fine enough that the calculations rapidly converge.

5.3 Results and Discussion

5.3.1 Oxygen Chemical Potential Exceeding Boundary Values

The parameters for each simulation are listed in Table 5-2. The calculated distribution of $\varphi(x)$, $\tilde{\mu}_{O^{2-}}(x)/2F$ and $\mu_{O_2}(x)/4F$ for the YSZ-1 cell are plotted in Figure 5-5(a). $\tilde{\mu}_{O^{2-}}(x)/2F$ is a linear function shown by the green curve; $\varphi(x)$ is highly nonlinear. The grey reference line shows the value of oxygen chemical potential outside oxygen electrode, which is 1.0645V. Once the red dashed line is above the grey reference line, oxygen chemical potential exceeds the boundary value. Oxygen partial pressure distribution is plotted in Figure 5-5(b).

Table 5-2: Simulation parameters for embedded probe design

Model	Electrolyte		Cathode		Anode				
	σ_e (S/cm)	σ_i (S/cm)	σ_e (S/cm)	σ_i (S/cm)	σ_e (S/cm)	σ_i (S/cm)	$\Delta\mu_{O_2}$ (eV)	$\Delta\phi$ (V)	$\Delta\mu_{O^{2-}}$ (eV)
2D no probe	5E-6	5E-4	5E-4	5E-4	2E-2	1E-3	1.1	1.085	0.015
2D bare probe	5E-6	5E-4	5E-4	5E-4	2E-2	1E-3	1.1	1.085	0.015
3D bare probe	5E-4	5E-4	5E-6	5E-4	2E-2	1E-3	1.1	1.074	0.026
3D coated probe	5E-4	5E-4	5E-6	5E-4	2E-2	1E-3	1.1	1.074	0.026
O_2 Separator1	1E-4	1E-6	1E-4	1E-6	2E-4	2E-4	0	1.1	-1.1
O_2 Separator2	1E-4	1E-6	1E-4	1E-4	2E-4	2E-4	0	1.1	-1.1

At very high oxygen chemical potential, crack and delamination tend to grow. The grey reference line in Figure 5-5(b) has a value of 100atm, above which the mechanical stability of electrolyte is assumed to fail. For this particular cell, YSZ-1, it is clearly shown that oxygen partial pressure is above 100atm throughout almost the whole electrolyte. The parameters of this cell are chosen with respect to the cell tested by Tietz et al. [3]. After 9000 hours of operation, they found cracks grow throughout the whole electrolyte, the driven force of which is clearly the high oxygen partial pressure. r_e^{ele} is calculated to be $85\Omega cm^2$, and electronic current is $0.019 Acm^{-2}$. Oxygen ion transference number is 0.985. Figure 5-5(d) clearly shows that the electrolyte exhibits hole conduction.

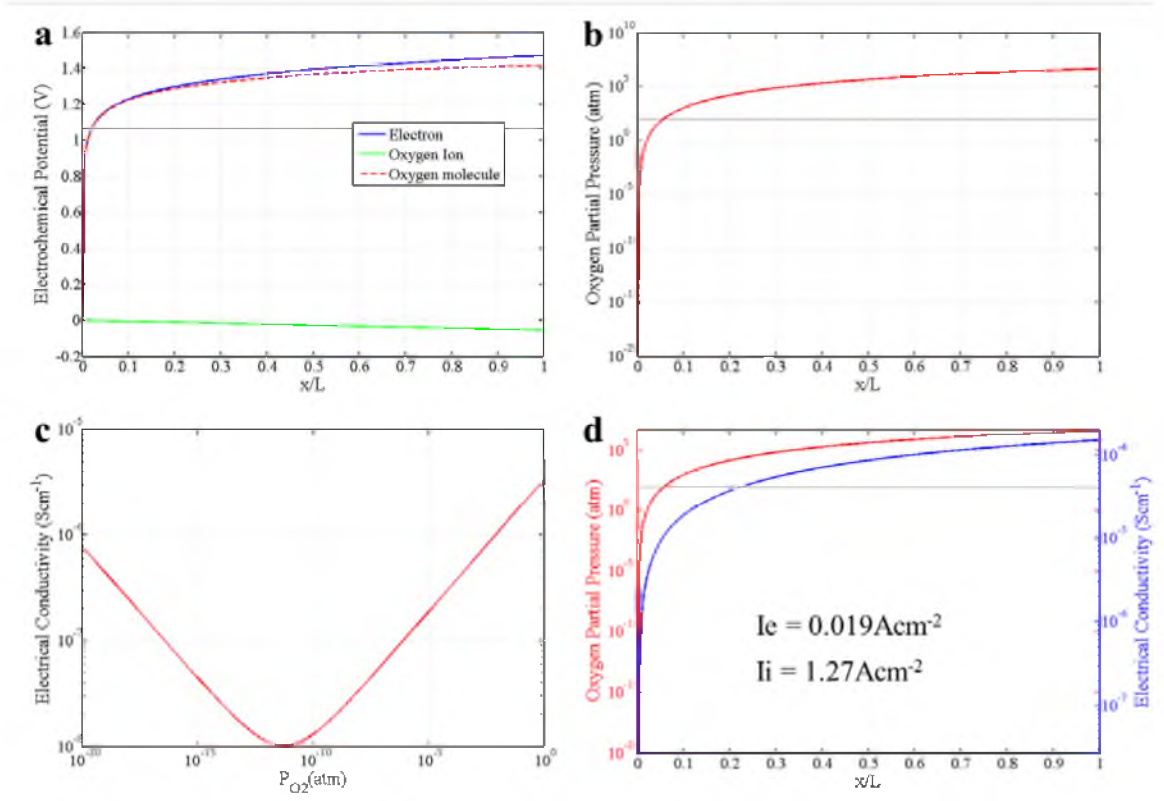

Figure 5-5: Calculated results for the YSZ-1 cell. (a) plots the distribution of $\varphi(x)$, $\tilde{\mu}_{O^{2-}}/2F$ and $\mu_{O_2}/4F$ in the electrolyte, the grey reference line indicates the value of oxygen chemical potential outside oxygen electrode; (b) plots the oxygen partial pressure, the grey reference line has an oxygen partial pressure of 100 atm; (c) plots the electronic conductivity as a function of oxygen partial pressure; (d) is a double y-axis plot, the red curve is the same as subplot b, the blue curve shows the electronic conductivity distribution in the electrolyte.

The oxygen chemical potential distribution in solid electrolyte has been studied by several groups [5]–[7]. However, none of them got to the conclusion that oxygen chemical potential would exceed the boundary values outside the oxygen electrode. Dr. Virkar for the first time discovered that the abrupt change in electrochemical potential of electron and oxygen ion across interface should not be ignored and actually this abrupt change accounted for the exceeded oxygen chemical potential in the electrolyte. In YSZ-

1, r_e^{ele} is much larger than r_e^a and r_e^c. Therefore most of the electric potential drop is distributed to the electrolyte. However, the ionic resistance at oxygen electrode is larger than electrolyte ionic resistance, and most of the oxygen ion electrochemical potential is distributed to the oxygen electrode interface. The difference in electrochemical potential distribution of electron and oxygen ion is believed to the reason for exceeded oxygen chemical potential.

YSZ-2 simulates that case where interface resistances are zero. The results are summarized in Figure 5-6. r_e^{ele} is calculated to be 1011Ωcm^2, and electronic current is 0.0015Acm^{-2}. Since the interface resistances are neglected, oxygen ion electrochemical potential is distributed to the electrolyte, which is similar to electron electrochemical

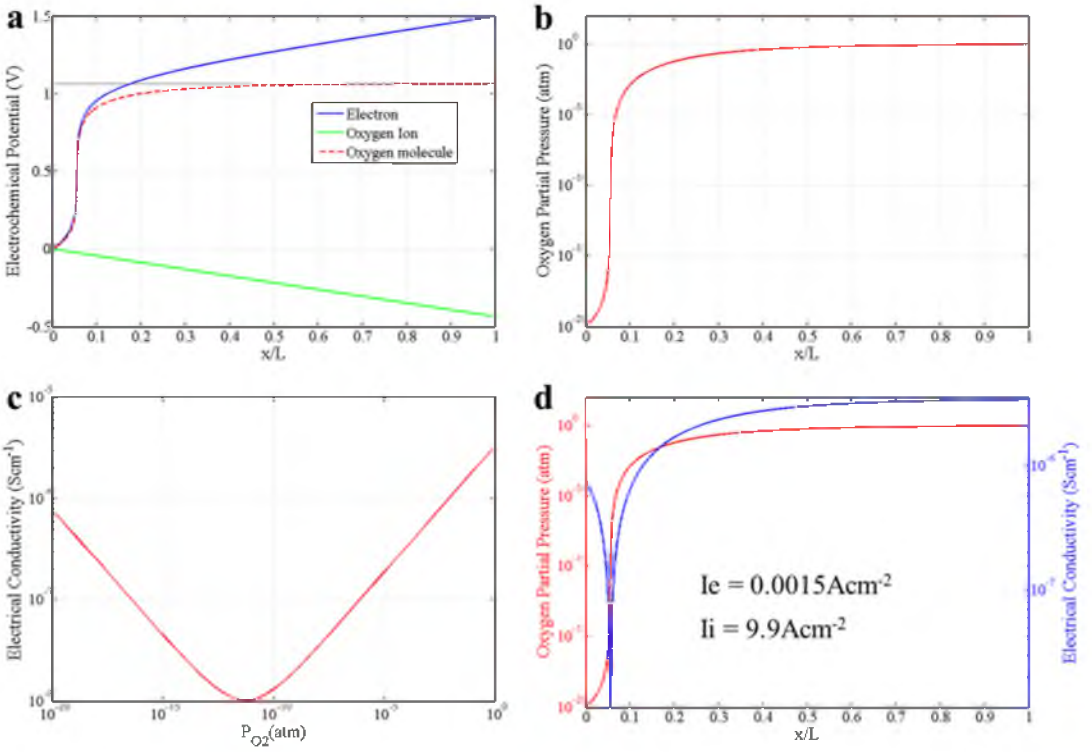

Figure 5-6: Calculated results for the YSZ-2 cell.

potential. As a result, oxygen chemical potential is limited within the boundary values. However, this result obviously cannot explain Tietz's observation.

The YSZ-3 cell has the same cell resistance, but it works at a lower current density. The results are summarized in Figure 5-7. The ionic current is about 0.39Acm^{-2}, r_e^{ele} is calculated to be 946Ωcm^2, and electronic current is 0.0013Acm^{-2}. In this case, most of the oxygen ion electrochemical potential is again distributed to the oxygen electrode interface, and it is almost flat within the electrolyte. The applied DC bias is 1.2V; as a result, the reduced oxygen chemical potential is no more than 1.2V. Therefore, the oxygen partial pressure is below 100atm throughout the whole electrolyte, which is much lower than the cell working at higher current density. Hughes et al. found that an SOEC

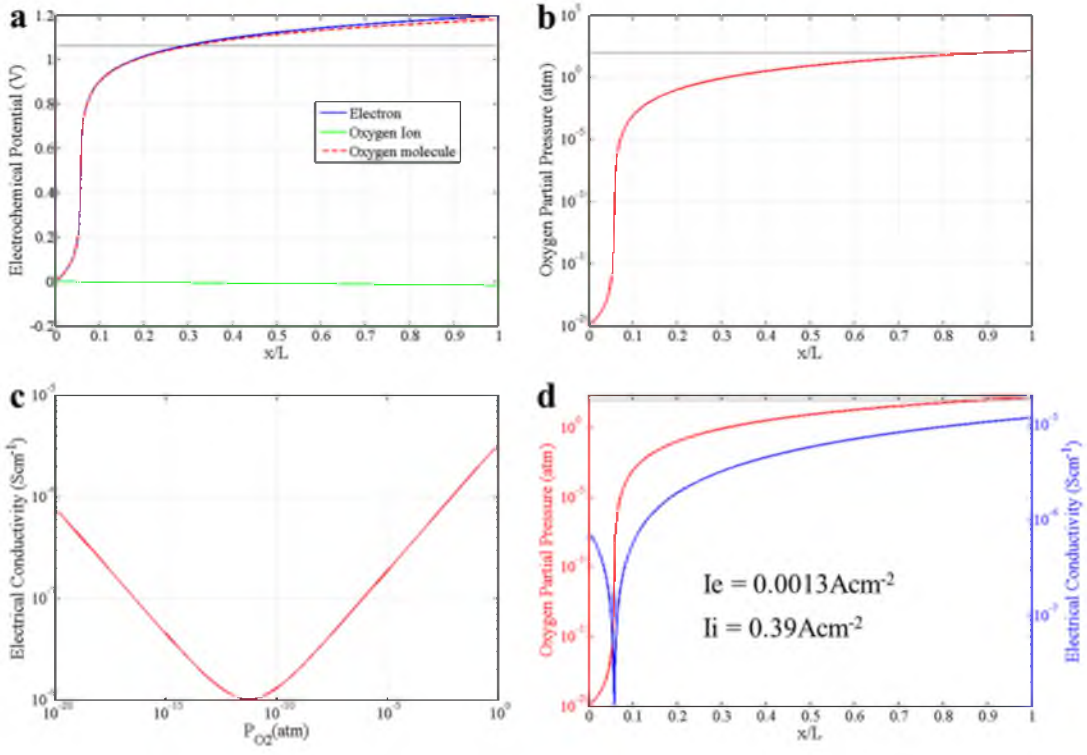

Figure 5-7: Calculated results for the YSZ-3 cell.

working at 0.5Acm^{-2} can avoid crack growth [4]. The simulation results explain Hughes' observation. However, it is not preferred to improve SOEC durability at the expense of lowering the oxygen generation rate. The comparison between YSZ-1 and YSZ-2 indicates that lowering electronic resistance in YSZ electrolyte could prevent oxygen chemical potential from exceeding boundary value.

5.3.2 Reducing Oxygen Chemical Potential by Increasing Electronic Conductivity

It is common to increase electronic conductivity in YSZ by doping certain amount of ceria. Cerium has variable valence between $Ce3^{+}$ and $Ce4^{+}$, and therefore ceria has significant electron conduction. Doping ceria into YSZ can significantly increase the electron conduction, while maintaining the hole conduction. In the simulation of YSZ-4, YSZ-5 and YSZ-6 cells, the electronic conductivity is changed by increasing the pre-exponential factor in equation (5.11). The pre-exponential factor is increased by 100, 1000 and 2000 times in these three simulations. The corresponding results are summarized in Figure 5-8, Figure 5-9 and Figure 5-10.

In YSZ-4 cell, r_e^{ele} is calculated to be 63Ωcm^2, and electronic current is 0.024Acm^{-2}. Different from the concave down feature in YSZ-1 cell, the oxygen chemical potential distribution in YSZ-4 is concave up near fuel electrode and becomes concave down near oxygen electrode. Thirty-five percent of electrolyte near the fuel electrode exhibits electron conductivity, and about 40% of the electrolyte would be free of crack growth. In YSZ-5 cell, r_e^{ele} is calculated to be 13.4Ωcm^2, and electronic current is 0.1Acm^{-2}. 95% of electrolyte near the fuel electrode exhibits electron conductivity, and about 97% of the

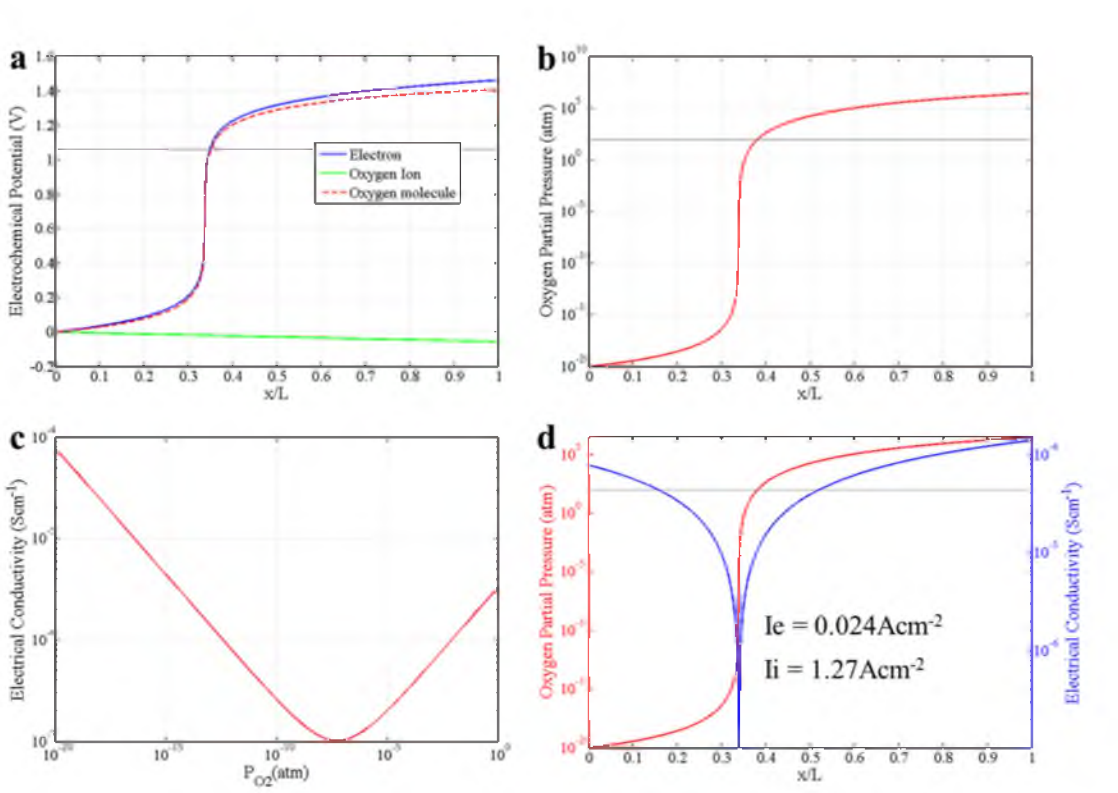

Figure 5-8: Calculated results for the YSZ-4 cell.

electrolyte would be free of crack growth. In YSZ-6 cell, r_e^{ele} is calculated to be 6.0Ωcm^2, and electronic current is 0.21Acm^{-2}. Nearly the entire electrolyte exhibits electron conductivity, and would be free of crack growth. The maximum value of oxygen chemical potential drops from 1.42V in YSZ-1 to 1.13V in YSZ-6.

Electronic leakage current seems to be a possible problem to introduce electronic conduction. The electronic leakage current increases from 0.019Acm^{-2} in YSZ-1 to 0.21Acm^{-2} in YSZ-6 under the simulated working condition. The oxygen ion transference number decreases to 0.86 in YSZ-6. However, this is not a problem in terms of electricity efficiency. A recent study by Dr. Virkar and Tao shows that, by deliberately chosen the working condition, an SOEC made of MIEC electrolyte (YSZ doped with ceria,

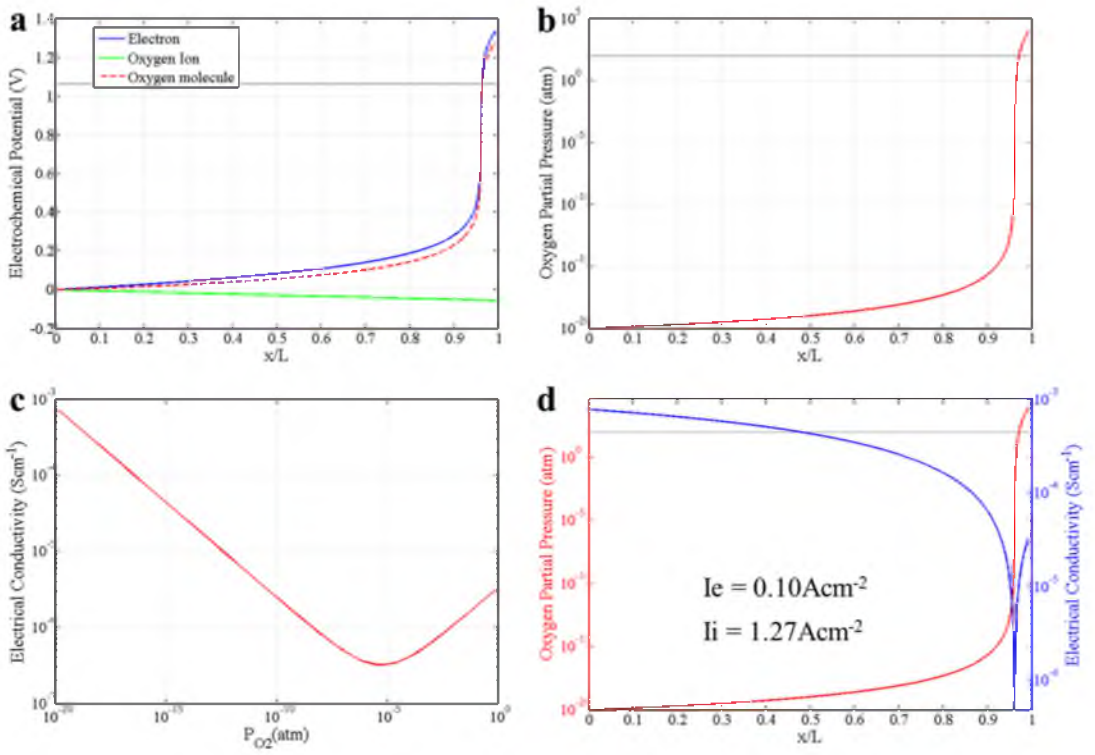

Figure 5-9: Calculated results for the YSZ-5 cell.

transference number of ~0.88) consumes the same amount of electricity, generates the same amount of joule heat, and generates the same amount of hydrogen as an SOEC made of purely ion conducting electrolyte [9]. In their study, it is found that the pure YSZ cell had significant voltage degradation over time and failed after 160 hours operation. While the doped YSZ cell had negligible voltage degradation, and no device failure was observed. These observations can be explained by the simulation result presented in this work.

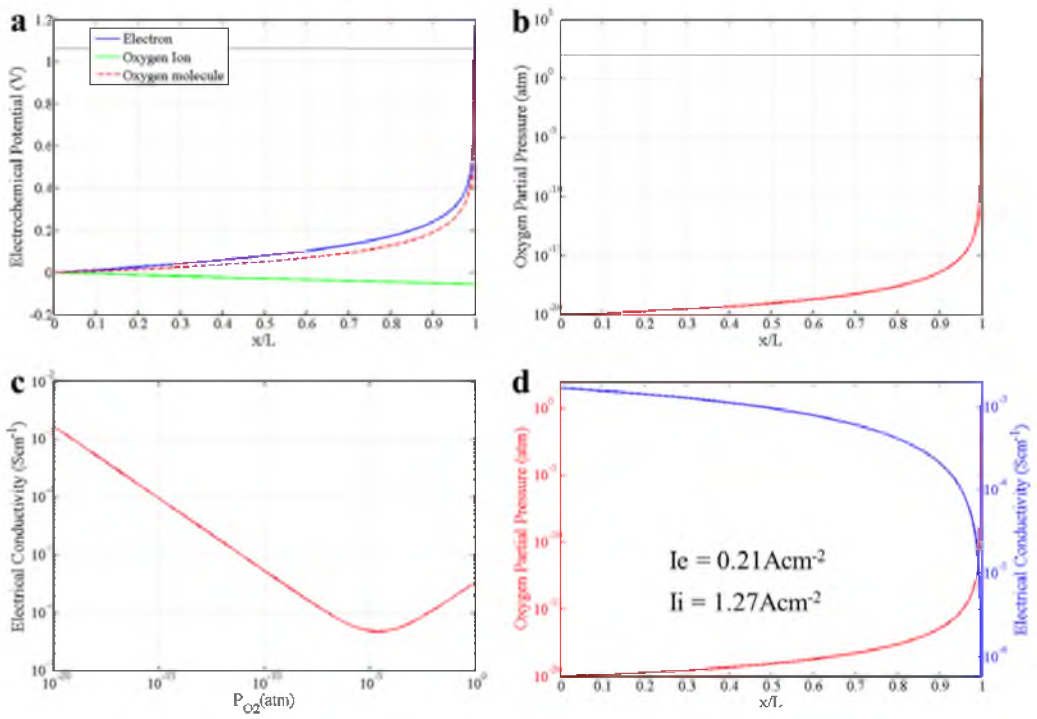

Figure 5-10: Calculated results for the YSZ-6 cell.

5.3.3 A Preferred Working Condition for SOEC Made of GDC

Up to now, pure GDC or SDC haven't been used as the electrolyte in SOECs. The reason is simply due to its high electronic conductivity. However, as pointed out in the above section, SOECs made of GDC electrolyte should have excellent durability. The simulations on GDC cell focus on optimizing the working condition. All the six GDC cells have the same transport property.

GDC-1 cell is simulated to have an oxygen partial pressure of 1E-20atm at the fuel electrode, and the applied DC bias is 1.5V. The simulation results are summarized in Figure 5-11. With such low oxygen partial pressure at the fuel electrode, the GDC electrolyte becomes predominantly electronic conductor [16]. Therefore, in the following simulation, the oxygen partial pressure is increased to 1E-15atm or 1E-10atm.

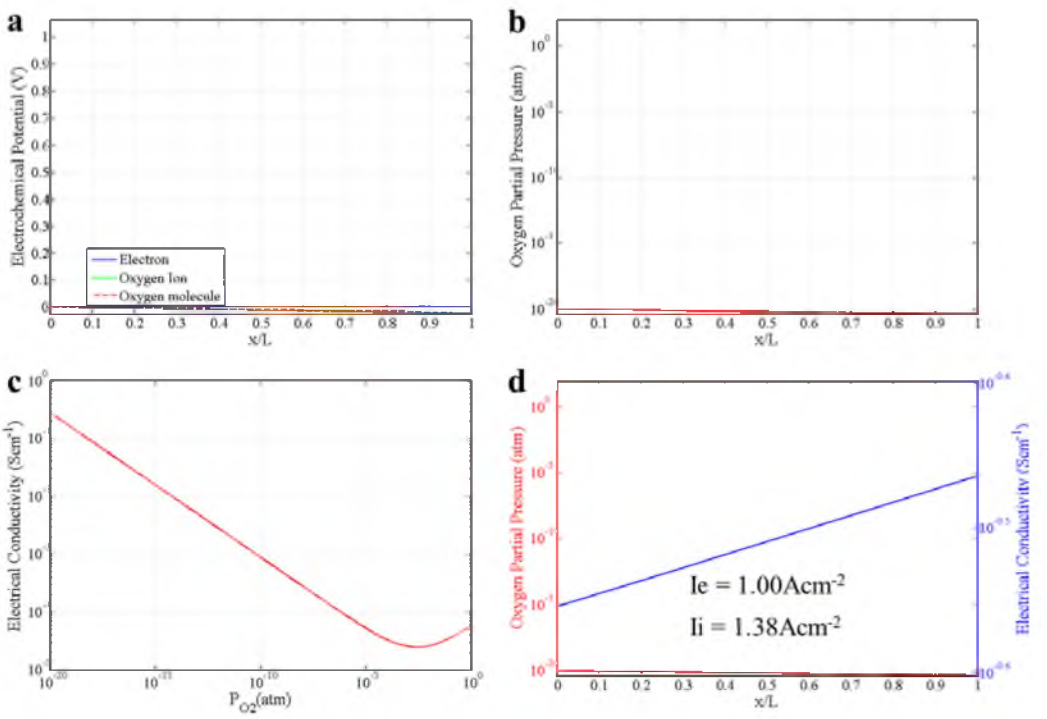

Figure 5-11: Calculated results for the GDC-1 cell.

GDC-2 cell is simulated to have an oxygen partial pressure of 1E-15atm at the fuel electrode, and the applied DC bias is 1.5V. The simulation results are summarized in Figure 5-12. At this working condition, the ionic conductivity in the GDC electrolyte is higher than electronic conductivity. However, oxygen transference number is rather low, which is 0.7. Figure 5-12(b) clearly shows that electron conduction dominates the electronic conductivity almost throughout the entire pressures range. If p_{O2} at the fuel electrode is low, the entire electrolyte will be electron conducting (Figure 5-12(d)). Therefore, oxygen partial pressure is still not high enough.

GDC-3 cell is simulated to have an oxygen partial pressure of 1E-10atm at the fuel electrode, and the applied DC bias is 1.5V. The simulation results are summarized in Figure 5-13. At this working condition, the oxygen partial pressure curve presents a

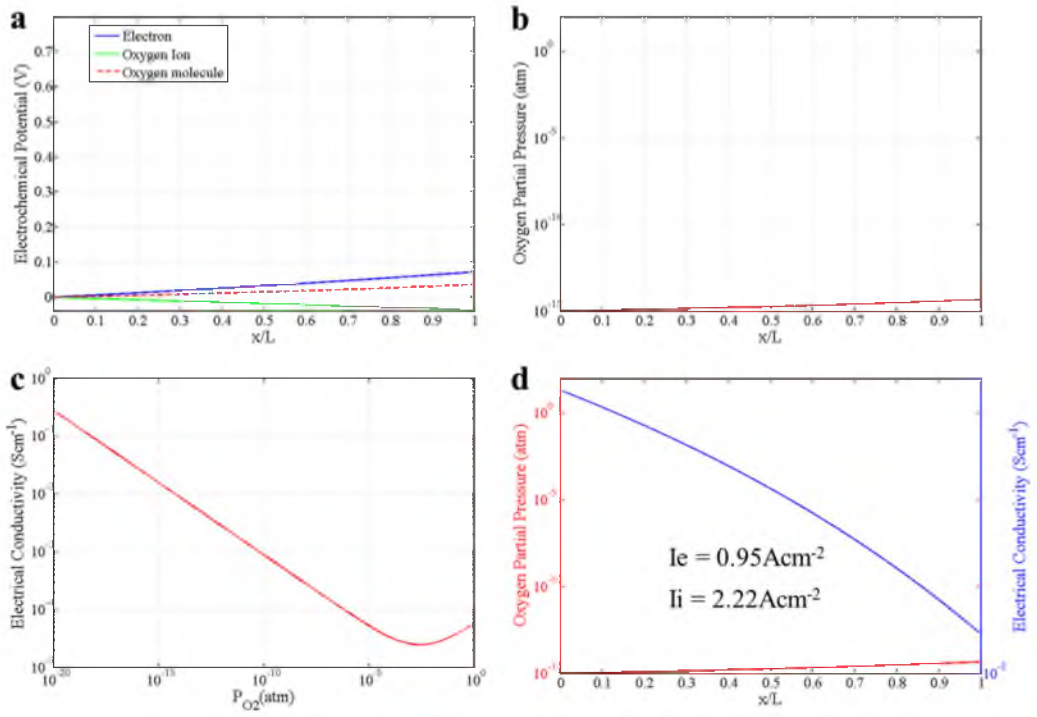

Figure 5-12: Calculated results for the GDC-2 cell.

similar feature as the YSZ cell. The curve is concave up near fuel electrode, and becomes concave down near the oxygen electrode. This feature is caused by the change in conducting species. From Figure 5-13(d), about 23% of the electrolyte near the fuel side is n-type, and the rest is p-type. Figure 5-13(b) indicates that about 70% of the electrolyte favors crack growth. However, the high oxygen partial pressure is now caused by the DC bias. Nernst potential of this cell is 0.53V, but the applied DC bias is as high as 1.5V. The faradic current is 3.06Acm^{-2}. In the following simulation, the DC bias is lowered to optimize the cell performance.

The DC bias is reduced to 1.2V, 1.0V and 0.8V in GDC-4, GDC-5 and GDC-6, respectively. Their simulation results are summarized in Figure 5-14 to Figure 5-16. It is found that the working condition of GDC-6 cell is preferred. In GDC-6 cell, r_e^{ele} is

Figure 5-13: Calculated results for the GDC-3 cell.

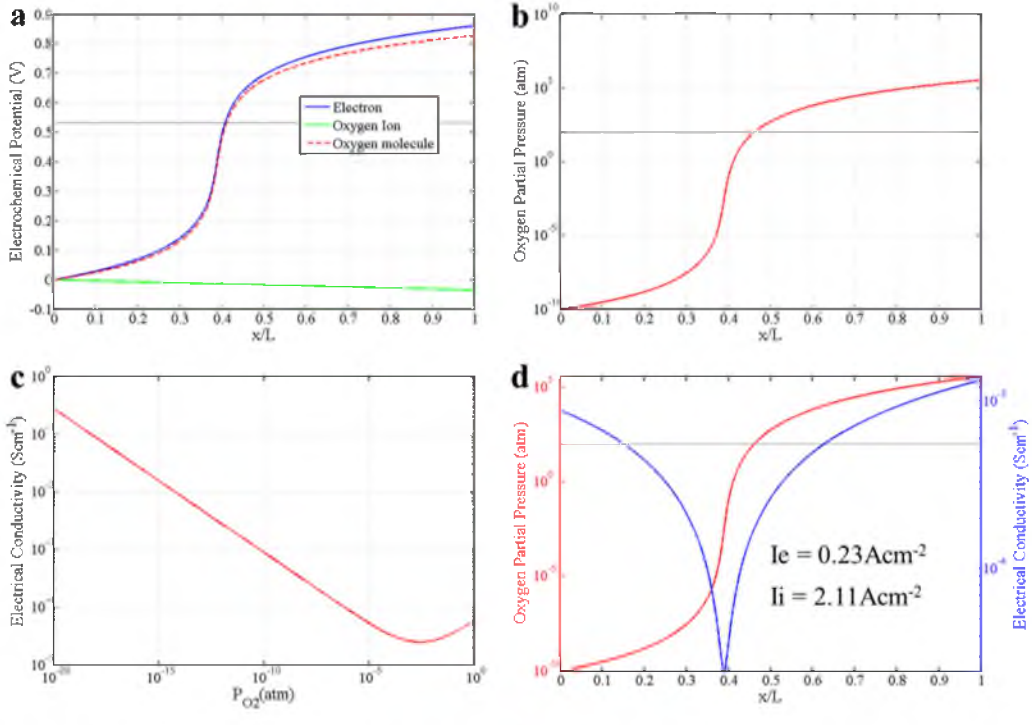

Figure 5-14: Calculated results for the GDC-4 cell.

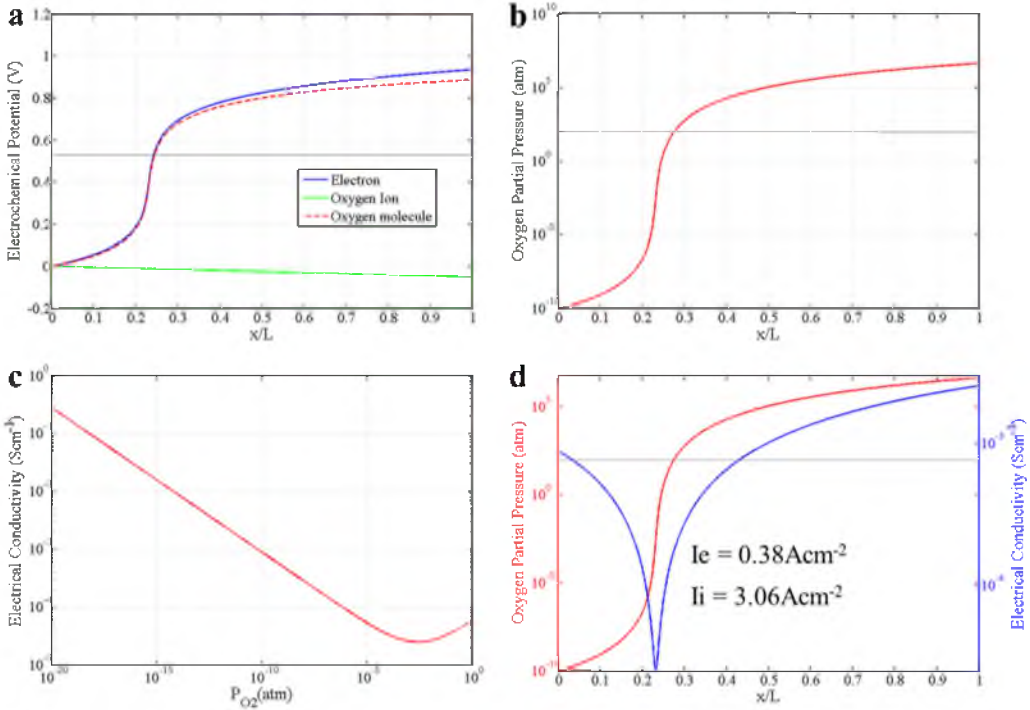
a
Electrochemical Potential (V)
x/L
Electron
Oxygen Ion
Oxygen molecule
b
Oxygen Partial Pressure (atm)
x/L
c
Electrical Conductivity (Scm-1)
P_O2(atm)
d
Oxygen Partial Pressure (atm)
Electrical Conductivity (Scm-1)
x/L
Ie = 0.38Acm-2
Ii = 3.06Acm-2

Figure 5-15: Calculated results for the GDC-5 cell.

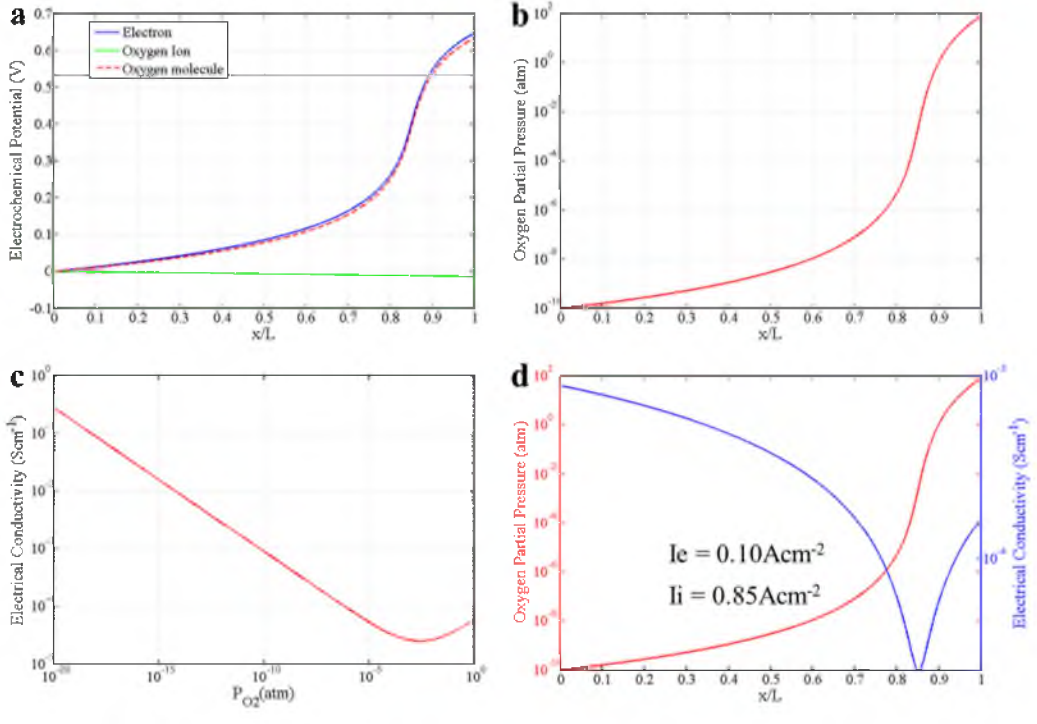

Figure 5-16: Calculated results for the GDC-6 cell.

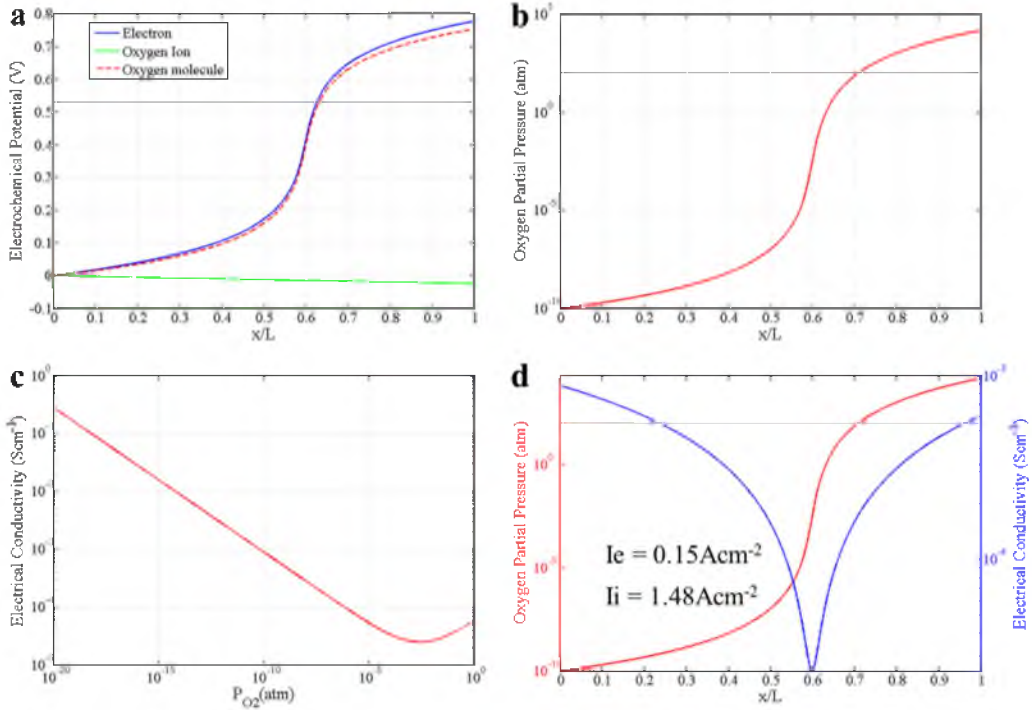
a
Electron
Oxygen Ion
Oxygen molecule
Electrochemical Potential (V)
x/L
b
Oxygen Partial Pressure (atm)
x/L
c
Electrical Conductivity (Scm-1)
P_O2(atm)
d
Oxygen Partial Pressure (atm)
Electrical Conductivity (Scm-1)
Ie = 0.15Acm-2
Ii = 1.48Acm-2
x/L

calculated to be $6.3\Omega cm^2$, electronic current is $0.1Acm^{-2}$, and the oxygen ion transference number is 0.89. The entire electrolyte has an oxygen partial pressure below 100atm, which prevents the crack formation.

5.3.4 Embedded Probe Design

An ideal embedded probe should be able to measure local electric potential without disturbing electric and ionic potential distributions inside the cell. Figure 5-17 shows the results of two-dimensional simulations with an embedded probe (Figure 5-17(a) and Figure 5-17(b)) and without an embedded probe (Figure 5-17(c) and Figure 5-17(d)). In Figure 5-17(a), the electric potential measured at the probe end near the electrolyte surface is the same as the value at probe tip inside the cell. However, the large difference between Figure 5-17(a) and Figure 5-17(c) as well as the difference between Figure 5-17(b) and Figure 5-17(d) shows that both electronic and oxygen ion electrochemical potentials distributions are disturbed by the embedded probe. Especially in Figure 5-17(b), there's a large ionic potential drop across the probe, which is inconsistent with the physical picture. This abrupt decrease results from the over-simplified model. A disc sample without an embedded probe can be simulated using a two-dimensional model (Figure 5-4(a)) due to the axial symmetry. However, when an embedded probe is introduced, axial symmetry no longer exists. A two-dimensional model with a probe represents a sample with embedded metal sheet, which completely blocks off the ionic current, leading to an abrupt ionic potential drop (Figure 5-17(b)).

Figure 5-18 shows the results of a three-dimensional simulation in the case of an embedded metal probe. Figure 5-18(a) and Figure 5-18(b) show the electric and the ionic

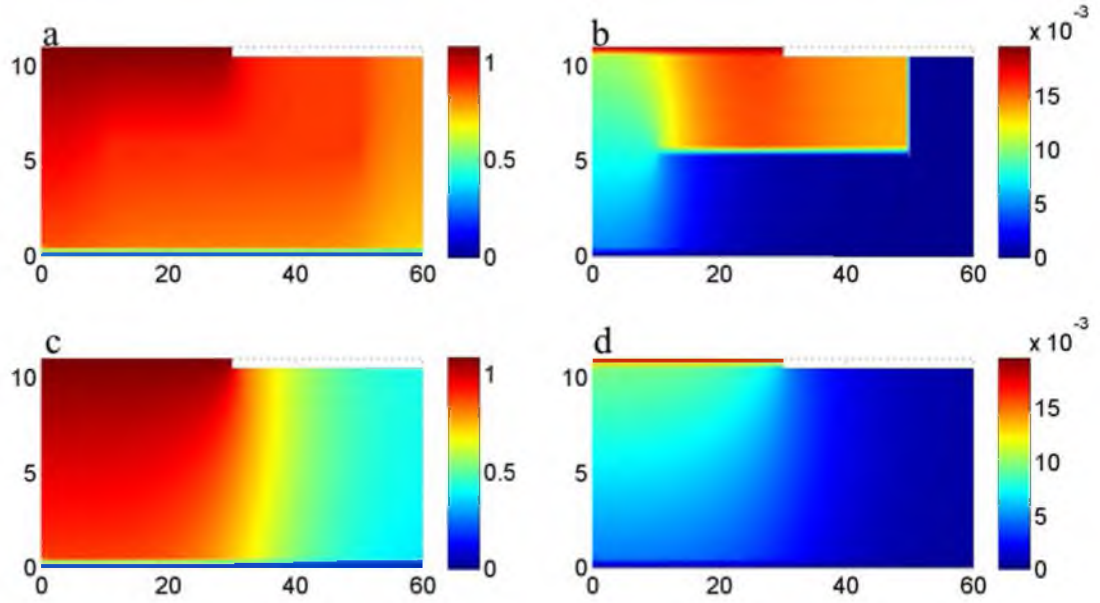

Figure 5-17: Electric and ionic potentials are plotted in (a) and (b), respectively, for samples with an embedded probe. The potentials plotted in (c) and (d) are for samples without an embedded probe, and they are used as a benchmark to determine whether the embedded probe disturbs the potential distributions across the cell.

potential distributions at the cross section, which passes through the probe, while Figure 5-18(c) and Figure 5-18(d) show the cross sections which are far away from the probe. The similarity between Figure 5-18(d) and Figure 5-17(d) indicates that oxygen ion electrochemical potential distribution is not much disturbed by the embedded probe. However, electronic potential distribution is still disturbed by the embedded probe as can be seen by comparing Figure 5-18(c) with Figure 5-17(c). This is attributed to the easy electron migration path along the probe.

Figure 5-19 shows the results of a three-dimensional simulation with an embedded

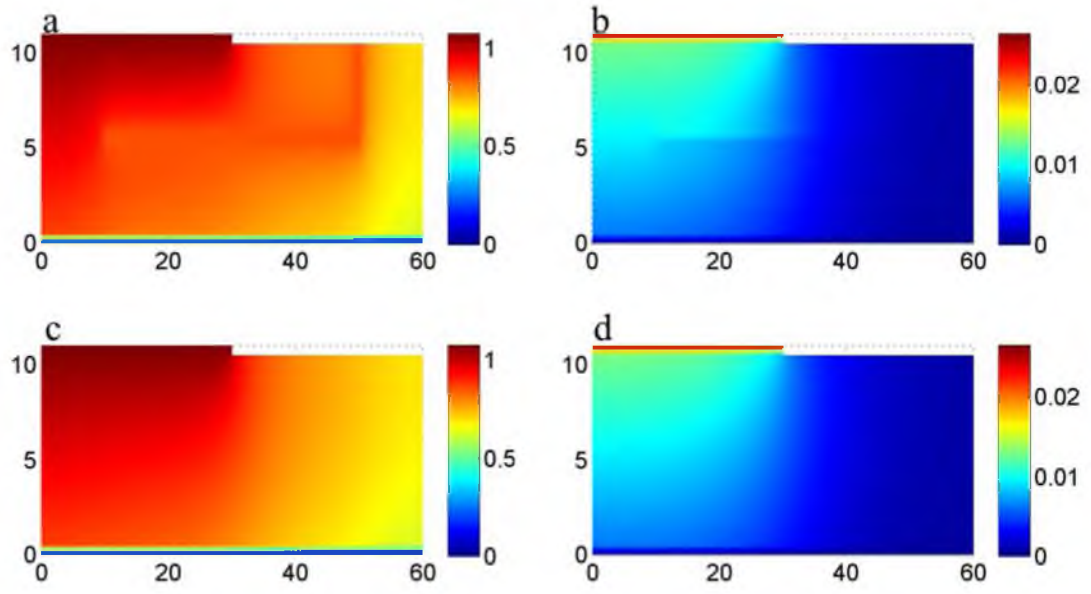

Figure 5-18: Three-dimensional simulation results, for sample with bare metal probe, are presented in a two-dimensional slide. (a) and (b) show electric and ionic potential distributions, respectively, at the cross section though the probe. (c) and (d) show the distributions at a cross section far away from the probe.

probe having an insulating coating on the surface of the probe except at the ends. Both electron and oxygen ion electrochemical potential distributions now remain undisturbed as can be seen by comparing Figure 5-19(c) with Figure 5-17(c) and Figure 5-19(d) with Figure 5-17(d). Note the electric potential measured at the probe end near the electrolyte surface is still the same as the value at the probe tip inside the cell. These features make an embedded probe with an insulating coating (except at the ends) ideal for electric potential measurement.

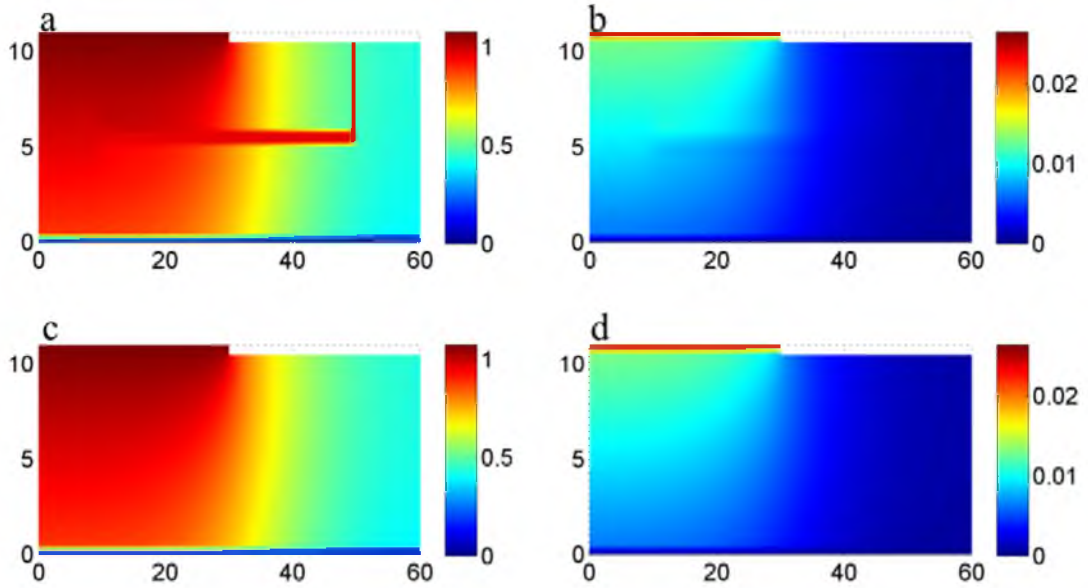

Figure 5-19: Three-dimensional simulation results for sample with a probe containing an insulating layer along its surface (except at the tips). Note that the presence of the embedded probe with an insulating coating does not significantly disturb the local potentials.

5.4 Summary

The mechanism behind crack and delamination growth in SOECs made of YSZ has been studied. Due to electronic and ionic resistances at the anode interface and cathode interface, oxygen chemical potential inside electrolyte could exceed the boundary values outside the electrodes. Increasing electronic conductivity in YSZ can significantly reduce oxygen partial pressure in the electrolyte. As a result, the cell durability can be improved. SOECs made of pure GDC are simulated, and the optimized working condition is found to have higher oxygen partial pressure at the fuel electrode and smaller applied DC bias.

Finite element analysis is used to optimize the embedded probe. A probe with an

electrically insulating shell (with ends uncoated) is shown to be ideal for the measurement of electric potential. In Chapter 7 and Chapter 8, the embedded probe is used in real application. It is found that embedded probe not only can measure potential more accurately, but can also manipulate materials property.

5.5 References

1. A. Brisse, J. Schefold, and M. Zahid, *Int. J. Hydrogen Energy*, **33**, 5375–5382 (2008)

2. M. A. Laguna-Bercero, R. Campana, A. Larrea, J. A. Kilner, and V. M. Orera, *J. Power Sources*, **196**, 8942–8947 (2011)

3. F. Tietz, D. Sebold, A. Brisse, and J. Schefold, *J. Power Sources*, **223**, 129–135 (2013)

4. G. A. Hughes, K. Yakal-Kremski, and S. A. Barnett, *Phys. Chem. Chem. Phys.*, **15**, 17257–62 (2013)

5. S. Yuan and U. Pal, *J. Electrochem. Soc.*, **143**, 3214–3222 (1996)

6. H. Näfe, *J. Appl. Electrochem.*, **31**, 1235–1241 (2001)

7. R. Singh and K. T. Jacob, *J. Appl. Electrochem.*, **33**, 571–576 (2003)

8. A. V. Virkar, *Int. J. Hydrogen Energy*, **35**, 9527–9543 (2010)

9. A. V. Virkar and G. Tao, *Int. J. Hydrogen Energy* , **40**, 5561–5577 (2015)

10. H.-T. Lim and A. V. Virkar, *J. Power Sources*, **180**, 92–102 (2008)

11. H.-T. Lim and A. V. Virkar, *J. Power Sources*, **192**, 267–278 (2009)

12. J. H. Park and R. N. Blumenthal, *J. Electrochem. Soc.*, **136**, 2867–2876 (1989)

13. K. Kobayashi, *Solid State Ionics*, **93**, 193–199 (1997)

14. S. Lubke, *Solid State Ionics*, **117**, 229–243 (1999)

15. L. F. Shampine, M. W. Reichelt, and J. Kierzenka, (2000) http://www.mathworks.com/bvp_tutorial.

16. B. Steele, *Solid State Ionics*, **129**, 95–110 (2000)

CHAPTER 6

MEASUREMENT OF IONIC AND ELECTRONIC CONDUCTIVITIES OF YTTRIA-STABILIZED ZIRCONIA BY AN EMBEDDED ELECTRODE METHOD: STEADY STATE TECHNIQUE

The embedded probe technique is used for the measurement of ionic and electronic conductivities in predominantly oxygen ion conducting materials such as 8YSZ. Cylindrical disc samples of 8YSZ with an embedded Pt wire electrode in the center and two surface porous Pt electrodes were fabricated. When a DC electrical potential is applied across one surface electrode and the embedded electrode, oxygen ions migrate through the YSZ towards the embedded electrode, while electrons transport in the external circuit. In this manner, neutral oxygen is electrochemically pumped to the embedded electrode raising the local oxygen chemical potential. Under the pressure built up, oxygen permeation occurs from the embedded electrode, through the YSZ sample, to the outer surfaces of the sample. In steady state, the electrochemical oxygen flux to the embedded electrode under applied voltage is exactly balanced by out permeation of oxygen governed by the electronic conductivity. Using this technique both the ionic and the electronic conductivities of YSZ were measured at a temperature as low as 500°C.

6.1 Introduction

Yttria-stabilized zirconia containing 8 mol.% yttria (8YSZ) is one of the most widely used oxygen ion conductors as a solid electrolyte for applications such as solid oxide fuel cells (SOFC), solid oxide electrolyser cells (SOEC) and for oxygen separators. 8YSZ is a predominantly oxygen ion conductor with negligible electronic conductivity over a wide range of temperatures and oxygen partial pressures. At 800°C, the ionic transference number is reported to be typically above 0.99. Also, at low oxygen partial pressures, the electronic conductivity is due to the transport of electrons (n-type) and at high oxygen partial pressures it is due to the transport of electron holes (p-type). Over a wide range of oxygen partial pressures and temperatures, the concentrations of electrons and holes are in the dilute limit and the law of mass action

$$np = f(T) \tag{6.1}$$

is obeyed, where n and p are, respectively, electron and hole concentrations.

A transition from n-type to p-type is reported to occur over an oxygen partial pressure, p_{O_2}, range between ~10^{-10} atm and 10^{-5} atm (depending upon the temperature). Thus, for a YSZ sample sintered and equilibrated in air, the electronic conductivity is in the p-type regime.

The measurement of electronic conductivity of predominantly ionic conductors such as YSZ is usually done by the Hebb-Wagner polarization technique [1,2]. In this technique, oxygen ion flux is electrochemically blocked under an applied DC voltage using ion blocking electrodes. (In some cases one of the electrodes is blocking but the

other electrode may be reversible or partially reversible). Thus, in steady state, the only current flowing through the sample is electronic (assuming at least one of the electrodes is perfectly ion blocking). When this condition is achieved the electrochemical potential gradient for oxygen ions is zero, that is

$$\nabla \tilde{\mu}_{O^{2-}} = 0 \tag{6.2}$$

where

$$\tilde{\mu}_{O^{2-}} = \mu_{O^{2-}} - 2F\Phi = \frac{1}{2}\mu_{O_2} + 2\tilde{\mu}_e = \frac{1}{2}\mu_{O_2} - 2F\phi \tag{6.3}$$

in which $\mu_{O^{2-}}$ is the chemical potential of oxygen ions, μ_{O_2} is the chemical potential of oxygen, $\tilde{\mu}_e$ is the electrochemical potential of electrons, Φ is the electrostatic potential, F is the Faraday constant and φ is the measureable electric potential given by

$$\phi = -\frac{\tilde{\mu}_e}{F} = -\frac{\mu_e}{F} + \Phi \tag{6.4}$$

in which μ_e is the chemical potential of electrons (Fermi level).

For the condition of blocked ionic current, we thus have

$$\nabla \tilde{\mu}_{O^{2-}} = 0 = \frac{1}{2}\nabla \mu_{O_2} - 2F\nabla\phi \tag{6.5}$$

under an applied DC voltage across the sample. Thus

$$\nabla \mu_{O_2} = 4F\nabla\phi \neq 0 \tag{6.6}$$

This means the chemical potential of oxygen necessarily varies through the YSZ sample, the magnitude of which in steady state is given by equation (6.6). Thus, inside the sample, the chemical potential of oxygen varies as a function of position and

$$\Delta\mu_{O_2} = \mu_{O_2}^{ii} - \mu_{O_2}^{i} = \int_{i}^{ii} \nabla\mu_{O_2}\, dx = 4F\int_{i}^{ii} \nabla\phi\, dx = 4F\left(\phi^{ii} - \phi^{i}\right) = 4F\Delta\phi \tag{6.7}$$

In equation (6.7), it is assumed that either both electrodes are fully ion blocking or at least one electrode is fully ion blocking. Thus, just under the electrode connected to the negative of the voltage source, the chemical potential of oxygen in the sample, $\mu_{O_2}^{i}$, is lower than the initial value, and just under the electrode connected to the positive of the voltage source, the chemical potential of oxygen in the sample, $\mu_{O_2}^{ii}$, is higher than the initial value.

The higher the applied voltage, $\Delta\varphi$, the higher the $\Delta\mu_{O_2}$. The electronic conductivity in many oxygen ion conductors with predominantly ionic conduction is usually a function of the local chemical potential of oxygen. If the local μ_{O_2} is sufficiently low, the dominant electronic defects are electrons and the local electronic conductivity is given by

$$\sigma_{el} \propto p_{O_2}^{-\frac{1}{n}} \tag{6.8}$$

where n is a positive, real number (often an integer), typically 4. If the local μ_{O_2} is sufficiently high, the dominant electronic defects are holes and the local electronic conductivity is given by

$$\sigma_h \propto p_{O_2}^{\frac{1}{n}} \tag{6.9}$$

Using a theoretical model (based on the relevant defect chemistry), the average electronic conductivity can be estimated from the applied voltage ($\Delta\varphi = \Delta\Phi$), the measured steady state current, and the sample dimensions. Using a theoretical model and the well-known Hebb-Wagner polarization equation, it is possible to obtain both electron and hole contributions to the total electronic conductivity [1,2]. The Hebb-Wagner equation is given by

$$I_{el} = \frac{RT}{F\ell}\left\{\sigma_e^c\left[1-\exp\left(-\frac{F\Delta\phi}{RT}\right)\right]+\sigma_h^c\left[\exp\left(\frac{F\Delta\phi}{RT}\right)-1\right]\right\} \tag{6.10}$$

where ℓ is the sample thickness, I_{el} is the steady state current density measured using ion-blocking electrodes, and $\Delta\varphi$ is the applied electric potential across the ion-blocking electrodes. The usual approach is to fit the measured steady state current to the Hebb-Wagner polarization equation or to obtain the electronic conductivity by measuring I_{el}

as a function of $\Delta\varphi$, in which the applied voltage is varied over some range and the electronic conductivity is obtained by differentiating I_{el} with respect to $\Delta\varphi$.

Depending upon the applied voltage, both n-type and p-type conduction can occur through the sample. Under such conditions, there also exists a spatial region of intrinsic conduction where $n \approx p$. For example, for an applied voltage of 1 V at a temperature of 800°C (1073 K), the p_{O_2} inside the sample can vary by as much as 18 orders of magnitude, which typically covers the n-type, the p-type and the intrinsic regions. The polarization technique also necessitates the establishment of a steady state, which requires the redistribution of oxygen inside the sample; specifically, the transport of oxygen (O or O_2) from the region of the sample connected to the negative of the voltage source to a region of the sample connected to the positive of the voltage source. This redistribution occurs by chemical diffusion of oxygen wherein the chemical diffusion coefficient of oxygen, $\tilde{D}_O$, depends upon the oxygen ion diffusion coefficient, $D_{O^{2-}}$, and the diffusion coefficient of electronic defects, e.g., of holes, D_h, and/or of electrons, D_e. For low values of electronic conductivity, the time required for the establishment of the steady state can be quite long, especially when using thick samples and at relatively low temperatures. As a result, many of the reported measurements of electronic conductivity in YSZ have been done above about 800°C.

Kobayashi et al. [3] measured the electronic conductivity of a 5 mol.% TiO_2-doped 8YSZ tubular sample of 1.3 mm wall thickness in various atmospheres over a temperature range from 800°C to 1000°C by the Hebb-Wagner method. The applied potential was varied between 0.25 V and 1.2 V. Above about 0.7 V, the measured current sharply increased indicating the occurrence of significant changes in the stoichiometry of

the sample due to a large variation in the oxygen chemical potential, $\Delta\mu_{O_2}$, across the sample. Note that at 800°C, for an applied voltage of 0.7 V, the $\Delta\mu_{O_2} = RT\ln\left(\frac{p_{O_2}^{ii}}{p_{O_2}^{i}}\right) = 4F\Delta\varphi = 270\,\text{kJ.mol}^{-1}$. The corresponding ratio of oxygen partial pressures is given by $\left(\frac{p_{O_2}^{ii}}{p_{O_2}^{i}}\right) \approx 10^{14}$. The lowest applied voltage in the work of Kobayashi et al. [3] was 0.25 V, for which the $\Delta\mu_{O_2} = RT\ln\left(\frac{p_{O_2}^{ii}}{p_{O_2}^{i}}\right) = 4F\Delta\varphi = 96.49\,\text{kJ.mol}^{-1}$ and the corresponding ratio of oxygen partial pressures at 800°C is given by $\left(\frac{p_{O_2}^{ii}}{p_{O_2}^{i}}\right) \approx 5\times10^{4}$, which is still quite large and necessitates the use of the Hebb-Wagner polarization equation covering a wide range in oxygen partial pressures.

Park and Blumenthal [4] used the oxygen permeation method for the measurement of permeation current, from which the electronic conductivity of YSZ was deduced. The measurements were conducted over a range of temperatures between 865°C and 1024°C. The permeation cell consisted of two YSZ discs (1.5 mm thick) each with porous Pt electrodes applied, attached by glass-sealing to an alumina cylinder. One of the YSZ discs with Pt electrodes was used to pump oxygen out, and the other was used to measure the oxygen partial pressure inside the chamber by measuring the Nernst potential. The steady state permeation current directly gives the oxygen permeation flux through the other disc. The oxygen chemical potential, $\mu_{O_2}^{in}$, inside the chamber was varied by varying the applied voltage. In steady state, the measured Nernst voltage was nearly the

same as the applied voltage (since the electronic conductivity is much lower than the oxygen ion conductivity). The outside oxygen chemical potential, $\mu_{O_2}^{out}$, was varied by varying the atmosphere. In these studies also the Hebb-Wagner polarization equation was used [1,2]. Two ranges of oxygen partial pressures were selected; one in the n-type regime (low p_{O_2} range) and the other in the p-type regime (high p_{O_2} range). No information on the applied voltage was given. At 865°C, in the n-type regime, the range of p_{O_2} covered was about 4 orders of magnitude (which corresponds to an applied voltage of about 0.25 V). In the p-type regime, the lowest temperature at which data were given was 902°C. The oxygen partial pressure range covered was about 10 orders of magnitude. This corresponds to an applied voltage of about 0.58 V. Based on this information, we estimate that the applied voltage ranged between about 0.25 V and 0.58 V in the work of Park and Blumenthal [4]. Thus, significant variation in the chemical potential of oxygen across the sample was present in both of these studies. In most of the other reported studies also, the applied voltage was typically well over 0.25 V [4] and in some cases as high as 2.0 V [5]. Thus, it appears that in virtually all reported studies, there was significant variation in $\Delta\mu_{O_2}$ through the thickness of the sample.

6.1.1 Time to Attain a Steady State in the Hebb-Wagner Method

Upon the application of an external voltage, redistribution of oxygen occurs within the sample. This redistribution occurs by the diffusion of oxygen which is governed by the chemical diffusion coefficient of oxygen, $\tilde{D}_O$. For a sample of thickness d, the approximate equilibration time is given by

$$t_{equilibration} \sim \frac{d^2}{4\tilde{D}_O} \tag{6.11}$$

Chemical diffusion of oxygen in a predominantly oxygen ion conducting material occurs as a coupled transport of oxygen ions (typically by a vacancy mechanism) and of electrons/holes. If the electronic conductivity is much lower than the ionic conductivity, such as for example in 8YSZ, then the chemical diffusion coefficient of oxygen, $\tilde{D}_O$, is on the order of the hole diffusion coefficient, $D_h / 2$, in the p-type regime or the electron diffusion coefficient, $D_e / 2$, in the n-type regime. At 800°C, according to the work by Park and Blumenthal [4], the D_h is 9.1 x 10^{-7} cm^2s^{-1}. Thus, for a sample of 1.5 mm thickness, the time required for equilibration is about 100 minutes. At 600°C, the time required will be over 2 days. This shows that it is difficult to measure the electronic conductivity in predominantly ionic conductors by the ion blocking electrodes method at low temperatures due to the long equilibration times required.

6.2 Theoretical Model

6.2.1 Measurement of Electronic Conductivity by a Steady State Technique Using an Embedded Electrode

In the present work, we propose a steady state technique with an embedded electrode to measure the electronic conductivity of a predominantly ionic conductor. Figure 6-1 shows a schematic of the sample. It consists of a disc-shaped sample of approximately 3 mm in thickness and 25 mm in diameter in which a platinum wire is embedded in the center. The sample is made by fabricating a compact of 8YSZ powder with a platinum

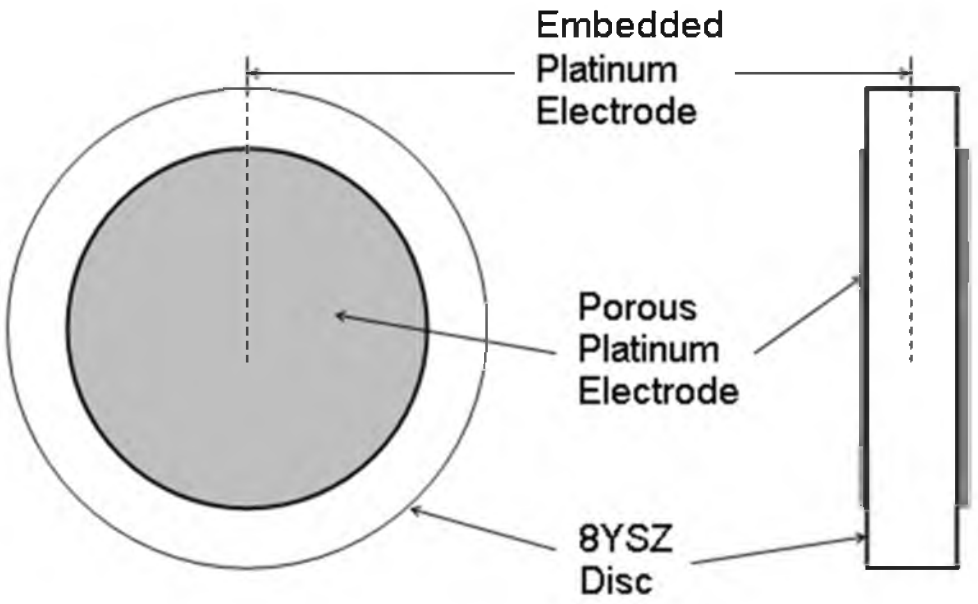

Figure 6-1: A schematic of the sample used to measure ionic and electronic conductivities of 8YSZ.

wire embedded in it. The green disc is then sintered at 1500°C for 5 hours. After sintering, platinum paste is applied over a diameter of ~13 mm on both surfaces followed by firing at 800°C for 1 hour. These form porous platinum electrodes. As long as the density of the sintered sample is high enough so that there is no open porosity, the only possible region through which any oxygen leakage can occur is along the periphery between the embedded platinum wire and the YSZ sample exposed to the atmosphere. By contrast, in the typical procedure used wherein YSZ discs are glass-sealed to an alumina cylinder, such as in the work of Park and Blumenthal [4], there is greater potential for oxygen leakage due to the much larger seal area. Two samples were used in the present study. In one sample, a glass sealant was applied on the joint where the buried platinum wire protruded out of the sintered YSZ sample. In the other sample, all exposed surfaces,

except those covered by porous platinum electrodes, were coated with glass. The details are described in the section on the experimental procedure.

The measurement procedure consists of heating a sample in air (or in another atmosphere of choice with a different oxygen partial pressure in which the sample is pre-equilibrated) to the desired temperature. A DC voltage is then applied across one of the porous electrodes and the embedded Pt wire electrode with an ammeter in series. The negative terminal of the voltage source is connected to the porous electrode and the positive terminal is connected to the embedded electrode. In this manner oxygen is electrochemically pumped from the atmosphere to the embedded electrode. Voltages between the embedded electrode and both porous electrodes are measured as a function of time throughout the test. As soon as voltage is applied between the embedded electrode and one of the porous electrodes, oxygen is electrochemically pumped from the atmosphere to the embedded electrode. At the porous platinum electrode connected to the negative of the voltage source, the reaction is

$$O_2(g) + 4e'(porous\ Pt) \rightarrow 2O^{2-}(YSZ) \qquad \text{(i)}$$

At the buried Pt electrode, the reaction is

$$2O^{2-}(YSZ) \rightarrow O_2(TPB\ near\ Pt\ probe) + 4e'(Pt\ probe) \qquad \text{(ii)}$$

The pumped oxygen cannot escape and leads to an increase in the chemical potential of oxygen in the YSZ at the embedded electrode. This sets up a Nernst voltage between

the embedded electrode and the porous electrodes (and also between the embedded electrode and the exposed surfaces not coated with glass), which opposes the influx of oxygen from the electrode connected to the negative terminal. At the same time, as the Nernst potential is developed, oxygen permeation flux is established from the embedded electrode to the outer surfaces of the disc (to the porous electrodes and also towards the exposed surfaces not covered with a glass coating), which occurs as a coupled transport of oxygen ions and electrons/holes. The corresponding reactions are

$$2O^{2-}\left(YSZ\right) \rightarrow O_2\left(TPB\ near\ Pt\ probe\right) + 4e'\left(Pt\ probe\right) \qquad \text{(iii)}$$

Note that there is no electron transfer across the Pt wire/YSZ interface in reaction (iii). The two oxygen ions migrate towards the two porous surface platinum electrodes in a symmetric fashion and also towards the other surfaces not covered with glass. At the two porous platinum electrodes as well as at the exposed surfaces not covered with glass, the following reaction occurs

$$2O^{2-}\left(YSZ\right) \rightarrow O_2\left(g\right) + 4e'\left(porous\ Pt\right) \qquad \text{(iv)}$$

Note that there is no electron transfer across the atmosphere/YSZ interface or the atmosphere-porous Pt electrode/YSZ interface in reaction (iv). The electrons transport from the YSZ/the porous platinum electrode interfaces and YSZ/the other exposed surfaces not coated with glass through the YSZ to the buried Pt electrode. This means effectively oxygen permeation occurs from the buried Pt wire to the porous platinum

electrodes and into the atmosphere, as well as towards exposed surfaces not covered with glass and into the atmosphere. In steady state, the net influx of oxygen due to the applied voltage is exactly balanced by the net out flux of oxygen by permeation due to the coupled transport. Also, in this steady state permeation process, no electron transfer reaction occurs at either the buried electrode/YSZ interface or the porous Pt electrode/atmosphere interface or the uncoated YSZ/atmosphere interface. As described in what follows, this experimental arrangement can be analyzed to estimate both the ionic and the electronic conductivities of the sample.

6.2.2 Steady State Equations

In what follows, we present relevant equations mainly for steady state. In the present case, the porous electrode is not blocking to either the ionic or the electronic species. At the porous electrode, (i) describes the overall reaction, which is not blocking to either O^{2-} ions or to electrons. There will be some activation overpotential associated with this charge transfer reaction. However, as long as the sample is sufficiently thick, the ohmic resistance dominates. In such a case, the porous electrode is a nearly reversible electrode. At the buried Pt electrode, reaction (ii) occurs, where the released electrons transport out of the Pt wire to the external circuit. The O_2 formed at the buried tip cannot escape to the atmosphere. However, it permeates out of the sample, exiting through the porous platinum electrodes and also through the exposed surfaces not covered with glass. This process is governed by the electronic resistance of the YSZ sample. Thus, under the application of a voltage, both ionic and electronic currents continue to flow through the sample. The net measured current includes ionic and electronic contributions.

The net measured steady state current under an applied voltage E_A between the surface porous Pt electrode connected to the negative of the voltage source and the buried Pt wire central electrode is given by

$$I_A(\infty) = \frac{E_A - E_N(\infty)}{R_i} + \frac{E_A}{R_e} \tag{6.12}$$

where $E_N(\infty)$ is the steady state Nernst voltage created between the atmosphere and the buried electrode, R_i is the ionic resistance of the sample between the surface porous electrode and the buried electrode, and R_e is the electronic resistance of the sample between the surface porous electrode connected to the negative of the voltage source and the buried electrode. In the early stages, before reaching the steady state, the measured current is time-dependent, $I_A(t)$, the developed Nernst voltage is also time-dependent, $E_N(t)$, and the corresponding equation is

$$I_A(t) = \frac{E_A - E_N(t)}{R_i} + \frac{E_A}{R_e} \tag{6.13}$$

Figure 6-2 shows the corresponding equivalent circuit. We will choose a sufficiently thick sample such that much of the resistance is associated with bulk transport (very little of the resistance is assumed to be associated with electrode reactions). Thus

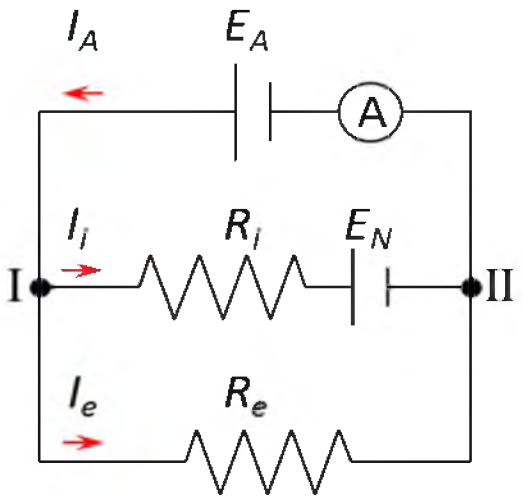

Figure 6-2: An equivalent circuit which describes the passage of a current under an applied voltage.

$$R_i = \frac{\left(\frac{\ell}{A}\right)_{eff}}{\sigma_i} = \rho_i \left(\frac{\ell}{A}\right)_{eff} \tag{6.14}$$

where $\sigma_i = \frac{1}{\rho_i}$ is the ionic conductivity (ρ_i is the ionic resistivity) of YSZ, and $\left(\frac{\ell}{A}\right)_{eff}$ is the effective geometric factor which takes into account the variable length to cross-sectional area for ion transport for the selected geometry (a planar surface electrode and a buried Pt wire electrode). Similarly

$$R_e = \frac{\left(\frac{\ell}{A}\right)_{eff}}{\sigma_e} = \rho_e \left(\frac{\ell}{A}\right)_{eff} \tag{6.15}$$

where $\sigma_e = \frac{1}{\rho_e}$ is the electronic conductivity (ρ_e is the electronic resistivity) of YSZ. Thus, note that

$$\frac{\rho_e}{\rho_i} = \frac{R_e}{R_i} \tag{6.16}$$

At the instant the external voltage is applied, assuming not much transport of oxygen has yet occurred to the buried electrode, the initial Nernst voltage is zero. Thus, at the time the external voltage source is connected to the cell, the initial current is given by

$$I_A^o = \frac{E_A}{R_i} + \frac{E_A}{R_e} = E_A\left(\frac{1}{R_i} + \frac{1}{R_e}\right) \tag{6.17}$$

where I_A^o is the initial current (current measured at time zero just after the voltage was applied). We are assuming that the material is a predominantly ionic conductor. That is $R_e >> R_i$.

Thus, from the initial measured current, we know

$$R_i \cong \frac{E_A}{I_A^o} \tag{6.18}$$

Once the steady state is established, the rate at which oxygen leaves the buried electrode by permeation is the same as the rate at which oxygen (as oxygen ions) arrives

at the buried electrode by permeation. We will first assume that the transport of oxygen from the buried electrode to the external surfaces with porous electrodes occurs in a symmetric fashion. Thus, during this dissipation, the ionic and the electronic resistances are given by

$$R_i^{diss} = \frac{R_i}{2} \tag{6.19}$$

and

$$R_e^{diss} = \frac{R_e}{2} \tag{6.20}$$

The factor of ½ arises because we assumed transport during permeation occurs only towards both surface electrodes. If permeation also occurs towards the exposed surfaces not coated with glass, then $R_i^{diss} \propto R_i$ and $R_e^{diss} \propto R_e$, but the proportionality constant will be different from ½. The possible validity of this assumption will be discussed later. The leakage (permeation) of oxygen from the buried electrode to the outer surfaces (which occurs as a coupled transport of ions and electrons/holes) may be described by the equivalent circuit given in Figure 6-3. In this case, note that the ionic and the electronic currents are of equal magnitude but of opposite signs so that no net current, that can be externally measured, flows in this process. The leakage/permeation is described by

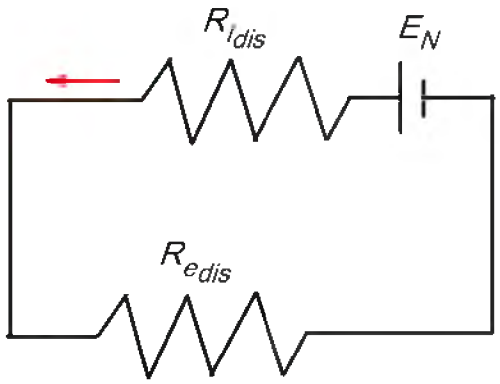

Figure 6-3: An equivalent circuit which describes the permeation of oxygen from the region near the embedded electrode to the outer surfaces of the sample.

$$\left|I_i^{diss}\right| = \left|I_e^{diss}\right| = \frac{E_N}{R_i^{diss} + R_e^{diss}} = \frac{2E_N}{R_i + R_e} \tag{6.21}$$

In steady state, the rate of oxygen (neutral) transport from the buried electrode to the surfaces of the porous electrodes is the same as the rate of oxygen (ion) transport from the porous surface electrode connected to the negative of the voltage source to the buried electrode. Thus, we have

$$\frac{E_A - E_N(\infty)}{R_i} = \frac{2E_N(\infty)}{R_i + R_e} \tag{6.22}$$

The overall process of electrochemical pumping of oxygen to the embedded electrode under an applied voltage and the permeation of oxygen out of the sample due to the

pressure built up at the embedded electrode is shown in Figure 6-4. Figure 6-4(a) and Figure 6-4(b) show the fluxes where the permeation occurs to all exposed surfaces. Figure 6-4(c) and Figure 6-4(d) show the fluxes where the permeation occurs only towards the porous electrodes. This would be the case when all exposed surfaces, other than those covered by porous Pt electrodes, are coated with glass.

Equation (6.22) gives

$$E_N(\infty) = \left(\frac{R_i + R_e}{3R_i + R_e} \right) E_A \tag{6.23}$$

Thus, the ionic current in steady state is given by

$$I_i(\infty) = \frac{E_A - E_N(\infty)}{R_i} = \frac{E_A \left[1 - \dfrac{R_i + R_e}{3R_i + R_e} \right]}{R_i} \tag{6.24}$$

which simplifies to

$$I_i(\infty) = \frac{2E_A}{3R_i + R_e} \tag{6.25}$$

Thus, the net measured current in steady state is

$$I_A(\infty) = I_i(\infty) + I_e = \frac{2E_A}{3R_i + R_e} + \frac{E_A}{R_e} \tag{6.26}$$

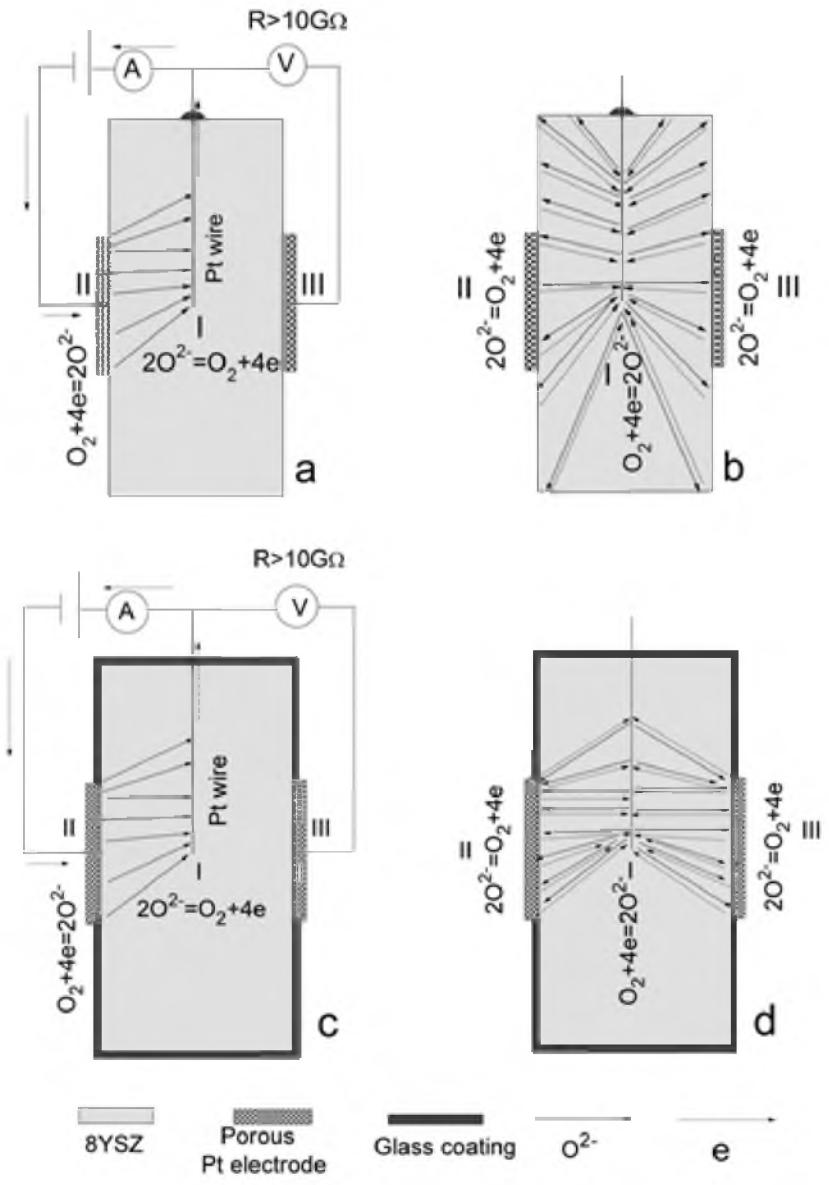

Figure 6-4: Schematics showing electrochemical pumping of oxygen to the embedded platinum electrode under an applied voltage with a glass coating at the Pt-YSZ joint (a) and with glass coating on all exposed surfaces except the porous platinum electrodes (c), respectively. Schematics showing permeation of oxygen under the pressure built up (Nernst potential) from the embedded electrode towards the outer surfaces with a glass coating at the Pt-YSZ joint (b) and with glass coating on all exposed surfaces except the porous platinum electrodes (d), respectively.

Note that I_e is time-independent for a given applied voltage, E_A, as long as it is small enough so that negligible changes in stoichiometry occur. The measured steady state current is given by

$$I_A(\infty) = \frac{3E_A}{R_e}\left(\frac{R_i + R_e}{3R_i + R_e}\right) \tag{6.27}$$

If $R_e >> R_i$, equation (6.27) simplifies to

$$I_A(\infty) \approx \frac{3E_A}{R_e} \tag{6.28}$$

Thus, the electronic resistance is given by

$$R_e \approx \frac{3E_A}{I_A(\infty)} \tag{6.29}$$

Equation (6.26) is a quadratic equation in R_e and may be written as

$$I_A(\infty)R_e^2 + 3\left(I_A(\infty)R_i - E_A\right)R_e - 3E_A R_i = 0 \tag{6.30}$$

Solution to equation (6.30) is

$$R_e = \frac{3\left(\frac{E_A}{I_A(\infty)} - R_i\right) + \sqrt{9\left(\frac{E_A}{I_A(\infty)} - R_i\right)^2 + \frac{12E_A R_i}{I_A(\infty)}}}{2} \tag{6.31}$$

Equation (6.31) should be used to determine the electronic resistance if the electronic conductivity is not too small compared to the ionic conductivity. It should be noted however that in such a case, it is necessary that the ionic resistance is known accurately (and cannot be estimated from the initial current upon the application of voltage).

If $\frac{E_A}{I_A(\infty)} >> R_i$, equation (6.31) reduces to equation (6.29).

6.2.3 The Embedded Electrode Method Under a Low Applied Voltage

As described previously, the Hebb-Wagner polarization method is based on the establishment of steady state using ion blocking electrodes (or one blocking electrode, and the other a reversible electrode) in which ion current becomes zero. Most of the reported studies have been conducted under applied voltages greater than 0.25 V [3,4], and in some cases as high as 2 V [5]. Such a large applied voltage creates a large oxygen chemical potential gradient inside the sample, often corresponding to several orders of magnitude variation in oxygen partial pressure across the sample. This necessitates a redistribution of oxygen within the sample by chemical diffusion (as well as possible incorporation/removal of oxygen from/to the atmosphere) – which is dictated by the chemical diffusion coefficient of oxygen, $\tilde{D}_O$. In the embedded electrode method described here under a low applied voltage, in steady state a nonzero finite oxygen ion flux transports from the porous electrode to the buried electrode, and oxygen flux of

equal magnitude flows away from the buried electrode to the porous electrodes and to the exposed surfaces not covered with glass. Also in the present method, as long as the applied voltage is small, negligible redistribution of oxygen occurs. For example, for an applied voltage of 0.05 V at 800°C, the maximum oxygen pressure ratio across the two porous electrodes and the buried electrode, $p^{i}_{O_2} / p^{ii}_{O_2}$, is less than an order of magnitude, and for an applied voltage of 0.01 V, the ratio is only ~1.55. Thus, the electronic conductivity throughout the sample is essentially constant. Under such conditions, equations such as (6.12) are DC equations with negligible time dependence involved. The only time dependence arises because of the finite rate of pumping oxygen to the embedded electrode – governed by the ionic resistance, R_i. This pumping rate can be quite fast, and a quasi steady state can in principle be achieved in a matter of minutes. Another difference is that in the often-used approach to the Hebb-Wagner method on oxygen ion conductors, one generally measures only one parameter, namely the current in steady state, I_{el} (which is different from the original work by Hebb [1] on silver sulfide wherein electric potential, $\varphi(x)$, was measured as a function of position, x, which allows a direct measurement of electronic conductivity as a function of the local chemical potential). In the present method, one measures two parameters: the current across the porous platinum electrode and the buried Pt electrode across which the voltage is applied, and also the voltage across the buried Pt electrode and the other surface electrode.

6.3 Experimental Procedure

6.3.1 Sample Fabrication

Disc-shaped samples of 8YSZ were made by die-pressing followed by sintering. About 12 gm. of 8YSZ powder was first placed inside a circular die of 32 mm in diameter. After leveling the surface of the powder in the die and lightly pressing, a platinum wire of 0.18 mm in diameter was placed along the radial direction from the center to the circumference. The length of the wire was about the same as the radius of the die. Subsequently, an equal amount of 8YSZ powder was placed over the top of the wire and the lightly pressed powder in the die. The powder compact was then pressed under a uniaxial force of 5 metric tons for 30 seconds. After removing the disc from the die, a small part of the disc perpendicular to the embedded platinum probe was cut out to expose part of the electrode (approximately 2 mm in length). The disc was then sintered in air at 1500°C for 5 h. After sintering, the Pt electrode was embedded into the disc with a small portion exposed, to which electrical connections could be made for subsequent testing.

The planar surfaces of the discs were then polished to a 2.5 micron finish, coated with a platinum paste (Heraeus) over a circular area of about 13 mm in diameter and heated in air at 800°C for 1 h to form porous platinum electrodes. In some samples, the circular edge area adjacent to the buried electrode was coated with a barium-calcium-alumina-silicate glass to minimize any possible oxygen leakage along the edge. Figure 6-5 shows photographs of the samples. In one sample, all exposed surfaces of the disc that were not covered with porous platinum electrodes were coated with glass. This ensured that the only oxygen exchange with the atmosphere occurred at the surfaces coated with porous

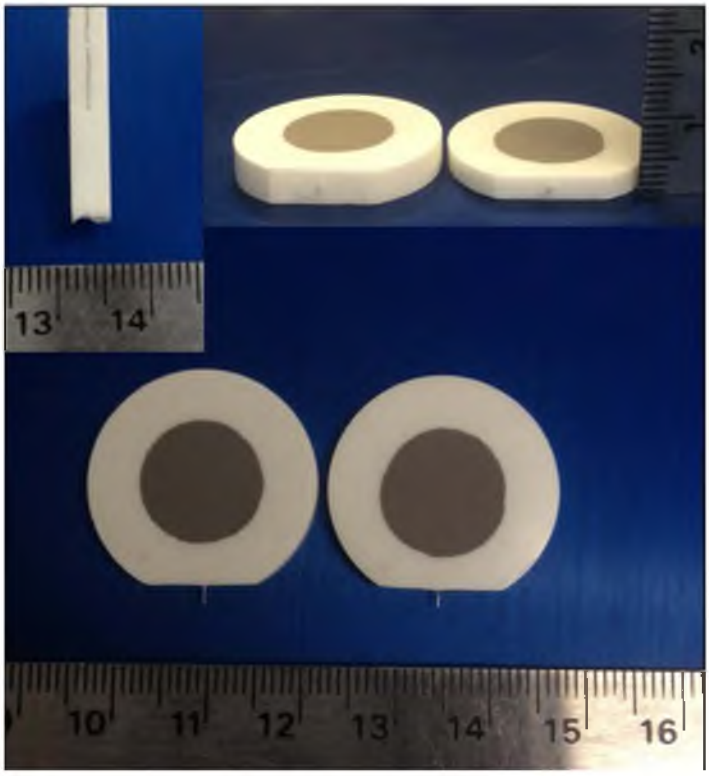

Figure 6-5: A photograph showing top and side views of YSZ discs with an embedded Pt electrode and porous Pt surface electrodes. The upper left hand corner photograph of a cut disc shows that the embedded electrode was symmetrically positioned.

platinum. In both cases, the samples were heated to 900°C to fuse the glass. Also shown in the figure is a photograph of a cut disc showing the position of the embedded Pt electrode.

6.3.2 Electrochemical Testing

Electrochemical measurements were conducted using the schematic diagrams shown in Figure 6-6. A photograph of the testing setup is shown in Figure 6-7. It consists of a horizontal tube furnace in which a sample can be heated over a range of temperatures. The sample was secured in alumina rings and alumina rods fixture. Two platinum wires

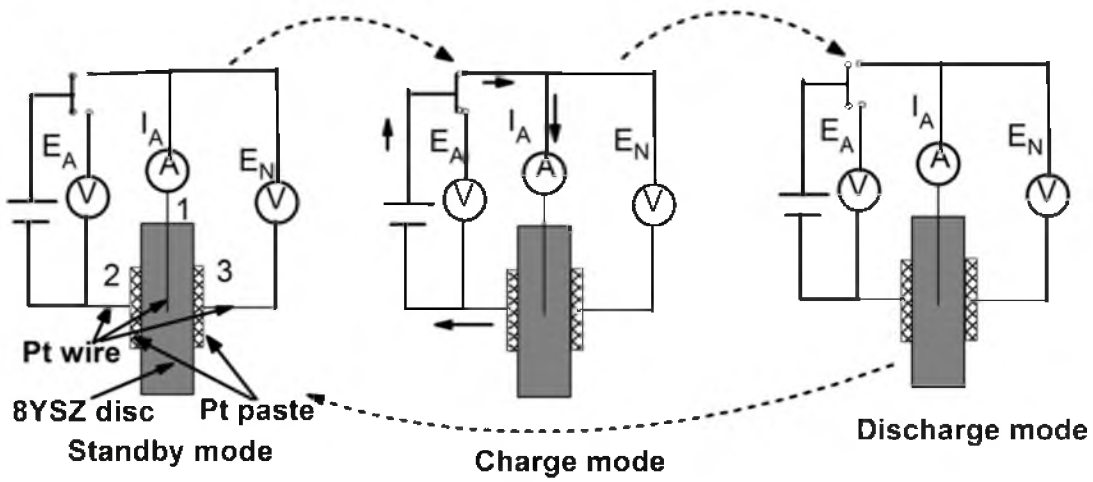

Figure 6-6: Schematic diagrams of electrochemical testing of YSZ discs with an embedded Pt electrode. Two high input impedance (10 GΩ) meters measure the voltage across electrodes 1 & 2 and across 1 & 3. (a) Standby mode: No voltage is applied across 1 and 2. (b) Charge mode: A DC voltage is applied across 1 and 2. An ammeter measures the current flowing when a DC voltage is applied across 1 and 2. A voltmeter measures voltage across 1 and 2, which is the applied voltage, and also across 1 and 3. (c) Discharge mode: The switch is opened so that no voltage is applied. A voltmeter measures the voltage across 1 and 3.

were connected to two platinum meshes (0.2 mm square opening with 0.1 mm wire diameter) which were pressed against the two surface porous platinum electrodes. One platinum wire was connected to the embedded Pt electrode. Electrochemical measurements were conducted using two types of meters: standard meters (Keithley 2000 6 1/2-Digit Digital Multimeter) and meters (National Instruments NI PXI-4065 6 1/2-Digit Digital Multimeter) capable of very fast sampling rates (3000S/s at 4 1/2-Digit). Data collection was done using LabView software.

In the present work, measurements were made on two samples. Most of the measurements were conducted on a sample with an edge glass seal at the YSZ/Pt wire but

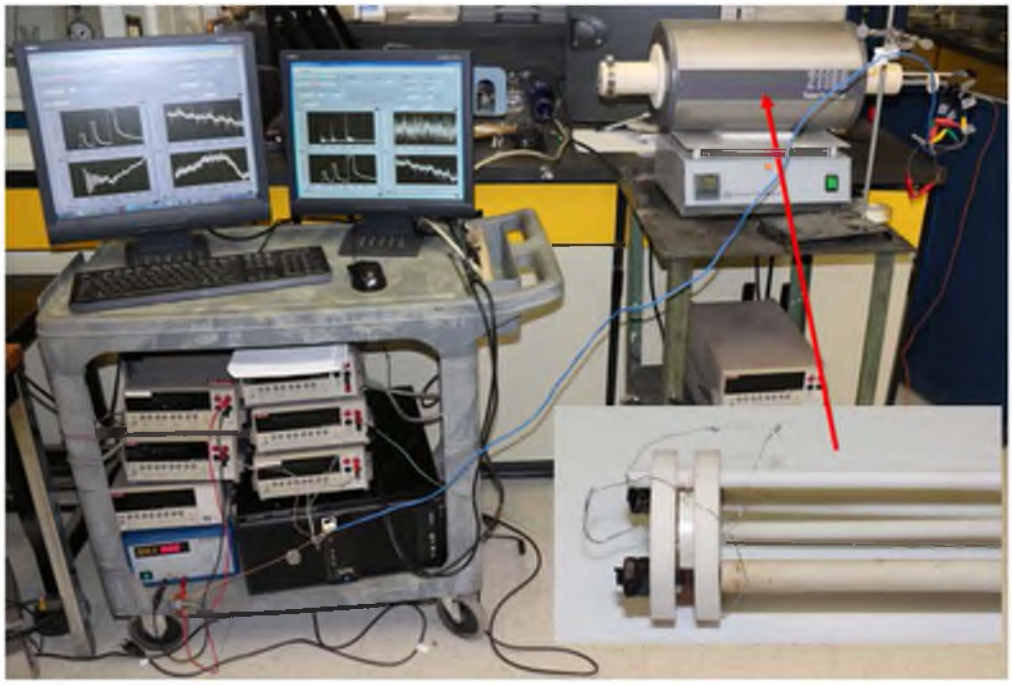

Figure 6-7: A photograph of the testing setup.

with no glass coating on the rest of the exposed surfaces. The applied voltage was fixed at 0.05 V for the measurements on this sample. On this sample, measurements were conducted from 500°C to 800°C. This corresponds to a maximum possible oxygen pressure at the buried Pt electrode of 4.23 atm at 500°C and 1.83 atm at 800°C. Another sample was used in which all exposed surfaces except those covered with porous platinum electrodes were coated with glass. This sample was used to investigate the effect of applied voltage. Measurements on this sample were conducted at one temperature, 800°C. The applied voltage was varied between 0.01 V and 0.1 V in increments of 0.01 V.

The furnace temperature was first increased to the desired value. Initially the setup was in a standby mode when no voltage was applied to the sample. Once a stable state

was achieved, the measured voltage across 1 and 3 electrodes, V_{13}, was initially zero. Then, a DC voltage (E_A) was applied across 1 and 2 with the positive connected to the embedded Pt electrode (2). As soon as the voltage was applied (switch in Figure 6-6 was closed), oxygen (as ions) is pumped from 2 to 1 through the sample. Electrons are released at the buried Pt electrode which transport out through the Pt electrode/wire to the external circuit forming neutral oxygen at the embedded electrode thereby increasing the local oxygen chemical potential (pressure) in YSZ near the embedded electrode. This creates a Nernst voltage, E_N, between the embedded Pt electrode and the porous Pt electrodes, and between the embedded Pt electrode and the exposed surfaces not coated with glass. This Nernst voltage opposes the current, consistent with the equivalent circuit given in Figure 6-2. This leads to an increase in the measured voltage between 1 and 3, V_{13}, and a corresponding decrease in the current, I_A, measured between 1 and 2. As the pressure builds up at the embedded electrode (increase in the Nernst voltage; this may occur by filling and pressurizing any pores existing at the buried electrode and/or slightly changing the local oxygen stoichiometry of the YSZ sample), a thermodynamic force exists for the out permeation of oxygen from the embedded electrode, through the YSZ disc, to the outer surfaces of the disc (to the porous platinum electrodes and to the exposed surfaces not covered with glass). This permeation occurs as a coupled transport of O^{2-} ions and electrons (or holes) through the YSZ, and thus is governed by the ionic resistance, R_i^{diss}, and the electronic resistance, R_e^{diss}, of the sample. This permeation occurs between the embedded Pt electrode and the porous surface platinum electrodes as well as between the embedded Pt electrode and the exposed surfaces not covered with glass. The corresponding equivalent circuit is given in Figure 6-3. In steady state the rate

of electrochemical pumping of oxygen to the embedded Pt electrode (equivalent circuit in Figure 6-2) is equal to the out permeation of oxygen from the electrode to the outer surfaces (equivalent circuit in Figure 6-3). Thus, once the steady state is achieved, the measured current, I_A (1 and 2), and the measured voltage across 1 and 3, V_{13}, become time independent for a given applied voltage E_A (1 and 2). Once this stage is reached, the switch is opened (in circuit in Figure 6-2). The applied voltage (E_A) and the corresponding current (I_A) then drop instantaneously to zero. No longer is oxygen being electrochemically pumped to the embedded electrode. However, a finite, nonzero Nernst voltage exists due to the difference in oxygen pressures established during the charging (pumping) stage. Thus, the permeation process continues. This leads to a continuous decrease in the oxygen pressure at the buried electrode, which means a decrease in the Nernst voltage E_N, and thus a decrease in the voltage measured across 1 and 3 (V_{13}). The rate at which this voltage decreases is governed by the rate of oxygen permeation, which in a predominantly ionic conductor such as YSZ is dictated by its electronic conductivity. After a sufficiently long time, the measured voltage across 1 and 3 approaches zero. This procedure is repeated at several temperatures ranging between 500°C and 800°C.

6.4 Results and Discussion

6.4.1 Microstructural Characterization

Figure 6-8(a) shows an optical micrograph of the Pt wire/YSZ interface taken perpendicular to the wire. Figure 6-8(b) shows a scanning electron micrograph (SEM) of the same sample taken parallel to the wire. The interface is seen to be well-formed with

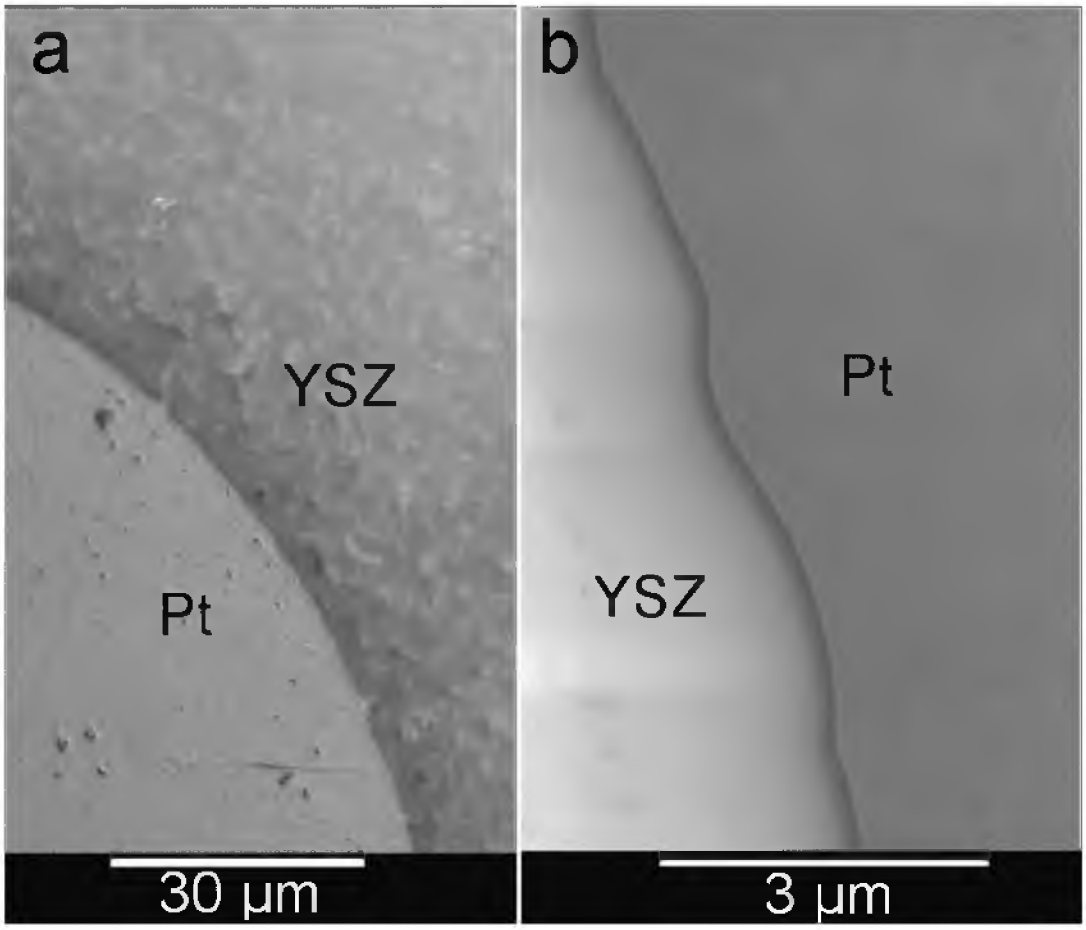

Figure 6-8: Microstructural characterization. (a) An optical microscope image showing the interface between the embedded Pt wire and the surrounding YSZ bulk perpendicular to the Pt wire at a low magnification. (b) An SEM image showing the interfacce between the embedded Pt wire and the surrounding YSZ bulk parallel to the Pt wire at a higher magnification. Note that the interface appears clean with no interfacial pores of cracks.

no pores or cracks.

6.4.2 Electrochemical Measurement Overview

Figure 6-9 shows the results of a typical experiment. The measurements were made using Keithley 2000 meters. This experiment was conducted at 500°C. Initially, in the

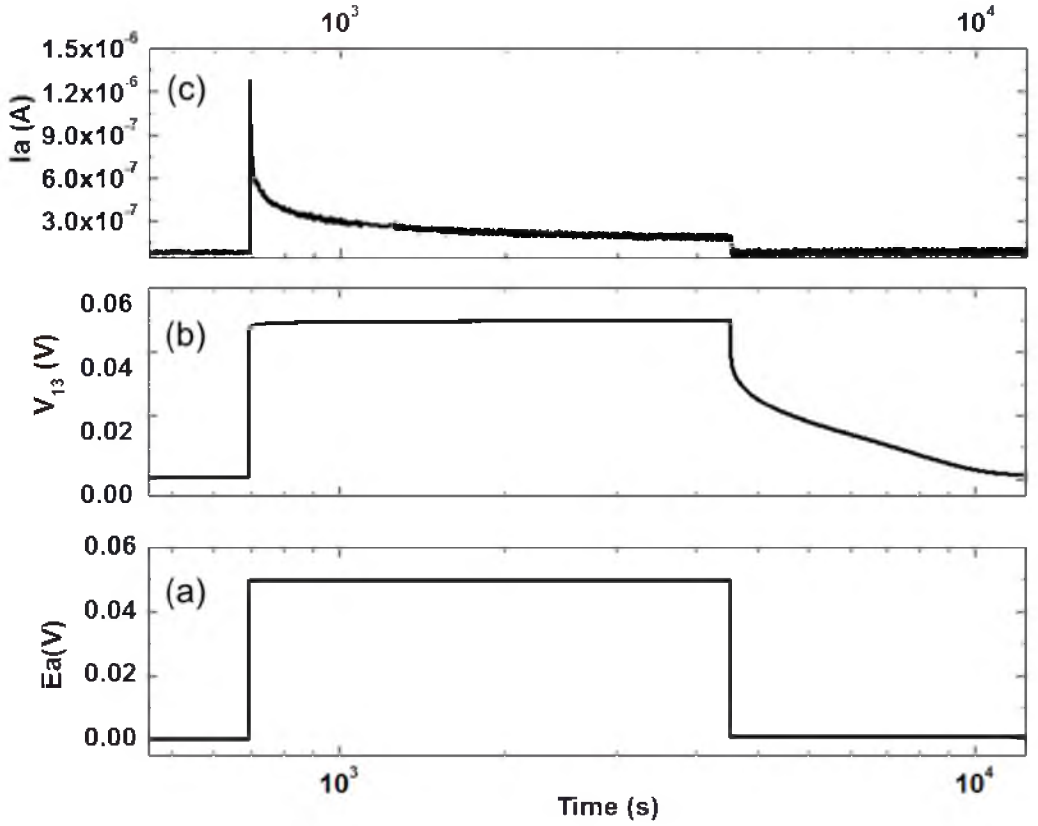

Figure 6-9: Measurements made at 500°C. (a) A plot of applied voltage across 1 and 2, E_A, vs. time. The switch was closed at ~700 seconds and opened at ~4,300 seconds. (b) Measured voltage across 1 and 3, $V_{13}(t)$, vs. time. The $V_{13}(t)$ sharply increases from the initial value of zero to a value close to (but less than) the applied voltage, E_A. After the switch was opened, the $V_{13}(t)$ initially decreased sharply followed by a slow decrease. (c) The measured current, $I_A(t)$, vs. time. As soon as the switch is closed, the $I_A(t)$ rises abruptly from the initial value of zero, then decreases sharply followed by a slow decay. It appears to attain a steady state value after about 2,000 seconds. After opening the switch, the current dropped to zero.

standby mode there was no applied voltage across 1 and 2 ($E_A = 0$). The corresponding measured voltage across 1 and 3 was also zero. This means the chemical potential of oxygen, μ_{O_2}, at the embedded electrode initially was the same as that in the atmosphere. Also, there was no current ($I_A = 0$) since the switch was open. After approximately 700 seconds, an external voltage of 0.05 V was applied across 1 and 2. This corresponds to an abrupt jump in E_A from zero to 0.05 V. The measured current sharply rose from zero to over 1 x 10^{-6} A, and thereafter rapidly decreased. The switching and the measurement of voltage and current were relatively slow in this experiment. Thus, the initial current, I_A^o, just after the voltage was applied could not be measured accurately. The initial current, I_A^o, as soon as the switch was closed must have been much higher than the measured value of ~1 x 10^{-6} A. This is evidenced by the observation that the measured voltage across 1 and 3 also rose rather sharply. This means the electrochemical pumping was very fast, and the initial rise in the voltage across 1 and 3 could not be captured accurately. Over approximately the next 3,000 seconds, the applied voltage E_A was maintained at 0.05 V. The measured voltage across 1 and 3 was also nearly constant and was close to (but slightly lower than) 0.05 V. The measured current, I_A, decreased rapidly from the initial value of ~1 x 10^{-6} A to ~4 x 10^{-7} A in the first ~100 seconds. Thereafter, the current decreased slowly over the next ~3,000 seconds and appeared to stabilize at ~2 x 10^{-7} A. Assuming the steady state had been established, the measured current can be used to estimate the electronic resistance of the sample using equation (6.29).

At approximately 3,800 seconds, the switch was opened. Correspondingly, the applied

voltage E_A and the measured current I_A instantaneously dropped to zero. No longer was oxygen being electrochemically pumped to the buried electrode. However, the permeation of oxygen from the buried electrode to the outer surfaces continued to occur. This resulted in a decrease in the voltage, V_{13}, measured across 1 and 3. Initially, this decrease occurred sharply, and then continued to occur gradually over the next ~8,200 seconds. After about 8,200 seconds since opening up the switch, the measured voltage gradually decreased to near zero, indicating that the oxygen pressure near the embedded electrode had decreased to about the initial value (~0.21 atm).

6.4.3 Measurement of Ionic Resistance

Figure 6-10(a) shows a plot of the measured current $I_A(t)$ vs. time for an applied voltage of $E_A = 0.05$ V at 550°C. The current sharply rose to over 1 x 10^{-4} A followed by an initial sharp decrease and then a gradual decrease. The figure is a superposition of data obtained using the fast response meter (NI PXI-4065 6 1/2-Digit Digital Multi-meter) in the first second and standard multimeters (Keithley 2000 6 1/2-Digit Digital Multi-meter) over the entire duration of the test. After about 1,000 s, the current reached a steady state value. Figure 6-10(b) shows the corresponding measured voltage $V_{13}(t)$ vs. time, which sharply increased to a stable value approaching the applied voltage, E_A. Figure 6-10(c) shows $I_A(t)$ and $V_{13}(t)$ as functions of time on an expanded time scale. Data in Figure 6-10(c) were measured using Keithley 2000 meters. Over this duration (~200 s), a decrease in $I_A(t)$ and an increase in $V_{13}(t)$ with time are clearly seen. Since $R_e >> R_i$, $V_{13}(t) \cong E_N(t)$, that is, the measured voltage between 1 and 3 is essentially the

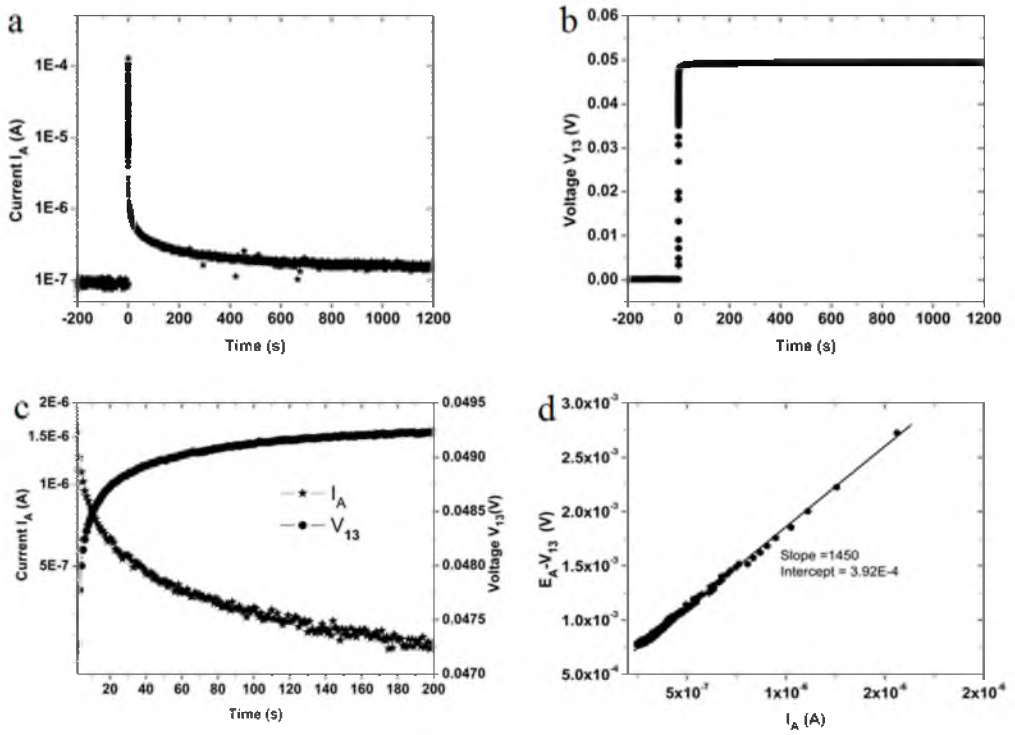

Figure 6-10: Measurements at 550°C. (a) Measured current, $I_A(t)$, as a function of time after applying a voltage, $E_A = 0.05\,\mathrm{V}$. (b) The corresponding measured voltage $V_{13}(t)$ as a function of time. (c) Plots of $I_A(t)$ and $V_{13}(t)$ vs time (up to ~200 seconds) in the early stages after the application of the voltage across 1 and 2. (d) A plot of $E_A - V_{13}(t)$ vs. $I_A(t)$ corresponding to the data shown in (c). The slope gives $R_i = 1,450\Omega$. The meter used for (c) and (d) was Keithley 2000 6 1/2-Digit Digital Multi-meter.

corresponding Nernst potential between the embedded electrode and the atmosphere. Then from equation (6.13), we have

$$I_A(t) = \frac{E_A - E_N(t)}{R_i} + \frac{E_A}{R_e} \cong \frac{E_A - V_{13}(t)}{R_i} \tag{6.32}$$

Thus, a plot of $E_A - V_{13}(t)$ on the y-axis vs. $I_A(t)$ on the x-axis should be a straight line with slope equal to R_i. Figure 6-10(d) shows such a plot.

As seen in Figure 6-10, the data fit well to a straight line with a slope 1,450 Ω. That is, at 550°C, the ohmic resistance is $R_i = 1{,}450\,\Omega$. Figure 6-11 shows similar plots at 800°C. The ohmic resistance at 800°C is estimated to be about $R_i = 39\,\Omega$. Data were obtained over the temperature range from 500°C and 800°C in 50 degree intervals.

Using the measured R_i from the slope of $E_A - V_{13}(t)$ vs. $I_A(t)$, the initial current, I_A^o, just when the switch was closed can be estimated from equation (6.18) and compare it

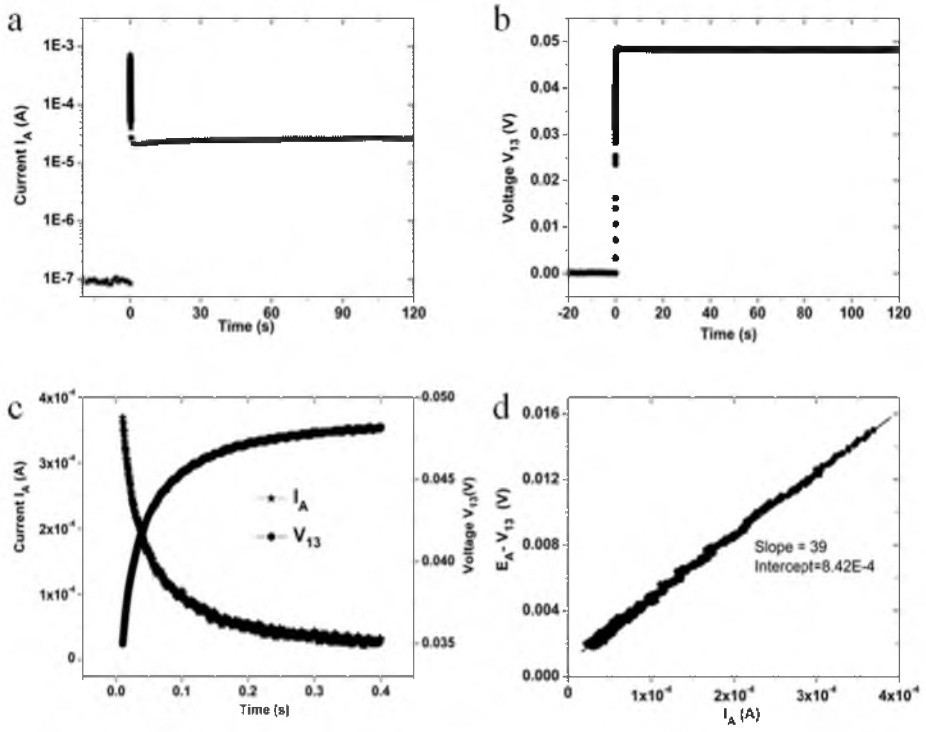

Figure 6-11: Measurements at 800°C. (a) Measured current, $I_A(t)$, as a function of time after applying a voltage, $E_A = 0.05\,\text{V}$. (b) The corresponding measured voltage $V_{13}(t)$ as a function of time. The $V_{13}(t)$ rises sharply and becomes stable approaching E_A. (c) Plots of $I_A(t)$ and $V_{13}(t)$ vs time (up to ~0.4 seconds) in the early stages after the application of the voltage across 1 and 2. On this expanded time scale, the time dependence of both $I_A(t)$ and $V_{13}(t)$ are clearly seen. (d) A plot of $E_A - V_{13}(t)$ vs. $I_A(t)$ corresponding to the data shown in (c).

with the experimentally measured using the fast data acquisition meter (NI PXI-4065 6 1/2-Digit Digital Multi-meter). At 800°C, the calculated value of I_A^o is ~1.28 x 10^{-3} A while the measured value is ~8 x 10^{-4} A. This result shows that the measured I_A^o is lower than the estimated value, suggesting that the initial current measurement was not accurate. At 550°C, the calculated value of I_A^o is ~3.45 x 10^{-5} A. However, the measured value using the fast meter (NI PXI-4065 6 1/2-Digit Digital Multi-meter) is ~1 x 10^{-4} A. It is clear that the measured I_A^o cannot be greater than the calculated value. It thus appears that there is an apparent 'overshoot' in the measurement of the current at the time switch was closed. Thus, the R_i estimated from the slope of $E_A - V_{13}(t)$ vs. $I_A(t)$ is deemed more accurate. An Arrhenius plot of $\ln\left(\frac{R_i}{T}\right)$ vs. $\frac{1000}{T}$ is shown in Figure 6-12. The measured activation energy is about 110 kJ.mol^{-1} (~1.14 eV). This value is typical of ionic conduction in YSZ, especially at low temperatures when grain boundary contribution is significant and cannot be neglected [6].

From the measured steady state current, $I_A(\infty)$, for a given applied voltage, E_A, the electronic resistance, R_e, was calculated using equation (6.29). Figure 6-13 shows an Arrhenius plot of $\ln\left(\frac{R_e}{T}\right)$ vs. $\frac{1000}{T}$. The corresponding activation energy is about ~153 kJ.mol^{-1} (~1.59 eV).

The estimated values of R_i and R_e are listed in Table 6-1. From the values of R_i and R_e over the range of temperatures from 500°C to 800°C, the ionic transference number of YSZ, given by $t_i = \frac{R_e}{R_i + R_e} > 0.99$, is in accord with expectations.

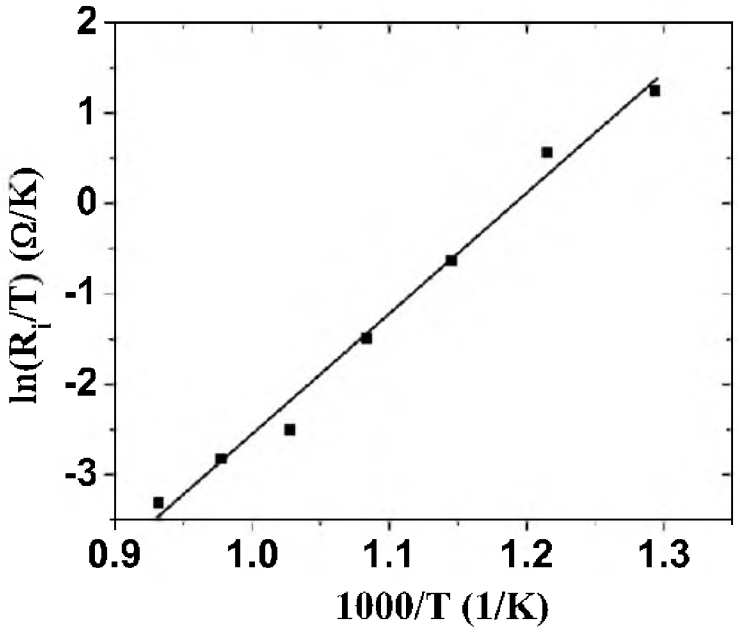

Figure 6-12: An Arrhenius plot of the measured R_i : $\ln\left(\frac{R_i}{T}\right)$ vs. $\frac{1000}{T}$. The measured activation energy is $Q_i \approx 110\,\text{kJ.mol}^{-1}$ (~1.12 eV).

The ionic resistivity of YSZ at 800°C is ~25 Ωcm. The measured R_i in the present work at 800°C was ~39 Ω. From these measurements, the geometric factor is estimated as

$$R\left(\frac{\ell}{A}\right)_{eff} = \frac{R_i}{\rho_i} = 1.56\ \text{cm}^{-1} \qquad (6.33)$$

It is in principle possible to calculate the geometric factor, which allows the measurement of the conductivities from the measured resistances. In the present work, using the above geometric factor obtained using the known ionic resistivity of YSZ at

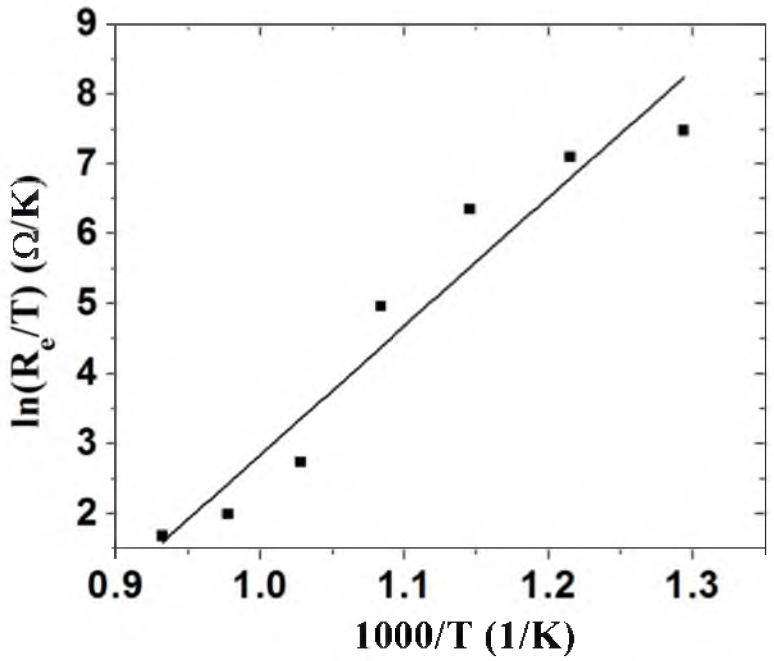

Figure 6-13: An Arrhenius plot of the measured R_e: $\ln\left(\frac{R_e}{T}\right)$ vs. $\frac{1000}{T}$. The measured activation energy is $Q_{el} \approx 153\ \text{kJ.mol}^{-1}$ (~1.56 eV).

800°C of 25 Ωcm, the ionic resistivity, ρ_i, was estimated over a range of temperatures from 500°C to 800°C. These values are listed in Table 6-2. The inverse of ρ_i is σ_i, the ionic conductivity. Figure 6-14 shows an Arrhenius plot of the ionic conductivity of 8YSZ determined in the present work over the temperature range from 500°C to 800°C. The ionic conductivity increases when temperature increases. This indicates the ionic transport to be a thermally activated process. The slope of the linear fitting function gives the activation energy, which is calculated to be 1eV. This value is very typical for yttria stabilized zirconia.

Table 6-1: Measured steady state current, and ionic and electronic resistances

$T\ (^{\circ}C)$	$I_A(\infty)\ (A)$	$R_i\ (\Omega)$	$R_e\ (\Omega)$
500	1.09E-07	2698	1.38E+06
550	1.50E-07	1450	1.00E+06
600	3.01E-07	464	4.98E+05
650	1.14E-06	207	1.32E+05
700	1.00E-05	80	1.50E+04
750	2.00E-05	61	7.50E+03
800	2.60E-05	39	5.77E+03

Table 6-2: Calculated ionic resistivity of 8YSZ

$T\ (^{\circ}C)$	$\rho_i\ (\Omega \cdot cm)$
500	1730
550	929
600	297
650	133
700	51
750	39
800	25[#]

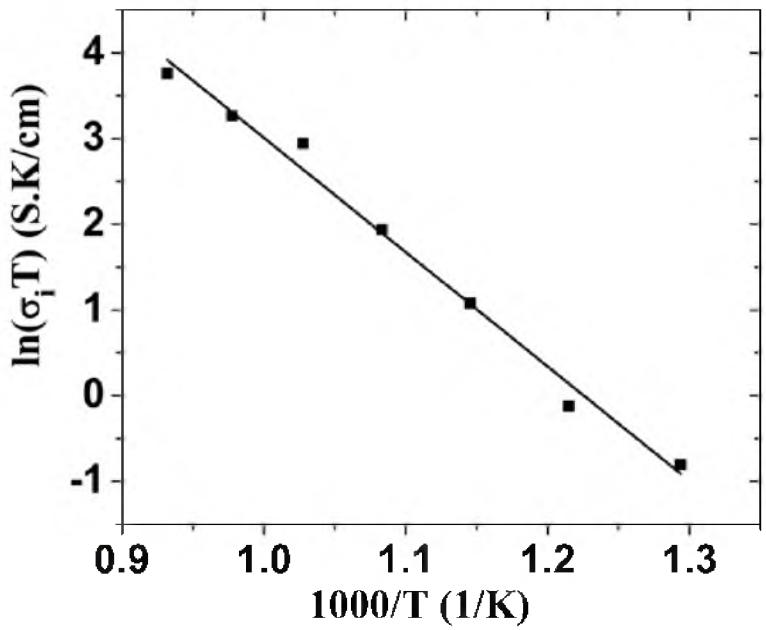

Figure 6-14: An Arrhenius plot of the measured ionic conductivity.

6.4.4 The Effect of Applied Voltage

For these experiments, a sample coated with glass on all exposed surfaces except the porous platinum electrodes (Figure 6-4(c)) was used. The experiments were conducted on the measurement of the electronic resistance as a function of applied voltage, E_A, over a range from 0.01 V and 0.1 V at 800°C. The corresponding oxygen partial pressure generated at the embedded electrode ranged between about 0.32 atm for 0.01 V to 15.89 atm for 0.1 V. All other measurements at various temperatures, the results of which are given in Figure 6-8 through Figure 6-14, were made on a sample which was glass-sealed only along the circular edge between the buried electrode and YSZ. Also, those measurements were conducted at an applied voltage of 0.05 V, which corresponds to a maximum oxygen pressure at the embedded electrode of 1.83 atm at 500°C.

Since the sample was glass coated on all exposed surfaces except those covered with porous platinum electrodes, equations (6.21), (6.22) and (6.23) are applicable. This means the electronic resistance during permeation is half of that during oxygen pumping, given by equation (6.20). Table 6-3 lists the applied voltage, E_A, the measured steady state voltage, V_{13} (which is assumed to be nearly the same as the Nernst voltage, E_N), the estimated oxygen pressure, p_{O_2}, at the embedded electrode (calculated from the E_N), the measured steady state current, $I_{A(\infty)}$, and the calculated electronic resistance, R_e.

Table 6-3: Measured ionic and electronic resistance at 800°C as a function of applied voltage.

$E_A\,(V)$	$p_{O_2}\,(atm)$	$E_N\,(V)$	$I_A(\infty)\,(A)$	$R_i\,(\Omega)$	$R_e\,(\Omega)$	$\rho_e\,(\Omega\cdot cm)$
0.00999	0.32	0.00998	1.15E-06	55.3	2.61E+04	1.24E+04
0.01995	0.50	0.01991	2.49E-06	50.0	2.40E+04	1.14E+04
0.02999	0.77	0.02998	4.57E-06	51.6	1.97E+04	9.33E+03
0.03987	1.19	0.03953	8.62E-06	50.9	1.39E+04	6.59E+03
0.04962	1.83	0.04928	7.28E-06	55.9	2.04E+04	9.67E+03
0.05986	2.82	0.05936	1.07E-05	50.4	1.68E+04	7.96E+03
0.06810	4.34	0.06730	1.65E-05	52.5	1.24E+04	5.88E+03
0.79960	6.69	0.79100	1.90E-05	52.5	1.26E+04	5.97E+03
0.08986	10.30	0.08869	2.53E-05	53.6	1.07E+04	5.07E+03
0.09987	15.90	0.09840	3.08E-05	54.9	9.73E+03	4.61E+03

The data show that for the sample geometry used, the lowest measured current was 2.49 x 10^{-6} A. Thus, using the method described here, it should be possible to measure current at rather low applied voltages, facilitating the measurement of electronic conductivity with virtually no redistribution of oxygen occurring within the sample.

Table 6-3 shows that the measured electronic resistance, R_e, varies from ~2.61 x 10^4 Ω at an applied $E_A = 0.01\,\mathrm{V}$ to ~9.73 x 10^3 Ω at an applied $E_A = 0.1\,\mathrm{V}$, a variation by a factor of ~1/2.69. This result is qualitatively consistent with expectations. As stated earlier, the samples were sintered in air. The corresponding electronic conduction in YSZ is expected to be in the p-type range. As the applied voltage, E_A, is increased, the corresponding Nernst voltage, E_N, also increases. This means an increase in p_{O_2} occurs at the embedded electrode as well as over the region from the porous electrode to the embedded electrode. This should lead to an increase in electronic conductivity such that at any position in the sample $\sigma_e(x) \sim p_{O_2}^{1/4}(x)$. Thus, we expect that as the applied voltage is increased, the electronic conductivity should also increase (the electronic resistance, R_e should decrease). Figure 6-15 shows a plot of $\ln R_e$ vs. $\ln pO_2$ where the p_{O_2} is the oxygen pressure at the embedded electrode. While a detailed calculation will require one to take into account the geometry factor and the spatial dependence of p_{O_2} between the surface and the embedded electrode, it is interesting to note that the slope of the line is -0.246, very close to a value of - ¼ based on the expected dependence of electronic conductivity on oxygen partial pressure in the p-type region. By contrast, the measured ionic resistance, R_i, is about 50 to 55 Ω, independent of the applied voltage. This is precisely the expectation since the ionic resistance is governed by the oxygen vacancy

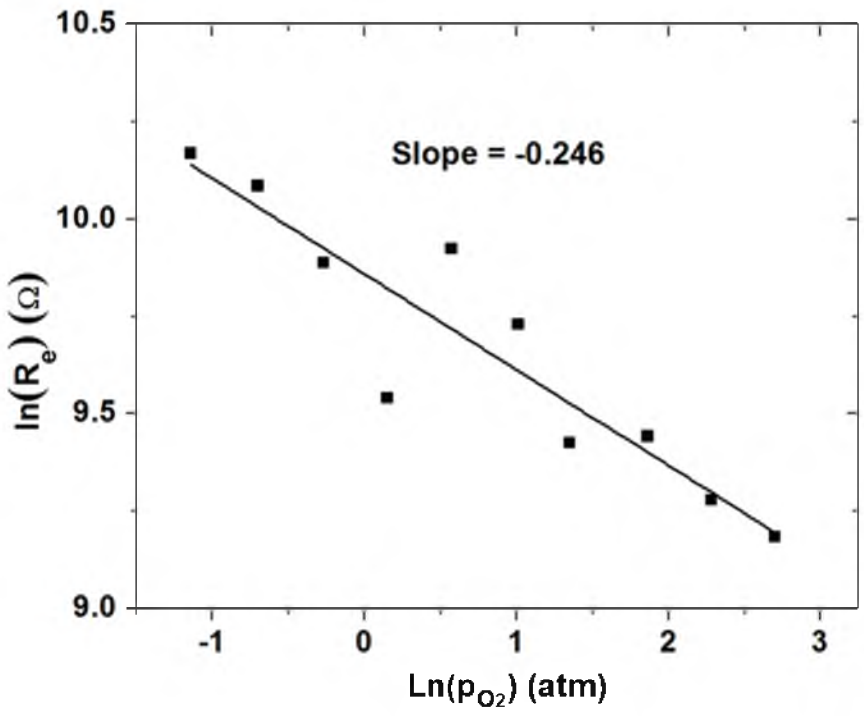

Figure 6-15: The measured electronic resistance at 800°C, R_e, as a function of the calculated p_{O_2} at the embedded probe. The applied voltage, E_A, was varied between 0.01 V and 0.1 V.

concentration, which is fixed by the dopant (yttrium) concentration and is not a function of p_{O_2} over the range of p_{O_2}'s in the present experiments.

Comparison of Table 6-1 and Table 6-3 shows that at 800°C, the measured R_i for the sample coated with glass on all exposed surfaces (except the porous electrodes) ranged from 50 to 55 Ω, which is greater than R_i of 39 Ω for the sample used for the data given in Figure 6-8 through Figure 6-14 (which was not glass-coated except for the edge seal). This difference is attributed to the small difference in electrode areas (electrode diameters of 13 mm vs. 11 mm).

6.4.5 Comparison Between Samples with and without Surface Glass Coating

The measured R_e at 800°C for an applied voltage of 0.05 V on a sample coated with glass on all exposed surfaces except the porous Pt electrodes was ~2.04 x 10^4 Ω, compared to that for a sample with only an edge glass seal along YSZ/Pt wire periphery (~5.77 x 10^3 Ω). That is, the R_e of the glass-coated sample was about ~3.53 times larger. Part of this difference must be related to the differences in surface areas exposed to the atmosphere. In the data given in Table 6-1, the sample was not glass-coated (except for the circular edge adjacent to the buried electrode). In the data given in Table 6-3, all exposed surfaces (except the porous platinum electrodes) were coated with glass. The total area of the porous platinum electrodes was $2\times\frac{\pi}{4}\times(1.1)^2=1.901\,\text{cm}^2$. This is the surface area through which oxygen permeates out of the glass-coated sample (Figure 6-4(d)). The total surface area of the sample was $2\times\frac{\pi}{4}\times(2.5)^2+\pi\times2.5\times0.3=12.174\,\text{cm}^2$. This is the surface area through which oxygen permeates out of the sample when the exposed surfaces are not glass coated (Figure 6-4(b)). That is, the ratio of the two areas through which permeation occurs in the two samples (without and with glass coating) is 6.4. The observation that the ratio of the areas is 6.4 while the ratio of the corresponding electronic resistances is ~3.53 suggests that the exposed surfaces uncoated with glass are probably as efficient in allowing oxygen to permeate out of the sample as the porous electrodes. An exact correspondence between the two numbers is not expected given the complicated geometry of the sample. That is, the ratio of electronic resistances in the two samples is not expected to be the same as the ratio of areas. However, the observation

that the exposed surfaces without porous platinum are effective in permeation as the ones coated with porous platinum may actually be very reasonable. This is because the following reaction occurs at the exposed surfaces (with or without porous Pt)

$$2O^{2-}(YSZ) \rightarrow O_2(gas) + 4e'(YSZ)$$

which is the same as reaction (iv). Note that in this reaction, there is no electron transfer across the gas-solid interface. The transfer of oxygen molecules occurs from the solid phase into the gas phase while retaining electrons in the solid (YSZ). As such, there is no role for porous platinum unlike the oxygen reduction reaction (reaction (i)). That is, effectively, there is no role for the porous platinum in permeation as it does not participate in any electrochemical reaction.

In order to estimate the electronic resistivity of YSZ from the measured electronic resistance on the sample without a glass coating over the range of temperatures, a factor of 3.53 (obtained from measurements at 800°C on the sample with and the sample without a glass coating) was used. That is, the electronic resistance as a function of temperature listed in Table 6-1 was multiplied by 3.53. The corresponding electronic conductivity of YSZ, σ_e, is given as an Arrhenius plot in Figure 6-16.

6.4.6 Comparison with Literature Data

The activation energy for ionic conduction determined in the present work is $Q_i \approx 110\,\text{kJ.mol}^{-1}$ (~1.14 eV). Reported activation energies for ionic conduction in 8YSZ using the same raw material (TZ-8Y, Tosoh, Japan) under similar sintering conditions

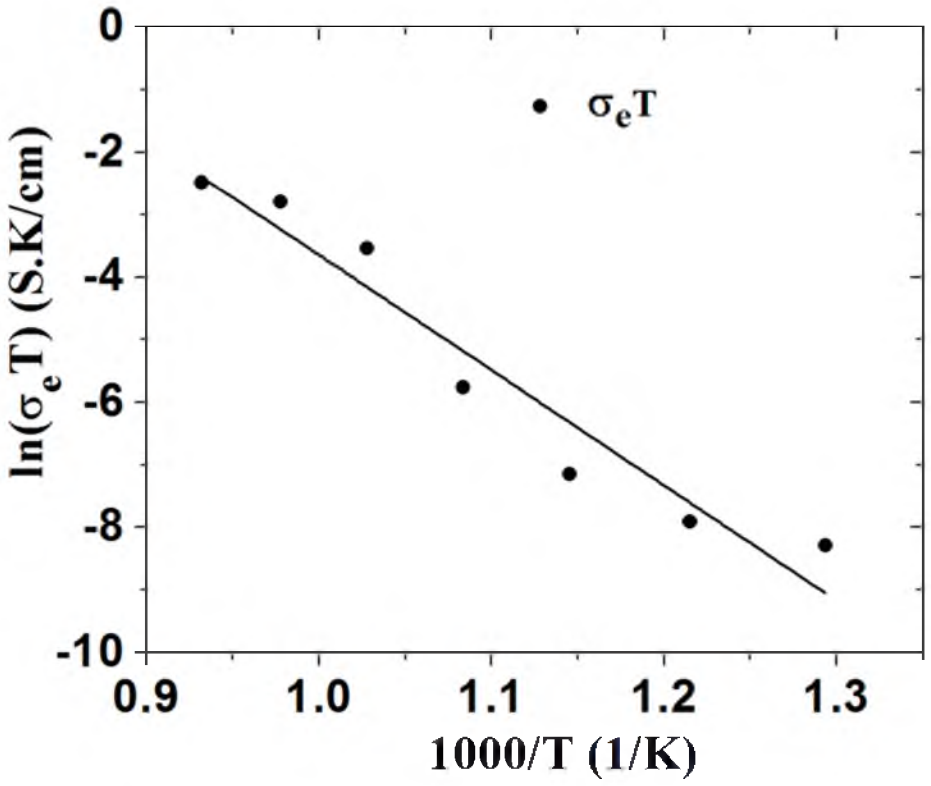

Figure 6-16: An Arrhenius plot of the measured electronic conductivity.

range between ~104 kJ.mol^{-1} and ~110 kJ.mol^{-1} [7-10], with higher values at lower temperatures. In the present work, the measured activation of ~110 kJ.mol^{-1} is for the temperature range 500°C (773 K) to 800°C (1073 K). The measured activation energy for ionic conduction in YSZ in the present work is thus in good agreement with literature values.

The activation energy for hole conduction in YSZ is reported to be ~1.67 eV [4]. In the present work, the estimated value of the activation energy is ~1.56 eV, again in good agreement with the reported literature values.

Park and Blumenthal [4] have given an equation for hole conductivity in 8YSZ as follows:

$$\sigma_h = 2.35 \times 10^{2} \times p_{O_2}^{-\frac{1}{4}} \times \exp\left[-\frac{1.67\ \text{eV}}{k_B T}\right] \tag{6.34}$$

Using equation (6.34), the estimated value of electronic conductivity in the p-type region at 800°C and at a $p_{O_2} = 0.21\text{atm}$ is ~3.37 x 10^{-6} Scm^{-1}. By contrast, the measured electronic conductivity in the present work is ~7.7 x 10^{-5} Scm^{-1}. Thus, the measured electronic conductivity is nearly 30 times higher than the value given by Park and Blumenthal [4]. Valov et al. [11] also measured an electronic conductivity of ~4 x 10^{-4} Scm^{-1} on 8YSZ at 800°C in air, which is in excellent agreement with the present results. It thus appears that there is a significant difference in the reported values of electronic conductivity of 8YSZ under similar conditions. It remains to be verified if this difference is related to possible differences in measurement techniques and/or possible small differences in composition (presence of impurities). In much of the reported work on the measurement of electronic conductivity of YSZ, a large voltage (> 0.25 V and as high as 2 V) was applied. This leads to large spatial variation in oxygen chemical potential within the sample (p_{O_2} inside the sample varying over several orders of magnitude). Under such conditions, the electronic conductivity is a function of position in the sample, and part of the sample is generally under intrinsic conditions, with correspondingly very low local electronic conductivity. Additionally, in most studies using the Hebb-Wagner technique, the electronic conductivity is deduced by fitting to the Hebb-Wagner equation. In the present work, by contrast, there is negligible variation in oxygen chemical potential due to the very small applied voltage (0.05 V and as low as 0.01 V). Thus, the electronic conductivity is essentially constant throughout the sample, which affords a direct

measurement of the electronic conductivity. In the present work, the measured electronic conductivity is that corresponding to air, and thus is p-type.

The ionic transference number of 8YSZ at 800°C is determined to be ~0.99 or larger over the range of experimental parameters used in the present work. When measurements were made as a function of applied voltage, the estimated ionic transference number (assumed here as the ratio E_N / E_A) at 800°C varies between 0.9990 for $E_A = 0.01\,\mathrm{V}$ and 0.9853 for $E_A = 0.1\,\mathrm{V}$. This is consistent with the higher estimated electronic conductivity at higher applied voltage. The estimated ionic transference number for an applied voltage $E_A = 0.1\,\mathrm{V}$ is given below as $t_i = \frac{R_e}{R_i + R_e} = \frac{9730}{53 + 9730} = 0.9946$. The present results thus show that the ionic transference number of 8YSZ is about 0.99 or greater over the measured temperature range.

6.4.7 Implications Concerning the Use of YSZ under Large Applied Oxygen Chemical Potential Differences

In the present work, the electronic conductivity of 8YSZ was estimated at 800°C to be about ~7.7 x 10^{-5} Scm^{-1}. This value is about the same as that measured by Valov et al. [11] under similar conditions, but is higher by a factor of ~30 than measured by Park and Blumenthal [4]. An important point to note is that the current measurement corresponds to air, and the corresponding electronic conductivity corresponds to the p-type regime. In many applications of YSZ, a large chemical potential difference of oxygen, $\Delta\mu_{O_2}$, is applied across a YSZ membrane or a disc. In such cases, the electronic conductivity of the membrane or the disc is a function of position and in the intrinsic part can be orders

of magnitude lower [3-5]. As a result the overall electronic conductivity may be dictated by the highly electrically insulating part (that corresponding to the intrinsic region) of the membrane or the disc. Under such conditions, the YSZ may exhibit very low electronic conductivity and thus a high ionic transference number. One such example of an application is the use of YSZ discs in coulometric titration. We present here an order of magnitude estimate of oxygen permeation through a disc at 800°C in coulometric titration.

At 800°C, the intrinsic behavior in YSZ occurs at a $p_{O_2} \approx 10^{-10}$ atm [3-5,11]. The corresponding electronic conductivity obtained by extrapolation, is about 10^{-8} to 10^{-7} Scm^{-1} [3-5,11]. We will select the high value. We assume a YSZ disc of ~2 mm thickness and further assume that about half the thickness (~1 mm) corresponds to a region of intrinsic electronic conductivity. For a sample of 1 cm^2 in area, the corresponding electronic resistance is 10^6 Ω. For net applied $\Delta\mu_{O_2}$, equivalent to 1 V, the net permeation current is 1 μA. The amount oxygen that would have transported by permeation in 1 week is ~0.6 Coulombs or about 1.56×10^{-6} moles of O_2 or about 5×10^{-5} gm of oxygen. Assuming the electrode masses are between several milligrams to several tens or hundreds of milligrams, this level of permeation will not likely cause significant changes in mass/stoichiometry of the electrodes used in such studies. That is, over a sufficiently large applied $\Delta\mu_{O_2}$, YSZ will be an essentially purely ionic conductor with negligible electronic conductivity. It is to be noted that an absolute measurement of electronic conductivity in the intrinsic regime is necessary to make a quantitative assessment of potential electronic leakage in devices with YSZ as the electrolyte.

6.5 Summary

A new technique for the measurement of both ionic conductivity and electronic conductivity of predominantly oxygen ion conductors was developed. Experimental results are reported on 8YSZ. The sample geometry consists of a YSZ disc with an embedded platinum wire as one electrode and two symmetrically positioned porous platinum surface electrodes. A DC voltage is applied between the embedded Pt electrode and one of the surface porous electrodes. The negative terminal of the voltage source is connected to the porous electrode and the positive terminal is connected to the embedded wire. During the test, the current is measured between the embedded electrode and the surface electrode connected to the voltage source, and the voltage is measured between the embedded electrode and the other porous electrode. Under the applied voltage, oxygen is electrochemically pumped to the embedded electrode. As the local oxygen pressure builds up, oxygen permeation occurs from the embedded electrode to the outer exposed surfaces of the sample. In steady state, the rate of electrochemical pumping of oxygen is exactly balanced by the out permeation of oxygen. Electrical measurements were made as a function of time. The analysis of the time dependence of the measured current, the measured voltage, and the measured steady state current allows one to determine both the ionic and the electronic conductivities. The technique allows for the measurement of electronic conductivity of YSZ at as low a temperature as 500°C and under very low applied voltages. In the present work, the measurements were made at an applied voltage of 0.05 V, and at as low as 0.01 V. This ensured that negligible re-distribution of oxygen occurred in the sample during the test. In the present work, the electronic conductivity of 8YSZ was measured in air, thus corresponding to

$p_{O_2} = 0.21\text{atm}$. The measured electronic conductivity was p-type. The ionic transference number of 8YSZ over the temperature range from 500°C to 800°C was greater than 0.99.

6.6 References

1. M. H. Hebb, *J. Chem. Phys.*, **20**, 185 (1952)

2. C. Wagner, *Proc. 7th Int. Conf Electrochem. Thermodyn. Kinet.*, 361 (1955)

3. K. Kobayashi, *Solid State Ionics*, **93**, 193–199 (1997)

4. J. H. Park and R. N. Blumenthal, *J. Electrochem. Soc.*, **136**, 2867–2876 (1989)

5. W. Weppner, *J. Solid State Chem.*, **20**, 305–314 (1977)

6. D. J. Fisher, *Diffus. Ceram. - 10 Years Res.*, **169-170** (1999)

7. Q. Dong et al., *Int. J. Hydrogen Energy*, **34**, 7903–7909 (2009)

8. R. M. Batista and E. N. S. Muccillo, *Ceram. Int.*, **37**, 1929–1934 (2011)

9. T. S. Zhang et al., *Solid State Ionics*, **180**, 1311–1317 (2009)

10. G. C. T. Silva and E. N. S. Muccillo, *Solid State Ionics*, **180**, 835–838 (2009)

11. I. Valov et al., *Solid State Ionics*, **180**, 1463–1470 (2009)

CHAPTER 7

ELECTRONIC CONDUCTIVITY MEASUREMENT IN SOLID ELECTROLYTES: A TRANSIENT TECHNIQUE

Measurement of both ionic and electronic partial conductivities in MIECs and solid electrolytes is of interest. Embedded probe technique is used here to measure electronic conductivity in YSZ as an example to measure and manipulate a material's properties. Cylindrical disc samples with embedded Pt probe and a cavity are made using die-pressing and sintering at 1500°C. Pt paste is applied to both surfaces to form electrodes (surface electrodes), and the rest of the bare YSZ surface is covered by a sealant glass. During charging, O^{2-} ions migrate through the YSZ electrolyte, and electrons migrate through the external circuit. Neutral oxygen molecules are effectively transported to the Pt probe. This process is governed by O^{2-} conductivity, and the ionic resistance can be obtained using Ohm's law. During discharging, both O^{2-} ions and electrons migrate through YSZ electrolyte driven by the Nernst potential generated between the surface electrode and the embedded electrode. This oxygen flux is limited by electron flux. The observed time dependence of Nernst potential can be used to estimate the electronic conductivity of YSZ.

7.1 Introduction

Predominantly ionic conductors and mixed ion and electron conductors (MIEC) have numerous applications in gas permeable membranes, solid oxide fuel cell (SOFC), and solid oxide electrolysis cell (SOEC) to name a few. Both ionic and electronic conductivities of MIEC are of interest. A traditional way to measure partial conductivity is the Hebb-Wagner polarization method [1-3]. In the original work by Hebb, electronic conductivity of Ag_2S was measured as a function of position by measuring position-dependent electric potential. Application of the Hebb-Wagner method to materials such as YSZ involves fitting to the Hebb-Wagner equation, since in most studies position-dependent electric potential cannot be readily measured. Most measurements are made under applied voltage large enough so that parts of the sample exhibit n-type and p-type conduction as well as the intrinsic region in which the electronic conductivity is exceptionally low. Here in the present work, a transient technique is designed and applied to measure the electronic conductivity in 8YSZ.

7.2 Experimental Details

7.2.1 Sample Fabrication

Disc samples of 8YSZ with embedded Pt probe and no cavity are made using the procedure described elsewhere [4]. Here in this paper, only the procedure for samples with embedded Pt probe and a center cavity is described. About 5g of 8YSZ powder is first placed into a cylindrical die with a diameter of 32mm. Slightly press the powder with the top piston, then place a metal disc with a diameter of 3mm and thickness of 0.28mm at the center of the powder. After applying a uniaxial pressure of 1ton, the top

piston is released, and the metal disc is removed from the prepressed powder compact. The prepressed powder compact is taken out from the cylindrical die. Following the above steps, another prepressed powder compact is made, but it remains in the cylindrical die. A platinum wire with a diameter of 0.18mm is placed along the radial direction from the center to the circumference. The length of the wire is the same as the radius of the cylindrical die. Subsequently, the first prepressed powder compact is pushed into the die again, with the cavity facing towards the second prepressed powder compact. After applying a uniaxial pressure of 5ton for 30 seconds, the top piston is released, and the green disc is removed. A small part of the disc perpendicular to the embedded platinum probe is cut off in order to expose part of the electrode (approximately 2 mm in length). The disc is then sintered in air at 1500°C for 5 h. After sintering, the Pt electrode and the center cavity is embedded into the disc.

Platinum paste (Heraeus) is applied on both surfaces of the sintered disc, with a circular area of about 13 mm in diameter. The disc is then fired in air at 800°C for 1 h to remove organic solvent to form porous platinum electrodes. All the exposed 8YSZ surfaces that are not covered with porous platinum electrodes are coated with SCZ-8 sealant glass (SEM-COM) and fired at 900°C for 1 hour. The glass coating is introduced to further eliminate gas leakage, as well as to prevent reaction at the triple phase boundary near the Pt probe.

7.2.2 Electrochemical Measurement

Figure 7-1 shows how the sample is measured. All tests are conducted over a range of temperatures from 550 °C to 800 °C by heating the sample in a tubular furnace. The disc

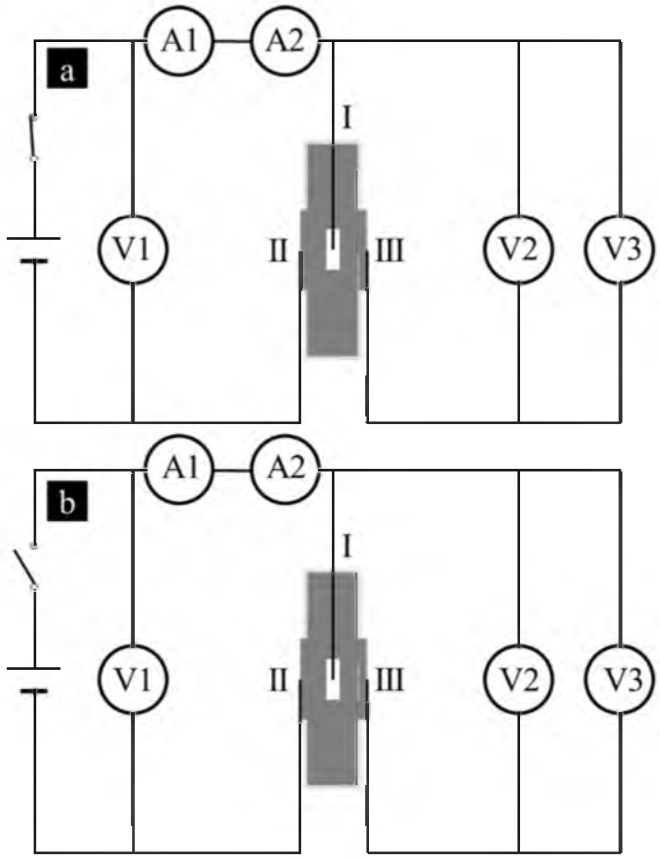

Figure 7-1: Electric Circuit used for the electrochemical measurement. 1a corresponds to charging stage; 1b corresponds to discharging stage. Electrode I is the embedded Pt probe, electrode II and III are porous Pt electrode. The power source has a constant voltage output of 0.03V. A low speed voltmeter (V1) is used to measure applied dc voltage bias. A low speed ammeter (A1) and a high speed ammeter (A2) measure the charging current. A low speed voltmeter (V2) and a high speed voltmeter (V3) measure the Nernst potential.

sample is placed in a sample holder made of alumina. Each of the two porous Pt electrodes is covered with Pt mesh, and Pt leads are used to connect the two meshes and embedded Pt probe with the electric meters.

The DC voltage bias between electrode I and II is provided by a National Instruments power source, and is monitored by a low speed (< 4sampling/second) Keithley 2000 digital multimeter.. The charging current through electrode I and II is monitored by a low

speed Keithley 2000 digital multimeter and a high speed (~3000 sampling/second) National Instrument PXI-4065 digital multimeter in serial. The Nernst potential between electrode I and III is monitored by a low speed Keithley 2000 digital multimeter and a high speed National Instrument PXI-4065 digital multimeter in parallel.

7.3 Theoretical Model

7.3.1 Charging Stage

When a DC voltage bias is applied between electrode I and II, oxygen ion migrates from electrode II to electrode I through the 8YSZ electrolyte (shown in Figure 7-2(a)). Electron migrates from electrode I to electrode II through the outer electric circuit. At electrode II, neutral oxygen molecule at triple phase boundary is reduced to oxygen ion; at electrode I, oxygen ion is oxidized to neutral oxygen molecule and stored in the cavity. As oxygen partial pressure in the cavity builds up, the Nernst potential between embedded Pt probe and the two porous Pt electrodes increases. The Nernst potential drives dissipation current of oxygen ion from electrode I to electrode II and III through 8YSZ electrolyte. The dissipation current eventually rises to the same value as charging current, so that the oxygen partial pressure in the cavity is maintained constant. The state in which dissipation current equals charging current is the steady state, and a detailed analysis about steady state was presented elsewhere [4].

7.3.2 Discharging Stage

Once DC voltage bias is shut off during the steady state, it begins the discharging stage. Oxygen molecules that are stored in the cavity continue to migrate from electrode I

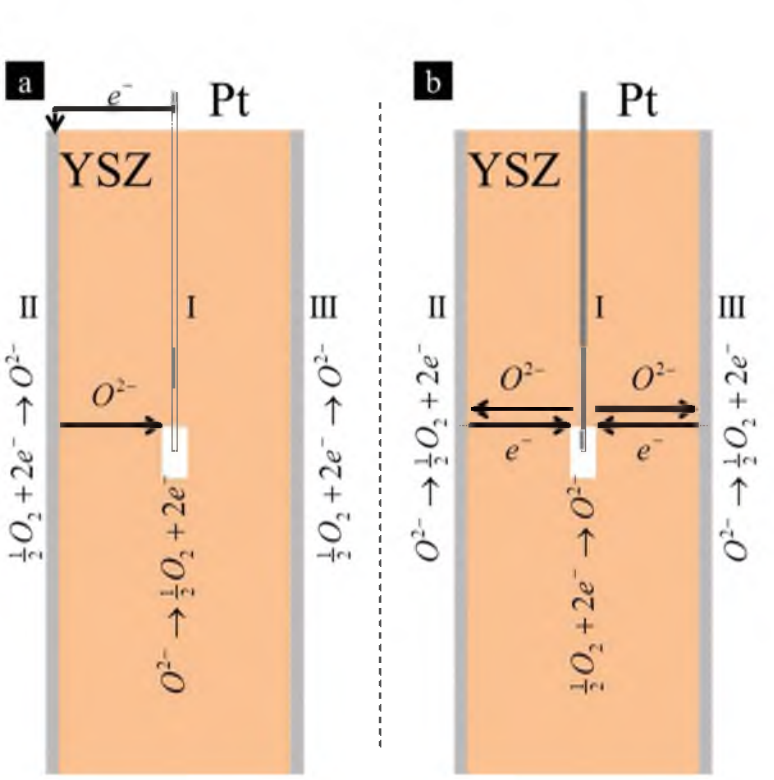

Figure 7-2: Cross section view of the 8YSZ disc sample with embedded Pt probe and a cavity. 2a shows the charge migration path and electrode reactions during charging stage; 2b shows the charge migration path and electrode reactions during discharging stage.

to electrode II and III driven by the Nernst potential. However, due to the absence of DC bias, there's no charging current any more. As a result, the amount of oxygen molecules in the cavity decreases leading to a decreasing Nernst potential. The dissipation current and redox reactions are shown in Figure 7-2(b). A quantitative description of the discharging stage is provided in the following.

Since the 8YSZ sample is symmetric, only half of the sample is considered.

At position I and time t, local equilibrium requires that

$$\begin{aligned} \tfrac{1}{2}\mu_{O_2}^{\mathrm{I}}(t) + 2\tilde{\mu}_e^{\mathrm{I}}(t) &= \tilde{\mu}_{O^{2-}}^{\mathrm{I}}(t) \\ \tilde{\mu}_e^{\mathrm{I}}(t) &= \mu_e^{\mathrm{I}}(t) - e\Phi^{\mathrm{I}}(t) \\ \tilde{\mu}_{O^{2-}}^{\mathrm{I}}(t) &= \mu_{O^{2-}}^{\mathrm{I}}(t) - 2e\Phi^{\mathrm{I}}(t) \end{aligned} \tag{7.1}$$

where $\mu_{O_2}^{\mathrm{I}}(t)$, $\mu_e^{\mathrm{I}}(t)$ and $\mu_{O^{2-}}^{\mathrm{I}}(t)$ are the chemical potential of oxygen molecule, electron and oxygen ion, respectively, at position I and time t; $\tilde{\mu}_e^{\mathrm{I}}(t)$ and $\tilde{\mu}_{O^{2-}}^{\mathrm{I}}(t)$ are the electrochemical potential of electron and oxygen ion, respectively, at position I and time t; $\Phi^{\mathrm{I}}(t)$ is the electrostatic potential at position I and time t.

At position II and time, local equilibrium requires that

$$\begin{aligned} \tilde{\mu}_{O^{2-}}^{\mathrm{II}}(t) &= \tfrac{1}{2}\mu_{O_2}^{\mathrm{II}}(t) + 2\tilde{\mu}_e^{\mathrm{II}}(t) \\ \tilde{\mu}_e^{\mathrm{II}}(t) &= \mu_e^{\mathrm{II}}(t) - e\Phi^{\mathrm{II}}(t) \\ \tilde{\mu}_{O^{2-}}^{\mathrm{II}}(t) &= \mu_{O^{2-}}^{\mathrm{II}}(t) - 2e\Phi^{\mathrm{II}}(t) \end{aligned} \tag{7.2}$$

where $\mu_{O_2}^{\mathrm{II}}(t)$, $\mu_e^{\mathrm{II}}(t)$ and $\mu_{O^{2-}}^{\mathrm{II}}(t)$ are the chemical potential of oxygen molecule, electron and oxygen ion, respectively, at position II and time t; $\tilde{\mu}_e^{\mathrm{II}}(t)$ and $\tilde{\mu}_{O^{2-}}^{\mathrm{II}}(t)$ are the electrochemical potential of electron and oxygen ion, respectively, at position II and time t; $\Phi^{\mathrm{II}}(t)$ is the electrostatic potential at position II and time t.

As a predominantly oxygen ionic conductor, ionic conductivity is much larger than electronic conductivity in 8YSZ. Therefore

$$R_e >> R_i \tag{7.3}$$

During discharging, oxygen ions migrate from electrode I to electrode II under gradient of electrochemical potential of oxygen ion forming ionic current, while electrons or holes migrate from electrode II to electrode I under the gradient of electrochemical potential of electron forming electronic current. Since no charge accumulates at both electrodes, the two currents should follow

$$I_{O^{2-}}(t) + I_e(t) = 0 \tag{7.4}$$

where $I_{O^{2-}}(t)$ and $I_e(t)$ are the electronic current and ionic current, respectively. It is known from Ohm's law that

$$\left|\Delta\tilde{\mu}_e(t)\right| = \left|eR_eI_e(t)\right| >> \left|\Delta\tilde{\mu}_{O^{2-}}(t)\right| = \left|2eR_iI_{O^{2-}}(t)\right| \tag{7.5}$$

where $\Delta\tilde{\mu}_e(t) = \tilde{\mu}_e^{\mathrm{I}}(t) - \tilde{\mu}_e^{\mathrm{II}}(t)$ and $\Delta\tilde{\mu}_{O^{2-}}(t) = \tilde{\mu}_{O^{2-}}^{\mathrm{I}}(t) - \tilde{\mu}_{O^{2-}}^{\mathrm{II}}(t)$. Since electronic resistance is much larger than ionic resistance, when electronic current equals ionic current, the difference in electrochemical potential of oxygen ion between electrode I and II is much smaller than the difference in electrochemical potential of electron. Subtracting equation (7.2) from equation (7.1) gives

$$\tfrac{1}{2}\Delta\mu_{O_2}(t) = \Delta\tilde{\mu}_{O^{2-}}(t) - 2\Delta\tilde{\mu}_e(t)$$

Limited by electronic resistance, the dissipation current is very small and it decreases with time. From equation (7.5), $\Delta\tilde{\mu}_{O^{2-}}(t)$ should be nearly zero and it is decreasing with time; $\Delta\tilde{\mu}_e(t)$ also decreases with time, which can be described by

$$\begin{aligned} \Delta\tilde{\mu}_{O^{2-}}(t) &\approx 0 \\ \Delta\tilde{\mu}_e(t) &= -\tfrac{1}{4}\Delta\mu_{O_2}(t) \end{aligned} \tag{7.6}$$

Among the quantities defined in equation (7.1) and equation (7.2), the electrostatic potential is not measurable, while electrochemical potential of electron is measurable, which is the measured Nernst potential between electrode I and electrode II using a voltmeter, that is

$$E_N(t) = \frac{\Delta\tilde{\mu}_e(t)}{-F} = \frac{\Delta\mu_{O_2}(t)}{4F}$$

The oxygen chemical potential difference between electrode I and II is $\Delta\mu_{O_2}(t) = RT\ln\left(\frac{P_{O_2}^{\mathrm{I}}(t)}{P_{O_2}^{\mathrm{II}}}\right)$ and $P_{O_2}^{\mathrm{II}} \equiv 0.21 atm$.

So that

$$E_N(t) = \tfrac{1}{4F}\Delta\mu_{O_2}(t) = \frac{RT}{4F}\ln\left(\frac{P_{O_2}^{\mathrm{I}}(t)}{P_{O_2}^{\mathrm{II}}}\right)$$

which is equivalent to

$$P_{O_2}^{\mathrm{I}}(t) = P_{O_2}^{\mathrm{II}} \exp\left(\frac{4FE_N(t)}{RT}\right) \tag{7.7}$$

As oxygen molecule continues to dissipate from the cavity near electrode I to electrode II, the amount of oxygen molecule decreases leading to a reduced oxygen partial pressure at electrode I. In order to have a quantitative description of how many oxygen molecules dissipate away while the Nernst potential changes, it is necessary to find the state function of the store oxygen gas. Ideal gas state function is the simplest description and it holds true as long as oxygen partial pressure is not too high inside the cavity. Otherwise, the Van Der Waals interaction between oxygen molecules needs to be considered. In the present work, the applied dc bias is as low as 0.03eV, which leads to oxygen partial of 0.77atm at 800°C. Therefore, the ideal gas state function can be used to describe oxygen gas inside the cavity as

$$P_{O_2}^{\mathrm{I}}(t)V = n(t)RT \tag{7.8}$$

where V is the volume of the cavity and n(t) is the number of oxygen molecule in mole. The dissipation flux of oxygen molecule from electrode I to electrodes II and III can be defined as

$$Flux \equiv -N_A \frac{dn(t)}{dt} \tag{7.9}$$

where N_A is the Avogadro's number. The dissipation flux of oxygen molecule is proportional to dissipation current as

$$Flux = \frac{1}{4e} I_e(t) \tag{7.10}$$

Combining equation (7.9) and equation (7.10), the dissipation current can be expressed as

$$I_e(t) = -4F \frac{dn(t)}{dt} \tag{7.11}$$

Together with equation (7.7) and equation (7.8), dissipation current can be further expressed as

$$I_e(t) = -\left(\frac{4F}{RT}\right)^2 P_{O_2}^{II} V \exp\left(\frac{4FE_N(t)}{RT}\right) \frac{dE_N(t)}{dt} \tag{7.12}$$

On the other hand, dissipation current follows Ohm's law, that is

$$I_e(t) = \frac{E_N(t)}{R_e} \tag{7.13}$$

where R_e is the electronic resistance of the whole sample. Combining equation (7.12) and equation (7.13), the electronic resistance can be expressed as

$$R_e = \frac{E_N(t)}{-\left(\frac{4F}{RT}\right)^2 P_{O_2}^{II} V \exp\left(\frac{4FE_N(t)}{RT}\right)\frac{dE_N(t)}{dt}} \tag{7.14}$$

Equation (7.14) is actually Ohm's law, with potential difference divided by current. However, the dissipation current cannot be measured, because there's no external circuit and all currents are running through the 8YSZ electrolyte. From ideal gas state function as well as Nernst equation, the dissipation current can be obtained by the rate of Nernst potential decay. This is the fundamental mechanism of using the transient technique to measure electronic resistant.

7.3.3 Volume of the Cavity

In equation (7.14), the only unknown parameter is the volume of the cavity. There are several possible ways to get its value, like SEM imaging and charging current integration. Here the method of charging current integration is discussed.

Charging current has been measured using both low speed ammeter and high speed ammeter, and the collected charging current is plotted by the red curve in Figure 7-3 as a function of time. In Figure 7-3, dissipation current is also plotted by the blue curve. However, dissipation current cannot be measured directly, but Nernst potential can be measured between embedded Pt electrode and electrode III. The value of dissipation current has been well discussed elsewhere [4], and it follows

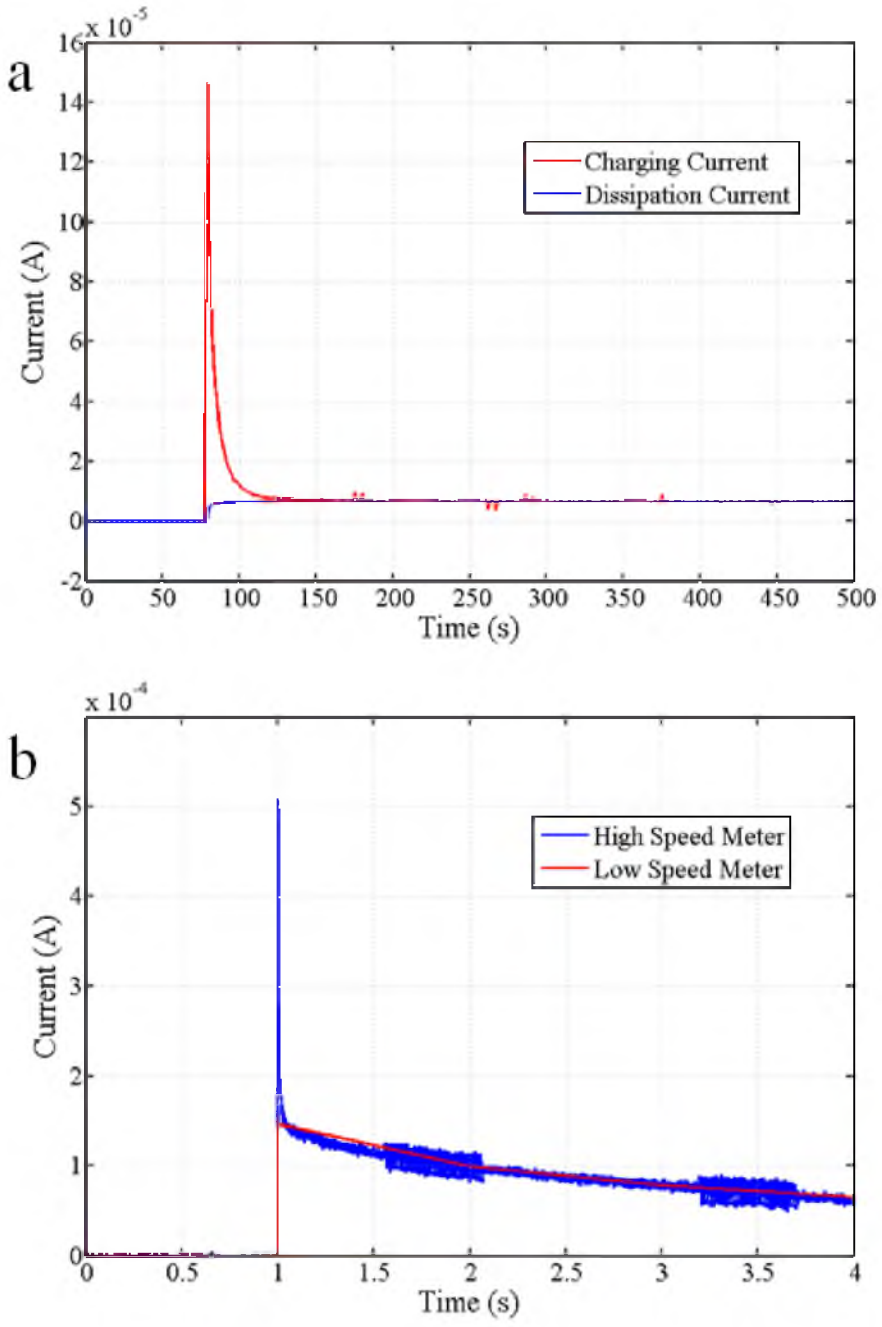

Figure 7-3: Charging current vs. dissipation current. a) Measured charging current (red) and calculated dissipation current (blue); b) comparison of the charging current measured using high speed ammeter (blue) and low speed ammeter (red).

$$I^{diss} = \frac{E_N}{R_i^{diss} + R_e^{diss}} \tag{7.15}$$

where R_i^{diss} and R_e^{diss} are the ionic and electronic resistance during oxygen dissipation. The two resistances are unknown, and it is impossible to calculate dissipation current. However, dissipation is linearly proportional to Nernst potential; therefore the curve of dissipation current should be the same as the curve of measured Nernst potential. At steady state, dissipation current equals charging current. As a result, the curves of the two currents eventually merge. Once the steady state value of dissipation current is known from charging current, dissipation current can be calculated which is plotted in Figure 7-3.

Initially there's no excess oxygen molecule in the cavity. As a result Nernst potential is zero and dissipation current is also zero. Immediately after dc voltage bias is applied, charging current reaches maximum. As Nernst potential builds up, charging current decreases gradually and merges with the increasing dissipation current. The area under charging current curve equals the amount of electrons formed in the oxygen ion oxidation reaction at embedded Pt probe. The area under the dissipation current curve equals the amount of electrons consumed in the oxygen molecule reduction reaction. The difference of the two areas calculates the amount of stored oxygen molecule in the cavity at certain temperature and applied potential by

$$n_{O_2} = \tfrac{1}{4} n_e = \tfrac{1}{4F} \int_0^\infty \left(I_{ch} - I_{diss} \right) dt \tag{7.16}$$

From equation (7.7) and equation (7.8), the volume of the cavity can be estimated as

$$V = \frac{n_{O_2} RT}{P_{O_2}^{III}} \exp\left(-\frac{4FE}{RT}\right) \tag{7.17}$$

7.4 Results and Discussion

7.4.1 Glass Sealing

All the samples are sealed with ceramic glass like the one shown in Figure 7-4(a). Glass Sealing has two different roles: preventing oxygen permeation through the bare YSZ surface where no porous Pt electrode is covered in order to have a well-defined geometry; preventing any possible gas leakage.

In order to measure electronic resistivity in YSZ, the geometry factor, L/A, is needed. In the sample, the two porous Pt electrodes have well defined circular structure; however the embedded Pt probe is a thin cylinder with finite thickness. It's difficult to calculate the geometry factor accurately. Also as pointed out elsewhere [4], if the bare YSZ surface is not sealed with glass, oxygen ion oxidation reaction can occur anywhere at the YSZ surface, because no electronic conducting phase is needed to collect formed electrons. As a result, the oxygen dissipation flux forms a radiate pattern, from the Pt probe to all exposed YSZ surface. This makes the geometry factor even more difficult to get.

By sealing bare YSZ surface with sealant glass, geometry factor can be estimated from ionic resistance. As shown in Figure 7-4(c), during charging oxygen ionic migrates from porous Pt electrode I to embedded Pt probe. The geometry factor of charging current is exactly twice as that of dissipation current, because the sample is made symmetrically and dissipation current flows to both electrodes. The ionic resistance can be calculated using the method discussed elsewhere [4], and therefore geometry factor can be calculated since ionic resistivity of 8YSZ is well known.

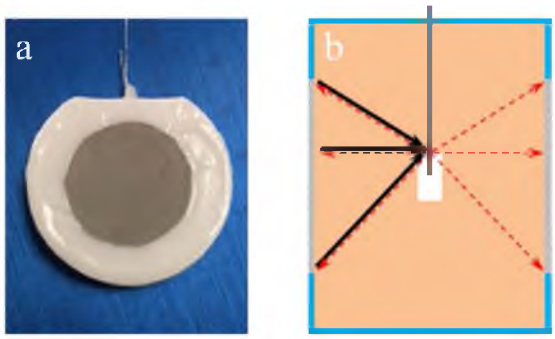

Figure 7-4: Sample geometry. a) A photo of the glass sealed sample; b) geometry of charging current path (solid black arrows) and dissipation current path (dash red arrows) when all bare YSZ surface is sealed with glass.

Glass sealing also ensures that there's no gas leakage due to any small cracks in the sample. In the case of transient technique presented in this work, equation (7.14) indicates that the rate of Nernst potential decay is inversely proportional to electronic resistance value. If there's gas leakage due to fine cracks, the rate of Nernst potential decay would be large, and consequently the calculated electronic resistance would be smaller. In the case of steady state technique [4], gas leakage due to fine cracks also leads to underestimated electronic resistance.

7.4.2 Volume of the Cavity – Charging Current Integration

A detailed discussion of volume calculation by integrating charging current is presented in the previous section. Figure 7-3(a) plots both charging current (red curve) and dissipation current (blue curve) measured at 800°C with an applied DC bias of 0.03V. Using equation (7.16) and (7.17), the volume is calculated to be 0.26mm^3. The metal disc used to make half cavity has a diameter of 3mm and a thickness of 0.28mm. Therefore, initially the volume was 3.96mm^3, which is much larger than the calculated value from

charging current. There are several possible reasons: firstly, when the prepressed powder compact was pressed by a uniaxial pressure of 5ton, the cavity shrank; secondly, sintering at 1500°C made the cavity shrink further; lastly, the charging current measured by low speed ammeter may not capture the very initial value of charging current, which might be orders of magnitudes larger.

To estimate how the very initial value of charging current matters, charging current measured by both high speed ammeter and low speed ammeter is plotted together in Figure 7-3(b). The high speed ammeter was working at a sampling rate of 3000 sample/s, and the low speed ammeter was working at 1 sample/s. It is clear that the very initial value of charging current captured by high speed ammeter is much larger than that captured by low speed meter. However, the high speed data quickly matched with low speed data in about 0.03 second. When using equation (7.16) to calculate the number of stored oxygen molecule, the difference is only 2.4%. The very initial value of charging current may be even higher, if a faster ammeter was used. However, the duration of that higher charging current is less than 0.3 millisecond, which is the time interval of the high speed ammeter used in the present work. The integration of any finite charging current in this limited time has negligible contribution. Therefore, the charging current measured by the high speed ammeter is accurate enough to calculate volume of the cavity.

7.4.3 Volume of the Cavity – Direct Observation

The disc sample was cut and ground all the way to the center of the cavity. Both optical and SEM cross section views of the cavity are shown in Figure 7-5.

Figure 7-5a shows an optical image of the cavity. The cavity has a uniform thickness

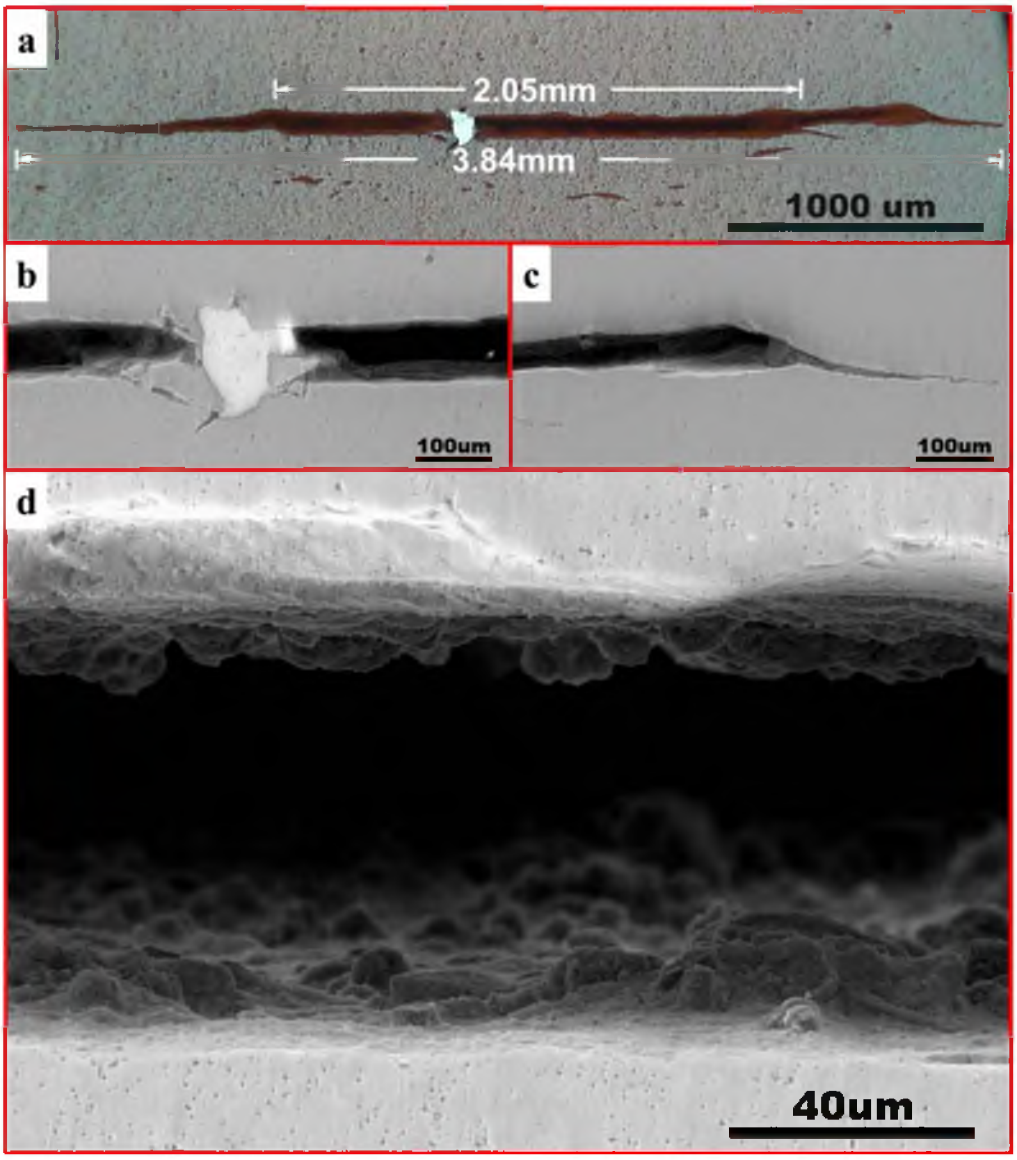

Figure 7-5: Microstructure of the cavity and embedded probe. a) Optical image of the cavity; b) SEM image of the embedded Pt probe; c) SEM image showing the edge of the cavity; d) SEM image showing the structure of the cavity.

in the middle part, which has a width of 2.05 mm; the thickness becomes nonuniform and gradually decreases to zero near the edge. The total diameter of the cavity is 3.84 mm. The metal disc has a diameter of 3mm, which is also the diameter of the initially created cavity. The shrinkage after sintering is about 23%. Therefore the cavity is expected to be 2.31mm in diameter, which is close to the width of the uniform region. The nonuniform edge may be created due to misalignment of the two prepressed power compacts and delamination during sintering.

Figure 7-5(b) shows the morphology of the embedded Pt probe. It has good contact with 8YSZ electrolyte, and there are no cracks formed at the interface. Part of the Pt probe is exposed to cavity, and the triple phase boundary along Pt probe is where electrochemical reaction occurs. Figure 7-5(c) shows the morphology of the cavity near the edge. It should be noticed that the edge is actually not an opening structure as the center of the cavity, and therefore the edge contributes little to the total volume. The optical image, taken when only the cavity edge presents, also confirms that part of the cavity edge is not connected to the center cavity. Figure 7-5(d) shows the morphology of the cavity at the uniform region. The average thickness of the cavity is measured to be 74.62 μm. Ignoring the edge of the cavity, the volume of the uniform region is calculated to be $0.246mm^3$. This value doesn't include the volume near the edge and doesn't exclude the volume of the Pt probe inside the cavity. Actually, due to the complex structure of the cavity edge, it is impossible to get an accurate value. However, the value of $0.246mm^3$ is a good approximation, and it is very close to the value calculated by charging current integration. This supports the charging current integration method.

7.4.4 Oxygen Storage – Cavity vs. Stoichiometry Change

The transient technique is based on the assumption that oxygen pumped into the sample is stored as gaseous oxygen molecule in the cavity. Equation (7.8), ideal gas state function, describes the relation between the number of oxygen molecules in cavity and the measured Nernst potential. However, when a dc bias is applied between the embedded Pt probe and electrode II, stoichiometry of the 8YSZ electrolyte will change, which will store a certain amount of oxygen [2]. In order to verify the assumption in this transient technique, samples without cavity are made using the procedure described elsewhere [4].

The measured charging current and Nernst potential of the sample with and without cavity are plotted together in Figure 7-6.

All the measurements were made at 800°C. For the sample without cavity, the applied dc bias is actually 0.05V, and as a result the Nernst potential is actually near 0.05V. However, to compare the change more straightforward, the data without cavity are normalized to have the same saturation value as the data with cavity. It is clearly noticed that, without cavity, both charging current and Nernst potential reached saturation value in less than 2 seconds. From equation (7.16), the stored oxygen is proportional to the integration of the difference between charging current and dissipation current, and therefore there's much less oxygen stored in the sample without cavity even at a slightly higher applied dc bias. Therefore, the much larger amount of oxygen pumped in the sample is stored in the cavity.

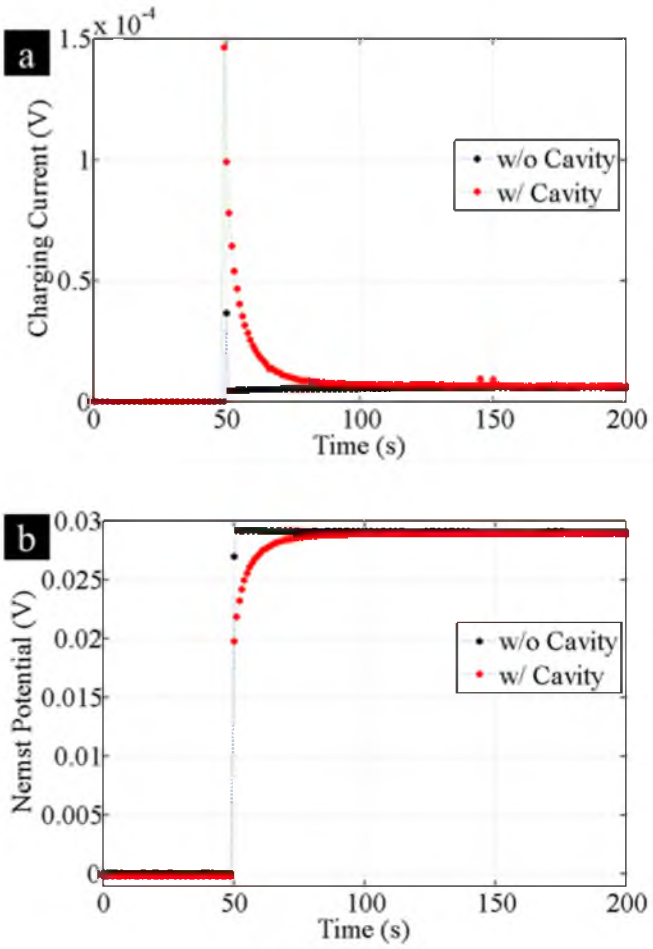

Figure 7-6: Comparison between samples with and without cavity. a) Measured charging current on the sample with and without cavity; b) measured Nernst potential on the sample with and without cavity.

7.4.5 Electrochemical Measurement Overview

The data measured at 650°C with low speed meter are plotted in Figure 7-7. E_A is the applied dc voltage bias between embedded Pt probe and porous Pt electrode II; E_N is the measured Nernst potential between embedded Pt probe and porous Pt electrode III; I_A is the charging current through embedded Pt probe. At t = 300s, a dc bias of 0.0296V was applied. Within one second, E_N rose to 0.0245V, and I_A reached maximum value of 9E-

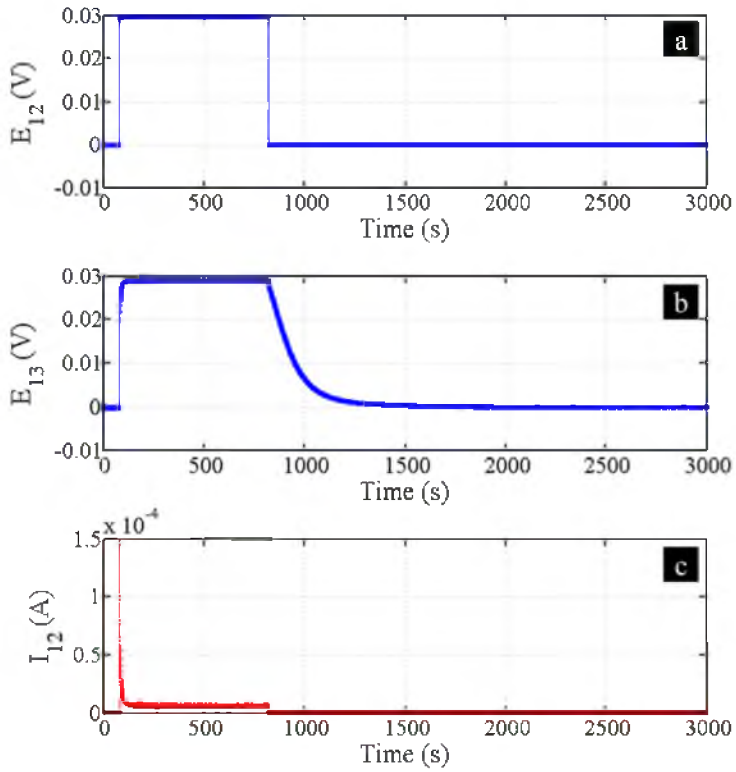

Figure 7-7: Measurement at 650C. a) DC voltage bias between electrode I and II; b) measured Nernst potential between electrode I and III; c) measured charging current.

6A. Due to the large cavity, a large amount of oxygen was pumped into the sample until steady state was established at around t = 1400s. During this period, I_A decreases with time, while E_N increases with time. From the time dependence of I_A and E_N [4], ionic resistance can be obtained by plotting E_A-E_N vs. I_A, and the slope of the linear plot gives Ri. It is to be noticed that Ri is the ionic resistance in half of the sample. Therefore, the total ionic resistance will be half of the value obtained from the slope.

At steady state, EN had a value of 0.0293V, and IA had a value of 2.9E-7A. Electronic resistance can be calculated using [4]

$$R_e^{steady} = \frac{3E_A}{I_A^{steady}} \tag{7.18}$$

where R_e^{steady} is the electronic resistance obtained at steady state, and I_A^{steady} is the charging current measured at steady state. It is to be noticed that R_e^{steady} is defined as the electronic resistance in half of the sample. Therefore the total electronic resistance will be half of R_e^{steady}, since the two half samples are in parallel when dissipation current is considered. The detailed results will be presented and discussed in the follow section. At t = 3910s, the applied dc was shut off, and charging current instantly drops to zero. However, Nernst potential decayed with time due to oxygen dissipation through 8YSZ electrolyte, which is limited by electronic resistance.

7.4.6 Summary of Electronic Resistance and Ionic Resistance

The calculated electronic resistance using equation (7.14) and (7.8) is summarized in Table 7-1, together with the calculated ionic resistance.

Both electronic resistance and ionic resistance decrease with increasing temperature. Oxygen ion transference number is calculated using both transient R_e and steady R_e, and the results turn out to be the same within 3 decimals. At low temperature (550°C and lower), 8YSZ exhibits predominantly ionic conductivity; as temperature increases, electronic conductivity becomes significant. Figure 7-8 shows the Arrhenius plot of electronic resistance and ionic resistance, all of which show very linear behavior. The activation energy of transient Re, steady Re and Ri is 2.1eV, 2.0eV and 1.1eV, respectively. These values agree with the reported value in literatures [2, 5, 6].

Table 7-1: Summary of electronic resistance and ionic resistance

Temperature (°C)	R_e (Ω) transient	R_e (Ω) steady	R_i (Ω)	Ionic Transference number
550	6.66E6	4.74E6	1.37E3	1.000
600	8.46E5	6.20E5	8.68E2	0.999
650	1.40E5	1.54E5	3.72E2	0.998
700	3.95E4	4.26E4	1.81E2	0.996
750	1.52E4	1.49E4	9.20E1	0.994
800	7.18E3	7.05E3	4.92E1	0.993

Geometry factor is needed to calculate electronic resistivity. Since ionic charging current shares the same path as electronic dissipation current, the geometry factor can be calculated from ionic resistance, provided ionic resistivity in 8YSZ is well known. At 800°C, ionic resistivity in 8YSZ is 25Ωcm. Therefore, the geometry factor is calculated to be 1.968cm^{-1}. The electronic resistivity has been calculated and summarized in Table 7-2.

7.4.7 Comparison Between Transient Technique, Steady State Technique and Hebb-Wager Method

The transient technique introduced in the present work utilized very similar experiment setup and sample structure to those used in steady state technique [4]. Both of the two techniques use embedded Pt probe to pump oxygen into the 8YSZ sample and, at the same time, measure the Nernst potential with the embedded Pt probe. One big

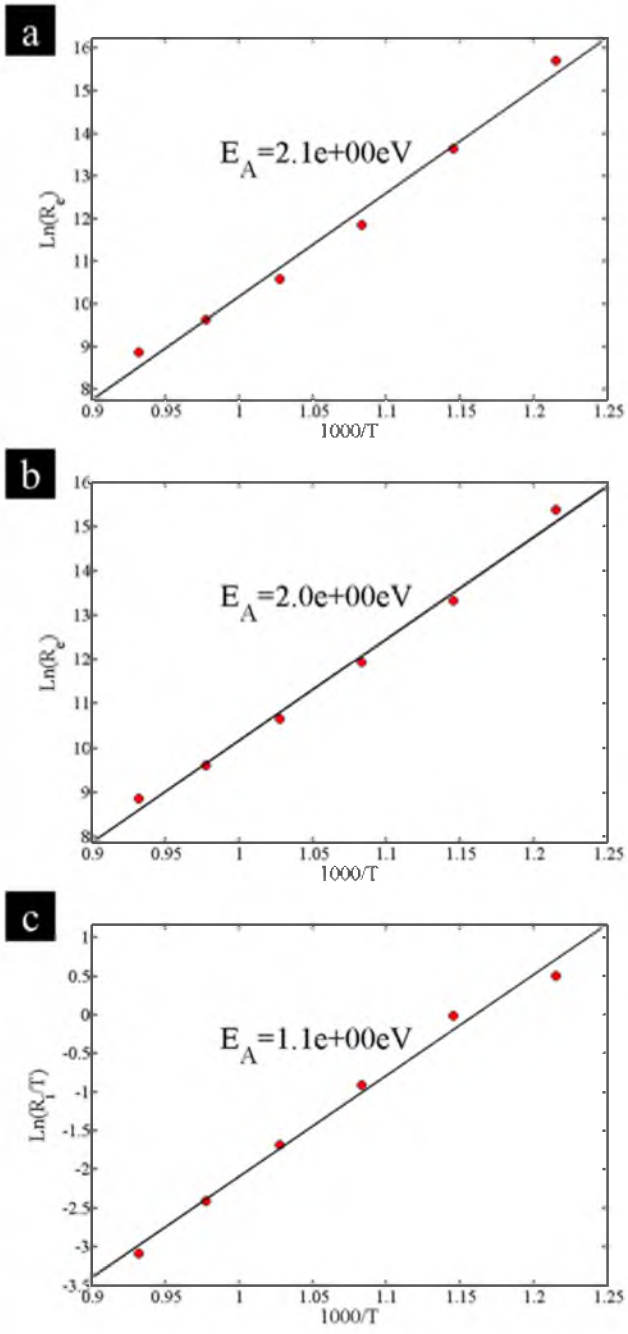

Figure 7-8: Summary. a) Arrhenius plot of electronic resistance obtained by transient technique; b) Arrhenius plot of electronic resistance obtained by steady state technique; c) Arrhenius plot of ionic resistance.

Table 7-2: Summary of electronic resistivity and ionic resistivity

Temperature (°C)	ρ_e (Ωcm) transient	ρ_e (Ωcm) steady	ρ_i (Ωcm)	Ionic transference number
550	3.38E6	2.41E6	6.94E2	1.000
600	4.30E5	3.15E5	4.41E2	0.999
650	7.11E4	7.80E4	1.89E2	0.998
700	2.01E4	2.16E4	9.19E1	0.996
750	7.72E3	7.55E3	4.67E1	0.994
800	3.65E3	3.58E3	2.50E1	0.993

difference is how data are interpreted. In steady state technique, electronic resistance is calculated using equation (7.18) and the data collected when both charging current and Nernst potential become steady. In transient technique, electronic resistance is calculated using equation (7.14) and the measured Nernst potential decay. The other difference is whether cavity is built into the sample. When there is no cavity, the amount of oxygen pumped into the sample is very small and oxygen is stored mainly by stoichiometry change. When there is cavity, a much larger amount of oxygen is pumped into the sample and stored in the cavity. Although Nernst potential decay was observed without cavity after voltage bias was shut off [4], the data could not be analyzed using equation (7.14), because the relation between the amount of stored oxygen and Nernst potential cannot be described by ideal gas state function.

The calculated electronic resistivity using the transient and steady state techniques are very close. Although these values are of around 30 times smaller than the values reported

in literature [2], the results in the present work are reasonable by considering the following facts. Firstly, the ionic transference number is near unity. Secondly, the activity energy agrees well with literature. Lastly, in the Hebb-Wagner method, there's a huge stoichiometry change in the 8YSZ, which may lead to overestimated electronic resistance.

7.5 Summary

A transient technique is designed to measure the electronic resistivity in 8YSZ using a sample with an embedded Pt probe and a cavity. When dc bias is applied between embedded Pt probe and porous electrode II, oxygen molecule is pumped into the cavity; when dc bias is shut off, oxygen molecule dissipates through the YSZ electrolyte in the form of oxygen ion and electron. The dissipation rate is determined by the electronic resistance, which can be obtained from the measured time dependence of Nernst potential decay. The only unknown parameter is the volume of the cavity. Charging current integration and SEM observation are presented to calculate the volume.

7.6 References

1. M. H. Hebb, *J. Chem. Phys.*, **20**, 185 (1952)

2. J. H. Park and R. Blumenthal, *J. Electrochem. Soc.*, **136**, 2867-2876 (1989)

3. I. Valov et al., *Solid State Ionics*, **180**, 1463-1470 (2009)

4. L. Zhu, L. Zhang and A.V. Virkar, *J. Electrochem. Soc.*, **162**, F298-F309 (2015)

5. L. Heyne and N.M. Beekmans, *J. Br. Ceram. Soc.*, **19**, 229-263 (1971)

6. W. Weppner, *J. Solid State Chem.*, **20**, 305-314 (1977)

CHAPTER 8

ADSORPTION AND DESORPTION OF CARBON MONOXIDE ON 1 NM PT FILM INVESTIGATED BY ELECTRICAL RESISTANCE MEASUREMENT

8.1 Introduction

Proton exchange membrane fuel cell (PEMFC) has potentially wide application in automotive industry since it has zero emission and a much larger driving range than lithium ion battery cars. The first commercial FC vehicle went to market in 2014. As PEMFC technology gets better, there will be more FC vehicles available. Currently, the relatively low durability of PEMFC is a significant barrier to its application [1]. One of the many factors lowering durability is catalyst contamination, which is carbon monoxide (CO) poisoning on anode platinum catalyst [2], [3]. Le Canut et al. found that by adding trace amount of CO in fuel, output voltage of the cell drops quickly and significantly. They noticed that this process was reversible; as CO is removed, output voltage recovers.

The equilibrium state of CO adsorption on Pt surface has been well studied decades ago [4], [5]. Adsorption is more favored at lower temperature and higher CO partial pressure. However, the equilibrium state information is not enough to understand the poisoning effect of CO on Pt, and the adsorption and desorption kinetics are needed.

Unfortunately, there are limited studies on the kinetic processes. Parker et al. studied

hydrogen-induced CO desorption on Pt surface using fluorescence yield near-edge spectroscopy [6]. Waszczuk et al. studied the CO adsorption on fuel cell nanoparticle electrodes using the radioactive isotope, 14C, to label CO [7]. Both of these two characterization techniques are not widely available, which hinders the study in this field.

In the present work, a new technique is developed by designing an electrochemical reaction chamber and measuring the electric resistance variation. Due to the difference in electron affinity, Pt loses electron to the adsorbed CO, and as a result the measured resistance increases as free electron density decreases. A theoretical model is developed to interpret the measured electric resistance. From the time dependence of resistance variation, the kinetic parameters are obtained.

8.2 Experimental Procedure

8.2.1 Design and Construction of the Test System

The test chamber consisted of a silica glass cylinder clamped between two metallic plates with O-rings to ensure gas-tight seals. An electrical heater and a sample holder were inserted into the chamber. A thermocouple was introduced into the chamber to measure the sample temperature. Electrical feed-throughs were inserted from the end plates into the chamber. Also connected to the end plates were gas inlet/outlet fittings. A gas supply system consisting of flow meters and valves was used to introduce various atmospheres into the chamber. Electrical measurements were conducted using Keithley Model 2000 meters. Data acquisition was done using LabView software. Figure 8-1 shows a photograph of the testing stand.

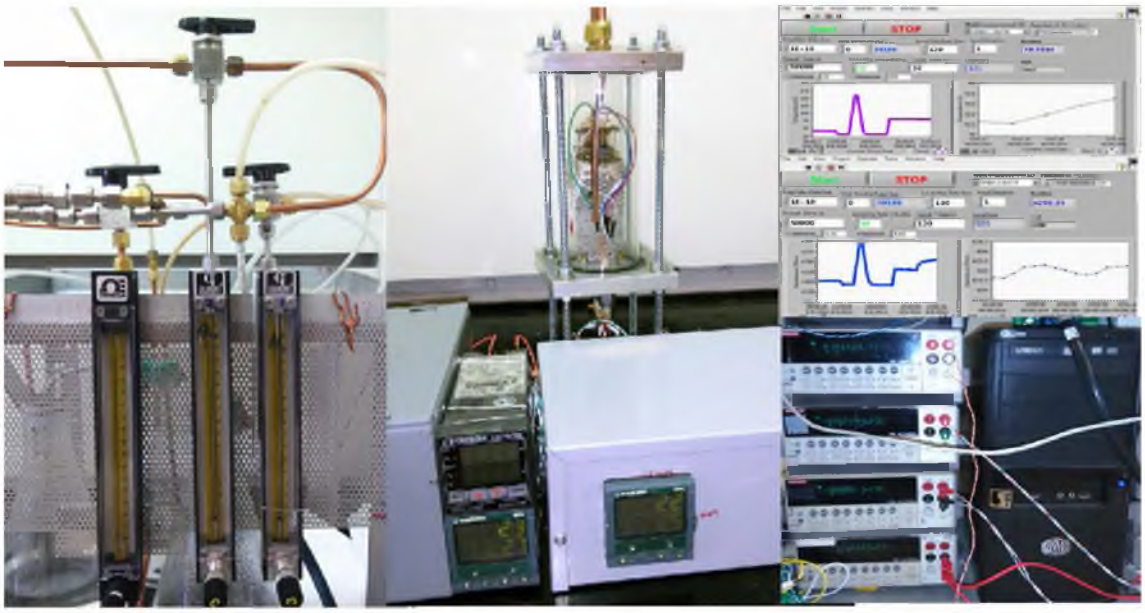

Figure 8-1: A photograph of the test setup.

8.2.2 Deposition of Thin Platinum Films on Sapphire Substrate

For the formation of thin Pt films, 10x10x1.0mm sapphire wafers (MTI Corp., CA, USA) of M plane orientation (1-100) were used as the substrate. The nominal roughness is less than 0.5 nm which is critical to form a flat Pt surface. Initially 400nm Au was deposited on the sapphire substrate by DC sputtering using Cr (10nm layer) as an adhesive layer between the sapphire and the Au. Using photolithography and etching, two Au contacts (1 mm long, 0.2 mm wide and 400 nm thick) were made at the two parallel edges of the sapphire substrate. The purpose of having the two Au contacts is to prevent the damage due to the compression between the metal electrodes and thin film during the testing stage, which also minimizes the contact resistance. The experimental results showed that having the two Au contacts could eliminate the sudden fluctuations that were occasionally seen in the films without Au contacts during the testing cycles. After making

the Au contacts, a layer of platinum of ~1nm thickness (estimated based on the average deposition rate) is deposited on top of the sapphire substrate with premade Au contacts using DC sputtering at 25W. The base pressure for Pt sputtering was 2×10^{-6} Torr.

8.2.3 Measurement of Electrical Resistance in Various Atmospheres

As shown in Figure 8-2, a complete test stage includes two sample holders sitting symmetrically on top of an electrical insulation board with a low-temperature-sensitive thermocouple added in between the two sample holders. The distance between the thermocouple and the two sample holders was minimized and almost equal. Each of the sample holders has electrical leads connected for a two-probe resistance measurement. The coil springs can maintain a proper contact between the Au contacts and the silver pads (0.12 mm thick), which have a flat surface and the same width as the Au contacts. The distance between the two inner edges of the two silver electrodes was adjusted to be 6 mm. The Pt film with Au contacts was inserted into one of the sample holders for testing. Initially, power to the heater was turned on, the test stage was heated using a temperature controller, and the sample temperatures and the electrical resistance of the sample were continuously recorded. A gas mixture of 10% H_2 + Ar was introduced into the chamber as the starting gas to reduce any platinum oxide(s) that may have formed prior to testing. Once the temperature reached the target value, and the film resistance had been stabilized for a few hours, 1 to 100 ppm CO in Ar gases were introduced to the chamber. Due to CO adsorption on Pt film, the resistance would go up. The mechanism that causes this resistance change will be discussed in the corresponding sections. Once the resistance reached a new stable value, meaning the rate of adsorption equals the rate

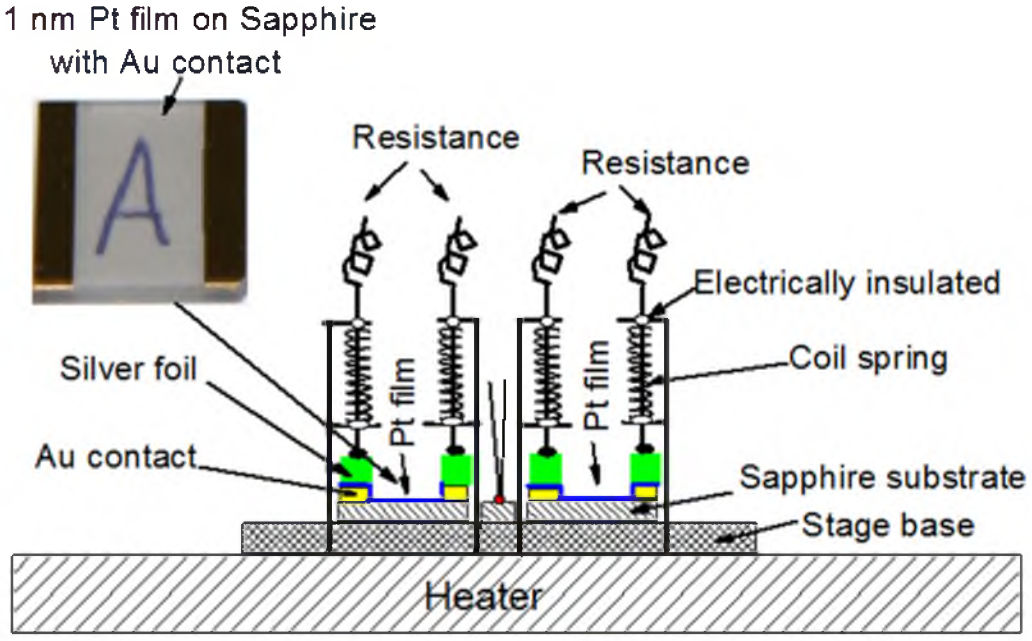

Figure 8-2: A schematic diagram showing the configuration of the sample holders. The inset shows a deposited Pt film of ~1 nm thickness on a sapphire substrate with premade Au contacts. The good transparency retained after film deposition indicates the film was very thin.

of desorption, 10% H_2 + Ar was introduced back to the chamber. This started the desorption of CO on Pt film. The resistance went down gradually under 10% H_2/Ar flow and nearly stabilized at the baseline resistance before CO introduction. The chamber was then cooled down to room temperature under the same H_2 containing gas mixture, this finished one cycle of test. This procedure was repeated several times for other temperatures and CO concentrations.

Once a relatively stable baseline film resistance (under H_2 gas flow at fixed temperatures <200°C) was realized, we believed the film was suitable to study the

kinetics of CO adsorption and desorption on a Pt surface, and thus a series of tests were designed and discussed below.

8.2.3.1 Electrical Resistance Change Upon CO Adsorption

Figure 8-3 shows the resistance response from the Pt film upon exposure to CO at ~60°C. Initially (negative time axis), the film was under 10% H_2 in Ar flow, it maintained a stable resistance of ~4192Ω. The temperature was also stabilized. At time zero, 100 ppm CO in Ar was introduced to the reaction chamber. This led to a sharp increase of resistance within the first half hour or 1 h or so, and then the film resistance gradually leveled off approximately after 8 h of exposure to CO. The temperature profile remained nearly constant throughout the whole testing period. Thus it is clear the resistance change here is attributed to CO adsorption on Pt surface.

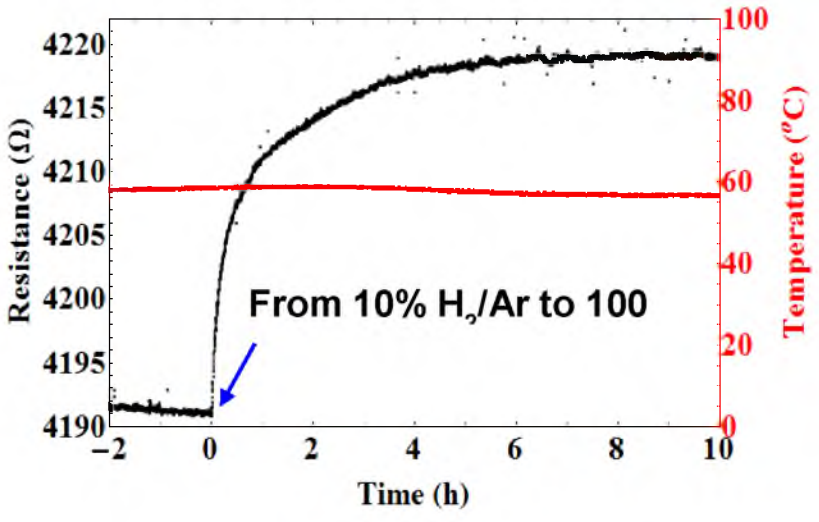

Figure 8-3: Plots of temperature and film resistance (1nm thickness) vs. time for a typical CO adsorption process.

8.2.3.2 Electrical Resistance Change Upon CO Desorption

After an equilibrium, where rate of adsorption equals rate of desorption, was reached, the atmosphere was switched from 100 ppm CO in Ar back to 10% H_2 in Ar, as shown in Figure 8-4. As seen from this figure, before time t_1 (~16.5h), the film resistance remained nearly unchanged for more than 5 h. As soon as CO containing gas mixture was replaced by H_2 containing gas mixture, the film resistance quickly dropped by about half of the maximum resistance gained during adsorption process within the first 2 to 3 h, then slowly approached the baseline value (~4192Ω) when CO was not introduced to the chamber. The film resistance was fully recovered near the end of the desorption process. Again, the temperature profile remained pretty constant during the whole testing period.

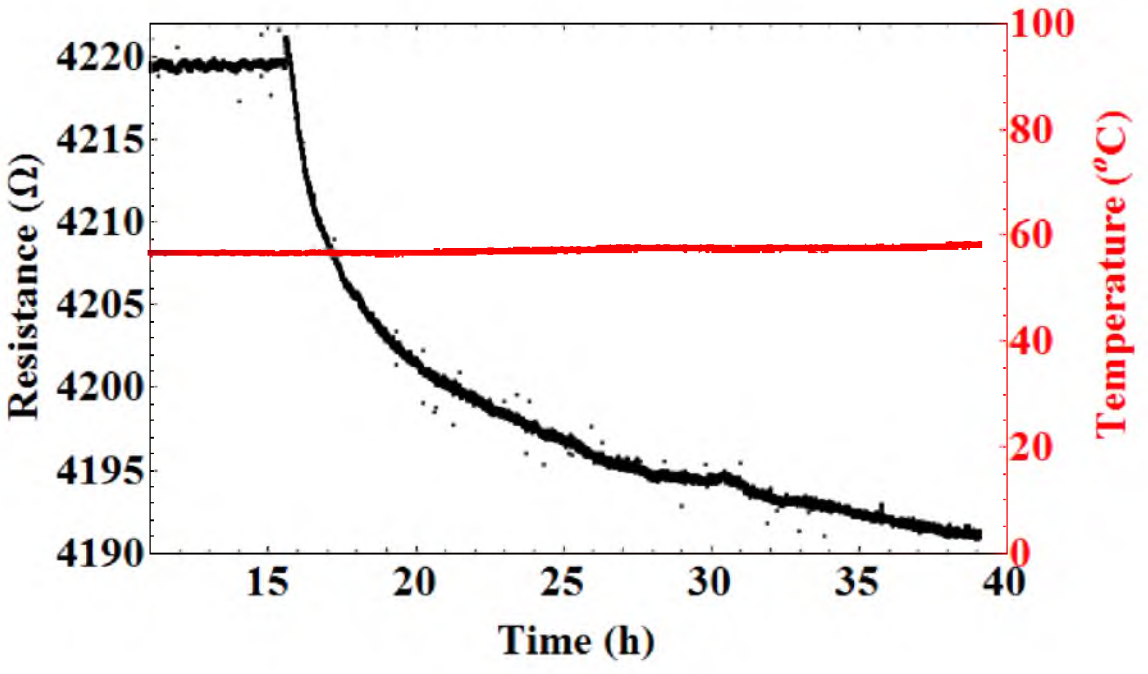

Figure 8-4: Plots of temperature and film resistance (1nm thickness) vs. time for a typical CO desorption process.

8.2.4 Characterization of Thin Platinum Films

The as-deposited Pt films and films exposed to various atmospheres were characterized by X-ray diffraction (XRD), scanning electron microscopy (SEM) and atomic force microscopy (AFM).

Figure 8-5 shows the 2D and 3D view of a clean sapphire substrate, an as-deposited 1 nm Pt film on sapphire substrate, and a 1 nm Pt film on sapphire substrate after going through all the testing cycles (including the tests to be discussed in the following sections after the baseline resistance of the film showed negligible time dependence at a given temperature under 10% H_2 gas flow). Intuitively, as shown in Figure 8-5(b) and Figure 8-5(c), the apparent particles under the same scale size were slightly larger in the tested film. The 3D view did not show much difference. Roughness was measured at the same time for the three samples. The root mean square roughness of the sapphire substrate was measured as 0.12 nm for a 250x250 nm region, and 0.17 nm for a 1x1 micron region, both of which were slightly lower than the factory reported roughness (0.5 nm). This difference could be related to the resolution difference of the AFM used for the corresponding measurements. However, the combined information indicates that the substrates used in this study are very flat, as clearly shown in Figure 8-5(a) and Figure 8-5(d), which is critical for having a relatively uniform thin Pt film at 1 nm scale. As expected, the film deposited by the sputtering technique cannot be perfectly smooth at 1 nm scale since it is not an atomic layer deposition technique. In comparison with Figure 8-5(d), the clearly distinguishable features in Figure 8-5(e) and Figure 8-5(f) with Pt deposited do imply the film is reliable (we were not testing a blank sapphire substrate of negligible Pt layer). The root mean square roughness for the as-deposited film was 0.39

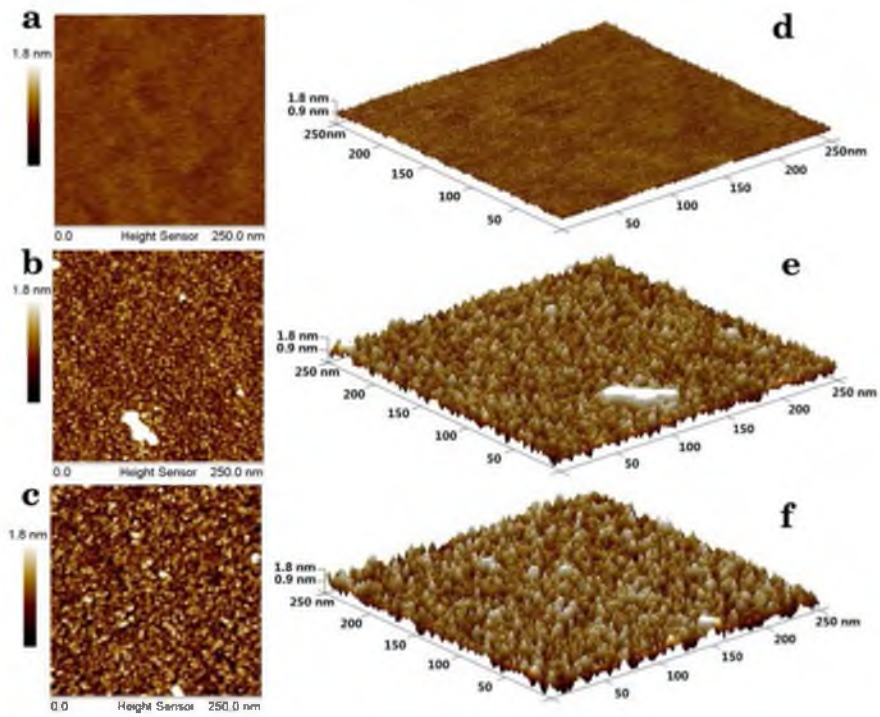

Figure 8-5: AFM images showing 2D view of: a) a clean sapphire substrate, b) an as-deposited 1 nm Pt film on sapphire substrate, and c) a 1 nm Pt film on sapphire substrate after going through all the testing cycles (including the tests to be discussed in the following sections after the baseline resistance of the film showed negligible time dependence at a given temperature under 10% H_2 gas flow). And 3D view e to f that corresponds to a to c, respectively.

nm for a 250x250 nm region and 0.85 nm for a 1x1 micron region. In comparison, the root mean square roughness for the film after testing was 0.34 nm for a 250x250 nm region and 0.36 nm for a 1x1 micron region. Since root mean square roughness is sensitive to the peaks and valleys in the surface profile, it is clear that the film after testing became smoother. This change might have contributed to the instability of the film at the initial testing period.

To verify the surface morphology observed by AFM, high resolution SEM images were also obtained for an as-deposited 1 nm Pt film. The two different imaging

approaches match well in terms of particle size and uniformity, as shown in Figure 8-6.

8.3 Theoretical Model Bridging Electrical Resistance Variation and CO Adsorption Kinetics

Gas adsorption and desorption process have been well described by different isotherm model, such as Langmuir isotherm. In the present work, it is first assumed that CO adsorption and desorption is a first-order kinetic process, and therefore Langmuir isotherm is followed.

$$\frac{d\theta}{dt} = k_a p_{CO}(1-\theta) - k_d\theta \tag{8.1}$$

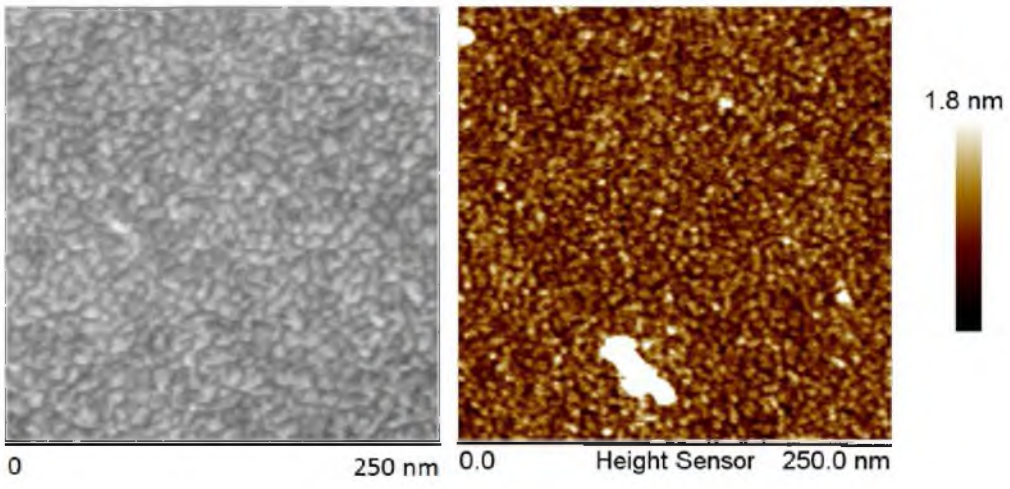

Figure 8-6: A SEM image (left) and a AFM image (right) showing 2D view of an as-deposited 1 nm Pt film on sapphire substrate.

At equilibrium, $\frac{d\theta}{dt} = 0$, therefore

$$\theta_{eq} = \frac{k_a p_{CO}}{k_a p_{CO} + k_d} \tag{8.2}$$

where θ_{eq} is the surface site coverage at equilibrium.

With a clean Pt surface ($\theta\big|_{t=0} = 0$), the kinetics of CO adsorption can be described by solving equation (8.1), and the solution is

$$\theta = \frac{k_a p_{CO}}{k_a p_{CO} + k_d}\left[1 - \exp\left(-\left(k_a p_{CO} + k_d\right)t\right)\right] \tag{8.3}$$

With a saturated Pt surface ($\theta\big|_{t=0} = \theta_{eq}$), the kinetics of CO desorption can be described also by solving equation (8.1), and the solution is

$$\theta = \frac{k_a p_{CO}}{k_a p_{CO} + k_d}\exp\left(-k_d t\right) \tag{8.4}$$

In experiment, the CO adsorption and desorption kinetics are observed in terms of Pt nano film resistance change with time. Therefore, the relation between nano film resistance and CO coverage is needed to understand CO adsorption and desorption kinetics.

CO has a larger electronegativity than Pt. Therefore Pt nano film loses free electron

upon CO adsorption. As a result, Pt nano film resistance goes up. It is assumed here that one CO molecule takes away one free electron from Pt nano film. Therefore

$$\sigma_e = e\mu_e n_e^{eff} = e\mu_e\left(n_e^0 - \frac{S_0}{d}\theta\right) = e\mu_e n_e^0\left(1 - \frac{S_0}{n_e^0 d}\theta\right) = \sigma_e^0\left(1 - \frac{S_0}{n_e^0 d}\theta\right) \tag{8.5}$$

where σ_e^0 and σ_e are the electronic conductivity before and after CO adsorption, respectively, e is the electron charge, μ_e is the electron mobility, n_e^0 is the free electron density in bulk Pt, S_0 is the surface density of available CO adsorption sites and d is the average Pt nano film thickness.

$$R = \frac{L}{A\sigma_e} = \frac{L}{A\sigma_e^0\left(1 - \frac{S_0}{n_e^0 d}\theta\right)} = \frac{R_0}{1 - \frac{S_0}{n_e^0 d}\theta} \tag{8.6}$$

Considering equation (8.3) and equation (8.4), the change of Pt nano film resistance with time is described by equation (8.7) (adsorption) and equation (8.8) (desorption).

$$R = \frac{R_0}{1 - \frac{S_0}{n_e^0 d}\frac{k_a p_{CO}}{k_a p_{CO} + k_d}\left[1 - \exp\left(-\left(k_a p_{CO} + k_d\right)t\right)\right]} \tag{8.7}$$

$$R = \frac{R_0}{1 - \frac{S_0}{n_e^0 d}\frac{k_a p_{CO}}{k_a p_{CO} + k_d}\exp\left(-k_d t\right)} \tag{8.8}$$

CO adsorption and desorption rate constant, ka and kd, can be derived from the experimental data. The best way to interpret experimental data is to find a linear plot. It is quite straightforward to convert equation (8.8) into a linear function of t, as equation (8.9).

$$\ln\left(1-\frac{R_0}{R}\right)=\ln\left(\frac{S_0}{n_e^0 d}\frac{k_a p_{CO}}{k_a p_{CO}+k_d}\right)-k_d t \tag{8.9}$$

From a plot of $\ln\left(1-\frac{R_0}{R}\right)$ vs. t, the slope gives the value of desorption rate constant, k_d. The detailed results will be discussed later.

However, it is impossible to linearize equation (8.7) in the same way as shown by equation (8.10).

$$\ln\left(1-\frac{R_0}{R}\right)=\ln\left(\frac{S_0}{n_e^0 d}\frac{k_a p_{CO}}{k_a p_{CO}+k_d}\right)+\ln\left(1-\exp\left(\left(k_a p_{CO}+k_d\right)t\right)\right) \tag{8.10}$$

The third natural log is not linear to time, t. The right way to linearize equation (8.7) is shown as follows. First, taking derivative on both sides of equation (8.6) gives

$$\frac{dR}{dt}=\frac{R^2}{R_0}\frac{S_0}{n_e^0 d}\frac{d\theta}{dt} \tag{8.11}$$

Together with equation (8.1) and equation (8.6), it can be derived that

$$\frac{1}{R}\frac{dR}{dt}=\frac{R}{R_0}\left(\frac{S_0}{n_e^0 d}k_a p_{CO}-\left(k_a p_{CO}+k_d\right)\right)+\left(k_a p_{CO}+k_d\right) \tag{8.12}$$

Based on equation (8.12), the experiment data can be interpreted linearly by plotting $\frac{1}{R}\frac{dR}{dt}$ vs. R, and the intercept with y axis gives the value of adsorption rate constant, k_a. Meanwhile, the slope gives the value of S_0, provided n_e^0 is known.

8.4 Results and Discussion

8.4.1 Desorption Rate Constant

Figure 8-7 shows the plots of $\ln\left(1-\frac{R_0}{R}\right)$ vs. t suggested by equation (8.9). Regardless of the periodic oscillation, all the plots show a linear relation between $\ln\left(1-\frac{R_0}{R}\right)$ and t. The slope of each linear plot gives the value of desorption rate constant, k_d. In Figure 8-7(c) and Figure 8-7(d), periodic oscillation is observed, which is due to temperature oscillation of the electric heater. In Figure 8-7(a) and Figure 8-7(b), the data collected immediately after gas change show small deviation from linearity. Two possible reasons may account for this. First, the atmosphere change may be slow causing the initial desorption rate to be different. Second, the Pt nano film has a rough surface, and desorption rates at different sites, such as edges or corners, are different. However, as an assumption, desorption rate constant is obtained only from the stable part in the plots. At 40°C, it has a value of $1.34\times10^{-5}s^{-1}$, and gradually rises to $9.52\times10^{-4}s^{-1}$ at120°C. k_d increases with temperature, indicating a thermally activated process.

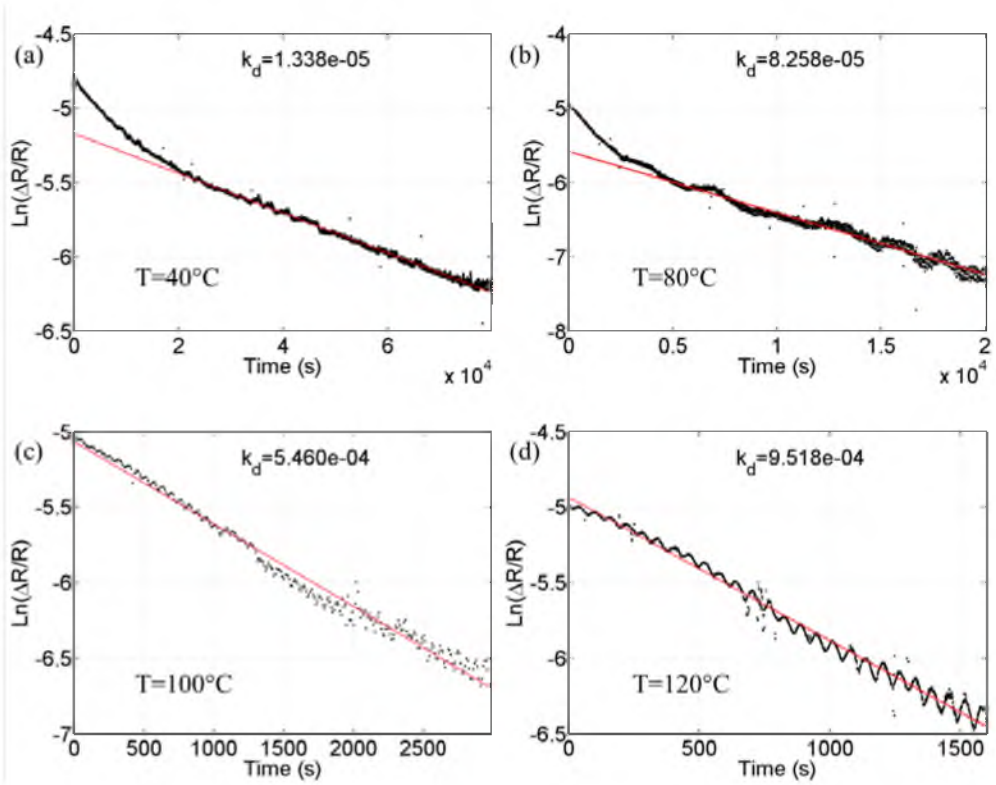

Figure 8-7: Linearized electronic resistance change with CO desorption. The black curves are the experimental data, while the red line is a linear fitting, whose slope gives the values of desorption rate constant. The value of k_d is listed in each figure. Subplots (a) to (d) correspond to measured data at 40°C, 80°C, 100°C and 120°C, respectively.

8.4.2 Adsorption Rate Constant

Determination of adsorption rate constant is not as straightforward as desorption. As presented by equation (8.12), the best way to linearize the resistance change during adsorption is to plot $\frac{1}{R}\frac{dR}{dt}$ vs. R. Since the collected resistance data contain much noise, it is useless to calculate $\frac{dR}{dt}$ simply by direct differential. An effective method is to fit the resistance data with a polynomial equation, and then take the derivative of the fitted

polynomial equation. Figure 8-8(a) plots the experimental data as well as the polynomial fitting. The order of polynomial fitting needs to be chosen carefully. If the order is too low, then the initial sharp rise in the resistance plot will be eliminated. If the order is too high, then divergence will occur near the end of the resistance plot.

Figure 8-8(b) is a double y-axis plot, in which the black curve plots $\frac{1}{R}\frac{dR}{dt}$ vs. R, and the red curve plots time vs. R. The purpose of having an additional y-axis is to clearly show the time evolution of $\frac{1}{R}\frac{dR}{dt}$. For example, the point (4277.5, 1.2e-6) in the black curve corresponds to the point (4277.5, 1000) in the red curve. Therefore, the density of data collected near the end of the black curve is much larger than that near the beginning of the black curve.

As is well known, adsorption rate is proportional to the product of adsorption rate constant and adsorbent partial pressure. Therefore, the unit of k_a is different from that of k_d, and the unit of k_a is $s^{-1}Pa^{-1}$. The y-intercept of the linear plot is exactly the sum of $k_a p_{CO}$ and k_d. Since k_d is determined from the slope of desorption curve, $k_a p_{CO}$ is the difference between y-intercept and k_d. The slope of adsorption plot gives the available surface adsorption site density, provided the free electron charge density in Pt is known.

8.4.3 Distinguishing Different Kinetic Processes

Figure 8-9 and Figure 8-10 summarize the adsorption rate constant at different temperatures. It is interesting to notice that the transformed data clearly show a slope change. The change occurs near the end of the rapid initial resistance increase. This slope change may indicate the existence of at least two different adsorption processes.

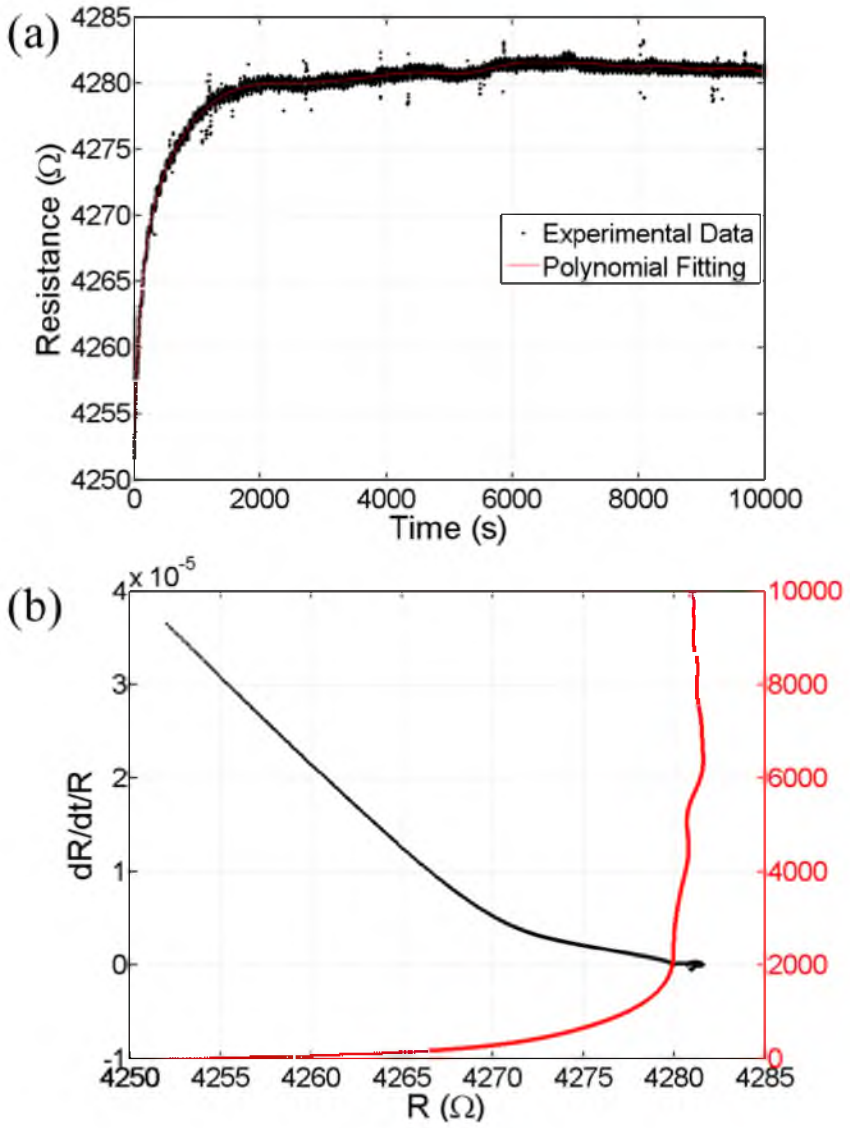

Figure 8-8: Adsorption data processing. a) The black curve shows the experimental data of resistance change with CO adsorption, and the red curve shows the polynomial fitting, which is used to eliminate noise in the calculation of dR/dt. b) A double y-axis plot of both $dR/dt/R$ vs. R and time vs. R. The two curves are summarized in one figure, in order to clearly show the time evolution of $dR/dt/R$.

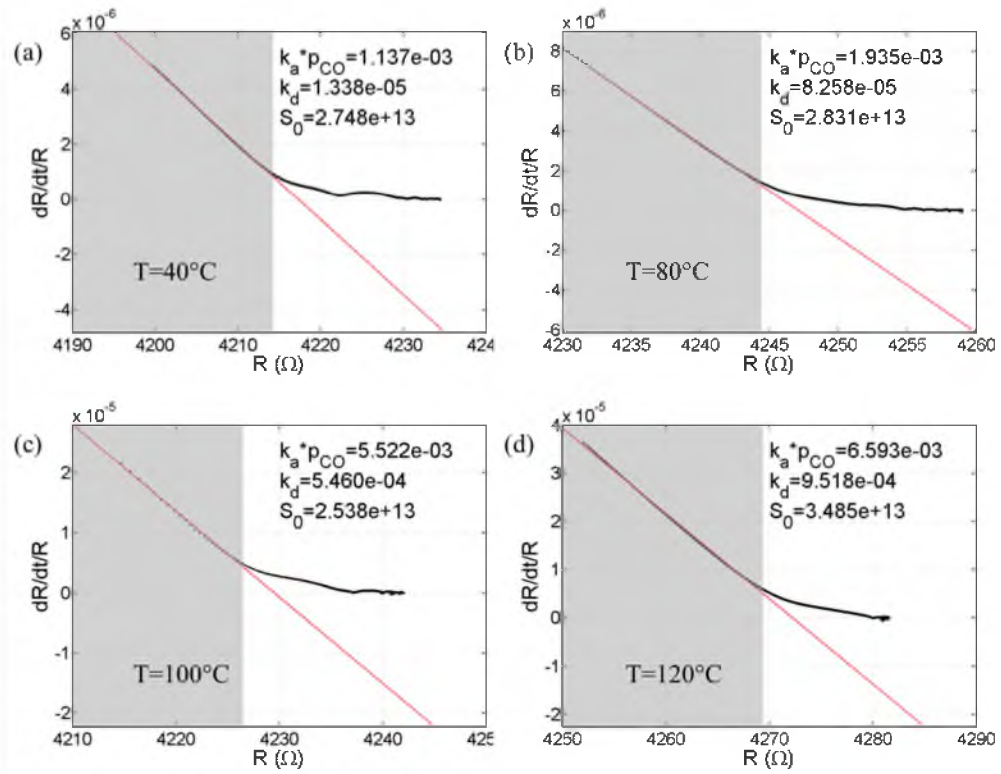

Figure 8-9: Linearized electronic resistance change with CO adsorption. The black curves are the experimental data, while the red line is a linear fitting corresponding to stage I, whose y-intercept gives the values of adsorption rate constant and slope gives surface site density. The value of $k_a p_{CO}$, k_d and S_0 is listed in each figure. Subplots (a) to (d) correspond to measured data at 40°C, 80°C, 100°C and 120°C, respectively.

As discussed previously, the Pt nano film has a rough surface. Therefore CO molecule will adsorb at different sites, such as edges or corners, which give different adsorption rate constant. Therefore, we have divided the adsorption curve into two stages, stage I and stage II. In Figure 8-9 and Figure 8-10, stage I is shaded and stage II is unshaded.

For example, Figure 8-9(a) and Figure 8-10(a) both show the linearized plot of resistance change at 40°C. In Figure 8-9(a), the y-intercept gives the value of adsorption

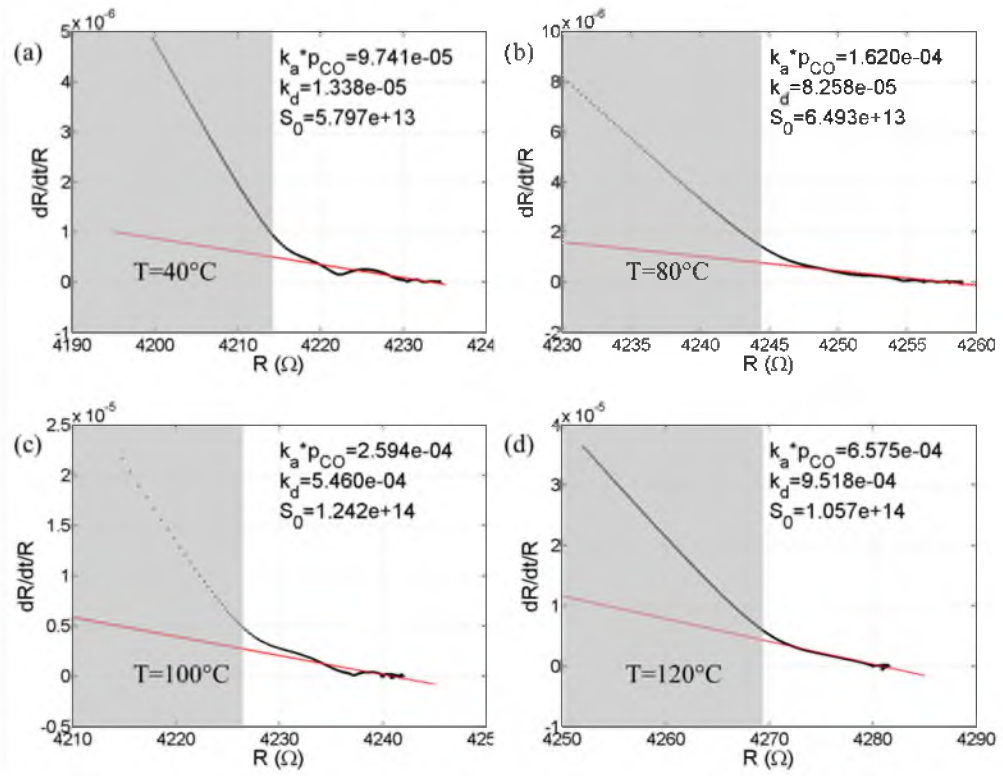

Figure 8-10: Linearized electronic resistance change with CO adsorption. The black curves are the experimental data, while the red line is a linear fitting corresponding to stage II. The value of $k_a p_{CO}$, k_d and S_0 is listed in each figure. Subplots (a) to (d) correspond to measured data at 40°C, 80°C, 100°C and 120°C, respectively.

rate constant at stage I, $k_a^I p_{CO}$, which is $1.14\times10^{-3}s^{-1}$, while in Figure 8-10(a), the y-intercept gives $k_a^{II} p_{CO}$, which is $9.74\times10^{-5}s^{-1}$. At 120°C, $k_a^I p_{CO}$ is $6.60\times10^{-3}s^{-1}$, and $k_a^{II} p_{CO}$ is $6.58\times10^{-4}s^{-1}$. The increase of k_a with temperature indicates the adsorption process to be thermally activated.

The reliability of the above data interpretation is discussed as follows. It is reasonable that CO adsorption on Pt involves different processes since the Pt film is rough. Even on

atomic flat Pt surface, different adsorption sites (such as atop, bridge and hollow) still give different adsorption rate constants. For simplicity and without generality, we assume two different adsorption processes exist. As long as k_a of the two processes differ significantly, the fast process always dominates at the initial stage and the surface sites get covered quickly. After the fast process stops, the slow process dominates at the later stage. Therefore, in each stage, only one adsorption stage dominates, and as a result equation (8.6) holds true. On the other hand, the changed slope in linearized plot indicates that the present technique can distinguish different adsorption process vigorously.

8.4.4 Activation Energy

Figure 8-11 shows a set of Arrhenius plots for adsorption rate constant, k_a, and desorption rate constant, k_d, as well as a schematic of CO adsorption coordination. The slope of Figure 8-11(a) calculates activation enthalpy (E_A^d) to be 0.6eV. Figure 8-11(c) and Figure 8-11(d) summarize k_a^I and k_a^{II}, respectively. The activation enthalpy (E_A^a) for these two different adsorption processes turns out to be quite similar and both are around 0.25eV. Therefore the difference between k_a^I and k_a^{II} may be attributed to a different entropy term, which is included in the pre-exponential factor.

The energy distribution at different CO adsorption coordination can be illustrated by Figure 8-11(b). E_A^d is expected to be larger than E_A^a, which favors adsorption. The difference between E_A^d and E_A^a is the binding energy between gas molecule with metal atom. In the case of CO adsorption on Pt, the binding energy is about 0.35eV. This value

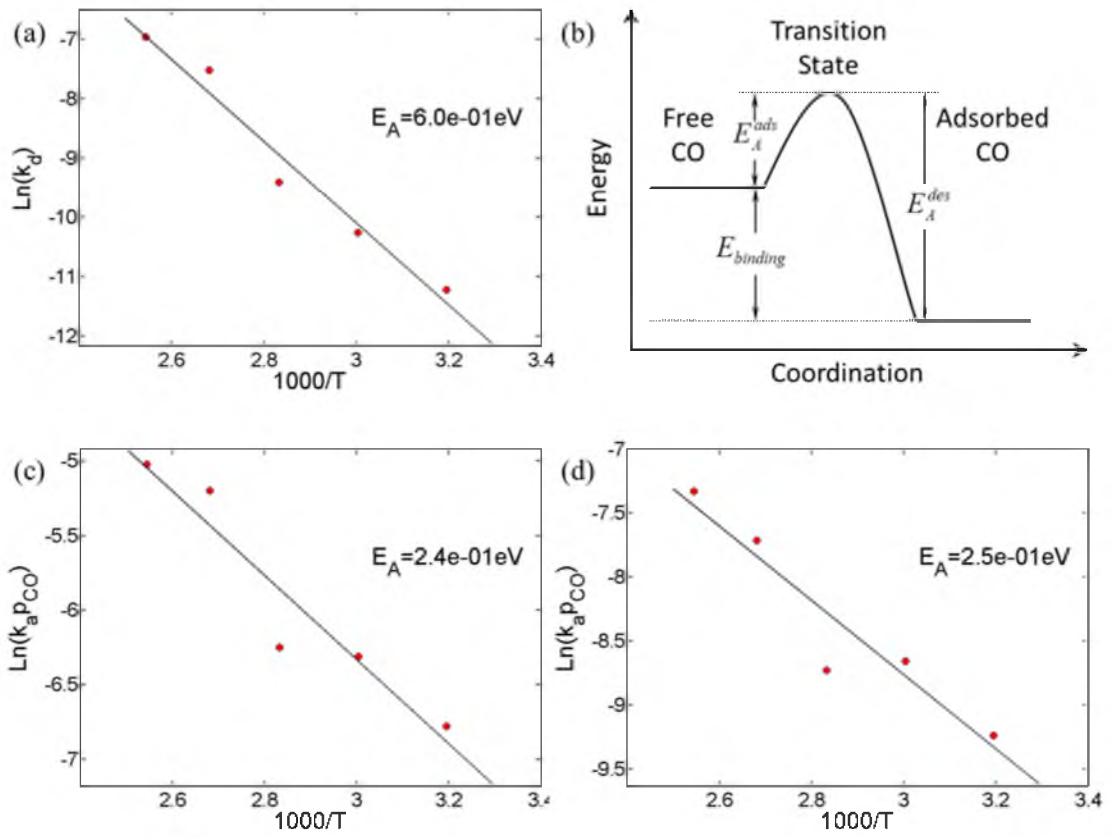

Figure 8-11: Arrhenius plots. (a), (c) and (d): Arrhenius plot of k_d, $k_a^I p_{CO}$ and $k_a^{II} p_{CO}$, respectively. (b) A schematic showing the free energy of CO at different adsorption coordinations.

is very reasonable by considering thermodynamic data. Therefore, the interaction between CO molecule and Pt atom is not as strong as chemical bonding, and it favors physisorption over chemisorption.

8.4.5 Surface Site Density

CO adsorption on well-defined Pt (111) surface has been thoroughly studied by G. Ertl [4]. In his study, the CO coverage can reach nearly one monolayer, which corresponds to

$1.5\times10^{15}cm^{-2}$. In the present study, the surface site density can be determined from the slope of linearized adsorption plot. Since there are two independent adsorption processes, the total available surface site for each process is also independent and is calculated separately. Figure 8-12 summarizes the value of S_0 at different temperatures. Both S_0^I and S_0^{II} are relatively constant at all temperatures tested. This result is very reasonable, because surface site density is determined only by number of available surface sites, which should be independent on temperature.

8.4.6 General Application

Both adsorption isotherm and charge transfer between adsorbent and Pt film are considered in the present model. It can be seen that CO can be replaced by any other gas

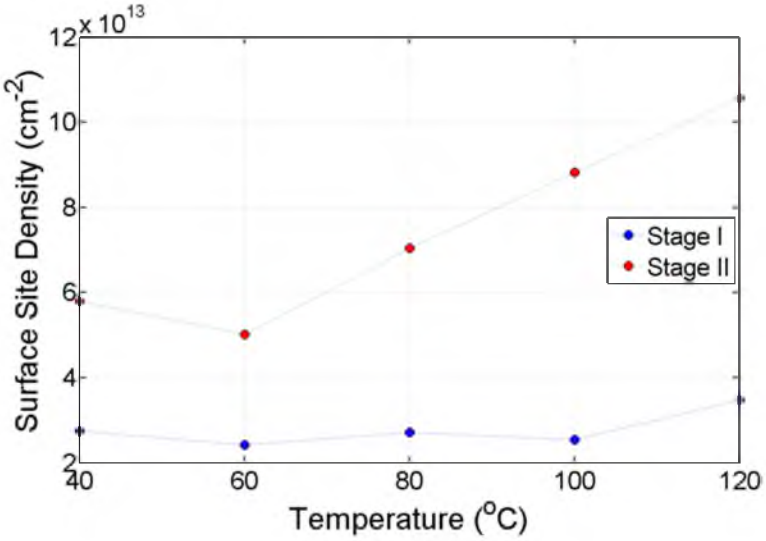

Figure 8-12: A plot of surface site density at all measured temperatures. The value of S_0 is almost constant at different temperatures.

species as long as it doesn't introduce other kinetic processes, while the feasibility of the current technique is maintained. As for the application of PEMFCs and other catalytic devices, the adsorption kinetics of other detrimental gases besides CO needs to be studied. For example, SO2 is detrimental. The current technique could provide very important information.

8.5 Summary

An electrochemical cell is designed to study the adsorption and desorption kinetics of carbon monoxide on Pt nano thin film. Due to the difference in electron affinity, electron transfers from Pt to CO molecule upon adsorption. For a 1 nm thin Pt film, there are only four atomic layers. Once CO covers the whole surface, the number of free electron decreases significantly. The decrease in free electron density leads to lower electronic conductivity, which can be in-situ measured with a high resolution multimeter. Upon CO adsorption, electronic resistance increases; upon CO desorption, electronic resistance decreases. A model is developed to interpret the resistance change based on Langmuir isotherm. From the desorption curve, CO desorption rate constant can be determined, and then from the adsorption curve, CO adsorption rate constant can be determined. It is found that there are different adsorption sites; as a result, two different adsorption rate constants are obtained.

8.6 References

1. W. Schmittinger and A. Vahidi, *J. Power Sources*, **180**, 1–14 (2008)

2. J.-M. Le Canut, R. M. Abouatallah, and D. A. Harrington, *J. Electrochem. Soc.*, **153**, A857 (2006)

3. J. J. Baschuk and X. Li, *Int. J. Energy Res.*, **25**, 695–713 (2001)

4. G. Ertl, M. Neumann, and K. M. Streit, *Surf. Sci.*, **64**, 393–410 (1977)

5. R. W. McCabe and L. D. Schmidt, *Surf. Sci.*, **66**, 101–124 (1977)

6. D. H. Parker, D. A. Fischer, J. Colbert, B. E. Koel, and J. L. Gland, *Surf. Sci.*, **258**, 75–81 (1991)

7. P. Waszczuk et al., *J. Electroanal. Chem.*, **511**, 55–64 (2001)